Linear and Star Block Copolymer Nano-architectures for Drug Delivery

A thesis

submitted in partial fulfilment of the requirements

for the degree of

Doctor of Philosophy

Mehak Malhotra

20132011

Indian Institute of Science Education and Research, Pune

2021

Dedicated to

My Nanu

For being the light that guides me

Declaration

I declare that this written submission represents my ideas in my own words, and where others' ideas have been included; I have adequately cited and referenced the original sources. I also declare that I have adhered to all principles of academic honesty and integrity and have not misrepresented or fabricated or falsified any idea/data/fact/source in my submission. I understand that violation of the above will be cause for disciplinary action by the Institute and can also evoke penal action from the sources that have not been properly cited or from whom proper permission has not been taken when needed.

Date: 15.07.2021

Mehak Malhotra

20132011

Certificate

Certified that the work incorporated in the thesis entitled

"**Linear and Star Block Copolymer Nano-architectures for Drug Delivery**"

submitted by

Ms Mehak Malhotra

was carried out by the candidate under my supervision.

The work documented in this thesis or any part of it has not been included in any other thesis submitted previously for the award of any degree or diploma from any other University or Institution.

Date: 15.07.2021

Prof. M. Jayakannan
PhD supervisor

Acknowledgements

This eight-year long journey has been no less than a roller-coaster ride of emotions filled with highs and lows. This journey has taught me resilience, patience, kindness, and empathy. All because I had the great fortune of meeting some of the kindest people filled with love for others. I have had the greatest adventures of my life during the course of this journey with the most spectacular bunch of people and I can't thank them enough. All their love, endless support and precious time has resulted in a beautiful culmination of this journey.

Foremost, I would like to express my sincere gratitude towards my thesis supervisor Prof. M. Jayakannan for his encouragement, constant support and guidance throughout the course of my PhD. His immense belief in me gave me the courage to explore unchartered territory and now that I look back, it has been an ever so rewarding experience. I thank him for believing in me without a shadow of a doubt and letting me pave my way. His passion towards science and his meticulousness have always inspired me. I thank him for shaping me into a scientist (a curious one!) and believing that I had what it took to be a successful one. Thank you Sir and I hope to make you proud someday!

A major contribution in shaping up the thesis is from the members of my Research Advisory Committee, Dr. Sandanaraj Britto and Dr. J. Nithyanandhan. Their constant evaluations, fiery questions, extremely useful suggestions and most importantly, their support has helped me to grow intellectually. I can't thank them enough for giving me their precious time.

This work would not have been possible without the state-of-the-art amenities provided by IISER, Pune. I would like to thank Dr. K. N. Ganesh**,** Former Director, IISER Pune for being the visionary responsible for making IISER, Pune the place "where tomorrow's science begins today". I thank IISER, Pune for supporting me financially for the first six years and CSIR, New Delhi for the remaining two years. I would like to thank Infosys Travel grant, IISER chemistry department, DST project fund and CSIR contingency for making it possible for me to attend International and National conferences.

I would like to take this opportunity to express my heartfelt gratitude to the most hardworking, devoted and helpful people in the IISER administration without whom I would have been

completely lost. A special shout out to Tushar sir, whom I always refer to as the “One-stop solution for all problems” for being ever so kind and willing to help, no matter what! Thank you, Sayalee Ma’am for being so very sweet and helpful regarding my fellowship related issues. It would not have been possible to carry out my work without the endless support of the Chemistry Technical staff, Mayuresh sir, Mahesh sir, Sandeep sir, Ganesh sir, Yathish sir, Megha ma’am, Hemlata ma’am and everyone else whom I may have missed. A special thanks to Mayuresh Sir, Mahesh sir and Megha ma’am, who have been my oldest connections here at IISER, Pune. I cannot explain in words how indebted I am to you people for showering me with so much love, respect and support. You people made everything easy, so Thank you for your generosity. I would also like to thank Kalpesh Sir for always lending a helping hand, especially with taking care of the tissue culture facility at G1. I want to thank Nilesh Dumbre sir and Anil sir for helping me always. I want to thank all the instrument operators at IISER, Pune for making my work so much easier, Nitin sir (NMR), Mahesh sir and Sandeep sir (MALDI/HR-MS), Megha ma’am (AFM), Anil sir and Yathish sir (FESEM), Prashant sir (HR-TEM).

I would like to thank all the staff at the IISER Pune imaging facility, National Centre for Gene Function in Health and Disease (NFGFHD) and BD Biosciences FACS facility for making all the *in vivo* work possible. A special mention to Vijay sir, Dhriti, Swati, Sonashree and Meenakshi who are responsible for whatever little I know about microscopy.

All the *in vivo* work in this thesis has been made possible by my collaborators Dr. Nixon M. Abraham and Ms. Meenakshi Pardasani. I can’t thank you enough for allowing me to use your lab facility and reagents and most importantly, for all the intellectual discussions, your precious time and effort. I would like to convey my sincere gratitude to Meenakshi for her willingness to teach me and showing patience when I made mistakes. Thank you, Meenakshi for being a great teacher and friend.

Special thanks to Ms. Shivani Bodas and Dr. Aurnab Ghose for providing me with the primary chick spinal culture and reagents for my uptake experiments (in chapter 5).

The chemistry and biology labs have been extremely gracious in providing reagents and open access to instrumentation, without which the thesis could not have been completed. I would also like to thank Dr. S. K. Asha for allowing me access to her lab facilities whenever needed

and also all the lab members for their constant help. Special thanks to Shekhar, Moumita and Shrikant for all their help and support. Thank you Moumita for helping me with SAXS measurements.

Research requires a conducive environment. I thank my lab members, past and present, for providing a healthy working environment, valuable suggestions during the lab meetings and for the constant questioning that always kept me on my toes. Special thanks to Dr. Bapurao Surnar, Dr. Sonashree, Dr. Bhagyashree (and the little bundle of joy, Sparsh), Dr. Nilesh Deshpande, Dr. Anantharaj, Anu, Sharada, Ruma, Rahul, Dheeraj and Akash for your willingness to help, intriguing scientific discussions and an enjoyable journey.

Thank you, Sonashree for always being there with your love and support, the morning chai routine, the beautiful Jeju experience, the crazy scientific discussions, and the most enjoyable tennis and poha sessions. I would like to thank Sharada for being the greatest student that I had the pleasure of mentoring. You made me a better teacher, thank you! Thank you, Bhagyashree for your constant support and for making me a massi! I would like to thank Ruma for being a great friend, for never saying no to any help I asked and for being so very sweet. Thank you, Reman for all the beautiful fun-filled memories.

Thank you, to my two closest and oldest friends, Lipsi and Kshitij! You guys have made me realize the meaning of true friendships. I want to thank you for always being there for me, no matter the long distance, for all your love and belief in me. Thank you, for never giving up on me and loving me immensely. This journey has been made special because of you guys.

I have been fortunate to have shared this journey with Bapurao Surnar, whose companionship I will forever cherish. I want to thank him for being an excellent mentor to me and making me a better researcher. His meticulous working culture, passion towards science and extreme devotion towards his work has always inspired me, something I aspire for myself too. Thank you, Bapu for sharing this journey with me, for happiness in the face of hardships, for your unyielding belief in me that made me realize my strengths. I can’t thank you enough for your kindness, respect and support, for teaching me the virtue of patience and for making me a better person. You made this journey memorable!

I can't imagine my PhD journey without my Int. PhD 2013 batch, by far the best group of people I have ever come across, the reason for my sanity. I have been so fortunate to have received all your love and there aren't enough words for me to thank you. You gave me a family for life, and I am forever indebted. Thank you, Aditi, Dhriti, Adarsh, Anshul, Deepak, Shivani, Swati, Sandy, Neelu, Ronnie, Bharat, Anish, Jay, Akhila, Divya, Amar, Kashyap and Harpreet for being the best batchmates ever! Thank you for all the travel diaries, the adventures, the dinners, the most interesting chat sessions, cooking sprees, for all the love, laughter and happiness, most importantly, for always checking up on me and not letting distance come between our friendships. You people are the reason for me getting here today, so thank you from the bottom of my heart.

My first friend on campus, Aditi! Like I always say, I could not have done this without you. You have been the best companion I could ever have asked for. Thank you, for always being there for me through thick and thin, for giving me the most cherished memories (there are so many!). Your resilience, hardwork and dedication have inspired me to do better. Thank you for being my constant pillar of strength, my partner in crime, my travel buddy, my go-to person.

A very special thanks to Tomin, my coffee buddy. You are an amazing human being with a golden heart. Thank you for always having my back, for being there when even I didn't know I needed a friend, for the love-filled coffee sessions and scintillating conversations. I am forever indebted to you for your love and your friendship.

I am so grateful for having had the opportunity to spend so much time with you, Dhriti (even though it was in the midst of a pandemic). You are an incredibly kind, empathetic and loving person. Thank you for showering me with so much love and care. I can't imagine reaching here if it weren't for your support. Thank you for giving me the pleasure of calling you my friend, a beautiful companion whom I will always cherish.

I am grateful for having met you Shivani Bodas, "pavam baccha"! Thank you for being such a fierce friend, with such a large heart and for all the love you have given me. I wish I had met you sooner.

Thank you Dhriti and Shivani for constantly feeding me, checking up on me and making sure my anxiety never got the best of me. Without you guys, this journey could not have been completed. Thank you for being a source of constant support.

Finally, I want to thank my lifelines and pillar of strength, my family! Their sacrifice and constant support is the reason for who I am today. Thank you, Papa, Mommy and Maggie, for loving me unconditionally, for believing in me always, for your words of encouragement. I would like to thank my grandparents, Nanu, nani, dadi and dadu for showering their love on me, for supporting me always and for making me feel special every single time. You are the reason for my happiness and your blessings have made it possible for me to achieve whatever little I have been able to. I can't thank my family enough. They have stood by me always, with no questions asked and allowed me to make my way in this world with their unwavering faith in me. You people are my inspiration to do better always! Thank you, Papa for making me realize my worth, Mommy for teaching me resilience and patience, Maggie for giving me a reason to keep proving myself. Thank you, Nanu for being my compass and always guiding me to do what's right. Your unyielding belief and love in me has made me the person I am today and I promise you that I will always strive to do better and be better and make you proud. Thank you, to my uncles and aunts, bhua, jiju, mamu and mami, for their love and blessings.

"I took the road less travelled by,
And that has made all the difference."
-Robert Frost

Abstract

Conventional chemotherapeutic clinical drugs are predominantly small molecules and they have many limitations such as poor biodistribution, lacking target specificity, short half-life and consequential side effects like cardiotoxicity, nephrotoxicity and neurotoxicity, etc. This obstacle in cancer treatment led to the development of "polymer therapeutics" that offer the advantage of passive selectively targeting the tumor tissue via the enhanced permeability and retention (EPR) effect. Herein, aliphatic polyesters seem to have gained impetus as polymeric drug delivery vehicles owing to their biodegradability facilitated by enzymes at the intracellular compartments, especially paving way for the environmentally stable and structurally tunable polycaprolactone (PCL) based scaffolds. The underlying principle of the thesis is to engineer amphiphilic fully biodegradable PCL nano-scaffolds and investigate the impact of polymer architecture on macromolecular self-assembly along with the ability to cross biological barriers. In this thesis work, new classes of amphiphilic linear block and random copolymers were developed via ring opening polymerization of ε-caprolactone and tailor-made ɣ-carboxylic substituted caprolactone. The difference in polymer topologies manifested in their solid-state assemblies, wherein the block copolymers were semi-crystalline in nature as opposed to the amorphous random copolymers. Their aqueous self-assemblies resulted in the formation of stable spherical nanoparticles with excellent loading capability of anticancer drug doxorubicin (DOX) in the hydrophobic pocket. These polymer scaffolds were found to be stable under physiological conditions and the *in vitro* release kinetics revealed selective rupturing in the presence of lysosomal esterase enzyme to deliver DOX at the intracellular compartment. The cytotoxicity study exhibited that the nascent polymers were highly biocompatible whereas the DOX-loaded nanoparticles resulted in > 90 % cell death. Further efforts have been taken to tweak the polymer architecture from linear to the highly branched star-shaped architectures to build single chain polymer nano-carriers, i.e. unimolecular micelles (UMs) whilst maintaining the same chemical composition and molecular weight. DOX-loaded unimolecular micelles were studied *in vivo* to understand the role played by polymer topology on the biodistribution, renal clearance, RES uptake of the star-shaped polymer UMs versus the linear polymer aggregated micelles. The UMs were able to selectively cross the impermeable blood brain barrier, evade RES uptake and result in reduced cardiotoxicity. The star-shaped architectures were further decorated with neutral, anionic and cationic charges and their respective UMs were studied to understand the role of surface charge on the ability of these single chain polymer nano-carriers to penetrate the cellular membrane and investigate the endocytosis mechanism.

Synopsis

Synopsis

Macromolecular drug delivery platform came into existence in 1975, when Helmut Ringsdorf proposed the first ever model of an ideal polymeric drug delivery nanocarrier. This advent changed the cancer treatment scenario wherein the conventional chemotherapeutic drugs are being replaced by nano-formulations. These formulations were developed to overcome the limitations of the small molecule drugs including reduced bioavailability, systemic toxicity, early clearance, and immunogenicity. For this purpose, fully biodegradable polycaprolactone based block copolymers seem to be an obvious choice owing to their well-established enzymatic degradability. The present thesis work focussed on primarily developing linear block and random copolymers from the carboxylic substituted caprolactone monomer via ring opening polymerization and studying them as doxorubicin delivery carriers *in vitro*. This understanding led to the development of higher order architectures like the star-shaped block copolymers and in combination with linear polymers were used to investigate the role of polymer topology on the *in vitro* and *in vivo* behavior. The star-shaped polymer architectures were further tweaked to design anionic, neutral and cationic nanoparticles to elucidate their interactions with cell membrane based on charge differentiation. The thesis has been divided into the following five chapters:

1. **Chapter 1**: This chapter compiles a detailed literature review starting from the need for nanoparticle-mediated drug delivery to the different types of nanoparticles available for use. Further attention was drawn to the various nanoparticle attributes that govern their biodistribution, pharmacokinetics and clearance. This was followed by the evolution of the polymeric drug delivery systems since their advent till date. Then the need for the development of unimolecular micelles was highlighted and the various topologies that can lead to their formation were discussed. Finally, the numerous biodegradable block copolymers were listed with their limitations and the aim of the thesis was described.
2. **Chapter 2**: Fully biodegradable amphiphilic polycaprolactone linear random and block copolymers were synthesized via ring opening polymerization. The impact of variation in composition of the hydrophobic and hydrophilic counterparts on the enzymatic cleavage of nano-scaffolds was investigated followed by their *in vitro* drug delivery capability in breast and cervical cancer cell line.

3. **Chapter 3**: Novel 6-arm star-shaped polycaprolactone block copolymers were devised using the in-house melt reactor set-up to achieve high molecular weight polymers with narrow polydispersity. Their self-assembly into unimolecular micelles was studied and compared to the conventional aggregated micelles for their drug loading content and *in vitro* cellular internalization in WT-MEF cells.
4. **Chapter 4**: The star and linear block copolymer DOX loaded nanoparticles were employed to understand the role of polymer topology on the *in vivo* biodistribution and pharmacokinetics. The ability of star block copolymer to breach the blood brain barrier was investigated at length via confocal imaging analysis.
5. **Chapter 5**: The star shaped block copolymers were tweaked in order to design nanoparticles with variable surface charges. These anionic, neutral and cationic nanoparticles were subjected to *in vitro* cellular uptake studies in WT-MEF, HEK293T and chick spinal neurons. The surface charge interactions with the membrane and the endocytosis pathway were investigated.

In chapter 2, the polymer topology design principle was investigated for programming the enzymatic-biodegradation and delivery of anticancer drugs at the intracellular compartments of breast and cervical cancers. To accomplish this goal, new classes of biodegradable amphiphilic block and random copolymers based on hydrophilic carboxylic functionalized polycaprolactone (CPCL) and hydrophobic polycaprolactone (PCL) units were designed via ring opening polymerization methodology. The inter-chain interactions and chain packing were directly controlled by the topology of the polymers and the block copolymers were found to be as semi-crystalline materials. These amphiphilic block and random polymers were readily dispersible in water and they self-assembled into < 200 nm nanoparticles.

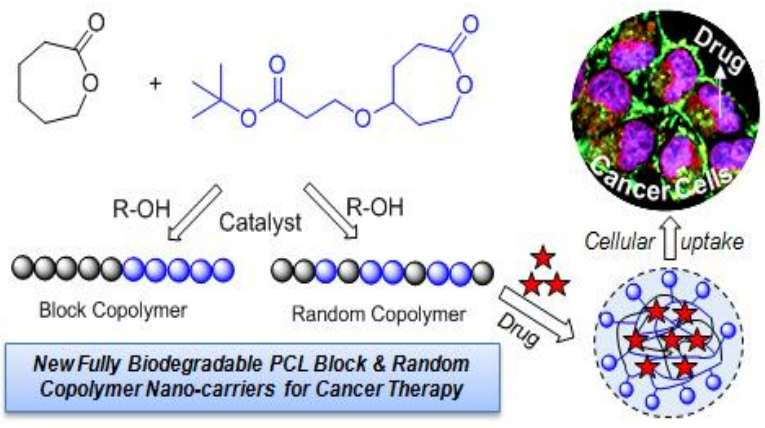

These nanoparticles exhibited excellent capability for loading anticancer drug doxorubicin (DOX) in the hydrophobic pocket. *In vitro* drug release kinetics revealed that the polymer nano-scaffolds were stable under physiological conditions and they exclusively ruptured in the presence of lysosomal esterase enzyme at the intracellular compartments to deliver DOX. The "burst" and "controlled" release of drugs from the polymer nano-carriers was directly controlled by length and chemical composition of block and random copolymers. *In vitro* cytotoxicity studies in breast cancer (MCF 7) and cervical cancer (HeLa) cells revealed that the nascent polymer nanoparticle was highly biocompatible and non-toxic to cells whereas their DOX loaded nanoparticles accomplished > 95 % cell killing. Confocal microscopy reinstated the cellular uptake of the DOX-loaded polymer scaffold wherein the nanoparticle was highly concentrated at the nucleus and revealed that the drugs were predominately delivered at the nucleus of the cells for apoptosis. Flow cytometry investigation confirmed the enhanced DOX delivering capability of block and random copolymer nanoparticles compared to free DOX. The newly designed fully biodegradable PCL based block and random nano-carriers are excellent scaffolds for enzyme-mediated intracellular delivery of DOX and the proof-of-concept was established in breast and cervical cancers.

In chapter 3, the impact of polymer architecture on macromolecular self-assembly and the ability to cross biological barriers has been investigated and this can help devise efficient nano-carriers to overcome the bottlenecks in the field of Polymer therapeutics. The idea was to understand if topological tweaks in architecture did in fact transcend directly onto their drug loading capability, self-assembly and *in vitro* cellular uptake kinetics of anticancer drug Doxorubicin. In order to accomplish this task, we opted to draw a comparison between the star and linear polymer topology by maintaining similar chemical composition and molecular weight. Herein, fully biodegradable amphiphilic

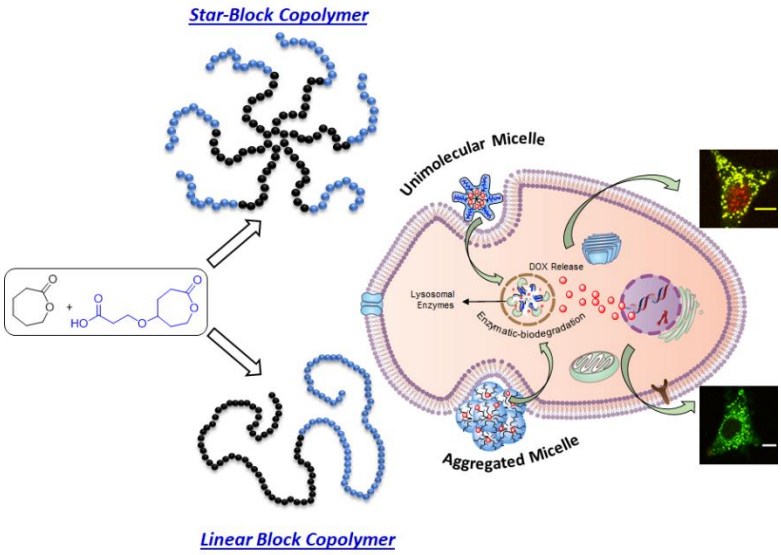

caprolactone based star and linear block polyesters were designed using an in-house tailor-made melt reactor set up. The 6-arm star block copolymers self-assembled in water to result in unimolecular micelles (UMs) in the size range of 18-30 nm as opposed to the multimolecular micelle formation of ~ 200 nm size for the linear block counterpart. The topology difference influenced the drug loading content capability of these nano-carriers wherein the star-shaped unimolecular micelles exhibited a 7-fold higher loading of the anticancer drug Doxorubicin with a DLC of ~ 14 %. The polyester backbone of the star block copolymer underwent complete degradation in the presence of esterase enzyme replicating the intra-cellular lysosomal compartment *in vitro*. The star block copolymer was found to be highly cyto-compatible and non-toxic to the Wild-type mouse embryonic fibroblast (WT-MEF) cell lines up to a concentration of 500 µg/ml. The DOX-loaded nano-carriers exhibited higher cell viability in comparison to free DOX after a 72 h incubation with WT-MEF cells. The live cell experiment in WT-MEF cells demonstrated the cellular uptake pathway of the UMs to be via endocytosis followed by lysosomal degradation and release of DOX into the nucleus. The unimolecular micelle cellular uptake was significantly higher than the linear polymer and the free DOX. Thus, the star-shaped unimolecular micelles proved to be excellent drug delivery candidates *in vitro* and should be exploited for *in vivo* applications.

In chapter 4, efforts have been put to understand nanocarrier mediated therapeutic delivery across the impermeable blood brain barrier (BBB). The next generation smart BBB crossing nanocarriers are mandatorily designed to be substantially stable to evade disassembly under infinite dilution *in vivo*, tiny-size sub-nanometer objects for penetrating the tightly regulated t-junction, high drug loading content, reduced cardiotoxicity, and most importantly biodegradable under physiological conditions. This multi-task problem has been addressed here by carefully choosing the two radically opposite

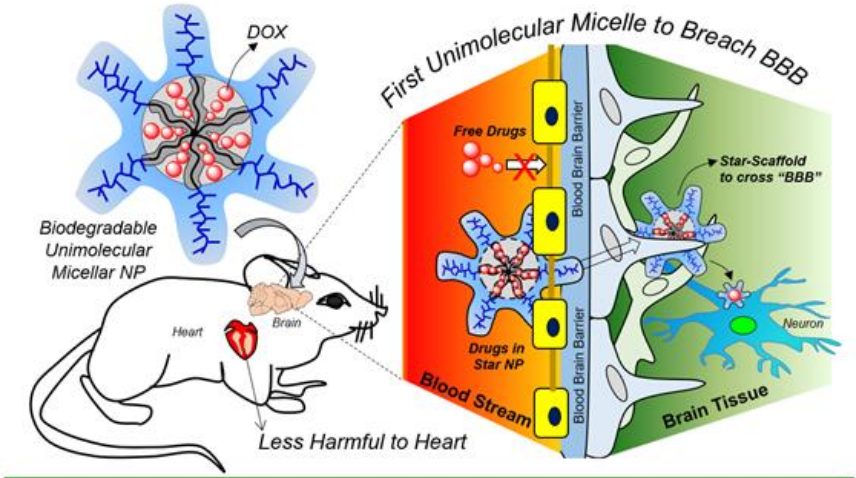

polymer architectures, i.e. the linear di-block and star-block topologies based on the biodegradable polycaprolactone (PCL) backbone. Amphiphilic linear and star-block PCL copolymers having identical chemical constituents and high molecular weights of 40-60 kDa with narrow polydispersity were structurally engineered using tailor-made functional caprolactone monomers via ring opening polymerization process, as has been explained at length in the previous chapter. The idea was to optimize the new star-shaped unimolecular micelle (UMM) nanocarriers, for the first time, to overcome the bottlenecks in the field of BBB crossing. The star polymer DOX loaded core-shell UMM of 25 ± 2.0 nm size and 14 % drug loading content (DLC) along with the linear polymer DOX-loaded aggregated micelle of 200 ± 10 nm size and 2 % DLC were chosen for comparison. *In vivo* studies established that the DOX loaded UMM exhibited very good stability under blood circulation with $t_{1/2}$ of 4.0 h and together with significant reduction in the cardiotoxicity in heart tissues. The UMM nano-vector has shown remarkable efficiency to breach the blood brain barrier and nearly 8 % of total taken up drug in mice was delivered to brain tissues which is equivalent (or above) to the bench-mark trend in BBB research. Confocal microscopic imaging of brain tissues confirmed that the BBB heterogeneity caused the uptake to decrease on going from the posterior to the anterior parts of the brain and the MAP 2 antibody staining revealed their localization within the mature neurons in the brain tissue. The newly designed star-shaped biodegradable UMM nanocarriers did not exhibit immunogenicity or any necrosis in the tissue highlighting their importance for long term impact in biomedical field including BBB research.

In chapter 5, nanotechnology mediated drug delivery in the field of cancer treatment has been revisited. The major hurdles faced by nanocarriers *in vivo* include opsonization leading to clearance via phagocytosis, non-specific interactions, systemic toxicity and renal clearance resulting in shorter half-life. Engineering the nanoparticle size, shape and surface properties can help overcome the aforementioned barriers. In this regard, surface charge plays a vital role in the nanoparticle colloidal stability, cellular internalization, biodistribution and pharmacokinetics. To this effect, star-shaped polycaprolactone based anionic, neutral and cationic block copolymers were designed maintaining the same topology, chemical composition and molecular weight with the only variation in their net surface charge. These star-block copolymers self-assembled into 40-100 nm size spherical nanoparticles with zeta values ranging from -40.7 mV to 33.2 mV. The anionic, neutral and cationic nanoparticles successfully encapsulated dye molecules such as Nile red (neutral dye) and 8-Hydroxypyrene-1,3,6-trisulfonic acid trisodium salt (anionic dye) whilst maintaining their morphology. The nanoparticles exhibited biocompatibility in WT-MEF cells up to a concentration of 50 µg/mL. Cellular uptake investigation executed in WT-MEF and HEK293T cells revealed the effect of surface charge on the ability to permeate cellular barriers as a function of the endocytosis pathway. Herein, anionic and neutral nanoparticles demonstrated much better uptake in WT-MEF cells via the caveolae-mediated endocytosis. On the other hand, the uptake of cationic nanoparticles was the most promising in HEK293T cells and they preferred internalization via the clathrin-mediated endocytosis. The neuronal cells also exhibited higher uptake of cationic nanoparticles owing to the presence of the clathrin pathway. Thus, these star-shaped anionic, neutral and cationic block copolymers proved to be excellent delivery candidates *in vitro* and should be exploited for *in vivo* applications, specifically their ability to cross the blood brain barrier dependent on their surface charge.

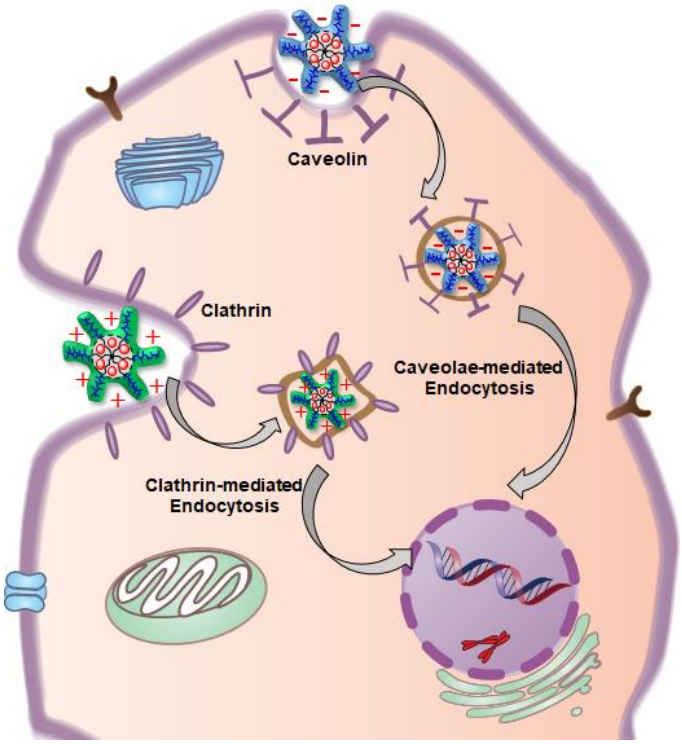

To conclude, star-shaped DOX loaded unimolecular micelles proved their mettle as efficient drug delivery nanocarriers with the unique ability to beach the blood brain barrier without any active targeting approach along with reduced cardiotoxicity overcoming the limitation of DOX. The thesis work gave a fundamental insight into the effect of polymer topology on all aspects of self-assembly, *in vitro* cellular internalization and *in vivo* biodistribution and pharmacokinetics. These polycaprolactone block copolymers were non-immunogenic with no hemolysis to the RBCs and no toxicity to the tissues. The surface charge variation led to difference in the endocytosis mechanism across different cell types. All of these observations have been summarized in the last chapter of "Summary and Future Directions". This thesis work has opened up avenues for the further exploitation of higher order architectures moving towards *in vivo* preclinical trials.

Table of Contents

Abstract 9

Synopsis 10

1 Introduction 22

1.1 Nanoparticle vs. Small Molecule 23

1.2 Types of Nanoparticles (NPs) 24

1.2.1 Lipid-based NPs 25

1.2.2 Inorganic NPs 25

1.2.3 Polymeric NPs 26

1.3 Impact of Nanoparticle attributes on Biodistribution, Pharmacokinetics and Clearance 28

1.3.1 Shape 29

1.3.2 Size 31

1.3.3 Charge 32

1.4 Evolution of Polymeric Drug delivery systems (DDS) 34

1.5 Unimolecular Micelles vs. Aggregated Micelles 36

1.5.1 Dendrimers 38

1.5.2 Hyperbranched 40

1.5.3 Brush-shaped 42

1.5.4 Star-shaped 43

1.6 Biodegradable polymers 46

1.7 Aim of the Thesis 52

2 Biodegradable Polycaprolactone Block and Random Copolymer Architectures for Drug Delivery to Cancer Cells 55

2.1 Introduction 57

2.2 Experimental Methods 60

2.2.1 Materials 60

2.2.2 Methods 61

2.2.3 Synthesis Procedures 62

2.2.4 Self-assembly of copolymers 71

2.2.5 Drug Encapsulation in the Copolymer Scaffolds 71

2.2.6 *In vitro* Drug Release Studies 71

2.2.7 Cell Viability Assay (MTT Assay) 72

2.2.8 Cellular Uptake of DOX-loaded Polymeric Nanocarriers by Confocal Microscopy 72
2.2.9 Flow Cytometry Measurements 73
2.3 Results and Discussion 73
2.3.1 Synthesis of Amphiphilic PCL Random Copolymers 73
2.3.2 Synthesis of Amphiphilic PCL Block Copolymers 78
2.3.3 Polymerization kinetics 81
2.3.4 Thermal Properties 83
2.3.5 Self-assembly and Encapsulation Capabilities 85
2.3.6 Drug Encapsulation 90
2.3.7 Enzyme-Responsive Drug Delivery 92
2.3.8 Cytotoxicity and Cellular Uptake 97
2.4 Conclusion 102
3 Development of Star block copolymer Unimolecular Nano-carriers: In vitro Cellular Uptake 104
3.1 Introduction 106
3.2 Experimental Methods 111
3.2.1 Materials 111
3.2.2 Methods 112
3.2.3 Synthesis Procedures 113
3.2.4 Self-assembly of copolymers 117
3.2.5 Photophysical studies 118
3.2.6 Drug Encapsulation in the Copolymer Scaffolds 118
3.2.7 *In vitro* DOX Release kinetics 118
3.2.8 Cell Viability Assay (MTT Assay) 119
3.2.9 Monitoring Cellular Uptake of DOX-loaded Polymeric Nanocarriers by Live cell experiment 120
3.3 Results and Discussion 121
3.3.1 Synthesis and structural characterization of PCL based Star architecture block copolymers 121
3.3.2 Self-assembly and Photophysics 130
3.3.3 DOX Encapsulation and Enzymatic Degradation 135
3.3.4 Cytotoxicity and Cellular Uptake 139
3.4 Conclusion 149
4 Tweaking Polymer Topology to Breach Blood Brain Barrier Together with Reduced Cardiotoxicity: In Vivo Analysis 151
4.1 Introduction 153
4.2 Experimental Methods 157
4.2.1 Materials 157

4.2.2 Methods ... 158
4.2.3 Mice handling and injection of nano-vehicles ... 158
4.2.4 Biochemical analysis of organs and blood samples ... 159
4.2.5 Histological analyses of organs ... 160
4.2.6 Quantification of biodistribution of Doxorubicin in organs using confocal microscopy ... 160
4.2.7 MAP 2 Antibody staining ... 161
4.2.8 Immunogenicity Analysis ... 161
4.2.9 Hemolysis Assay ... 162
4.2.10 Statistics ... 163
4.3 Results and Discussion ... 163
4.3.1 Biodistribution and Pharmacokinetics ... 163
4.3.2 Immunogenicity, Histology and Hemolysis ... 166
4.3.3 DOX uptake visualization using Confocal imaging ... 169
4.3.4 Blood Brain Barrier Crossing ... 178
4.4 Conclusion ... 182
5 Role of Surface Charge on the Star-Block Nanoparticle Cellular Internalization ... 183
5.1 Introduction ... 185
5.2 Experimental Methods ... 189
5.2.1 Materials ... 189
5.2.2 Methods ... 190
5.2.3 Synthesis of the carboxylate substituted star-block copolymers SB-X (Anionic) ... 191
5.2.4 Synthesis of the chlorine substituted star-block copolymers SB-X (Cationic) ... 191
5.2.5 Self-assembly of copolymers ... 191
5.2.6 Dye Encapsulation in the Copolymer Scaffolds ... 191
5.2.7 Cell Viability Assay (MTT Assay) ... 192
5.2.8 Monitoring Cellular Uptake of NR and HPTS-loaded Star block polymer Nanocarriers ... 193
5.2.9 In vitro cellular uptake in Primary Neuronal cells ... 193
5.3 Results and Discussion ... 194
5.3.1 Synthesis of PCL based Star architecture block copolymers ... 194
5.3.2 Self-assembly and Dye Encapsulation ... 196
5.3.3 Cytotoxicity and Cellular Uptake ... 202
5.4 Conclusion ... 211
6 Summary and Future Directions ... 212
7 References ... 217

8 List of Publications 248

9 Appendix 250

1

Introduction

1.1 Nanoparticle vs. Small Molecule

Cancer is one of the leading causes of mortality, as per the recent report by World Health Organization (WHO) in March 2021. The uncontrolled autonomous growth of cells resulting from genetic mutations or environmental factors is referred to as "Cancer". The progress of cancer can be accredited to the inactivation of tumor suppression genes such as p53 that are responsible for programmed cell death, i.e. Apoptosis in case of failure to repair the DNA damage; or oncogenes such as RAS responsible for inducing tumorigenesis[1]. The most often used treatments to cure, shrink or stop the progression of cancer are as follows: i) surgical removal of cancer, most often used for solid tumor, ii) chemotherapy, iii) radiation therapy, iv) adjuvant therapy, v) hormone therapy, vi) immunotherapy depending upon the stage and type of cancer.[2] Amongst the aforementioned arsenal of therapeutic treatments, Chemotherapy has been exploited the most and it dates back to the 1930s, wherein a German scientist Paul Ehrlich proposed the concept of using alkylating agents as chemotherapeutic drugs.[3]

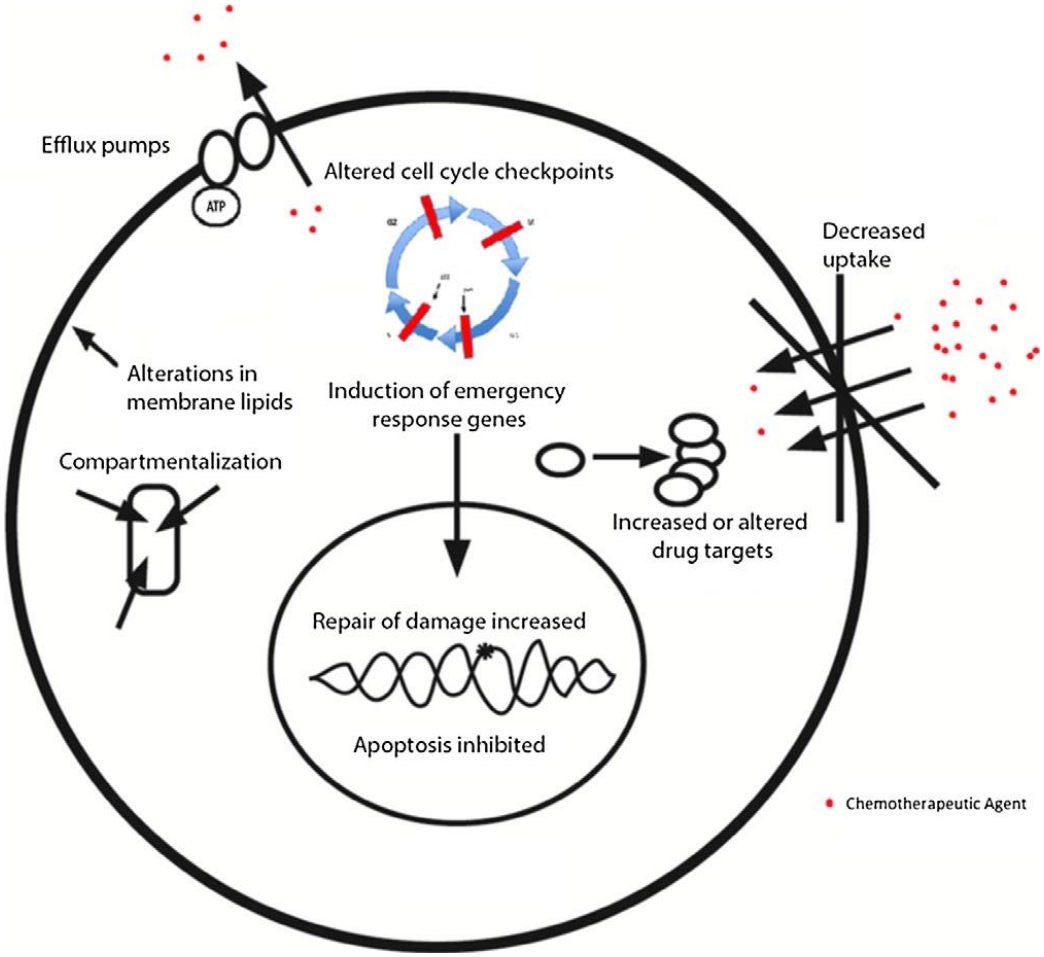

Figure 1.1. *Multidrug resistance (MDR) mechanism of cancer cells (adapted from Cerqueira et al. Eur. J. Pharm. Biopharm.* **2015**, *97, 140–151).*

Conventional chemotherapeutic clinical drugs are predominantly small molecules and they have many limitations such as poor biodistribution, lacking target specificity, short half-life, low therapeutic index and consequential systemic side effects like cardiotoxicity, nephrotoxicity, and neurotoxicity, etc.[4] Another reason contributing to the growing failure of chemotherapy is the rise of multi-drug resistance (MDR) that renders the drugs ineffectual due to increased resistance as well as increased efflux out of the cells by the P-glycoprotein (P-gp) pumps.[1] Nanotechnology has emerged as the answer to these problems in terms of overcoming systemic and cellular biological barriers translating to improved half-life and biodistribution, differentiating between normal and cancer cells resulting in reduced cytotoxicity, increased solubility and non-immunogenicity.[4,5]

1.2 Types of Nanoparticles (NPs)

Nanotechnology refers to the engineering of materials in the size range of 5-250 nm at the molecular level that offers the following advantages when employed for pharmaceutical applications: i) enhanced and targeted delivery of drugs with poor solubility, ii) drug delivery across the tightly regulated endothelial and epithelial barriers via transcytosis, iii) combination therapy by co-delivery of multiple therapeutic entities, iv) use as theranostic tool to achieve visualization along with the drug delivery application, v) real-time *in vivo* tracking of drug biodistribution etc.[4,6,7]

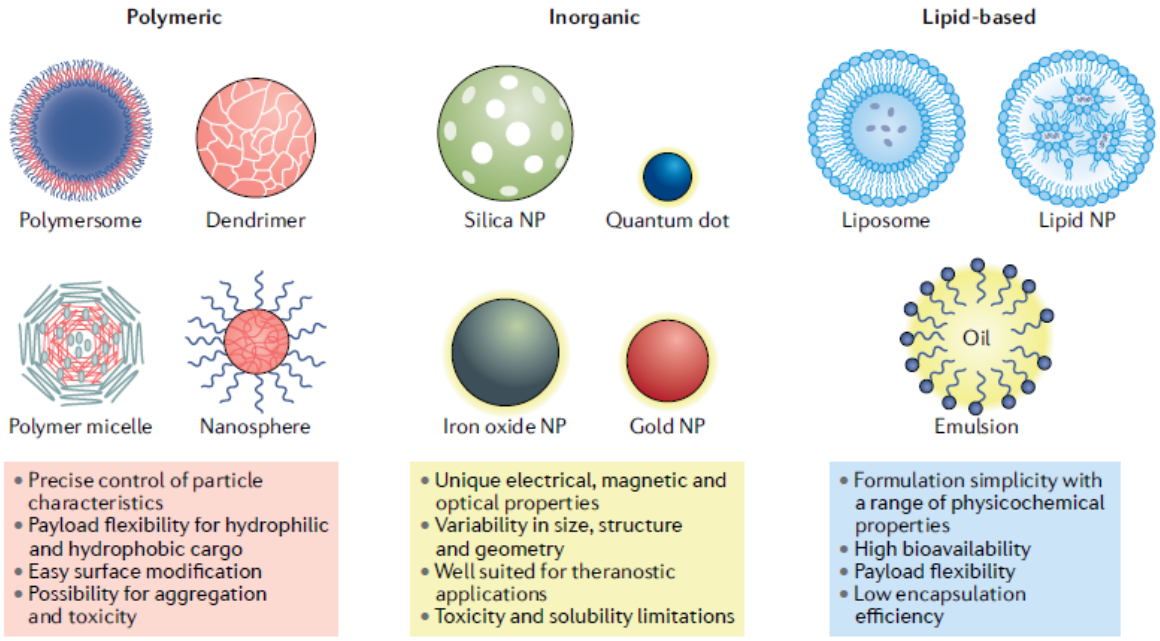

Figure 1.2. *Various classes of nanoparticles (NPs) (adapted from Mitchell et al. Nat. Rev. Drug Discov.* ***2021****, 20, 101–124).*

1.2.1 Lipid-based NPs

This class of NPs is the most commonly exploited nanotechnology-based FDA-approved drug delivery platform, since the first ever formulation was approved in the 1990s for cancer treatment. Liposomes are spherical colloidal structures composed of a lipid bilayer surrounding an aqueous compartment with sizes around 100 nm and above.[8] The lipid bilayer is commonly composed of phospholipids and these determine the surface properties such as charge, size and permeability of the liposomal formulations.[4] The lipid bilayer, in the presence of aqueous medium, folds into a vesicular architecture trapping an aqueous space that is capable of encapsulating hydrophilic, hydrophobic as well as lipophilic cargo. Liposomal formulations offer great advantages as drug delivery vehicles in terms of their biocompatibility, large capacity for loading drug molecules, high bioavailability etc.[9] An important example is the PEGylated-liposome containing the anticancer drug Doxorubicin (DOX), namely Doxil that exhibited 100-times longer half-life than free DOX as well as reduced cardiotoxicity. It was first employed for the treatment of AIDS-related Kaposi's sarcoma and is now being used to treat patients with multiple myeloma and ovarian cancer.[10] However, the major limitations in liposomal drug delivery are the inability to control drug release kinetics, inefficient intracellular drug delivery and easy uptake by the reticuloendothelial system (RES).[9,10]

1.2.2 Inorganic NPs

Inorganic NPs demonstrate unique magnetic, optoelectronic, plasmonic properties coupled with precision synthesis and control over size/shape rendering them ideal for various imaging, diagnostics, drug delivery and photothermal therapy applications.[11–14] Typically comprised of mesoporous silica NPs (MSNs), Gold nanoparticles (Au NPs), iron oxide NPs, carbon-based structures (carbon nanotubes), these inorganic NPs have demonstrated wide-spread usage in the field of drug delivery and bioimaging. MSNs are basically silica-based nanoparticles with numerous mesopores in a stable structure, high surface area, facile functionalization, and sizes in the range of 50-300 nm.[15] Being biocompatible with reduced immune response, these NPs have been used for delivery of drugs, genes, enzymes etc.[16–19] The other widely used inorganic NPs are the gold nanostructures that are used in various forms such as nanocages, nanorods, nanospheres etc. Their unique photothermal and optical

properties makes them highly suitable for both cancer treatment and diagnostic applications.[11,20–23] In a particular example, Au nanocages with PEGylated surface exhibited significant tumor reduction in mice via photothermal treatment monitored via PET imaging.[24] Iron oxide nanoparticles have gained traction recently as the most FDA-approved medicines amongst inorganic NPs and their superparamagnetic properties makes them ideal candidate for not only drug delivery but also as contrast agents and for thermal therapy.[12,13,25] However, their poor solubility and non-biodegradable structures makes them toxic for clinical applications *in vivo*.

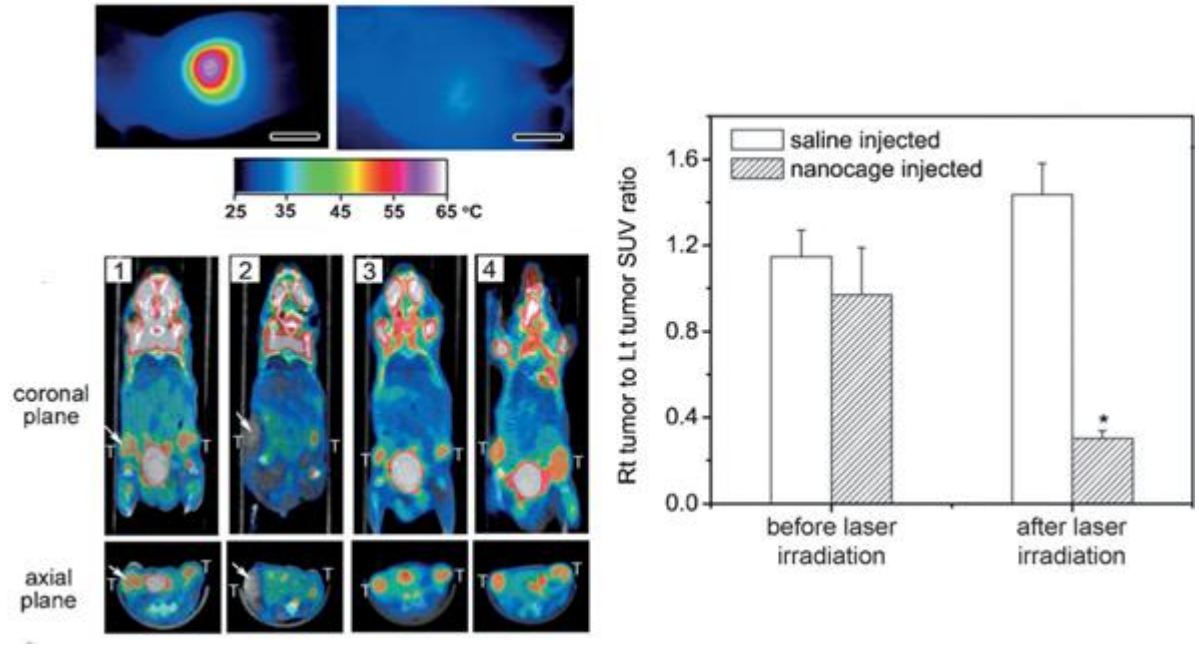

Figure 1.3. *Figures depicting the in vivo data of a tumor-bearing mice injected with PEGylated Au nanocages exposed with NIR laser and monitored the tumor after irradiation (adapted from Sun et al. Angew. Chem. Int. Ed.* **2014**, *53, 12320 – 12364)*

1.2.3 Polymeric NPs

Polymeric NPs are by far the most often utilized drug delivery carriers owing to their biocompatibility, easy functionalization, relatively facile formulations and control over molecular weight, surface properties, hydrophobicity etc. These can be composed of both natural or synthetic molecules, wherein the synthetic polymers exhibit the advantage of tunability in terms of composition, architecture, molecular weight and surface charge.[26,27] They

demonstrate the ability to efficiently load both hydrophobic as well as hydrophilic dye/drug molecules in the polymer core or matrix as well as via chemical conjugation to the NP with better control over drug release kinetics.[28–32] Another important application of polymeric NPs is the ability to co-deliver multiple therapeutic moieties such as small molecules like drugs and large biomacromolecules like oligopeptides, proteins, genes and siRNA.[33–35] The various substructures in this class of NPs are the polymersome, polymeric micelles, polymeric nanoshells and dendrimers. Polymersomes are similar to liposomes in their bilayer assembly with the difference being in the fact these are synthetic/artificial vesicles mostly composed of amphiphilic block copolymers based on polyethylene glycol and poly(dimethylsiloxane).[36–38] Their improved water solubility, biocompatibility and stable formulations has rendered them useful for drug delivery applications.[39] Polymeric micelles are self-assembled nanospheres composed of a hydrophobic core surrounded by a hydrophilic shell that allow for high drug loading content and readily modifiable surface to attach targeting ligands/drugs to achieve targeted delivery.[40] Numerous polymeric micelles are being tested in clinical trials, and a very small fraction has been FDA-approved, wherein Genexol-PM was the first ever polymeric micelle based system to enter clinical trials in the USA.[6] Dendrimers are frequently exploited for the delivery applications of drugs and nucleic acids;[41,42] wherein poly(amidoamine) (PAMAM) dendrimers are the favorite choice. Several dendrimer-based therapeutic nano-carriers have entered clinical trials for applications including transfection, drug delivery and as contrast agents.[43,44]

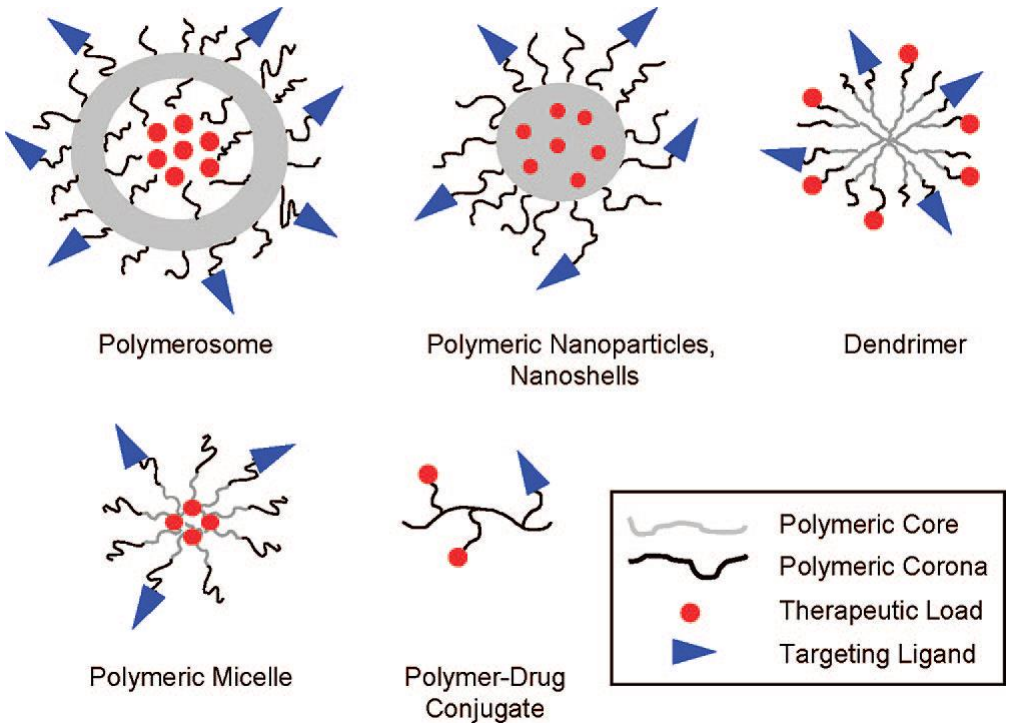

Figure 1.4. *Figure depicting various types of polymeric nanoparticles for drug delivery applications (adapted from Alexis et al. Mol. Pharm.* **2008***, 5,* 505-515*)*

1.3 Impact of Nanoparticle attributes on Biodistribution, Pharmacokinetics and Clearance

Nanoparticle mediated drug delivery relies on the stability, non-immunogenicity, longer half-life and reduced clearance for achieving effective and targeted delivery without any systemic toxicity. The physicochemical parameters of a nanoparticle determine their interactions with the local environmental factors such as serum proteins, phagocytes, monocytes, macrophages, dendritic cells etc.[45,46] The corona formation of serum proteins results in opsonization followed by reticuloendothelial system (RES) uptake, whereas interaction with phagocytic cells, especially macrophages, causes clearance by mononuclear phagocytic system (MPS). These non-specific interactions, in turn, reflect on the nanoparticle pharmacokinetics, biodistribution, clearance from the body and extravasation into tumor. Engineering the nanoparticle physicochemical parameters such as size, shape, surface charge, hydrophobicity etc. can, in principle, result in a biologically inert formulation with longer blood circulation time and reduced clearance.

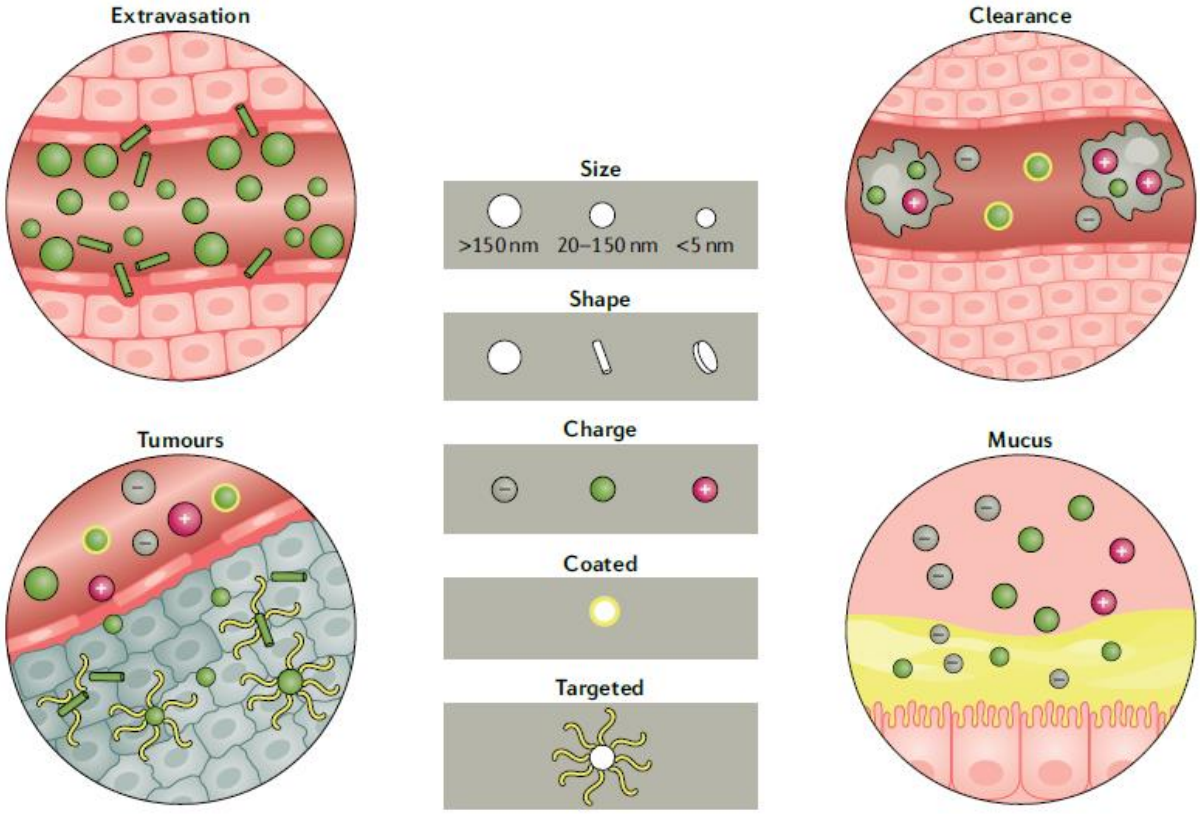

Figure 1.5. *Figure depicting the various nanoparticle attributes and their impact on extravasation, tumour accumulation, biodistribution and clearance (adapted from Mitchell et al. Nat. Rev. Drug Discov.* ***2021****, 20, 101–124).*

1.3.1 Shape

Nanoparticle shape greatly influences the clinical performance owing to their impact on membrane adhesion, cellular uptake ability and pathway, hydrodynamics and interactions with macrophages, vascular targets, serum proteins etc.[47–51] In a particular example, filomicelles (filament-like micelles) exhibited a 10-fold increase in blood half-life compared to the counterpart spherical micelles. The nanoparticle tendency to interact with macrophages is dependent on their internalization and attachment separately, which in turn determines the phagocytosis rate. This was investigated at length by Sharma et al. wherein the role of particle shape on the internalization and attachment separately by macrophages was studied.[52,53] They found that oblate ellipsoids exhibited much higher phagocytosis when compared to the prolate ellipsoids or the spheres. The internalization process during phagocytosis requires the remodeling of actin framework and lesser the remodeling required, faster the internalization.[54–

[56] Further, the nanoparticle interactions with MPS triggers an immune response characterized by the secretion of interleukins (ILs), tumor necrosis factors (TNF) and interferons resulting in inflammation and other toxic effects.[57] Rod-shaped nanoparticles have been known to exhibit higher phagocytic cellular uptake than star-shaped or spherical NPs and also resulted in greater inflammation in macrophages.[58–60] The figure 1.6 demonstrates examples of a few drug delivery carriers along with their representative shape/conformations and the repot by Fox et al. outlines the role of macromolecular shape and flexibility on pharmacokinetics, tumor penetration and glomerular filtration.[61] The loosely coiled flexible polymer can easily deform to pass through a pore, whereas dendrimers, hyperbranched polymers, proteins etc. adopt a more rigid sphere conformation that cannot deform for pore penetration without compromising on their stability. Elongated rigid rod like polymers can easily penetrate the tumor vasculature and for branched architectures to be able to achieve extravasation into tumor, there needs to be ample flexibility and stability that rely on the branching density. By increasing the number of arms, the renal filtration of these branched structures can be reduced thereby enhancing their blood half-life.

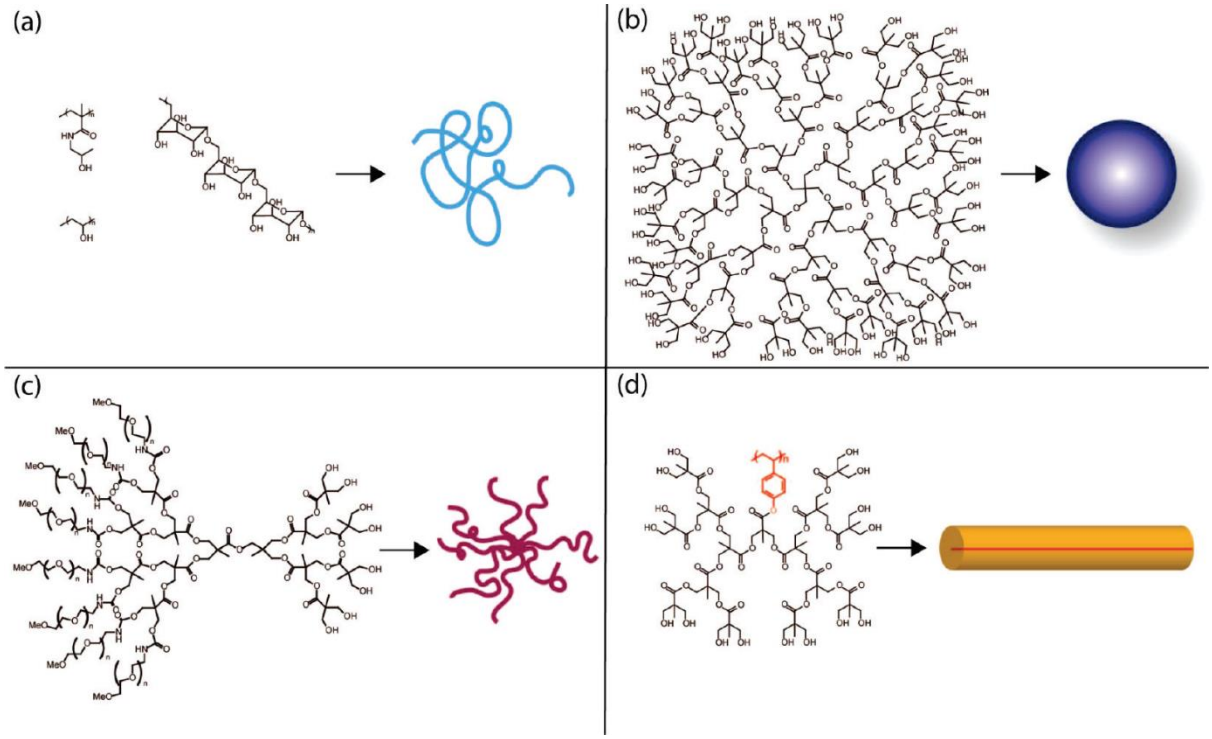

Figure 1.6. *Schematic depicting the various polymer architectures and their respective conformations in solution namely, loose coil-like, hard sphere, branched star-like and rigid rod (adapted from Fox et al. Acc. Chem. Res.,* **2009**, *8,* 1141-1151*)*

1.3.2 Size

In order to achieve long-circulating nanoparticles for effective biodistribution and targeted payload delivery, it is important to consider the quintessential factors governing the nanoparticle fate *in vivo* including renal clearance, hepatic filtration, tissue extravasation and diffusion.[6] All the aforementioned parameters are highly influenced by the nanoparticle physicochemical properties, especially the size. The nanoparticle size also impacts the drug loading and release kinetics, solubility, *in vitro* cellular internalization and degradation, and *in vivo* stability. Smaller particles tend to aggregate over longer storage conditions and during *in vitro* experiments, however, they exhibit longer half-life under circulation.[62,63] Nanoparticles with size less than 10 nm tend to undergo rapid renal clearance owing to the glomerular filtration that is composed of pores with approximate size of 4 nm by 14 nm.[64,65] Hence, particles with sizes less than the glomerular pore size permeate easily through the pores and undergo elimination by the kidney. Macromolecules with sizes larger than 200 nm, on the other hand, are recognized by the complement system and removed from circulation via the RES system (liver and spleen). This size limit stems from the fact that the fenestrae size of the liver Kupffer cells and the spleen sinusoid size lies in the range of 150-200 nm.[66] These large nanoparticles undergo opsonization, wherein opsonin proteins bind to the nanoparticle surface resulting in a corona formation, making them easily recognizable by the MPS system limiting their circulation half-life.[61,67] The leaky vasculature of the tumor tissue renders the endothelial cell gap in the range of 100-800 nm, varying as per the stage and tumor type.[4] Nanoparticles smaller than 100 nm undergo easy extravasation into the tumor tissue, however, these particles can escape back to the blood vessels via the vascular gaps and undergo MPS clearance. There seems to be a particle equilibrium and smaller size nanoparticles, ideally in the 30-200 nm size range, push the equilibrium towards retention in the tumor tissue.[68] Thus, nanoparticles with size in the range of 30-200 nm offer the ideal window for passive targeting of tumor tissue, increased tumor extravasation, enhanced accumulation and retention, which is referred to as the Enhanced permeability and retention (EPR) effect (explained at length in section 1.4). In an *in vivo* study with polystyrene nanoparticles (PS NPs), Nagayama and co-workers designed PS NPs with similar composition but different sizes (50 nm and 500 nm) and observed higher hepatic uptake of the larger nanoparticles.[69] Amidon et al. carried out a study employing nanoparticles in the size range from 100 nm to 10 μm and found that smaller particles exhibited

6-fold higher cellular uptake in Caco-2 cells and better penetration across submucosal layers in an in situ rat intestinal loop model.[70,71]

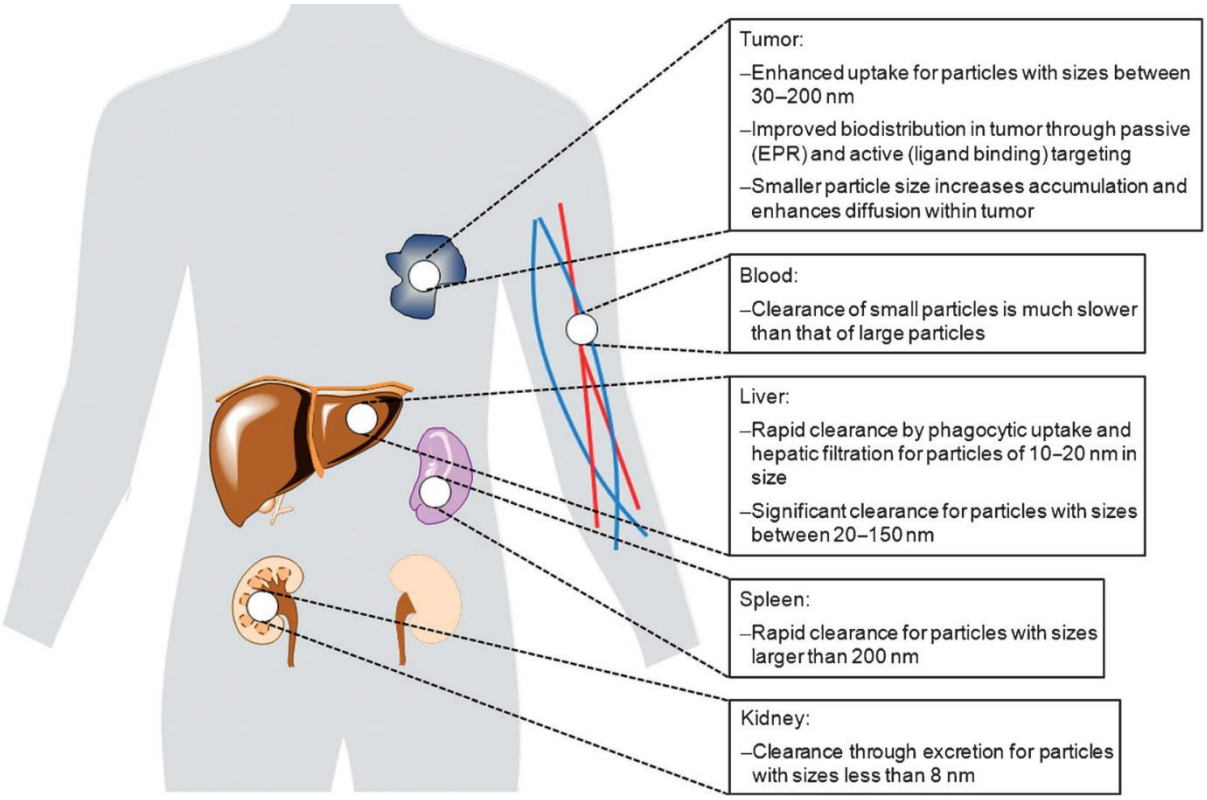

Figure 1.7. *Impact of size of nanoparticles on their biodistribution and clearance (adapted from Sun et al. Angew. Chem. Int. Ed.* **2014**, *53, 12320 – 12364).*

1.3.3 Charge

The surface charge of nanoparticles can be determined using the zeta potential measurements, however, it is important to understand that this is not an intrinsic property of the particle but depends on environmental factors such as the pH and ionic strength of the medium.[72,73] Surface potential is also a key player in determining the membrane permeability, circulation half-life, systemic toxicity and intratumoral processes.[1,74,75] The protein adsorption on the nanoparticle surface is governed by the charge density and nature of charge, such that cationic or anionic nanoparticles exhibit higher opsonization rate as compared to neutral counterparts.[76] This in turn results in more rapid clearance from the blood of positively charged nanoparticles followed by the negatively charged particles, whereas slightly anionic and neutral macromolecules demonstrate the longest circulation half-life. Nanoparticles with high surface

potential, negative or positive, are more readily scavenged by the macrophages and cleared from the body via the mononuclear phagocytic system. In a particular example, amine-functionalized (cationic) polystyrene microparticles exhibited greater phagocytosis as compared to their sulfate, carboxyl (anionic) and hydroxyl-functionalized (neutral) counterparts.[6] Positively charged nanoparticles also exhibit nonspecific interactions resulting in hemolysis and platelet aggregation *in vivo*.[67] Atul and co-workers designed cerium oxide nanoparticles with variable surface charges, i.e. negative, neutral and positive in order to investigate the role of surface charge on cellular internalization for healthy and cancer cells. They observed that neutral or cationic particles were readily taken up by the cells, however, anionic nanoparticles were selective towards cancer cell lines. The surface charge properties impacted cellular internalization and subcellular localization with variation across cell types and this, in turn, affected the cytotoxicity profiles. The negatively charged particles showed no uptake in HEK293 cells and thus, displayed no toxicity, whereas, they exhibited cytotoxicity towards A549 cells due to enhanced uptake by these cells.[77]

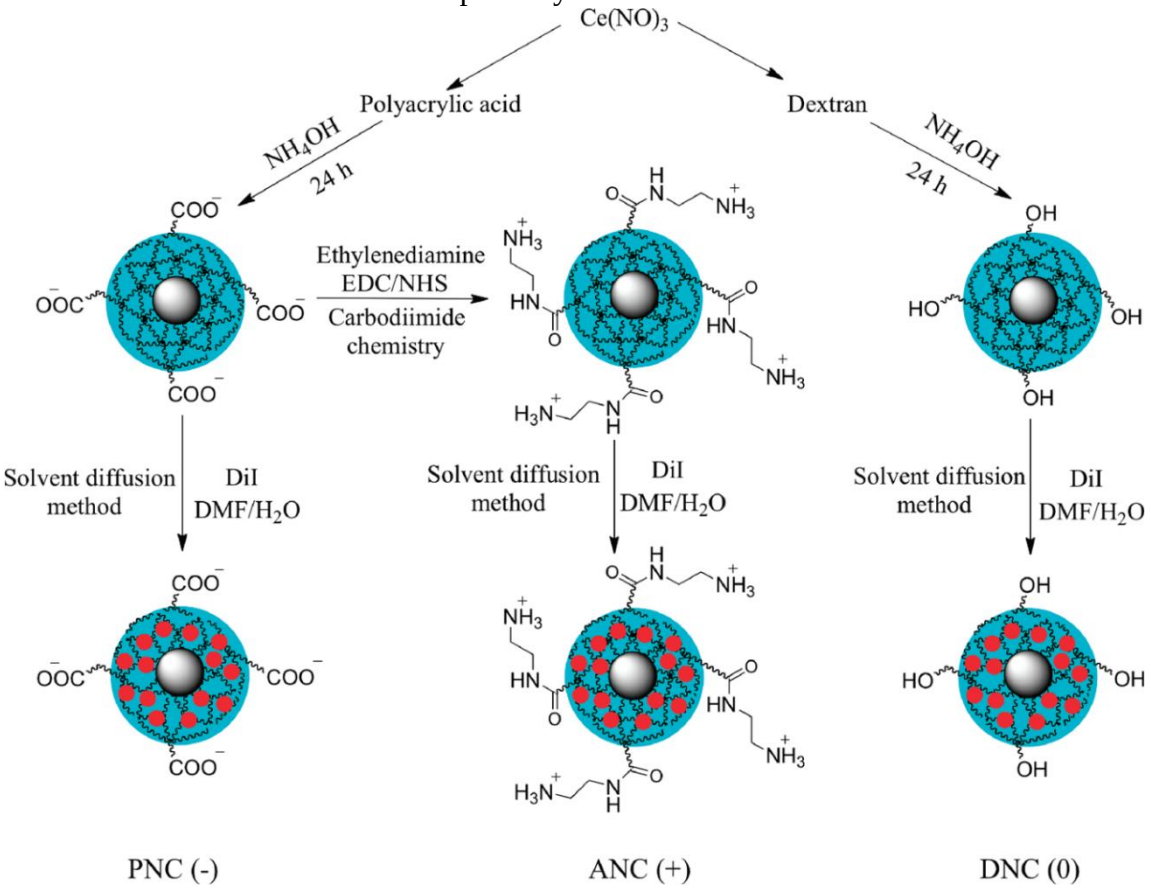

Figure 1.8. *Synthetic design of cerium oxide nanoparticles surface modified with polymer coatings to yield anionic, neutral and cationic surfaces (adapted from Asati et al. ACS Nano,* **2010**, *4*, 5321-5331*).*

1.4 Evolution of Polymeric Drug delivery systems (DDS)

The advent of polymeric drug delivery systems (DDS) can be traced back to the 1960s and the reason it has gained such impetus can be attributed to the limitations of the existing therapeutics that include nonspecific interactions resulting in shorter circulation half-life and immunogenicity.[78] Exemplary and pioneering work has been done in this field by distinguished researchers namely, Ringsdorf, Langer, Peppas, Higuchi, Heller, Folkman, Speiser and Roseman.[79–96] The polymeric drug delivery platform has evolved from the macroscopic drug carrier depots and implants to injectable drug delivery carriers in the microscopic scale (work pioneered by Robert Langer) to the era of nanoscale DDS.

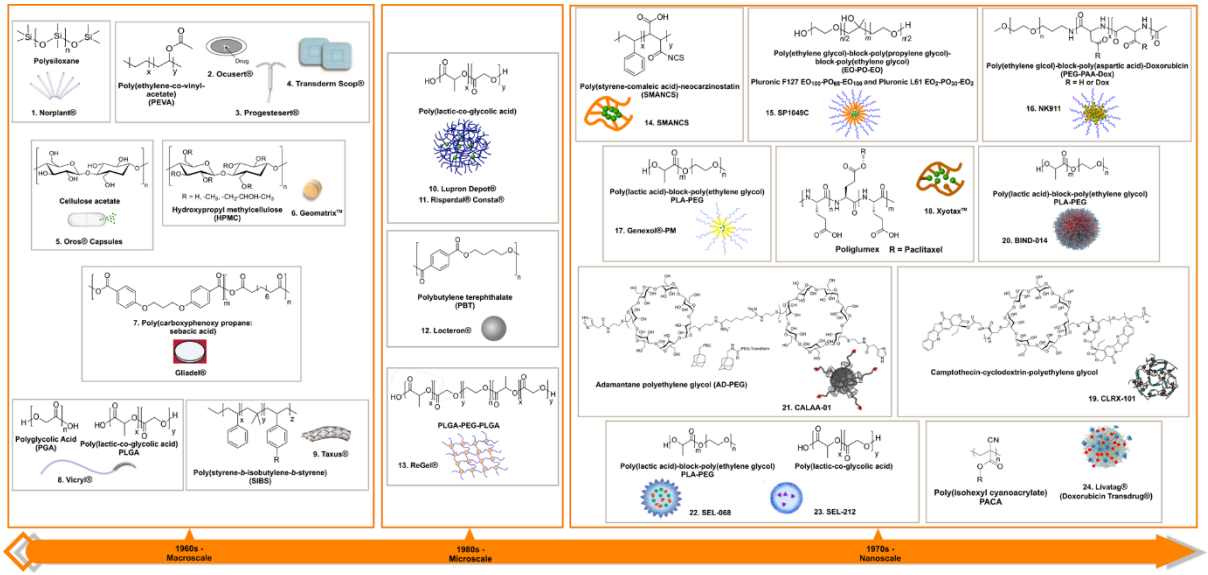

Figure 1.9. *Polymeric drug delivery system evolution in the biomedical field over 50 yeras (adapted from Kamaly et al. Chem. Rev.* **2016**, *116,* 2602−2663*).*

The first major breakthrough in the nanoscale-based DDS was the development of SMANCS by Maeda et al. in 1984 by conjugating neocarzinostatin, an anticancer peptide, to styrene-maleic anhydride. This study led to the discovery of the Enhanced Permeability and retention (EPR) effect by Hiroshi Maeda of the Sojo University, Japan.[97] The work explained that macromolecular drug carriers exhibited the tendency to easily permeate through the endothelial cell gap junctions of the tumor tissue as compared to the healthy tissue owing to the leaky vasculature and poor lymphatic drainage of tumors. These nanocarriers were able to extravasate into the tumor tissue as well as demonstrated higher retention against clearance

resulting in enhanced accumulation. The EPR effect paved way for the development of numerous passive targeting macromolecular drug delivery nanocarriers for caner therapy.

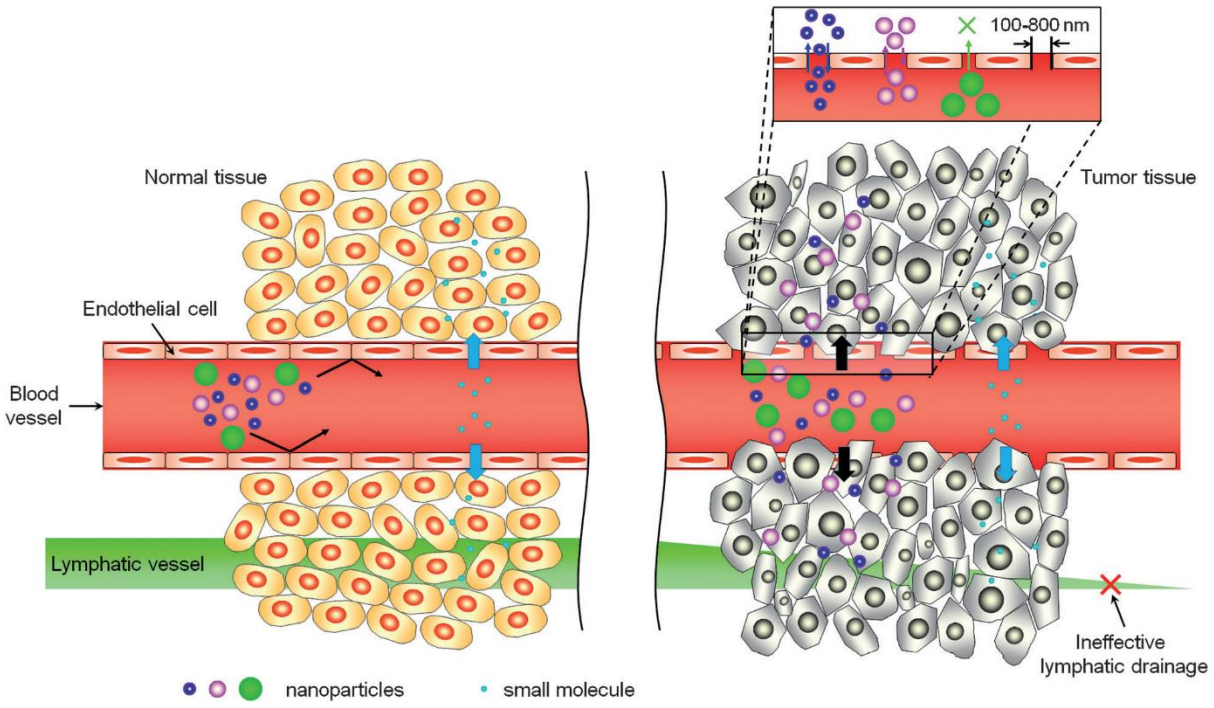

Figure 1.10. *Concept of Enhanced Permeability and retention effect ((adapted from Sun et al. Angew. Chem. Int. Ed.* **2014**, *53, 12320 – 12364)*

Kataoka and co-workers made another significant contribution in terms of the development of block copolymer micelles comprising of the hydrophobic amino acids conjugated to the hydrophilic PEG for anticancer drug delivery applications.[98,99] On similar lines, Matsumura et al. designed a PEG-poly(aspartic acid) micellar NP encapsulated with Doxorubicin (DOX), namely NK911.[100] Various polymeric drug delivery carriers were able to successfully translate into clinics with FDA-approval including NK911, SP1049C, Genexol-PM and several others are currently being explored for cancer treatment via clinical trials.[100–105] The DOX-encapsulated pluronic polymeric nanoparticle, SP1049C, entered the clinical trial for treatment of metastatic esophageal cancer. These polymeric micelles have exhibited superior efficacy against tumor as opposed to free DOX due to their ability to bypass the p-glycoprotein (p-gp) mediated drug resistance. Genexol-PM is a formulation of the PEG-poly(lactide) micelle encapsulated with Paclitaxel (PTX) that has been approved for use against

various types of cancers in South Korea and is under clinical trials in USA and Europe. These PTX loaded micelles demonstrated an increase in the maximum tolerated dose (MTD) for PTX against breast cancer treatment along with better treatment response rates.

Farokhzad et al. designed PLA-PEG micelles encapsulated with docetaxel (DTX) specifically targeting the receptor namely, prostate-specific membrane antigen (PSMA), that is overexpressed on prostate cancer cells. This led to the development of the first ever targeted polymeric NP, BIND-014 and it's clinical translation for cancer chemotherapy in humans.[106,107] Another targeted polymeric NP to have entered the clinic is CALAA-01 based on a three-component system comprising of cyclodextrin polymer (CDP), adamantine-PEG and a human Tf conjugated adamantine-PEG encapsulated with siRNA. This nano-formulation has depicted significantly high pH-triggered siRNA delivery.[108,109] Thus, the area of polymeric drug delivery systems has seen the evolution from 1st-generation passive tumor-targeting polymeric NPs to the 2nd-generation targeted DDS capable of selective tumor binding and now heading towards the 3rd-generation smart DDS capable of stimuli-triggered payload release.

1.5 Unimolecular Micelles vs. Aggregated Micelles

Conventional self-assembled polymeric micelles are essentially an aggregation of multiple amphiphilic molecules in a thermodynamically driven process above the critical micelle concentration (CMC).[110] However, these multimolecular micelles face challenges such as dilution, flow rate and environmental factors like pH, temperature, ionic strength, protein adsorption etc. that impact the *in vivo* stability of micelles under circulation.[111–115] These result in disassembly of the multimolecular (or aggregated) micelles into individual polymer chains resulting in premature cargo release. A recent report on the NK911 polymeric micelle, in the early clinical trial, highlighted the poor stability of the micellar structure resulting in the burst release of cargo following the i.v. injection.[116] Another study pointed out the instability of the PEG-polyester micelles wherein > 80 % micelles dissociated *in vivo* within an hour of administration.

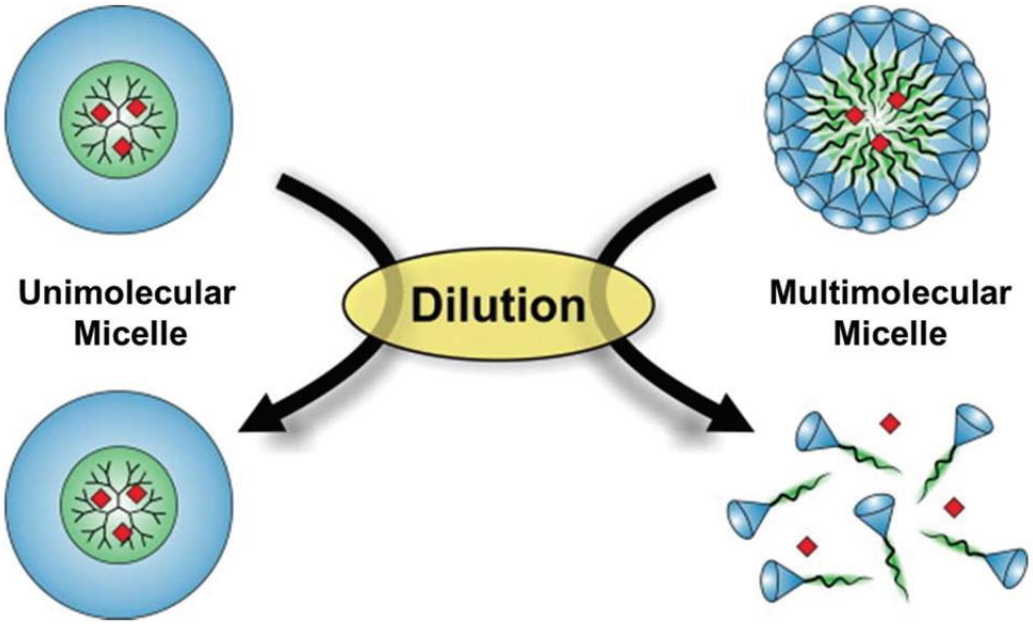

Figure 1.11. *Impact of environmental factors such as dilution on the stability of the multimolecular micelles vs. the unimolecular micelles (adapted from Lukowiak et al. Biotechnol. Adv.,* **2015**, *33,* 1327–1341*).*

Cross-linking of the core and/or shell was adopted as an approach to overcome the aforementioned limitation of conventional micelles, i.e. their thermodynamic instability. In this regard, Leroux et al. synthesized an 8-arm star-shaped poly(glycidyl methacrylate) (PGMA) polymer utilizing the ATRP approach with a cross-linked core that resulted in stable micellar formation.[117] In another work, Gong et al. synthesized nanovesicles based on ABA-type amphiphilic cross-linked triblock copolymers encapsulated with cargo in the hydrophobic pocket and utilized for drug delivery.[118] The cross-linking of the core and/or the shell renders structural stability to the micelles, however, their drug release kinetics and biodegradability are all affected.[119–121] Another strategy to overcome the issue of unstable micelles, that has gained much traction since it's introduction in the 1990s, is the utilization of unimolecular micelles.[122–124] "Unimolecular micelles" constitute a class of single polymer chain micelles composed of a core and a shell that are covalently bound; that exhibit extreme stability under infinite dilution and other microenvironmental factors rendering them ideal for *in vivo* biomedical

applications.[125,126] These unimolecular micelles can be composed of different types of polymer architectures, all of which have been discussed at length in the following sections.

1.5.1 Dendrimers

Dendrimers are tree-like branched architectures with radial symmetry, large number of functional groups, monodisperse and globular properties[127] that have been widely explored for various applications including drug[128–130] and gene delivery[131,132], catalysis[133,134], biosensors[135] etc. Their compact structure with small hydrodynamic volume helps them avoid RES uptake and fast renal clearance rendering them suitable for *in vivo* therapeutic applications. These branched macromolecules are synthesized via a convergent or divergent approach.[136] The first ever report on amphiphilic dendrimers was by Fréchet et al. in 1993, wherein they utilized 3,5-dihydroxybenzyl alcohol as the monomer unit for the synthesis of polyether dendrimers via the convergent approach.[137] The carboxylate end groups on the dendrimer structure gave them the desired water solubility and they were able to encapsulate hydrophobic drugs such that the drug loading increased linearly with increase in the dendrimer concentration establishing their unimolecular nature. In another example, Meijer et al. encapsulated Rose Bengal (hydrophilic dye) into the cavities of the amphiphilic poly(propylene imine) dendrimer followed by conjugation of t-BOC protected phenylalanine on each of the chain ends to seal the dye molecules. As can be seen in figure 1.12, this was referred to as steric blocking of the dye-loaded dendrimer and only exposure to acidic conditions would result in the regeneration of the amine end groups resulting in controlled dye release, called the steric de-blocking.[138]

Poly(amidoamine) (PAMAM) dendrimers are another class of commonly used dendrimers following surface functionalization modification from amine end groups to hydroxyl or carboxylic making them versatile in their application as unimolecular micelles.[139–142] In a particular example, a hydroxyl functionalized G4 PAMAM dendrimer was used to grow poly(L-lactide)-PEG amphiphilic block copolymer giving the PAMAM-PLA-PEG macromolecule. These self-assembled into stable unimolecular micelles with around 20 % drug loading content.[143,144]

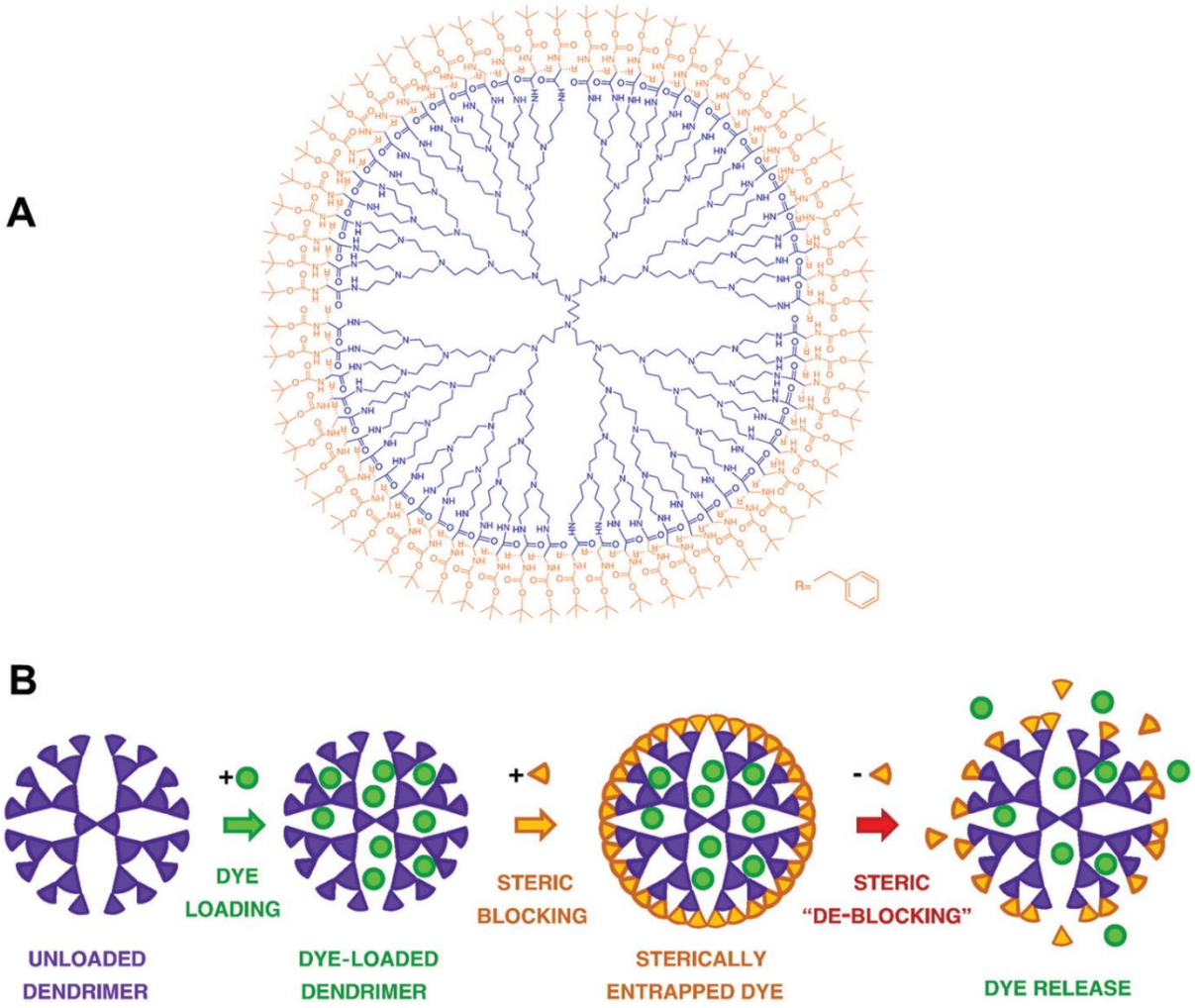

Figure 1.12. *Schematic representing the poly(propylene imine) dendrimer regulating drug release via steric blocking and de-blocking (adapted from Fan et al. Polym. Chem.* **2016**, *7*, 5898–5919*).*

1.5.2 Hyperbranched

Hyperbranched polymers (HBP) have relatively easier one-pot synthesis as opposed to the tedious multi-step synthesis of dendrimers via different approaches such as polycondensation, self-condensation, ring-opening polymerization etc.[110,145] Hyperbranched polyesters are the most sought-after class of hyperbranched polymers owing to their biocompatible backbones ideal for therapeutic applications, wherein Boltorn (H30 and H40) are the most widely used comprising of 2,2-bis(methylol) propionic acid as the monomeric unit.[146–149] In order to impart amphiphilicity to a fully hydrophobic H40 polymer, it is usually conjugated with PEG resulting in unimolecular micelles. However, their extremely small sizes (< 3 nm) results in significantly low drug loading content (paclitaxel DLC < 0.3 %).[150] To overcome this limitation, various block copolymers were grown on top of the H40 core such as (poly (L-lactide) (PLA) and polycaprolactone (PCL))-PEG rendering appropriate amphiphilicity (see figure 1.13).[151,152] In a particular example, H40-based multi-arm PLA-PEG amphiphilic block copolymer was synthesized using H40 as the macroinitiator for ROP to yield H40-PLA followed by PEG conjugation. They self-assembled into water dispersible unimolecular micelles with drug loading content of around 12 % for doxorubicin and 33 % for 5-fluorouarcil.[153,154]

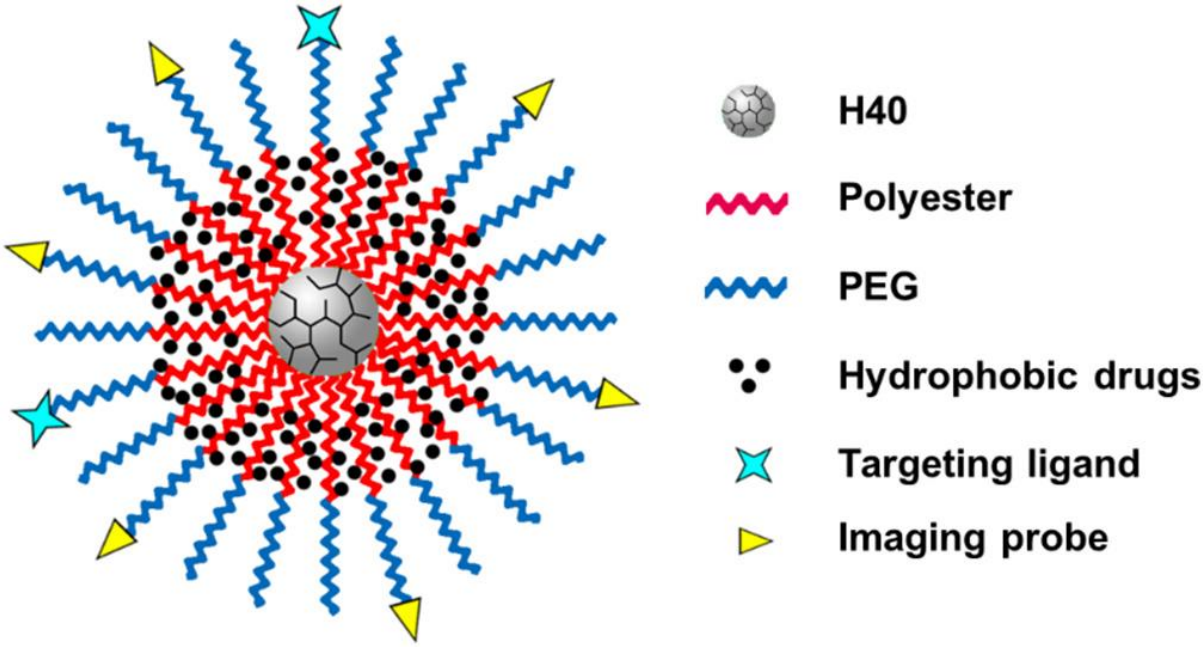

Figure 1.13. *Schematic representation of a unimolecular micelle formed from H40-based amphiphilic block copolymer (adapted from Chen et al. Adv. Drug Deliv. Rev.* **2018**, *130*, 58–72*)*

Xiao et al. synthesized a H40-based poly (L-glutamate)-*b*-PEG amphiphilic block copolymer conjugated with DOX via a hydrazone bond and a targeting moiety, cRGD peptide (see figure 1.14).[155] The unimolecular micelle surface was conjugated to NOTA for *in vivo* PET imaging application in U87MG tumor-bearing mice. PET imaging demonstrated enhanced tumor accumulation of the cRGD-conjugated targeted polymeric micelles as opposed to the non-targeted counterpart. This was re-instated from the ex vivo fluorescence imaging of the excised U87MG tumor through the DOX emission. Another class of HBP is the hyperbranched polyglycerol (HPG) that are water-soluble and biocompatible. These have been explored for topical drug delivery applications such as the HPG-PCL-PEG unimolecular micelles.[156,157]

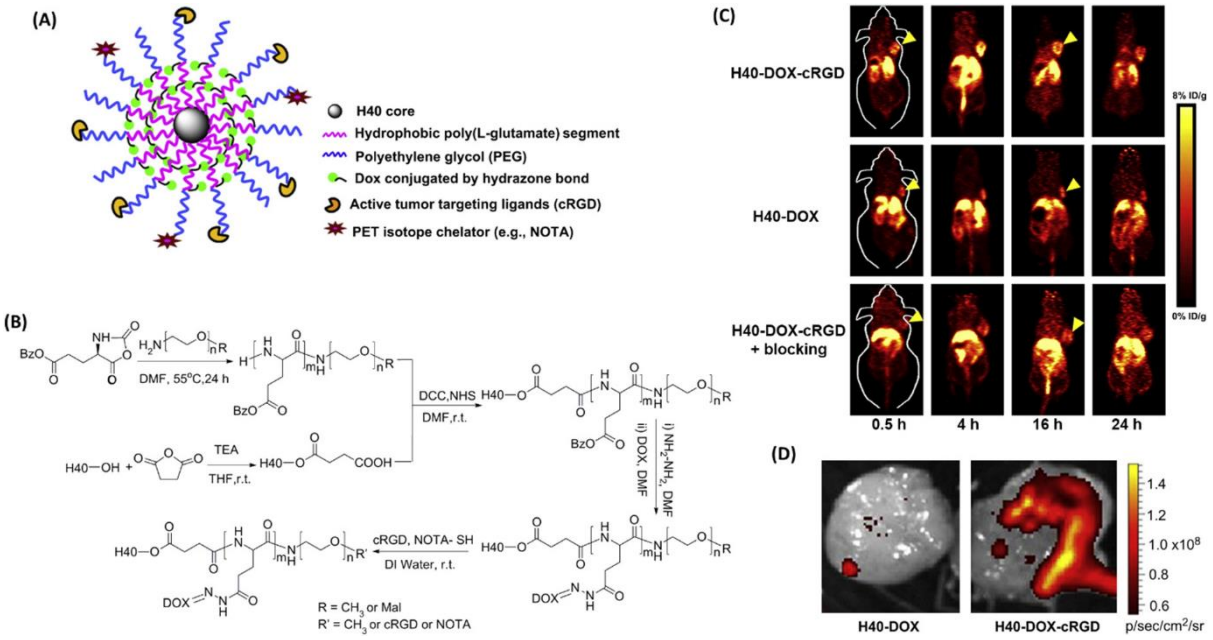

Figure 1.14. *Schematic representation of a H40-based poly (L-glutamate)-b-PEG amphiphilic block copolymer for simultaneous DOX delivery and in vivo PET imaging (adapted from Xiao et al. Biomaterials* **2012**, *33,* 3071–3082*).*

1.5.3 Brush-shaped

Brush-shaped polymers are macromolecular architectures containing multiple side chain arms grafting/stemming from a main polymer backbone[158] and these are usually synthesized via three different approaches: grafting through, grafting onto, grafting from.[159–161] In a particular example, poly(methacrylate)-*g*-(PCL-*b*-PEO) brush polymer resulted in the formation of DOX encapsulated unimolecular micelles exhibiting wormlike conformation as depicted via AFM images.[162] Gong et al. synthesized an amphiphilic brush-shaped block copolymer composed of a poly (2-hydroxyethyl methacrylate) (PHEMA) backbone with side chains comprising of PLLA-PEG (see figure 1.15).[163] These brush-shaped polymers resulted in the formation of unimolecular micelles encapsulated with DOX and were employed for targeted drug delivery utilizing TRC105 (CD105-targeting antibody). *In vivo* PET imaging revealed higher accumulation of ^{64}Cu-labelled targeted unimolecular micelle in 4T1 tumor compared to the non-targeted micelle.

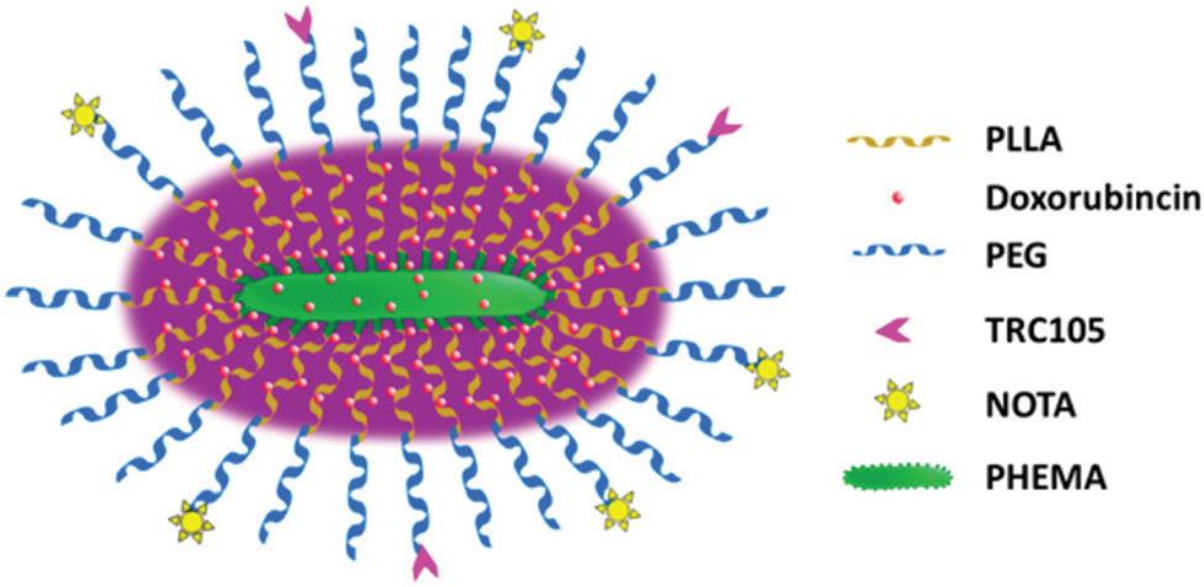

Figure 1.15. *Schematic illustration of a PHEMA brush block copolymer for targeted drug delivery and in vivo PET imaging (adapted from Gong et al. ACS Appl. Mater. Interfaces,* **2014**, *6,* 21769–21779*).*

In a recent report by Tu and co-workers, cyclic brush and bottlebrush copolymers were synthesized based on poly(2-hydroxyethyl methacrylate-*g*-poly(N-isopropylacrylamide-*st*-N-hydroxyethylacrylamide)) (P(HEMA-g-P(NIPAAm-st-HEAAm)).[164] The consequent unimolecular micelles were compared for their anti-proliferation effect and it was found that

cyclic brush copolymers yielded more stable unimolecular micelles with higher tendency to inhibit proliferation compared to the bottlebrush analogue.

1.5.4 Star-shaped

Star-shaped polymers are characterized by macromolecular architectures with a number of arms emanating from a central core and can be synthesized using three approaches, namely: core-first, coupling onto and arm-first.[165–169] These architectures offer the advantage of structural and functional tunability, easy and versatile synthesis, a defined core and shell rendering them suitable for biomedical applications. In a particular example, Pang et al. demonstrated the unimolecular micelle formation from a 21-arm β-cyclydextrin (β-CD) based poly(acrylic acid)-*b*-polystyrene (PAA-*b*-PS) amphiphilic star block copolymer (see figure 1.16).[170] Herein, β-CD was employed as the bromo-substituted macroinitiator for the ATRP of t-butyl acrylate (t-BA) and styrene monomers in a sequential manner and following hydrolysis, resulted in a hydrophilic core and hydrophobic shell. This amphiphilic 21-arm star block copolymer self-assembled into 19 nm size unimolecular micelles and demonstrated an increase in size up to 65 nm with increase in the molecular weight.

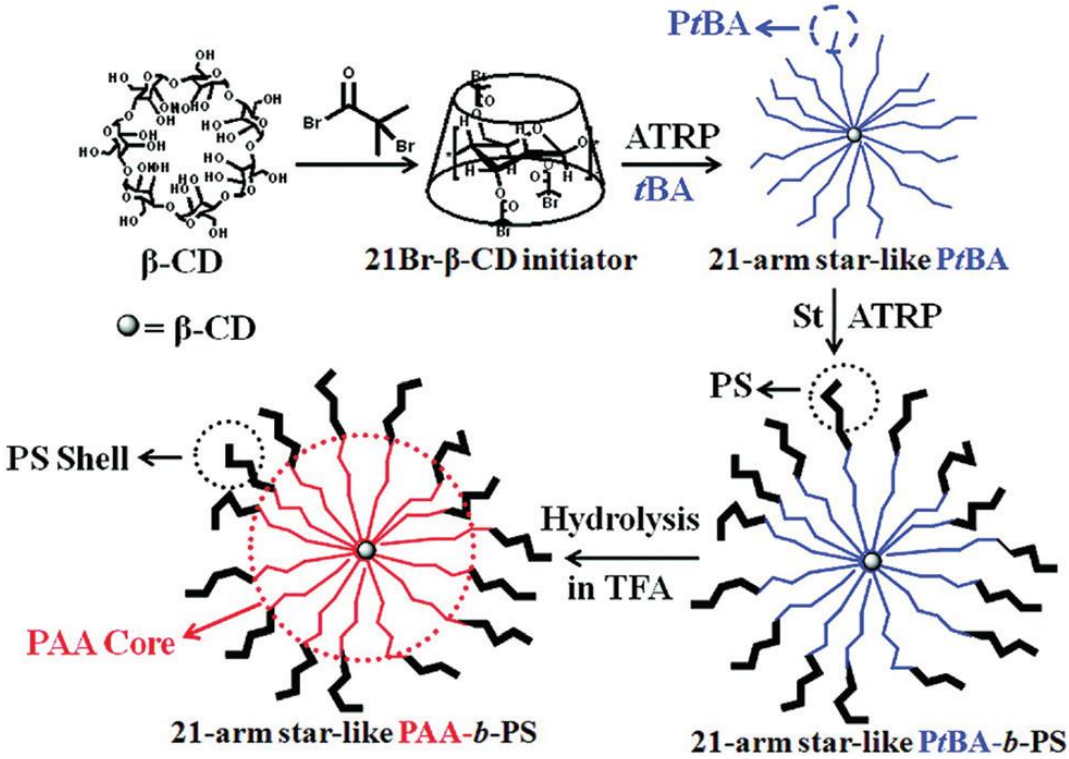

Figure 1.16. *Synthetic design of a 21-arm β-CD based PAA-b-PS unimolecular micelle (adapted from Pang et al. Macromolecules* **2011**, *44*, 3746–3752*).*

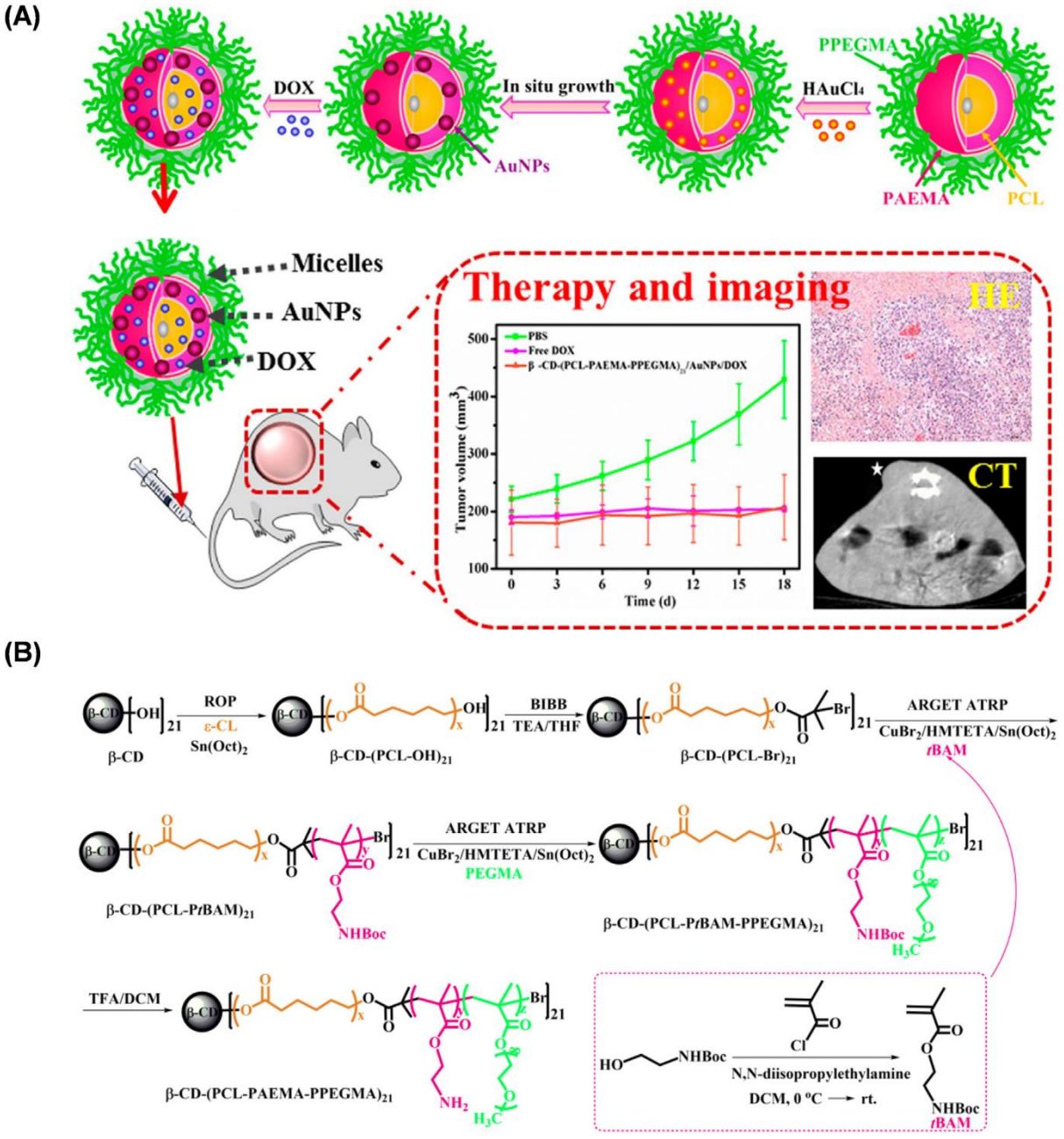

Figure 1.17. *Synthetic design of a 21-arm β-CD based star triblock copolymer for theranostic applications in vivo (adapted from Lin et al. Biomacromolecules* **2017**, *18,* 3869–3880*).*

As can be seen in figure 1.17, Lin et al. reported the synthesis of a 21-arm β-CD based amphiphilic star triblock copolymer that yielded unimolecular micelles utilized for targeted

chemotherapy and computed tomography (CT) imaging *in vivo*.[171] As is highlighted in the synthetic scheme in figure 1.17B, the ring opening polymerization of ε-caprolactone using β-CD as the initiator resulted in the formation of β-CD-PCL, which was then employed as the macroinitiator for a sequential ATRP yielding the triblock copolymer β-CD-(PCL-PAEMA-PPEGMA). This star-block copolymer was encapsulated with doxorubicin (DOX) and used for the fabrication of gold nanoparticles (Au NPs) yielding a theranostic nanomedicine for chemotherapy along with CT imaging as the diagnostic tool. The *in vivo* CT imaging revealed a much better CT signal in the case of the unimolecular micelles, i.e. β-CD-(PCL-PAEMA-PPEGMA)/AuNPs/DOX as opposed to a commercially available contrast agent, i.e. Omnipaque from the tumor site. These unimolecular micelles also demonstrated their antitumor efficacy by resulting in 87 % tumor reduction when compared to the PBS control group.

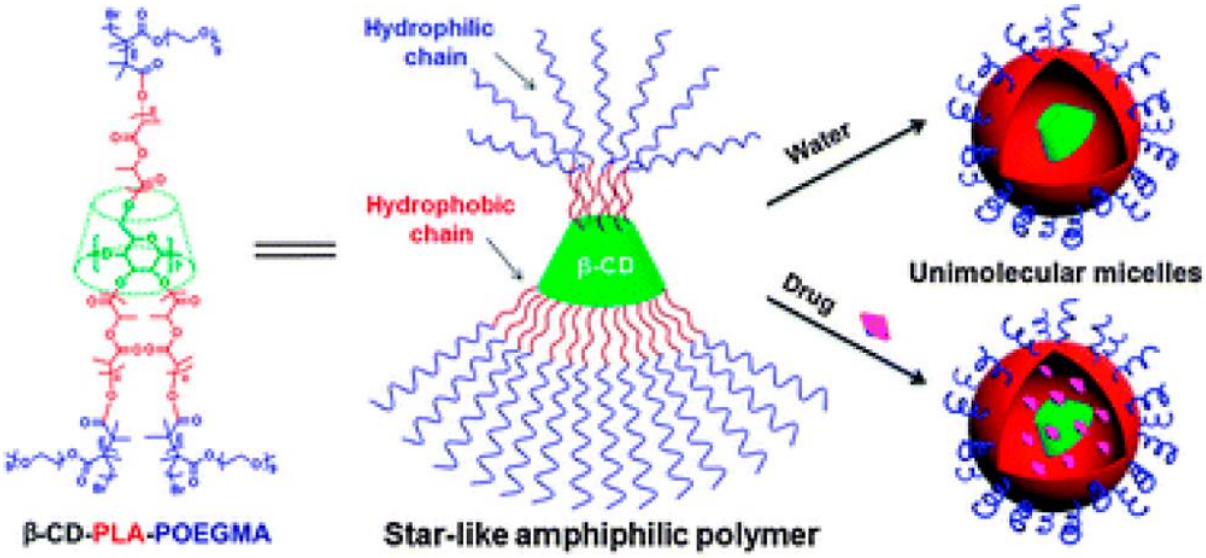

Figure 1.18. *Schematic illustration of a pH-responsive star amphiphilic polymer (adapted from Wang et al. Chem. Commun.* **2015**, *51,* 15768−15771*).*

In yet another example, Wang and co-workers designed a biocompatible β-CD based star-shaped amphiphilic block copolymer for a pH triggered drug release *in vitro* (see figure 1.18).[172] Herein, β-CD was employed as initiator for the ROP followed by ATRP resulting in the star block copolymer β-CD-PLA-POEGMA that self-assembled into stable unimolecular micelles. These unimolecular micelles exhibited high drug loading content for the anticancer drug doxorubicin in the range of 6.3-10 %, varying as per the degree of polymerization of the

hydrophilic POEGMA block. The DOX-loaded micelles demonstrated enhanced cellular uptake and a controlled DOX release triggered by pH in the tumor tissues.

1.6 Biodegradable polymers

Biodegradability is an extremely important attribute of a drug delivery carrier such that the fate of the nanocarrier after the cargo delivery is expulsion from the system via a complete breakdown of the nanocarrier.[4] This is extremely crucial to overcome any toxicity or immune response due to the nonspecific interactions of the drug carrier. The first ever use of biodegradable polymers was in the 1960s, wherein the polyesters such as poly(glycolic acid) (PGA), poly(D,L-lactic acid) (PLA) and poly(lactic-*co*-glycolic acid) (PLGA) were employed as biodegradable sutures.[173] These biodegradable polymers have come a long way since then in terms of their usage as drug delivery systems owing to their unique ability to degrade under physiological conditions and undergo elimination from the system.[174] Several biodegradable polymers have been exploited for the nanomedicine platform such as poly(esters), poly(ortho esters), poly(anhydrides), poly(amides), poly(ester amides), poly(phosphoesters), poly(alkyl cyanoacrylates) and naturally occurring chitosan and hyaluronic acid (see figure 1.19).

Poly(ortho esters) have been exploited since the 1970s as biodegradable sutures for surgical applications[175] and now are being used as carriers to deliver cargo such as nucleic acids and analgesics.[176] These degradable polymers release drugs in a diffusion-controlled manner via the initiation of polymer chain hydrolysis at the outer matrix shell[78] and is accelerated under acidic conditions.[177] However, their highly hydrophobic backbone limits water penetration making these architectures unsuitable for biomedical applications.[178] Poly(anhydrides) are surface-eroding polymers wherein the drug cargo and it's dissolution rate determine the drug release kinetics.[179] Poly(anhydride) based nanoparticle formulations have been employed for drug and other therapeutics delivery applications either intravenous or oral.[180–183] Among the group of poly(amides), the preferrable choice for drug delivery applications is poly(amino acids) owing to their non-immunogenicity.[184] These are known to be stable against hydrolysis and undergo enzymatic degradation, however, the rate and ease of degradation is dependent on the hydrophilicity of the polymeric backbone.[185–187] The two most widely used poly(amino acids) for therapeutic applications are poly(ɣ-glutamic acid) and poly(L-lysine).[188–191] The carboxylic group on the poly(ɣ-glutamic acid) chain acts as a functional handle for conjugation

of drug molecules or targeting ligands and these polymers have proven to be efficient chemotherapeutics delivery carriers.[175,192] The poly(L-lysine) macromolecules are known for their use as gene delivery nanocarriers, since the positively charged polymer backbone stabilizes the negatively charged siRNA/DNA payloads.[193] These polymers are known to undergo endosomal escape however, their *in vivo* applications are still limited due to the toxic effect of the positively charged backbone.[194]

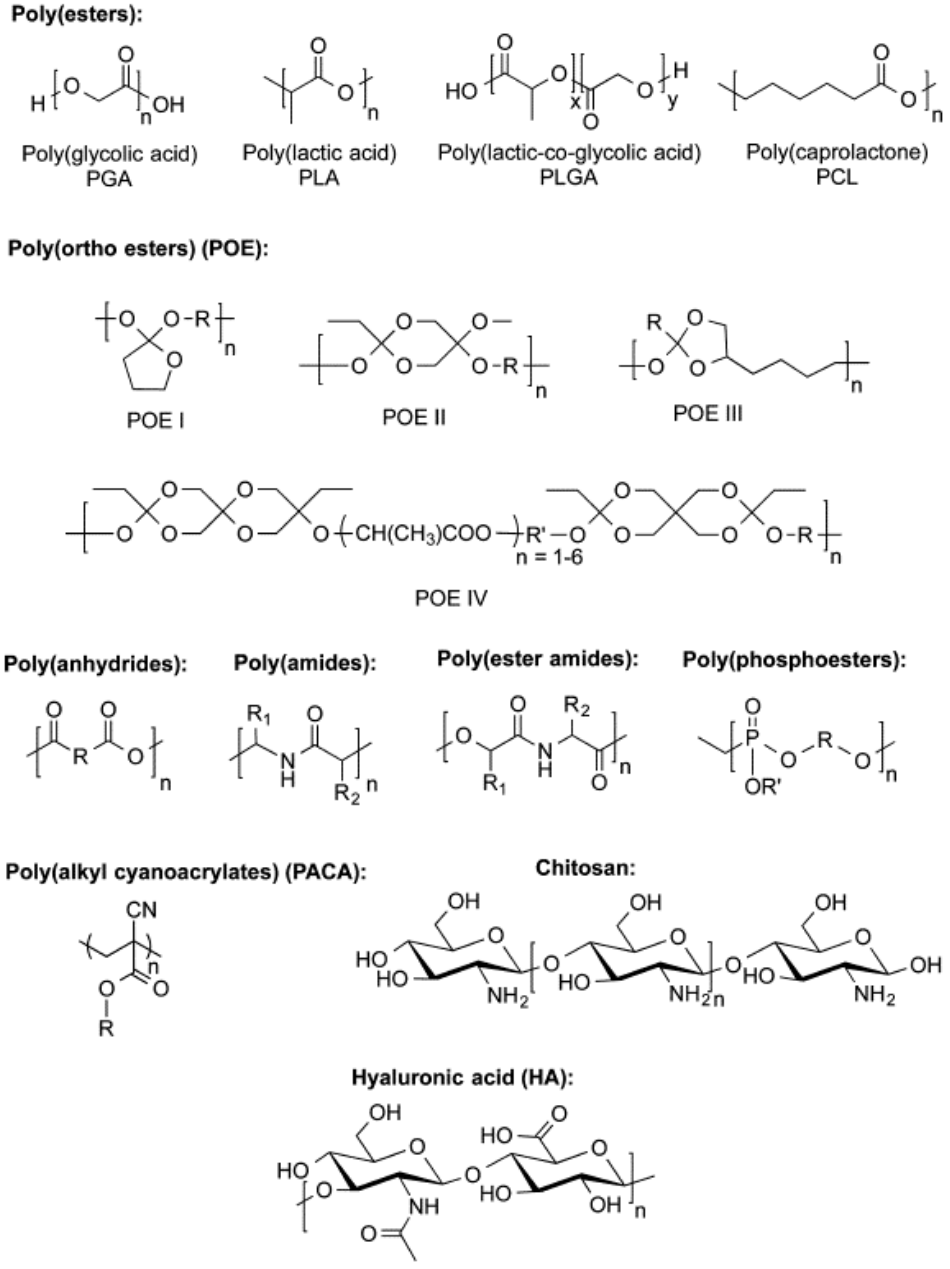

Figure 1.19. *Various types of biodegradable polymers (adapted from Kamaly et al. Chem. Rev.* **2016**, *116*, 2602−2663*).*

Poly(ester amindes) are composed of both amide and ester linkages in the polymeric backbone giving them the mechanical and therapeutic advantages of the two components. The amino acid based poly(ester amides) have been widely explored for pharmaceutical applications.[195,196] These polymers are known to undergo hydrolysis, however, at a very slow rate whereas their biodegradation catalyzed via enzymes follows a faster kinetics. The rate of degradation is greatly affected by the ratio and composition of ester and amide linkages in the backbone.[78] Poly(phosphoesters) can be synthesized vis multiple routes such as condensation or addition polymerization, however, the most often used route is the ring-opening polymerization.[175] The degradation of this polymer results in non-toxic byproducts and hence, they have found application in both drug delivery and tissue engineering.[197,198] They have also been used for nucleic acid delivery since the charged cargo is readily stabilized by interactions with the phosphate side chain. Since these polymers resemble the biopolymers, hence they are also degraded easily via the hydrolytic mechanism as well as enzyme catalyzed.[198,199] These polymers are most often used in conjunction with polyesters, especially for drug delivery applications.[200–202]

Amongst the naturally occurring polymers, two polysaccharides are the most widely accepted namely, chitosan and hyaluronic acid. Chitosan, a biodegradable polysaccharide derived from chitin,[203] has been widely employed as oral drug delivery vehicle.[204,205] It undergoes degradation via the lysozyme and the breakdown kinetics can be fastened by introducing bulky groups in the side chain in order to interfere with the hydrogen bonding network.[78,175] The anti-inflammatory, antibacterial and mucoadhesive properties of chitosan renders them useful for various applications including wound healing and dressing, gene and pulmonary drug delivery.[206–209] However, chitosan is highly crystalline in nature making these polymers water insoluble and limits their use as formulations for therapeutic delivery applications. Hyaluronic acid (HA) is a linear biodegradable polysaccharide composed of two units, namely: N-acetyl-D-glucosamine disaccharide and D-glucuronic acid.[210] This polymer has high water absorption capability coupled with it's non-immunogenicity makes HA an ideal system for hydrogel based drug delivery.[78] Hyaluronic acid is known to selectively interact with cells expressing the CD44 receptor (also known as hyaluronan receptors) giving them the targeting ability, that is being utilized for delivery of bioconjugates of HA.[211,212]

Aliphatic polyester structures, composed of ester linkages in their backbone, are important classes of biomaterials having been extensively used for biodegradable sutures, resorbable implants, tissue engineering, sustained drug delivery carriers, etc.[213–216] Poly(L-lactide), poly(L-glycolide), poly(L-lactide-*co*-glycolide)s and polycaprolactones (PCL) are some of the widely studied aliphatic polyesters in biomedical and eco-friendly engineering thermoplastics for domestic application.[78] Poly(ε-caprolactone) (PCL), an aliphatic polyester with an exquisite combination of mechanical stability, biocompatibility and high miscibility with a range of other polymers makes it a polymer of great importance both for industrial and biomedical purposes.[217] In general, PCL chains are highly hydrophobic and they are found to exhibit extremely slow degradation rates under physiological condition of around 2-3 years.[78,218] As a result, the accomplishment of complete and fast biodegradability of PCL at the intracellular level is found to be one of the major obstacles in employing them as nano-scaffold materials especially for the delivery of anticancer drugs. To improve the enzymatic degradation kinetics of PCL and provide handle for anchoring drugs or targeting agents, substituted caprolactone monomers with hydroxyl,[213,219] ketone,[220] imine,[221] amine,[222] azide,[223] carboxylic,[224] alkoxyloxy[225–227] and cholesteryl[228] units were developed. These substituted PCL block copolymers were employed as thermo-responsive or pH responsive micelles for delivering chemotherapeutics.[221,229,230] Our group contribution to the literature, a carboxylic-substituted caprolactone, was synthesized by Bapurao et al. which opened up avenues for polymer-drug conjugates, post-polymerization modifications and stimuli-responsive triggers[231] (M15 in figure 1.20).

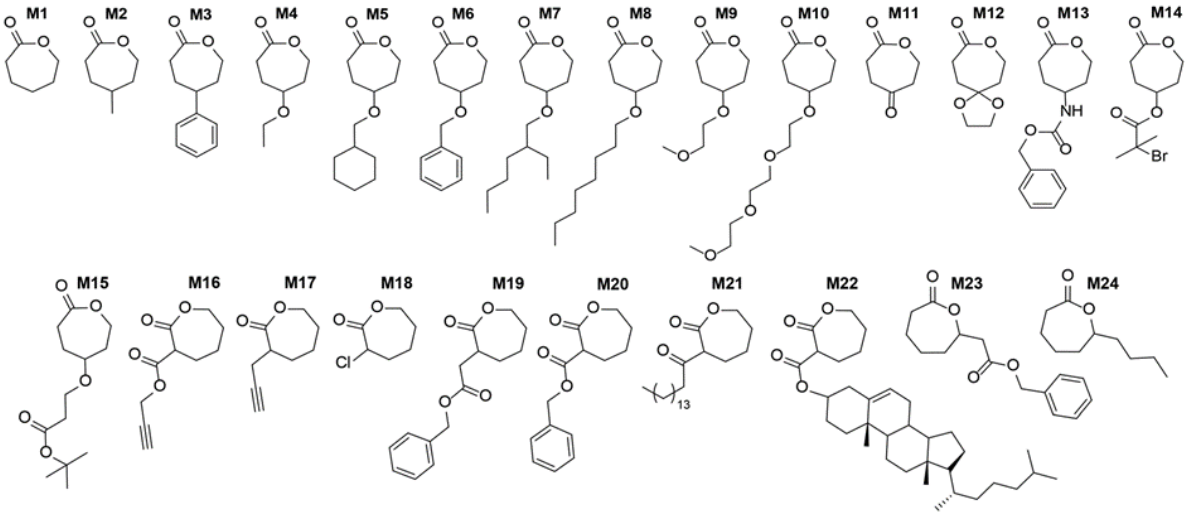

Figure 1.20. *Different types of substituted caprolactone monomers*

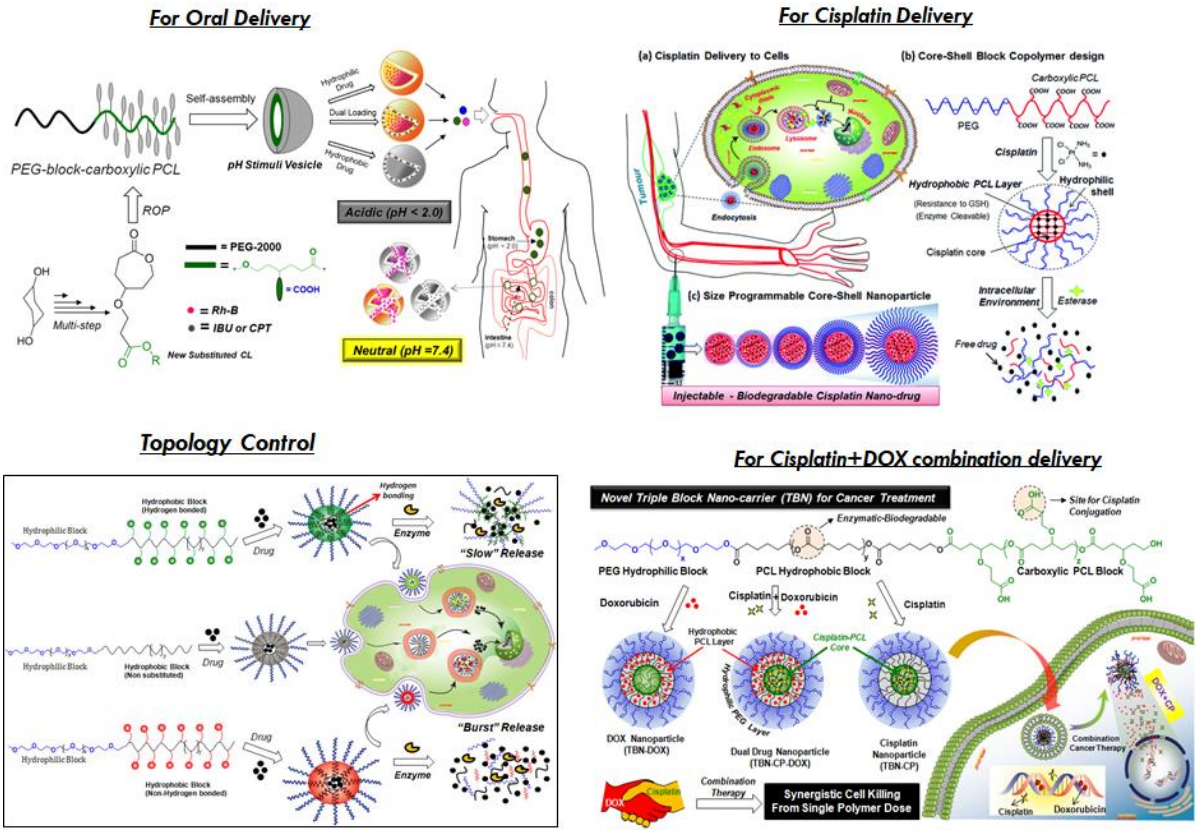

Figure 1.21. *Schematic representation of the work done using the carboxylic substituted monomer for drug delivery applications.*

In the last half-decade, our lab has taken new efforts to engineer PCL block copolymer nano-assemblies as efficient intracellular enzyme-responsive nano-carriers to improve efficacies in cancer treatment. The novel carboxylic substituted caprolactone monomer was employed in controlled ring opening polymerization to yield carboxylic functionalized di and tri-block PCL copolymers. The PEG-*b*-carboxylic PCL diblock copolymer self-assembled into pH-responsive nano-vesicles for efficient oral drug delivery of ibuprofen and camptothecin under GI tract conditions.[231] Further, di- and tri-block PCL copolymers were complexed with cisplatin residues to produce PCL-cisplatin prodrugs[232] that exhibited synergistic combination therapy for antagonistic drugs cisplatin and doxorubicin in a single polymer dose against breast cancer treatment.[233] The preliminary efforts indicated that these PCL block copolymers could deliver both hydrophilic and hydrophobic drugs, and their drug release mechanism was understood in greater depth. Fluorescent π-conjugated chromophores were introduced to study their cellular entry and also develop PCL based luminescent nano-probes for bioimaging.[234,235] FRET probes were designed based on a π-conjugated chromophore (donor) in a PCL backbone encapsulated with nile red (acceptor) and were employed for *in vitro* bioimaging.[236] The polycaprolactone platform was recently explored as a biodegradable fluorescent theranostic probe for it's antibacterial activity against *E. coli*.[237]

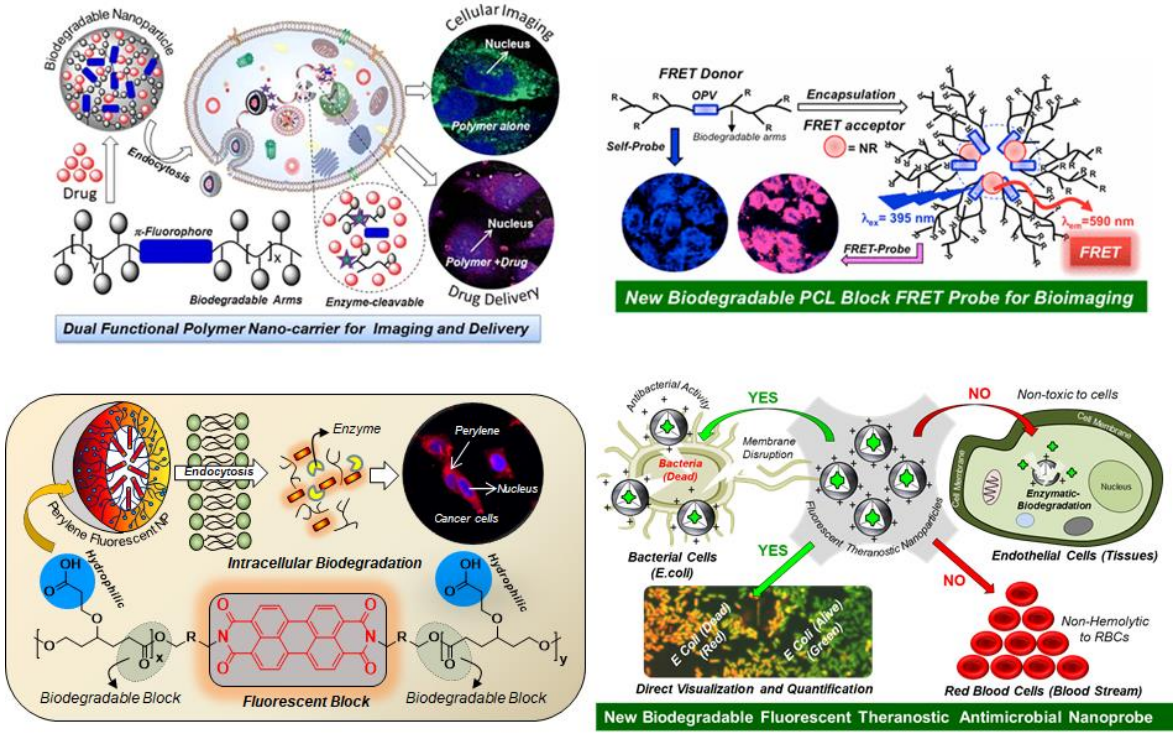

Figure 1.22. *Schematic representation of the work done using the carboxylic substituted monomer for bioimaging and antimicrobial applications.*

The water insolubility of polycaprolactones, owing to their semi-crystalline nature, puts them under scrutiny for its self-assembling property; and this was overcome by the introduction of polyethylene glycol (PEG) as the hydrophilic counterpart for the hydrophobic PCL. Based on this approach, several di and tri-block copolymers have been designed for controlled drug delivery applications.[238–240] However, according to a report in Nature Chemistry, PEG is not always the ideal choice as a hydrophilic part. Since their conjugation to proteins reduces their bioavailability, interferes with receptor binding interactions due to sterics and hence, in turn, will affect the therapeutic efficiency of the drug.[241] Though the example here discusses about PEG-conjugated proteins, however, same concept can be extended to the polymeric systems where PEG conjugation might affect their interactions within the cell or reduce the drug bioavailability. Also PEG chains are biocompatible but not completely biodegradable.[242] Hence, the next question is to come up with the design of a scaffold that relieves PEG without disturbing the hydrophobic-hydrophilic balance. Hence, the development of new classes of fully biodegradable amphiphilic PCL based block copolymers for drug delivery applications *in vitro* and *in vivo* seems to be the need of the hour.

1.7 Aim of the Thesis

With the aforementioned detailed literature review, it was easy to comprehend the cracks in the system understanding so far. All the topics discussed in the previous sections were slowly laying down the way for designing an ideal nano-formulation for chemotherapeutics delivery *in vivo*. Amongst the different types of nanoparticles, polymeric NPs stood out in terms of their structural versatility, functional modifications and most importantly, biocompatibility. In order to achieve a fully biodegradable polymer platform, we chose the polycaprolactone system as the hydrophobic part and based on our lab expertise, the carboxylic-substituted polycaprolactone constituted the hydrophilic shell. Our aim was to study the role played by polymer topology on the self-assembly, drug loading content, *in vitro* cellular uptake as well as on the biodistribution and pharmacokinetics *in vivo*. Further, we also wanted to investigate the effect of surface charge on the cellular permeability and the endocytosis pathway. As can be seen in figure 1.23, my entire thesis work has been represented schematically highlighting the four different tasks I tried to achieve during the course of my PhD.

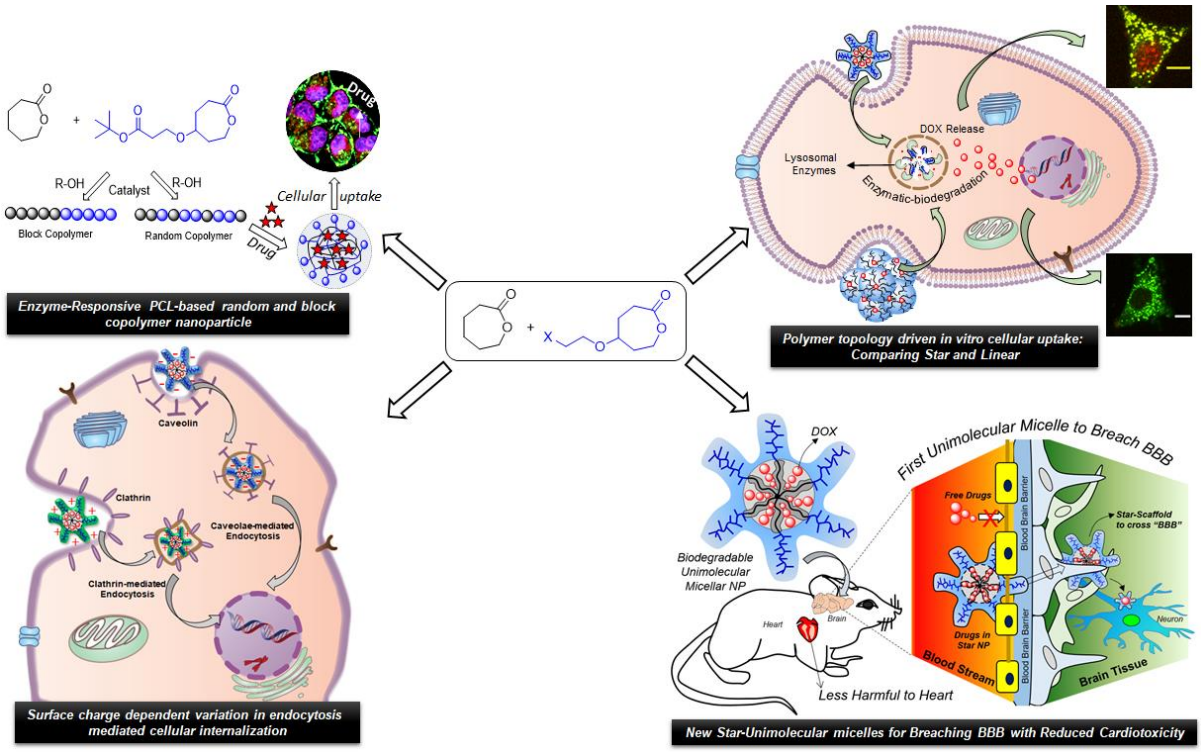

Figure 1.23. *Schematic representation of the consolidated thesis work.*

The thesis work has been divided into four chapters and an insight into these have been explained below.

1. In **chapter 2**, new classes of fully biodegradable carboxylic functional PCL and PCL based random and block copolymers have been engineered to gain fundamental insight into the enzyme-controlled drug delivery of PCL nano-scaffolds. The role of composition of hydrophobic PCL and hydrophilic carboxylic PCL in the random copolymer backbone on the enzyme-cleavage of the nano-assemblies to release the DOX at the intracellular level was investigated. *In vitro* cellular uptake and cytotoxicity of doxorubicin loaded random and block copolymers was studied in both breast and cervical cancer cells.
2. **Chapter 3** highlights the design and development of star-shaped macromolecular architectures utilizing ring opening polymerization in a sequential manner. The star and linear block copolymer topologies were compared in terms of their self-assembly, drug loading content and *in vitro* cellular uptake whilst maintaining similar chemical composition and molecular weight. The formation of unimolecular micelles was established employing the pyrene encapsulation experiment along with DLS, SAXS,

FESEM, AFM and HR-TEM. Live cell imaging was performed using confocal laser scan microscopy (CLSM) to elucidate the uptake mechanism.

3. In **chapter 4**, the star-shaped and linear polycaprolactone block copolymers, synthesized in the previous chapter, were chosen as model systems to investigate the role of polymer topology on the *in vivo* biodistribution and pharmacokinetics. For the *in vivo* study, doxorubicin (DOX) was selected as the model drug and DOX-loaded star and linear block copolymers constituted the other two groups. Herein, the plasma samples were collected at different time intervals to understand the pharmacokinetics. Further, the biodistribution study was carried out in five different organs namely, brain, heart, kidneys, liver and spleen via quantification assay and visualization via CLSM. The biocompatibility of the nanoparticles was investigated via the cytokine analysis, hemolysis assay and H&E histological analysis.
4. In **chapter 5**, the role of surface charge on the cellular internalization and the opted endocytosis pathway were examined using the star-shaped PCL block copolymers. Anionic, neutral and cationic star-shaped polymers were synthesized via the ring opening polymerization. Their encapsulation capability was determined by employing multiple dyes such as Nile red (neutral), HPTS (anionic), IR 780 (cationic), Cardiogreen (zwitterionic) and an anticancer drug, DOX. The surface charge of nanoparticles was determined based on zeta potential values. The dye-loaded nanoparticles were subjected to *in vitro* cellular uptake study in WT-MEF, HEK293T and primary neuronal culture (from chick embryo) cell lines

Finally, the entire work was summarized and directions towards the future research have been highlighted in the last section.

2

Biodegradable Polycaprolactone Block and Random Copolymer Architectures for Drug Delivery to Cancer Cells

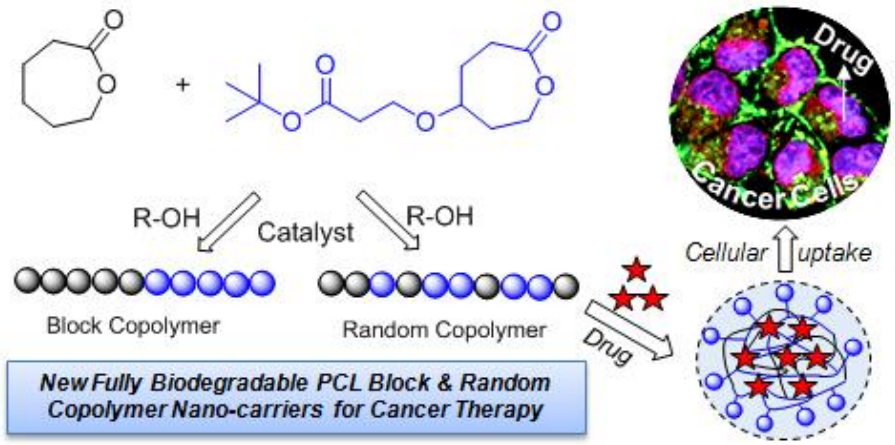

Abstract

This chapter reports polymer topology design principle for programming the enzymatic-biodegradation and delivery of anticancer drugs at the intracellular compartments of breast and cervical cancers. To accomplish this goal, new classes of biodegradable amphiphilic block and random copolymers based on hydrophilic carboxylic functionalized polycaprolactone (CPCL) and hydrophobic polycaprolactone (PCL) units were designed via ring opening polymerization methodology. The inter-chain interactions and chain packing were directly controlled by the topology of the polymers and the block copolymers were found to be as semi-crystalline materials. These amphiphilic block and random polymers were readily dispersible in water and they self-assembled into < 200 nm nanoparticles. These nanoparticles exhibited excellent capability for loading anticancer drug doxorubicin (DOX) in the hydrophobic pocket. *In vitro* drug release kinetics revealed that the polymer nano-scaffolds were stable under physiological conditions and they exclusively ruptured in the presence of lysosomal esterase enzyme at the intracellular compartments to deliver DOX. The "burst" and "controlled" release of drugs from the polymer nano-carriers was directly controlled by length and chemical composition of block and random copolymers. *In vitro* cytotoxicity studies in breast cancer (MCF 7) and cervical cancer (HeLa) cells revealed that the nascent polymer nanoparticle was highly biocompatible and non-toxic to cells whereas their DOX loaded nanoparticles accomplished > 90 % cell killing. Confocal microscopy reinstated the cellular uptake of the DOX-loaded polymer scaffold wherein the nanoparticle was highly concentrated at the nucleus and revealed that the drugs were predominately delivered at the nucleus of the cells for apoptosis. Flow cytometry investigation confirmed the enhanced DOX delivering capability of block and random copolymer nanoparticles compared to free DOX. The newly designed fully biodegradable PCL based block and random nano-carriers are excellent scaffolds for enzyme-mediated intracellular delivery of DOX and the proof-of-concept was established in breast and cervical cancers.

2.1 Introduction

Aliphatic polyesters are important classes of biomaterials and they are extensively used in biodegradable implants,[214] tissue engineering,[215,243] drug and gene delivery,[216,244] etc. Polyethyleneglycol (PEG)-block-polyesters have very good hydrophilic-hydrophobic balance in the backbone and they self-assembled into nano-carriers such as micelles.[245] PEG-b-poly(L-lactide)[246] or PEG-b-poly(L-gylycolide)[247] were excellent biodegradable materials; however, the poor hydrolytic and environmental stability[248,249] of their self-assembled nano-carriers in aqueous medium induced additional difficulties in handling them as drug carriers. PEG-b-poly(α-hydroxy esters) were made by the ring opening polymerization of α-hydroxy L-amino acid cyclic monomers[250] and few attempts were made to explore these aliphatic polyesters for drug delivery.[251,252] PEG-b-polycaprolactone (PCL) is one of the most prominent polyester due to its excellent mechanical strength, environmental stability, rheological and visco-elastic properties and so on so forth.[217] PCL is known to undergo degradation in a two-step process wherein random chain scission occurs first via hydrolytic cleavage at the tissues followed by the enzymatic biodegradation at the intracellular level.[253] PCL chains are highly hydrophobic and are most often found to experience slow degradation under physiological conditions for more than 24 months.[218] To introduce stimuli-responsiveness and also make provision for anchoring drugs or targeting agents; substituted PCL with hydroxyl,[213,219] ketone,[220] imine,[221] amine,[222] azide,[223] carboxylic,[213,224] alkoxyloxy,[225,226,229] cholesteryl,[228] oligoethyleneoxy,[254] propargyl[255–257] and menthide[258] functional groups were developed.

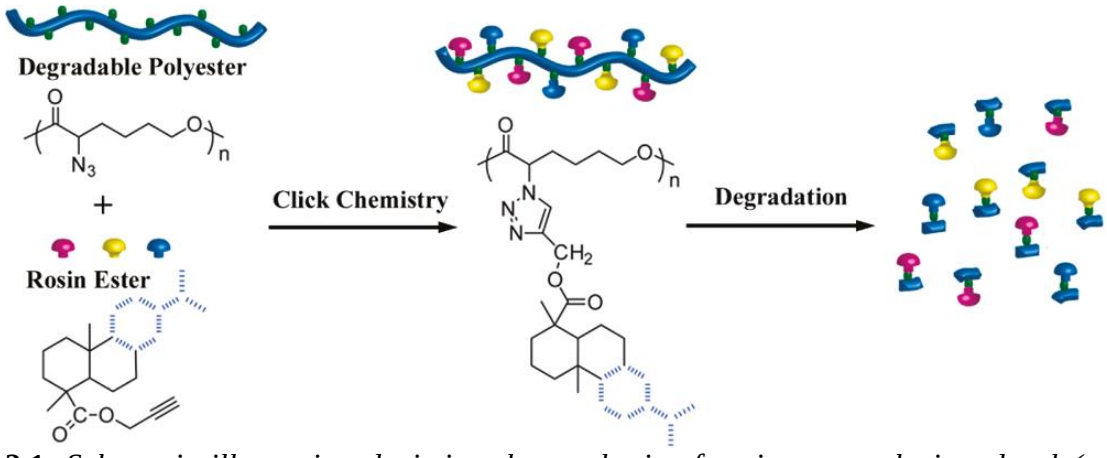

Figure 2.1. *Schematic illustration depicting the synthesis of rosin-ester substituted poly(ε-caprolactone) via click chemistry (adapted from Yao et al. Biomacromolecules* **2011**, *12,* 2171–2177).

Most of these substituted PCL copolymers were primarily developed to study the structure-property relationship.[259] Few of these substituted PCL copolymers were self-assembled in aqueous medium as pH[230] or thermo-responsive nanoparticles[229] for delivering anticancer drugs and siRNA.[221] From our group, we have reported pH-responsive carboxylic substituted PCL diblock copolymers for oral delivery of camptothecin and ibuprofen under GI tract conditions (see figure 2.2).[231] The carboxylic acid PCL block copolymers were conjugated with cisplatin drug to facilitate it's delivery against glutathione (GSH) detoxification in breast cancer cells.[232,260] Fluorescent-tagged PCL block copolymers were also reported for accomplishing both drug delivery as well as bio-imaging together in a single system.[234]

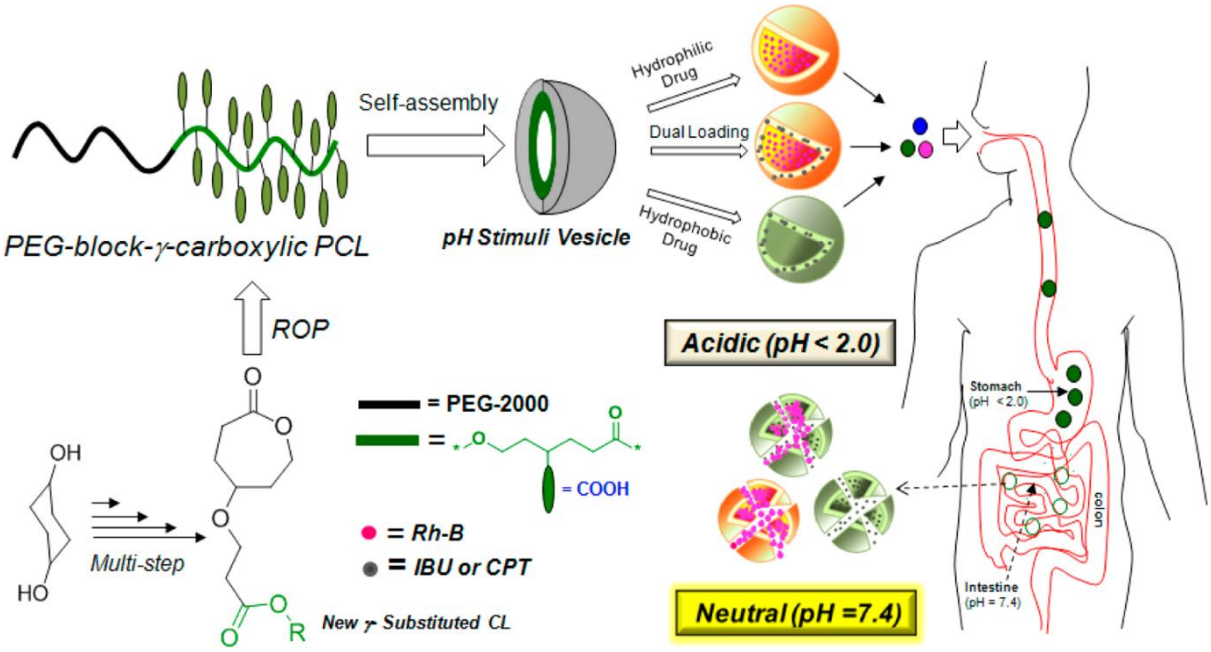

Figure 2.2. *Development of pH-responsive carboxylic substituted PCL based vesicles for oral drug delivery applications. (adapted from Surnar et al. Biomacromolecules* **2013**, *14,* 4377−4387)

Recently, Bapurao et al. from our laboratory had reported the enzymatic-biodegradation of DOX loaded PEG-b-PCL system with substituted PCL block copolymers.[261] It was found that the PCL segment unit was relatively less accessible by the enzymes whereas the substituted PCL chains were found to exhibit excellent enzymatic-biodegradation. Polymer topology in PCL systems were reported to play significant role on the vesicular[262] and nanoparticle self-assembly,[263] lamellar morphologies,[264] semi-crystalline properteis[265,266] and so on.

Unfortunately, no effort has been taken to study the role of polymer topology on the enzymatic-biodegradation of PCL copolymers for drug delivery applications. Further, most of the PCL reports paid more importance to study their structure-property relationships and very less attention has been paid towards understanding biodegradation under physiological conditions. To address these important problems; here we have engineered new classes of carboxylic PCL-co-PCL random copolymers and carboxylic PCL-*block*-PCL block copolymers that are capable of loading anticancer drug doxorubicin for the treatment of breast and cervical cancers. By controlling the composition of hydrophobic PCL and hydrophilic carboxylic PCL (named as CPCL) in random copolymers and the lengths of the segments in block copolymers; we could precisely programme the enzyme-cleavage of these polymer nano-assemblies to release DOX exclusively at the intracellular level. This fully biodegradable PCL nano-carrier approach is schematically shown in figure 2.3.

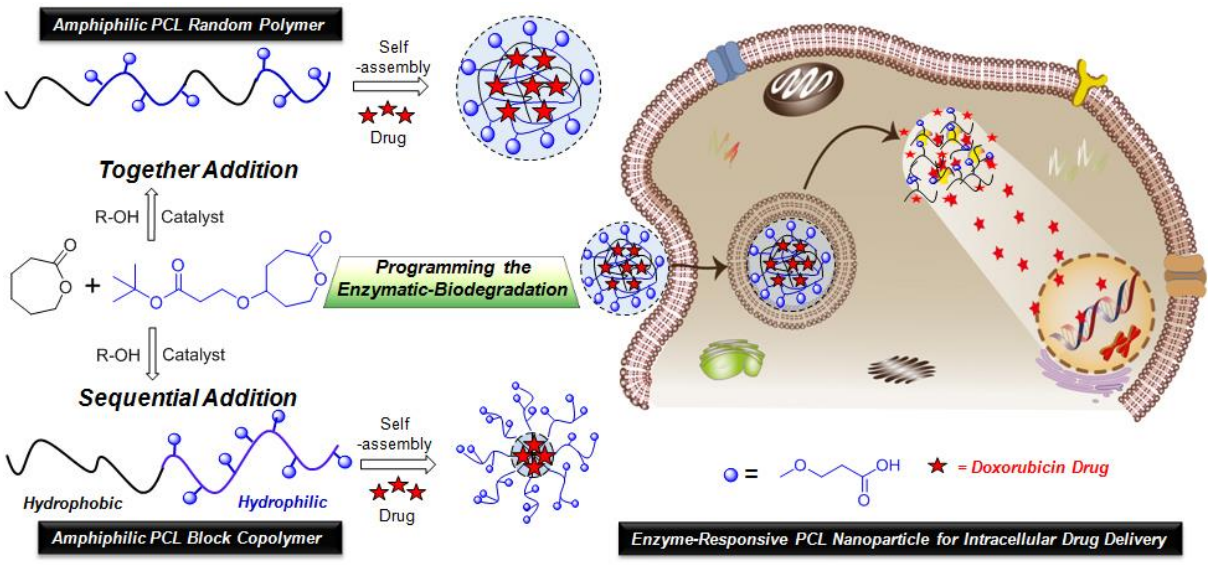

Figure 2.3. *Programming the enzymatic-biodegradation of amphiphilic block and random polycaprolactone copolymer nano-carriers and delivery of anticancer drug to cancer cells.*

The present investigation has emphasized to develop new classes of biodegradable amphiphilic PCL random and block copolymers from identical monomers and programme their enzyme-responsiveness for the delivery of anticancer drug DOX at the intracellular level. Ring opening polymerization of custom designed carboxylic substituted caprolactone and ε-

caprolactone (CL) monomers produced new classes of random and block copolymers. These copolymers were found to self-assemble in water as nanoparticles with sizes ranging from 60-150 nm. The polymeric nanoparticles exhibited good loading for the hydrophobic anticancer drug doxorubicin. The scaffold being composed of aliphatic polyester backbone was responsive to the intracellular lysosomal esterase enzyme action. The degradation kinetics of these polymeric micelles was selectively tuned in the presence of esterase by varying the composition of the hydrophobic PCL and the hydrophilic carboxylic PCL. The nascent polymer was highly biocompatible and non-toxic whereas the DOX loaded nanoparticles accomplished > 90 % cell death in breast and cervical cancer cell lines. Confocal microscopy and flow cytometry studies showed exorbitant cellular uptake of the DOX-loaded random and block copolymer nanoparticles in comparison to free DOX. Thus, we were able to successfully demonstrate one of the first examples of fully biodegradable carboxylic substituted PCL amphiphilic block and random copolymer nano-carriers to efficiently deliver DOX to cancer cells by programming the enzymatic-cleavage at the intracellular compartments.

2.2 Experimental Methods

2.2.1 Materials

Cis, trans-1,4-cyclohexanediol, potassium t-butoxide, tertiary butyl acrylate, pyridinium chlorochromate (PCC), molecular sieves (4Å), m-chloroperbenzoic acid (m-CPBA), triethyleneglycol monomethylether (TEG), tin(II) 2-ethylhexanoate ($Sn(oct)_2$), caprolactone (CL), pyrene, horse-liver esterase were acquired from Sigma Aldrich. Doxorubicin hydrochloride was purchased from Alfa Aesar. All the salts were purchased locally (Vetec chemicals). TEG was vacuum dried before use. Human breast cancer cells (MCF 7) and cervical cancer cells (HeLa) were maintained in DMEM (Gibco) containing 10 % (v/v) fetal bovine serum (FBS) and 1 % (v/v) penicillin–streptomycin at 37 °C under a 5 % CO_2 humidified atmosphere. Cells were washed with 40 % DPBS (Gibco), trypsinised using 0.05 % trypsin (Gibco) and seeded in 96 well or 6 well (as per experiment) flat bottomed plastic plates (Costar) for all assays. Tetrazolium salt, 3-(4, 5 dimethylthiazolyl)-2,5 diphenyltetrazolium bromide (MTT), DMSO, DAPI and 4 % paraformaldehyde were obtained from Sigma Aldrich chemicals. Fluoromount was purchased from Southern Biotech. Alexa fluor-488 conjugated Phalloidin was purchased from Invitrogen. Tetrahydrofuran (THF),

methanol, petroleum ether, and trifluoroacetic acid (TFA) solvents were distilled and purified prior to use.

2.2.2 Methods

Bruker 400 MHz spectrophotometer was used for recording NMR samples in $CDCl_3$ solvent using TMS as the standard. Size exclusion chromatography (SEC) data acquisition was carried out by a Viscotek VE 1122 pump, Viscotek VE 3580 RI, 3210 UV-Vis and Light scattering detectors. Samples for SEC were prepared in THF and executed from method files obtained after calibration using polystyrene standards. The mass determination for all the compounds was carried out using high-resolution mass spectrometry-electrospray ionization-quantitative time-of-flight liquid chromatography-mass spectrometry (HRMS-ESI-Q-TOF LC-MS) and Applied Bio system 4800 PLUS matrix-assisted laser desorption/ionization (MALDI) TOF/TOF Analyzer. The Perkin-Elmer thermal analyzer STA 6000 model was used to determine the polymer's thermal stability at 10 °C/min heating rate under nitrogen atmosphere. Thermal properties of polymers were analyzed using a TA Q20 differential scanning calorimeter (DSC), wherein the polymers were first heated to melt in order to remove any pre-thermal history and then subsequent heating-cooling cycles were recorded at 10 °C/min under inert conditions to generate the respective thermograms. Water Contact angle measurements were performed very carefully at room temperature (25 °C) making sure that the image was recorded within a minute to reduce the evaporation effects. GBX Model (DIGIDROP instrument) was used for the experiment. Perkin-Elmer Lambda 45 UV-Visible Spectrophotometer was used for the absorption studies. Emission spectra for determining the Critical Micelle Concentration (CMC) were recorded using a SPEX Fluorolog HORIBA JOBIN VYON fluorescence spectrophotometer. A 450 W Xe lamp serves as the source of excitation at room temperature. Pyrene was used as the fluorophore, which has excitation maxima at 337 nm. The emission spectrum gives five distinct vibronic levels, amongst which the intensity of levels I_1 and I_3 are known to be extremely sensitive of the hydrophobic environment. As a result, pyrene when encapsulated within a micelle will give different I_1 and I_3 values. The ratio of I_1/I_3 v/s log C is plotted in order to determine the critical aggregate concentration (CAC). Dynamic light scattering (DLS) was performed using Nano ZS-90 setup (Malvern instruments). DLS utilizes a 633 nm laser as the light source, and the detector collects the scattered light at 90° angle. This gives information about the correlation function [$g^2(t)$],

from which the diffusion coefficient (D) is calculated using cumulant method and further the diameter of the particle is determined using the Stock-Einstein equation. The experiment was performed thrice with independent amphiphilic solutions to yield reproducible data. FE-SEM analysis requires the sample to be drop casted on silicon wafer followed by gold-coating to make it conducting and the experiment was done on a Zeiss Ultra Plus scanning electron microscope. Polymer solutions were drop casted on mica plates for carrying out atomic force microscopic (AFM) analysis using Agilent instruments. Again the reproducibility of the data was confirmed using three independent polymer solutions. Transmission electron microscopic (TEM) images were acquired by drop casting the samples onto Formvar-coated copper grid via a Technai-300 instrument. Polarized light microscope (PLM) LEICA DM2500 P was used to record the crystallization event taking place in the polymers. This PLM was equipped with Linkam TMS 94 heating and cooling stage. Confocal microscopic analysis was done using LSM 710 microscope. The cell viability determination was done by measuring the absorbance of the formazan crystals on a microplate reader (Varioskan Flash).

2.2.3 Synthesis Procedures

Synthesis of t-butyl 3-((4-hydroxycyclohexyl) oxy) propionates (1): 1,4-Cyclohexanediol (20.0 g, 172.4 mmol) was dissolved in dry THF (300 mL) followed by addition of catalytic amount of potassium t-butoxide (200 mg) and the mixture was stirred for 30 min under inert conditions. To this solution t-butyl acrylate (15.4 g, 120.6 mmol) in dry THF (50 mL) was added drop wise and the reaction mixture was refluxed under nitrogen atmosphere for 30 h. THF was removed using rotavapor and the mixture was neutralized with 1N HCl (20 mL). It was extracted with ethyl acetate and the organic layer was dried over anhydrous Na_2SO_4. The solvent was evaporated and the product was obtained as a pale coloured viscous liquid. It was further purified by passing through column chromatography using ethyl acetate and petroleum ether (3:20 v/v). Yield = 14.0 g (49 %). ^{1}H NMR (400 MHz, $CDCl_3$) δ ppm: 3.66 (m, 3H, O−C**H**$_2$− and O−C**H**), 3.37−3.25 (m, 1H, C**H**−OH), 2.44 (t, 2H, −C**H**$_2$CO-), 1.94−1.81 (m, 4H, OCH(C**H**$_2$)$_2$), 1.63−1.30 (m, 4H, CO(C**H**$_2$)$_2$), 1.43 (s, 9H, −C(C**H**$_3$)$_3$). ^{13}C NMR (100 MHz, $CDCl_3$) δ ppm: 171.08, 80.43, 69.50, 63.94, 63.53, 32.54, 30.33, 29.17 and 27.44. FT-IR (cm^{-1}): 3407, 2975, 2934, 2867, 1731, 1454, 1393, 1367, 1255, 1152, 1101, 1065, 994, 953, 896, 845, 753 and 620. HRMS (ESI+): m/z [M+Na$^+$] calcd. for $C_{13}H_{24}O_4$[M$^+$] : 267.15; found: 267.1564

Synthesis of tert-butyl 3-((4-oxocyclohexyl)oxy)propanoate (2): Compound **1** (14.0 g, 57.3 mmol) was dissolved in dry DCM (280 mL) under nitrogen atmosphere and stirred at 25 °C. PCC (24.7 g, 114.7 mmol) was added slowly to the above solution followed by molecular sieves (4Å) to absorb the moisture. The reaction mixture was stirred for 6 h and then filtered using DCM. It was then purified by passing through silica column using ethyl acetate and petroleum ether (1:10 v/v). The product was obtained as a colourless liquid. Yield = 13.0 g (94 %). ^{1}H NMR (400 MHz, $CDCl_3$) δ ppm: 3.71 (m, 3H, O−C**H₂** and O−C**H**), 2.48 (t, 2H, −C**H₂**−CO), 2.55 (m, 2H, −(C=O)C**H₂**−), 2.22 (m, 2H, −(C=O)C**H₂**−), 2.06 (m, 2H, −(CO)C**H₂**−), 1.86 (m, 2H, −(C=O)C**H₂**−), 1.42 (s, 9H, −C(C**H₃**)$_3$). ^{13}C NMR (100 MHz, $CDCl_3$) δ ppm: 211.40, 170.9, 80.8, 72.9, 64.20, 37.20, 36.61, 30.60 and 28.23. FT-IR (cm^{-1}): 2978, 2938, 2872, 1716, 1453, 1418, 1393, 1368, 1307, 1251, 1206, 1155, 1110, 1059, 959, 893, 847, 757, 686. HRMS (ESI+): m/z [M+Na^+] calcd. for $C_{13}H_{22}O_4$[M^+] : 265.14; found: 265.1407.

Synthesis of tert-butyl 3-((7-oxooxepan-4-yl) oxy) propanoate (monomer 3-BPCL): m-CPBA (27.7 g, 161.5 mmol) was added to a solution of **2** (13.0 g, 53.7 mmol) in dry DCM (150 mL) under inert conditions with continuous stirring. It was followed by the addition of anhydrous $NaHCO_3$ (13.5 g, 161.5 mmol) and the reaction mixture was stirred at 25 °C for 12 h. The solvent was evaporated and the crude was quenched with saturated aqueous solution of $NaHCO_3$ and $Na_2S_2O_3$. It was extracted with ethyl acetate, and the organic layer was dried over anhydrous Na_2SO_4. The solvent was evaporated and the crude product was purified by passing over silica column using ethyl acetate and petroleum ether (1:5 v/v). The product was obtained as a colourless liquid. Yield = 10.0 g (72 %). ^{1}H NMR (400 MHz, $CDCl_3$) δ ppm: 4.43 (dd, 1H, COOC**H**), 4.00 (dd, 1H, COOC**H**), 3.63 (m, 3H, OC**H₂** and OC**H**), 2.92 (dd, 1H, COC**H**), 2.42 (t, 2H, COC**H₂**), 2.36 (dd, 1H, COC**H**), 1.99−1.76 (m, 4H, OCH−(C**H₂**)$_2$), 1.40 (s, 9H, C(C**H₃**)$_3$). ^{13}C NMR (101 MHz, $CDCl_3$) δ ppm: 176.00, 170.91, 80.79, 73.79, 63.91, 63.30, 36.63, 34.11, 28.07, 27.75 and 27.29. FT-IR (cm^{-1}): 2981, 2929, 2876, 1725, 1458, 1390, 1367, 1252, 1152, 1104, 1056, 1008, 951, 898, 841, 755 and 664. HRMS (ESI+): m/z [M+Na^+] calcd. for $C_{13}H_{22}O_5$[M^+] : 281.13; found: 281.1354.

Synthesis of butyl ester substituted Polycaprolactone Random copolymers: The typical synthetic procedure for ring opening polymerization of CL (M_1) and the γ-substituted caprolactone (M_2) using triethylene glycol as the initiator in the presence of $Sn(Oct)_2$ as catalyst

under inert conditions is outlined here for butyl ester substituted PCL_{50}-*r*-$BPCL_{50}$ (BPCL-50) copolymer. The feed was maintained as 0.5:0.5 for both monomers and $[M_1+M_2]/[I]$ was taken to be 100. TEG (8.6 mg, 0.0526 mmol) and $Sn(Oct)_2$ (10.6 mg, 0.0263 mmol) were taken in a flame dried schlenk tube followed by caprolactone (300 mg, 2.63 mmol) and **3** (679 mg, 2.63 mmol) under N_2 atmosphere. This polymerization mixture was evacuated under vacuum (0.1 mm of Hg) for 30 min with continuous stirring at room temperature. The tube was then immersed in a preheated oil bath at 130 °C and the polymerization was continued for 24 h with constant stirring. The mixture was precipitated in petroleum ether and cold methanol. The polymer was re-dissolved in THF and again precipitated in cold methanol. The precipitation was carried out at least twice to obtain highly pure polymer. Yield = 0.8 g (82 %). ^{1}H NMR (400 MHz, $CDCl_3$) δ ppm: 4.13 (t, 2 H), 4.05 (t, 1.96 H), 3.65 (m, 2.20 H), 3.43 (s, 1.04 H), 2.43 (t, 2.04 H), 2.37 (t, 2.04 H), 2.30 (t, 1.98 H), 1.81 (s, 2.15 H), 1.79 (t, 2.15 H), 1.64 (t, 4.12 H), 1.44 (s, 9.02 H), 1.37 (t, 2 H). ^{13}C NMR (101 MHz, $CDCl_3$) δ ppm: 207.0, 173.6, 173.5, 170.9, 80.6, 75.5, 64.8, 64.2, 64.1, 61.2, 61.1, 36.5, 34.1, 32.9, 30.9, 29.7, 28.9, 28.3, 28.1, 25.5, 24.6, 24.5. FT-IR (cm^{-1}): 2937, 1726, 1458, 1363, 1249, 1156, 1099, 1062, 960, 899, 846, 758.

Similar procedure was followed for other random copolymers varying the compositions from 10 to 80 mole %. Two homopolymers PCL and butyl ester BPCL-100 were also synthesized following the same procedure using caprolactone or monomer 3, respectively. The detailed synthesis is provided herewith.

Synthesis of PCL_{90}-*r*-$BPCL_{10}$ (BPCL-10): mTEG (4.79 mg, 0.0292 mmol), Sn $(Oct)_2$ (5.91 mg, 0.0146 mmol), CL (300 mg, 2.63 mmol), BCL (75.39 mg, 0.29 mmol). Yield = 0.34 g (91 %). ^{1}H NMR (400 MHz, $CDCl_3$) δ ppm: 4.13 (t, 2 H), 4.06 (t, 17.96 H), 3.64 (m, 3.04 H), 3.43 (s, 1.02 H), 2.44 (t, 2.22 H), 2.37 (t, 2.50 H), 2.30 (t, 17.6 H), 1.85 (s, 2.23 H), 1.78 (t, 2.23 H), 1.65 (t, 36.26 H), 1.44 (s, 9.32 H), 1.38 (t, 17.86 H). ^{13}C NMR (101 MHz, $CDCl_3$) δ ppm: 173.6, 173.5, 173.4, 170.8, 80.6, 75.5, 71.9, 70.5, 64.8, 64.2, 64.1, 61.2, 61.1, 36.5, 34.2, 34.1, 32.9, 32.3, 29.8, 29.0, 28.3, 28.1, 25.5, 24.6. FT-IR (cm^{-1}): 2942, 2865, 1721, 1470, 1365, 1293, 1240, 1157, 1104, 1043, 961, 842, 730. SEC molecular weights: M_w = 21,800 g/mol, M_n = 13,500 g/mol, M_w/M_n = 1.61.

Synthesis of PCL_{80}-*r*-$BPCL_{20}$ (BPCL-20): mTEG (7.20 mg, 0.0438 mmol), Sn $(Oct)_2$ (8.87 mg, 0.0219 mmol), CL (400 mg, 3.508 mmol), BCL (226.26 mg, 0.877 mmol). Yield = 0.5 g (80 %). ^{1}H NMR (400 MHz, $CDCl_3$) δ ppm: 4.13 (t, 2 H), 4.06 (t, 7.2 H), 3.65 (m, 2.52 H), 3.43 (s, 1.16 H), 2.44 (t, 2.28 H), 2.37 (t, 2.24 H), 2.31 (t, 7.22 H), 1.86 (s, 2.36 H), 1.78 (t, 2.36 H), 1.64 (t, 15.16 H), 1.45 (s, 9.82 H), 1.38 (t, 7.26 H). ^{13}C NMR (101 MHz, $CDCl_3$) δ ppm: 173.6, 173.5, 173.4, 170.8, 80.6, 75.5, 71.9, 70.5, 64.8, 64.2, 64.1, 62.6, 61.2, 61.1, 59.0, 36.5, 34.2, 34.1, 32.9, 32.3, 29.8, 29.0, 28.3, 28.1, 25.5, 25.3, 24.7, 24.6. FT-IR (cm^{-1}): 2937, 2867, 1725, 1457, 1424, 1390, 1366, 1237, 1156, 1099, 1061, 1003, 960, 898, 841, 750, 736, 645. SEC molecular weights: M_w = 26,000 g/mol, M_n = 18,500 g/mol, M_w/M_n = 1.41.

Synthesis of PCL_{70}-*r*-$BPCL_{30}$ (BPCL-30): mTEG (6.17 mg, 0.0375 mmol), Sn $(Oct)_2$ (7.59 mg, 0.0188 mmol), CL (300 mg, 2.6315 mmol), BCL (290.76 mg, 1.127 mmol). Yield = 0.45 g (76 %). ^{1}H NMR (400 MHz, $CDCl_3$) δ ppm: 4.13 (t, 2 H), 4.05 (t, 3.98 H), 3.65 (m, 2.36 H), 3.43 (s, 1.02 H), 2.44 (t, 2.12 H), 2.37 (t, 2.12 H), 2.30 (t, 3.98 H), 1.86 (s, 2.06 H), 1.78 (t, 2.06 H), 1.64 (t, 8.02 H), 1.45 (s, 9.04 H), 1.38 (t, 4.02 H). ^{13}C NMR (101 MHz, $CDCl_3$) δ ppm: 207.0, 173.6, 173.5, 173.4, 170.8, 80.6, 75.5, 67.9, 64.8, 64.2, 64.1, 61.2, 61.1, 36.5, 34.1, 32.9, 30.9, 29.8, 29.0, 28.3, 28.1, 25.5, 24.6, 24.5. FT-IR (cm^{-1}): 2938, 2867, 1729, 1457, 1419, 1395, 1366, 1247, 1156, 1103, 1065, 1003, 961, 898, 846, 755, 655. SEC molecular weights: M_w = 26,000 g/mol, M_n = 17,100 g/mol, M_w/M_n = 1.52.

Synthesis of PCL_{60}-*r*-$BPCL_{40}$ (BPCL-40): mTEG (7.2 mg, 0.0438 mmol), Sn $(Oct)_2$ (8.87 mg, 0.0219 mmol), CL (300 mg, 2.63 mmol), BCL (452.4 mg, 1.75 mmol). Yield = 0.54 g (72 %). ^{1}H NMR (400 MHz, $CDCl_3$) δ ppm: 4.11 (t, 2 H), 4.03 (t, 2.98 H), 3.63 (m, 2.30 H), 3.42 (s, 1.02 H), 2.42 (t, 2.06 H), 2.35 (t, 2.08 H), 2.28 (t, 3.08 H), 1.84 (s, 2.15 H), 1.76 (t, 2.15 H), 1.62 (t, 6.16 H), 1.43 (s, 9.24 H), 1.36 (t, 3.14 H). ^{13}C NMR (101 MHz, $CDCl_3$) δ ppm: 207.0, 173.6, 173.5, 173.4, 170.8, 80.5, 75.4, 68.0, 64.8, 64.2, 64.1, 61.2, 61.1, 36.5, 34.1, 32.9, 32.3, 29.8, 29.0, 28.3, 28.1, 25.5, 24.5. FT-IR (cm^{-1}): 2938, 1726, 1459, 1421, 1363, 1248, 1156, 1099, 1063, 961, 898, 846, 756. SEC molecular weights: M_w = 21,400 g/mol, M_n = 14,100 g/mol, M_w/M_n = 1.52.

Synthesis of PCL_{40}-*r*-$BPCL_{60}$ (BPCL-60): mTEG (7.20 mg, 0.0437 mmol), Sn $(Oct)_2$ (8.85 mg, 0.0218 mmol), CL (200 mg, 1.75 mmol), BCL (677.3 mg, 2.62 mmol). Yield = 0.61 g (70 %). ^{1}H NMR (400 MHz, $CDCl_3$) δ ppm: 4.13 (t, 2 H), 4.05 (t, 1.24 H), 3.65 (m, 2.20 H), 3.44

(s, 1.00 H), 2.44 (t, 2.06 H), 2.37 (t, 2.00 H), 2.30 (t, 1.24 H), 1.86 (s, 2.01 H), 1.78 (t, 2.01 H), 1.63 (t, 2.74 H), 1.45 (s, 9.00 H), 1.38 (t, 1.28 H). ^{13}C NMR (101 MHz, $CDCl_3$) δ ppm: 207.0, 173.6, 173.5, 173.4, 170.8, 80.6, 75.5, 75.4, 64.8, 64.6, 64.2, 61.2, 36.5, 34.1, 32.9, 30.9, 29.8, 28.3, 28.1, 25.5, 24.6. FT-IR (cm^{-1}): 2936, 1726, 1458, 1363, 1250, 1156, 1099, 1062, 1004, 960, 898, 846, 758. SEC molecular weights: M_w = 20,900 g/mol, M_n = 14,800 g/mol, M_w/M_n = 1.41.

Synthesis of PCL_{30}-*r*-$BPCL_{70}$ (BPCL-70): mTEG (9.56 mg, 0.058 mmol), Sn $(Oct)_2$ (11.75 mg, 0.029 mmol), CL (200 mg, 1.75 mmol), BCL (1.05 g, 4.08 mmol). Yield = 0.85 g (68 %). ^{1}H NMR (400 MHz, $CDCl_3$) δ ppm: 4.13 (t, 2 H), 4.05 (t, 1.02 H), 3.65 (s, 2.16 H), 3.43 (s, 1.00 H), 2.43 (t, 2.02 H), 2.37 (t, 1.98 H), 2.30 (t, 1.04 H), 1.85 (s, 2.01 H), 1.78 (t, 2.01 H), 1.64 (t, 2.14 H), 1.44 (s, 9.00 H), 1.37 (t, 0.98 H). ^{13}C NMR (101 MHz, $CDCl_3$) δ ppm: 207.0, 173.6, 173.4, 170.8, 80.6, 75.5, 64.8, 64.2, 64.1, 61.2, 61.1, 36.5, 36.3, 34.1, 32.9, 30.9, 29.7, 28.9, 28.3, 28.1, 25.5, 24.5. FT-IR (cm^{-1}): 2972, 2933, 2872, 1730, 1452, 1420, 1395, 1367, 1252, 1157, 1099, 1061, 1004, 955, 898, 846, 755, 650. SEC molecular weights: M_w = 20,700 g/mol, M_n = 14,600 g/mol, M_w/M_n = 1.42.

Synthesis of PCL_{20}-*r*-$BPCL_{80}$ (BPCL-80): mTEG (7.20 mg, 0.044 mmol), Sn $(Oct)_2$ (8.87 mg, 0.022 mmol), CL (100 mg, 0.877 mmol), BCL (905.06 mg, 3.508 mmol). Yield = 0.63 g (63 %). ^{1}H NMR (400 MHz, $CDCl_3$) δ ppm: 4.13 (t, 2 H), 4.05 (t, 0.54 H), 3.65 (s, 2.12 H), 3.44 (s, 1.02 H), 2.43 (t, 2.02 H), 2.37 (t, 2.00 H), 2.30 (t, 0.58 H), 1.86 (s, 2.08 H), 1.78 (t, 2.08 H), 1.64 (t, 1.14 H), 1.44 (s, 9.12 H), 1.37 (t, 0.60 H). ^{13}C NMR (101 MHz, $CDCl_3$) δ ppm: 207.0, 173.6, 173.4, 170.8, 80.5, 75.5, 75.4, 64.8, 64.6, 64.2, 61.2, 61.1, 36.5, 36.3, 34.1, 32.9, 30.9, 29.7, 28.9, 28.3, 28.1, 25.5, 24.5. FT-IR (cm^{-1}): 2972, 1726, 1457, 1363, 1251, 1156, 1099, 1062, 1004, 960, 898, 846, 758, 634. SEC molecular weights: M_w = 19,300 g/mol, M_n = 13,900 g/mol, M_w/M_n = 1.39.

Synthesis of Teg-$BPCL_{100}$ (BPCL-100): mTEG (3.18 mg, 0.019 mmol), Sn $(Oct)_2$ (3.90 mg, 0.009 mmol), BCL (500 mg, 1.93 mmol). Yield = 0.3 g (60 %). ^{1}H NMR (400 MHz, $CDCl_3$) δ ppm: 4.14 (t, 2 H), 3.64 (s, 2.13 H), 3.43 (s, 1 H), 2.43 (t, 2.08 H), 2.36 (t, 2 H), 1.86 (s, 2.04 H), 1.77 (t, 2.04 H), 1.44 (s, 9.02 H). ^{13}C NMR (101 MHz, $CDCl_3$) δ ppm: 173.8, 171.0, 80.5, 75.5, 64.8, 64.7, 61.2, 60.0, 36.5, 36.4, 32.9, 29.7, 29.0, 28.5, 28.1. FT-IR (cm^{-1}): 2972, 2931,

1726, 1456, 1363, 1251, 1156, 1100, 1062, 1004, 961, 898, 846, 758. SEC molecular weights: M_w = 21,100 g/mol, M_n = 15,000 g/mol, M_w/M_n = 1.41.

Synthesis of Teg-PCL$_{100}$: mTEG (7.19 mg, 0.0438 mmol), Sn (Oct)$_2$ (8.87 mg, 0.0219 mmol), CL (500 mg, 4.38 mmol). Yield = 0.41 g (82 %). ^{1}H NMR (400 MHz, $CDCl_3$) δ ppm: 4.07 (t, 2 H), 3.65 (m, 0.12 H), 2.30 (t, 2.03 H), 1.64 (t, 4.24 H), 1.37 (t, 2.00 H). ^{13}C NMR (101 MHz, $CDCl_3$) δ ppm: 173.7, 64.2, 34.2, 28.4, 25.5, 24.6. FT-IR (cm^{-1}): 2938, 1720, 1467, 1363, 1291, 1238, 1174, 1104, 1040, 958, 832, 769, 728, 635. SEC molecular weights: M_w = 40,400 g/mol, M_n = 19,150 g/mol, M_w/M_n = 2.11.

Synthesis of Carboxylic functionalized PCL random copolymers (PCLy-r-CPCLx): The synthetic protocol for deprotection of t-butyl group is described for carboxylic substituted polymer **PCL$_{50}$-*r*-CPCL$_{50}$ (CPCL-50)**. Trifluoroacetic acid (TFA, 5.0 mL) was added slowly to a round-bottom flask containing the butyl ester polymer BPCL-50 (500 mg) at 0 °C followed by sonication to completely dissolve the polymer. The reaction was continued for 30 min at 0 °C with constant stirring. TFA was completely removed by repeated washings with toluene. The deprotected polymer was dissolved in THF and precipitated in cold methanol. The precipitation was repeated thrice to obtain pure polymer. Yield = 0.4 g (94 %). ^{1}H NMR (400 MHz, $CDCl_3$) δ ppm: 4.14 (t, 2 H), 4.06 (t, 2.01 H), 3.70 (s, 2.24 H), 3.48 (s, 1 H), 2.57 (t, 1.97 H), 2.38 (t, 2.06 H), 2.31 (t, 2.01 H), 1.87 (s, 2 H), 1.78 (t, 2 H), 1.64 (t, 4.17 H), 1.37 (t, 2.17 H). ^{13}C NMR (101 MHz, $CDCl_3$) δ ppm: 173.9, 173.8, 75.8, 64.5, 64.3, 61.2, 46.0, 35.3, 35.1, 34.2, 32.9, 29.8, 28.9, 28.4, 25.6, 24.6. FT-IR (cm^{-1}): 2933, 1722, 1393, 1355, 1168, 1098, 1061, 961, 735, 705, 661.

Synthesis of PCL$_{90}$-*r*-CPCL$_{10}$ (CPCL-10): BPCL-10 polymer (300 mg), TFA (3.0 mL). Yield = 0.27 g (94 %). ^{1}H NMR (400 MHz, $CDCl_3$) δ ppm: 4.12 (t, 2 H), 4.04 (t, 18.26 H), 3.64 (s, 3.28 H), 3.44 (s, 1.01 H), 2.51 (t, 2.09 H), 2.34 (t, 2.66 H), 2.29 (t, 18.28 H), 1.83 (s, 2.05 H), 1.76 (t, 2.05 H), 1.63 (t, 37.79 H), 1.36 (t, 19.32 H). ^{13}C NMR (101 MHz, $CDCl_3$) δ ppm: 173.7, 75.8, 64.2, 62.6, 61.2, 35.4, 34.2, 33.8, 32.9, 29.8, 29.0, 28.4, 25.6, 24.6, 24.4. FT-IR (cm^{-1}): 2942, 2865, 1722, 1470, 1365, 1293, 1240, 1171, 1104, 1045, 960, 840, 730, 632. SEC molecular weights: M_w = 6,100 g/mol, M_n = 2,500 g/mol, M_w/M_n = 2.44.

Synthesis of PCL$_{80}$-*r*-CPCL$_{20}$ (CPCL-20): BPCL-20 polymer (300 mg), TFA (3.0 mL). Yield = 0.27 g (98 %). ^{1}H NMR (400 MHz, $CDCl_3$) δ ppm: 4.13 (t, 2 H), 4.04 (t, 7.92 H), 3.68 (s,

2.70 H), 3.44 (s, 0.98 H), 2.53 (t, 2.09 H), 2.33 (t, 2.29 H), 2.29 (t, 8.03 H), 1.84 (s, 1.97 H), 1.76 (t, 1.97 H), 1.63 (t, 16.09 H), 1.36 (t, 7.96 H). ^{13}C NMR (101 MHz, $CDCl_3$) δ ppm: 173.9, 173.7, 75.7, 64.5, 64.2, 62.6, 61.0, 40.5, 35.2, 34.1, 33.8, 32.8, 32.1, 29.8, 28.9, 28.3, 25.5, 25.3, 24.6, 24.3. FT-IR (cm^{-1}): 2942, 1722, 1362, 1237, 1162, 1101, 1063, 960, 731. SEC molecular weights: M_w = 4,500 g/mol, M_n = 2,800 g/mol, M_w/M_n = 1.61.

Synthesis of PCL_{70}-*r*-$CPCL_{30}$ (CPCL-30): BPCL-30 polymer (300 mg), TFA (3.0 mL). Yield = 0.26 g (97 %). ^{1}H NMR (400 MHz, $CDCl_3$) δ ppm: 4.14 (t, 2 H), 4.05 (t, 4.65 H), 3.69 (s, 2.68 H), 3.45 (s, 0.98 H), 2.53 (t, 1.99 H), 2.35 (t, 2.11 H), 2.30 (t, 4.61 H), 1.85 (s, 2 H), 1.77 (t, 2 H), 1.64 (t, 9.09 H), 1.39 (t, 4.65 H). ^{13}C NMR (101 MHz, $CDCl_3$) δ ppm: 173.8, 75.9, 64.7, 64.3, 62.6, 61.2, 40.7, 35.4, 34.2, 33.8, 32.9, 32.2, 29.8, 28.9, 28.4, 25.6, 24.6, 24.4. FT-IR (cm^{-1}): 2935, 1727, 1355, 1162, 1100, 1063, 952, 737. SEC molecular weights: M_w = 3,700 g/mol, M_n = 2,200 g/mol, M_w/M_n = 1.68.

Synthesis of PCL_{60}-*r*-$CPCL_{40}$ (CPCL-40): BPCL-40 polymer (300 mg), TFA (3.0 mL). Yield = 0.25 g (96 %). ^{1}H NMR (400 MHz, $CDCl_3$) δ ppm: 4.15 (t, 2 H), 4.09 (t, 2.95 H), 3.71 (s, 2.27 H), 3.47 (s, 0.99 H), 2.55 (t, 2.01 H), 2.36 (t, 1.99 H), 2.31 (t, 3 H), 1.86 (s, 2 H), 1.80 (t, 2 H), 1.65 (t, 6.10 H), 1.40 (t, 3 H). ^{13}C NMR (101 MHz, $CDCl_3$) δ ppm: 173.7, 75.9, 64.8, 64.2, 61.2, 40.5, 35.5, 34.1, 32.9, 30.9, 29.8, 28.9, 28.3, 25.5, 24.6, 24.5. FT-IR (cm^{-1}): 2935, 1722, 1355, 1165, 1100, 1061, 959, 798, 723, 660. SEC molecular weights: M_w = 1,230 g/mol, M_n = 1,160 g/mol, M_w/M_n = 1.06.

Synthesis of PCL_{40}-*r*-$CPCL_{60}$ (CPCL-60): BPCL-60 polymer (300 mg), TFA (3.0 mL). Yield = 0.24 g (97 %). ^{1}H NMR (400 MHz, $CDCl_3$) δ ppm: 4.15 (t, 2 H), 4.08 (t, 1.34 H), 3.71 (s, 2.21 H), 3.47 (s, 1 H), 2.55 (t, 1.99 H), 2.37 (t, 2.03 H), 2.31 (t, 1.33 H), 1.86 (s, 2.02 H), 1.79 (t, 2.02 H), 1.64 (t, 2.69 H), 1.40 (t, 1.36 H). ^{13}C NMR (101 MHz, $CDCl_3$) δ ppm: 173.8, 75.8, 64.6, 41.0, 39.8, 35.0, 34.0, 32.5, 29.6, 28.7, 28.4, 25.5, 24.5. FT-IR (cm^{-1}): 2936, 1721, 1355, 1165, 1098, 1061, 960, 898, 732, 661. SEC molecular weights: M_w = 1,130 g/mol, M_n = 1,120 g/mol, M_w/M_n = 1.01.

Synthesis of PCL_{30}-*r*-$CPCL_{70}$ (CPCL-70): BPCL-70 polymer (300 mg), TFA (3.0 mL). Yield = 0.23 g (95 %). ^{1}H NMR (400 MHz, $CDCl_3$) δ ppm: 4.16 (t, 2 H), 4.08 (t, 0.87 H), 3.74 (s, 2.22 H), 3.50 (s, 0.99 H), 2.58 (t, 2.03 H), 2.39 (t, 2.08 H), 2.33 (t, 0.88 H), 1.86 (s, 2 H), 1.81 (t, 2 H), 1.66 (t, 1.79 H), 1.40 (t, 0.90 H). ^{13}C NMR (101 MHz, $CDCl_3$) δ ppm: 173.7, 75.9,

64.8, 64.5, 35.2, 34.2, 32.8, 29.9, 28.9, 28.3, 25.6, 24.6, 24.3. FT-IR (cm^{-1}): 2938, 1710, 1351, 1165, 1100, 1057, 964, 835, 798, 723, 652. SEC molecular weights: M_w = 1,140 g/mol, M_n = 1,120 g/mol, M_w/M_n = 1.01.

Synthesis of PCL_{20}-*r*-$CPCL_{80}$ (CPCL-80): BPCL-80 polymer (300 mg), TFA (3.0 mL). Yield = 0.23 g (96 %). ^{1}H NMR (400 MHz, $CDCl_3$) δ ppm: 4.15 (t, 2 H), 4.06 (t, 0.62 H), 3.73 (m, 2.19 H), 3.50 (s, 1.01 H), 2.57 (t, 2.11 H), 2.39 (t, 2.01 H), 2.31 (t, 0.51 H), 1.86 (s, 2.04 H), 1.79 (t, 2.04 H), 1.65 (t, 1 H), 1.40 (t, 0.53 H). ^{13}C NMR (101 MHz, $CDCl_3$) δ ppm: 173.8, 75.7, 70.5, 64.6, 40.8, 36.5, 34.2, 32.9, 29.7, 28.9, 28.3, 25.5, 24.6, 24.5. FT-IR (cm^{-1}): 2935, 1712, 1355, 1170, 1098, 1059, 959, 845, 672. SEC molecular weights: M_w = 1,140 g/mol, M_n = 1,130 g/mol, M_w/M_n = 1.01.

Synthesis of Teg-$CPCL_{100}$ (CPCL-100): BPCL-100 polymer (300 mg), TFA (3.0 mL). Yield = 0.23 g (97 %). ^{1}H NMR (400 MHz, $CDCl_3$) δ ppm: 4.14 (t, 2 H), 3.70 (m, 2.1 H), 3.47 (m, 1 H), 2.54 (t, 2 H), 2.36 (t, 2 H), 1.88 (s, 2 H), 1.78 (t, 2 H). ^{13}C NMR (101 MHz, $CDCl_3$) δ ppm: 173.6, 75.5, 64.8, 40.7, 36.5, 34.1, 32.9, 29.7, 28.9, 28.5, 28.3. FT-IR (cm^{-1}): 2974, 2932, 1725, 1456, 1364, 1251, 1156, 1099, 1061, 1004, 959, 898, 846, 758. SEC molecular weights: M_w = 11,700 g/mol, M_n = 9,000 g/mol, M_w/M_n = 1.30.

Synthesis of PCL-block-carboxylic PCL (PCLm-b-CPCLn): The detailed procedure for synthesis of the block copolymers is described here for the **PCL_{50}-*b*-$BPCL_{50}$** block. Ring-opening polymerization of the ε-caprolactone monomer (M_1) was carried out using TEG as the initiator and $Sn(Oct)_2$ as the catalyst under neat conditions at 110 °C for 6 h. This served as the macro-initiator (MI) for ROP of the butyl ester substituted caprolactone monomer (M_2) which resulted in the block copolymer. The initiator, TEG (8.6 mg, 0.0526 mmol) and the catalyst, $Sn(Oct)_2$ (10.6 mg, 0.0263 mmol) were taken in a dry schlenk tube followed by addition of the CL monomer (300 mg, 2.63 mmol). The polymerization was carried out in a pre-heated oil bath at 110 °C for 6 h. This was followed by the addition of the butyl ester substituted caprolactone monomer **3** (679 mg, 2.63 mmol) and continued the polymerization at 130 °C for 24 h with constant stirring. The resultant polymer was precipitated in petroleum ether and cold methanol. Re-dissolved the polymer in THF and again precipitated in cold methanol. The precipitation was carried out at least twice to obtain polymers with high purity. Yield = 0.77 g (79 %). ^{1}H NMR (400 MHz, $CDCl_3$) δ ppm: 4.10 (t, 2 H), 4.03 (t, 2.10 H), 3.62 (s, 2.22 H),

3.41 (s, 0.98 H), 2.41 (t, 1.98 H), 2.34 (t, 2.02 H), 2.27 (t, 2.12 H), 1.83 (s, 2.05 H), 1.75 (t, 2.05 H), 1.61 (t, 4.54 H), 1.41 (s, 8.82 H), 1.35 (t, 1.96 H). ^{13}C NMR (101 MHz, $CDCl_3$) δ ppm: 173.5, 170.8, 80.5, 75.5, 71.9, 70.5, 64.8, 64.1, 61.2, 36.5, 34.1, 32.9, 29.7, 28.9, 28.2, 25.6, 24.7. FT-IR (cm^{-1}): 2942, 1722, 1457, 1365, 1243, 1156, 1100, 1062, 962, 898, 845, 800.

The butyl ester substituted polymer PCL_{50}-*b*-$BPCL_{50}$ (0.5 g) was hydrolyzed into carboxylic acid using trifluoroacetic acid (5.0 mL), wherein the addition was carried out at 0 °C slowly along the sides of the round-bottom flask. The reaction was continued at 0 °C for 30 min with constant stirring. TFA was removed completely by washings with toluene. The de-protected polymer **PCL_{50}-*b*-$CPCL_{50}$** was dissolved in minimum amount of THF and precipitated in cold methanol. The precipitation was repeated at least thrice in order to obtain pure polymer. Yield = 0.41 g (97 %). ^{1}H NMR (400 MHz, $CDCl_3$) δ ppm: 4.14 (t, 1.96 H), 4.05 (t, 2.24 H), 3.71 (s, 2.16 H), 3.50 (s, 0.98 H), 2.56 (t, 1.80 H), 2.38 (t, 1.96 H), 2.30 (t, 2.08 H), 1.86 (s, 1.84 H), 1.78 (t, 1.84 H), 1.64 (t, 5.2 H), 1.37 (t, 2.20 H). ^{13}C NMR (101 MHz, $CDCl_3$) δ ppm: 176.3, 173.9, 173.7, 75.8, 64.5, 64.2, 61.3, 35.2, 34.2, 32.8, 29.8, 28.8, 28.4, 25.6, 24.6. FT-IR (cm^{-1}): 2941, 1720, 1390, 1355, 1235, 1164, 1098, 1060, 962, 914, 730, 646.

Synthesis of Teg-PCL_{75}-b-$BPCL_{25}$: mTEG (10.28 mg, 0.0626 mmol), Sn $(Oct)_2$ (12.60 mg, 0.0313 mmol), CL (500 mg, 4.385 mmol), BCL (484.96 mg, 1.879 mmol). Yield = 0.8 g (81 %). ^{1}H NMR (400 MHz, $CDCl_3$) δ ppm: 4.12 (t, 2 H), 4.04 (t, 6.22 H), 3.63 (m, 2.48 H), 3.42 (s, 1.00 H), 2.42 (t, 2.12 H), 2.35 (t, 2.20 H), 2.28 (t, 6.16 H), 1.84 (s, 2.19 H), 1.76 (t, 2.19 H), 1.63 (t, 12.76 H), 1.43 (s, 9.36 H), 1.36 (t, 6.22 H). ^{13}C NMR (101 MHz, $CDCl_3$) δ ppm: 173.5, 173.4, 170.8, 80.6, 75.5, 70.5, 65.0, 64.3, 61.2, 36.5, 34.1, 32.9, 29.7, 28.9, 28.3, 28.1, 25.5, 24.6. FT-IR (cm^{-1}): 2941, 2868, 1723, 1465, 1364, 1290, 1240, 1156, 1100, 1046, 959, 898, 845, 730. SEC molecular weights: M_w = 13,300 g/mol, M_n = 6,350 g/mol, M_w/M_n = 2.09.

Synthesis of Teg-PCL_{75}-*b*-$CPCL_{25}$: PCL_{75}-*b*-$CPCL_{25}$ polymer (400 mg), TFA (4.0 mL). Yield = 0.35 g (96 %). ^{1}H NMR (400 MHz, $CDCl_3$) δ ppm: 4.11 (t, 2 H), 4.03 (t, 6 H), 3.68 (s, 2.54 H), 3.44 (s, 1 H), 2.51 (t, 1.89 H), 2.32 (t, 2.12 H), 2.28 (t, 6.21 H), 1.82 (s, 2.03 H), 1.76 (t, 2.03 H), 1.62 (t, 12.63 H), 1.35 (t, 6.26 H). ^{13}C NMR (101 MHz, $CDCl_3$) δ ppm: 178.5, 173.7, 75.8, 64.6, 64.2, 62.6, 61.2, 35.3, 34.2, 33.8, 32.8, 32.1, 29.8, 28.9, 28.4, 25.6, 25.3, 24.6, 24.4. FT-IR (cm^{-1}): 2943, 2867, 1721, 1461, 1362, 1238, 1164, 1099, 1061, 961, 914, 730, 648. SEC molecular weights: M_w = 14,500 g/mol, M_n = 6,500 g/mol, M_w/M_n = 2.23.

2.2.4 Self-assembly of copolymers

In an archetypal experiment, 10.0 mg of the polymer was dissolved in 2 mL DMSO followed by drop wise addition of 8 mL milli pore water with continuous stirring at 25 °C for 4 h. These polymer solutions were then transferred to the dialysis bag (MWCO = 1000) and dialyzed against large amount of water for 48 h. The water was changed at regular intervals in order to remove DMSO completely and facilitate the self-assembly of polymer chains.

2.2.5 Drug Encapsulation in the Copolymer Scaffolds

A comprehensive protocol is provided for DOX (DOX.HCl treated with triethylamine) encapsulation. In a typical experiment, 10.0 mg of the polymer and 0.5 mg of DOX were dissolved in 2 mL DMSO. To this solution, millipore water (3 mL) was added dropwise with constant stirring at 25 °C for 4 h. The solutions were transferred to the dialysis bag of molecular weight cut off (MWCO = 1000) and dialyzed against huge amount of water for 24 h. Fresh water was replaced periodically to ensure complete removal of unencapsulated molecules and DMSO from the dialysis tube.

Similar protocol was followed for the preparation of DOX-loaded block copolymer nanoparticles, i.e. PCL_{50}-*b*-$CPCL_{50}$-DOX and PCL_{75}-*b*-$CPCL_{25}$-DOX.

The drug loading efficiency (DLE) and drug loading content (DLC) were determined by UV-Visible spectroscopy using the following equations:

DLE = wt % EE = [wt of encapsulated DOX/ wt of total DOX added] x 100

DLC = wt % LC = [wt of encapsulated DOX/ wt of polymer] x 100

2.2.6 *In vitro* Drug Release Studies

The drug loaded micelles were subjected to release studies against PBS (pH = 7.4) and in the presence of esterase at 37 ^{o}C in order to understand their stability and release kinetics. The dialysate (3.0 mL) was taken in a dialysis tube, immersed in a 100 mL beaker and dialyzed at 37 °C with constant stirring. At periodic intervals 3 mL of the aliquot was taken and replaced with same volume of fresh buffer. Each aliquot was quantified for the amount of drug present in it using absorption spectroscopy and measured the cumulative release percentage. In case of esterase assisted release studies, 10 units of the esterase enzyme was used following the above procedure.

Cumulative release (%) = C_n x V_o/m x 100, where C_n is the amount of loaded cargo in the n^{th} sample, V_o is the total volume and m is the total amount of drug loaded in nanoparticles.

2.2.7 Cell Viability Assay (MTT Assay)

To comprehend the cytotoxicity of polymers alone, free drug and drug loaded micelles cell viability assay was performed in HeLa and MCF 7 cell lines using the tetrazolium salt, 3-(4,5-dimethylthiazol-2-yl)-2,5-diphenyltetrazolium bromide (MTT). In a 96-well plate (Corning, U.S.A.) 10^3 cells were seeded in each well in 100 µL of DMEM with 10 % FBS (fetal bovine serum) and left for 16 h to adhere. Media from each well was aspirated prior to feeding the sample and then cells were treated with various concentrations of polymer, free drug and drug loaded micelles. A blank control, that is DMEM with FBS in the absence of the compound, was used for all experiments. The control and treated experiment wells were taken in triplicates. Cells were incubated for 72 h without changing the media and post incubation, drug containing media was aspirated. A freshly prepared stock of MTT in sterile DMEM (0.5 mg/mL) and 100 µL of this solution was added to each well. After MTT addition the cells were incubated for 4 h at 37 °C. Following which the media was aspirated and the purple formazan crystals formed owing to the reduction of MTT by the mitochondrial dehydrogenase enzyme from cells were dissolved in 100 µL of DMSO for each well. The absorbance rendered by these formazan crystals was immediately measured using the microplate reader at 570 nm (Varioskan Flash). Mean of the triplicate set was used for further calculations and this number is indicative of the number of viable cells per well. The value from the untreated control well was taken to be 100 % and with respect to that the relative percentage values for the treated wells were determined.

2.2.8 Cellular Uptake of DOX-loaded Polymeric Nanocarriers by Confocal Microscopy

HeLa and MCF 7 cells were seeded at a density of 10^5 cells on flame-dried coverslips placed in 6-well plates containing DMEM media with 10 % FBS and incubated for 16 h at 37 °C. Cells were exposed to the desired concentration of DOX alone and DOX-loaded polymer nanoparticles for 4 h in a CO_2 incubator at 37 °C. Drug containing media was then aspirated and cells were washed twice with PBS (2 x 1 mL) followed by fixation with 4 % paraformaldehyde solution in PBS for 10 min at room temperature. Washings were given twice with PBS (2 x 1 mL). Cells were stained with DAPI solution in PBS and incubated for 2 min at room temperature in dark. The cells were then washed twice with PBS (2 X 1mL) and stained with Alexa fluor-488 conjugated Phalloidin diluted 1:100 in 5% BSA solution in PBS under

dark conditions. Excess dye was washed off from the plate and cells were gently rinsed with PBS for 1 min. Coverslips were mounted onto the slides using fluoromount mounting medium (Southern Biotech) and then dried overnight at room temperature in the dark. Cellular imaging was carried out using a confocal microscope employing λ 420 nm (blue channel), λ 488 nm (green channel) and λ 568 nm (red channel) lasers. The images were analyzed in Image J software by separating images for each channel.

2.2.9 Flow Cytometry Measurements

The cellular uptake of free DOX and DOX-loaded random and block copolymer nanoparticles in cervical cancer cells was assessed using the flow cytometry cell analyzer. HeLa cells were seeded in 6-well plate at a density of 10^5 cells containing DMEM media and incubated for 16 h at 37 °C. Cells were treated with desired concentration (1 μg/mL) of free DOX and DOX-loaded nanoparticles. After 9 h incubation, the drug containing media was aspirated and cells washed with PBS (1 x 1mL). Further the cells were digested using 500 μL trypsin followed by 1 min incubation. The suspension in media was centrifuged at 10,000 rpm for 5 min and re-suspended the pellet in 1 mL PBS. Flow cytometry studies were carried out by employing the BD LSRFortessa SORP cell analyzer that is equipped with five lasers and can detect 18 colours simultaneously. The 561 nm laser was used for the excitation of DOX and the band pass filter was chosen as 610 ± 10 nm. The fluorescence histograms were recorded from a population of 10, 000 cells.

2.3 Results and Discussion

2.3.1 Synthesis of Amphiphilic PCL Random Copolymers

The synthesis of substituted caprolactone monomer is shown in scheme 1. The monomer was prepared via multi-step reactions starting from commercially available 1,4-cyclohexanediol. 1,4-cylcohexanediol underwent Michael addition with t-butyl acrylate in the presence of potassium t-butoxide to give mono-substituted product (**1**). **1** was then subjected to oxidation using PCC to generate the cyclohexanone derivative (**2**) which was further converted to substituted caprolactone monomer (**3**) (**BPCL**) through the Baeyer villiger oxidation (see scheme 2.1).

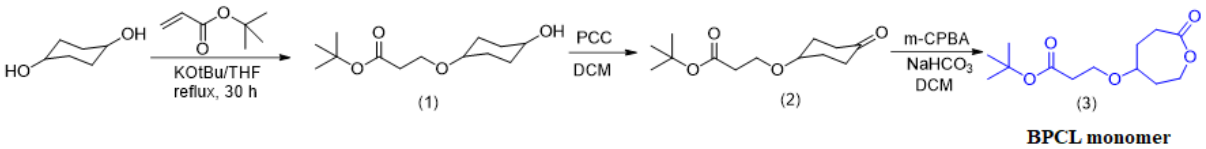

Scheme 2.1. *Synthetic scheme of substituted caprolactone monomer (BPCL monomer) via a multi-step approach.*

The random copolymers constituting caprolactone unit (**M_1**) and substituted caprolactone monomer unit (**M_2**) were synthesized via the ring opening polymerization (ROP) employing triethylene glycol monomethyl ether (TEG) as an initiator (R-OH) as shown in scheme 2.2. TEG was chosen since it is a very good initiator for the ROP of caprolactone monomers[231] and it's weight at the chain ends is negligible compared to the entire mass of the resultant high molecular weight of PCL random or block copolymers. $Sn(Oct)_2$ was employed as catalyst and the initiator-to-catalyst ratio was taken as 2:1 to produce requisite amount of the active initiator species TEG-O-Sn-O-TEG *in situ*.[231] For the random copolymers, the monomers to initiator ratio was maintained as $[M_1+M_2]/[I] = 100$ throughout whilst changing the relative mole ratios of the two monomers from 10 to 80 %. Further the t-butyl ester group in the polymer was hydrolyzed into corresponding carboxylic acids using trifluoroacetic acid. These random copolymers were referred to as PCL_y-*r*-$BPCL_x$ (BPCL-x) or PCL_y-*r*-$CPCL_x$ (CPCL-x) where "x" represents the average number of the butyl ester (B) or its de-protected carboxylic acid (C) in the substituted PCL chains. By this method, series of random copolymers BPCL-x were made, and they were de-protected to give their corresponding carboxylic acid substituted random copolymer CPCL-x (see scheme 2.2). Two homopolymers PCL and BPCL (also its CPCL counterpart) were also prepared using the same methodology by maintaining the [M]/[I] ratio as 100. The ^{1}H NMR spectra of the homopolymers PCL, BPCL and the random copolymer **BPCL-50** are shown in figure 2.4.

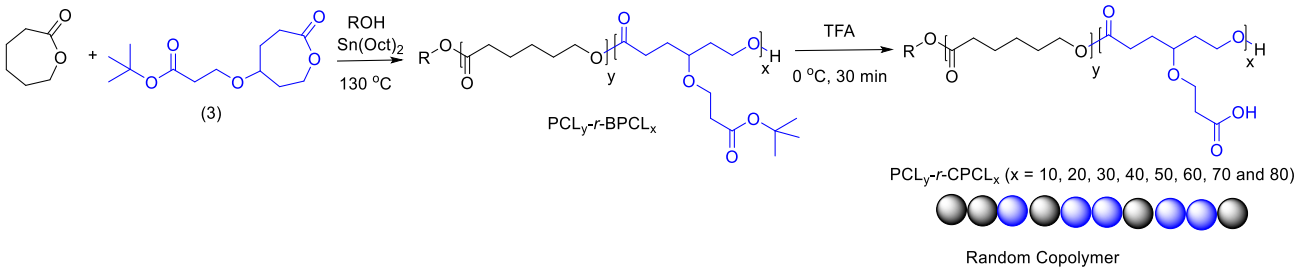

Scheme 2.2. *Synthetic scheme of substituted caprolactone monomer and PCL based random copolymers via ring-opening polymerization methodology.*

In the PCL homopolymer the peaks corresponding to the TEG part appeared at 3.63 ppm (proton 'a') and protons 'b' and 'f' for the newly formed ester appeared at 2.31 ppm and 4.03 ppm, respectively (see figure 2.4a). The comparison of the peak intensities of 'a' versus 'b' (or 'a' versus 'f') gave the number average degree of polymerization (DP_n). In the present case, for the feed ratio of M/I = 100, the DP_n value was obtained from ^1H NMR as 107 units. Similarly, the butyl ester substituted homopolymer BPCL showed new ester peaks at 4.13 ppm and 2.37 ppm for proton 'k' and proton 'g', respectively (see figure 2.4b). The peak at 3.63 ppm corresponds to both the TEG (protons *'a')* and side chain substitution protons *'l*'. The peak intensity at 3.63 ppm (protons a+*l)* was subtracted by peak at 4.13 ppm (proton 'k') to obtain the actual value for protons 'a'. The ratio of proton 'a' to proton 'k' (or with proton 'g') gave the number average degree of polymerization in the substituted PCL homopolymer as 100 units. The ^1H NMR spectra of random copolymer BPCL-x (see figure 2.4c) showed peaks corresponding to both PCL and butyl ester PCL part together. For instance the peaks at 4.03 ppm and 4.13 ppm represented the amount of PCL and BPCL units in the random copolymer. The actual incorporation of BPCL units determined by ^1H NMR is referred in their sample name as BPCL-x. The comparison of these peak intensities yielded the composition of the random copolymers; thus, from the ^1H NMR analysis, both the compositions as well as the actual DP_n were determined and the values are given in the table 2.1.

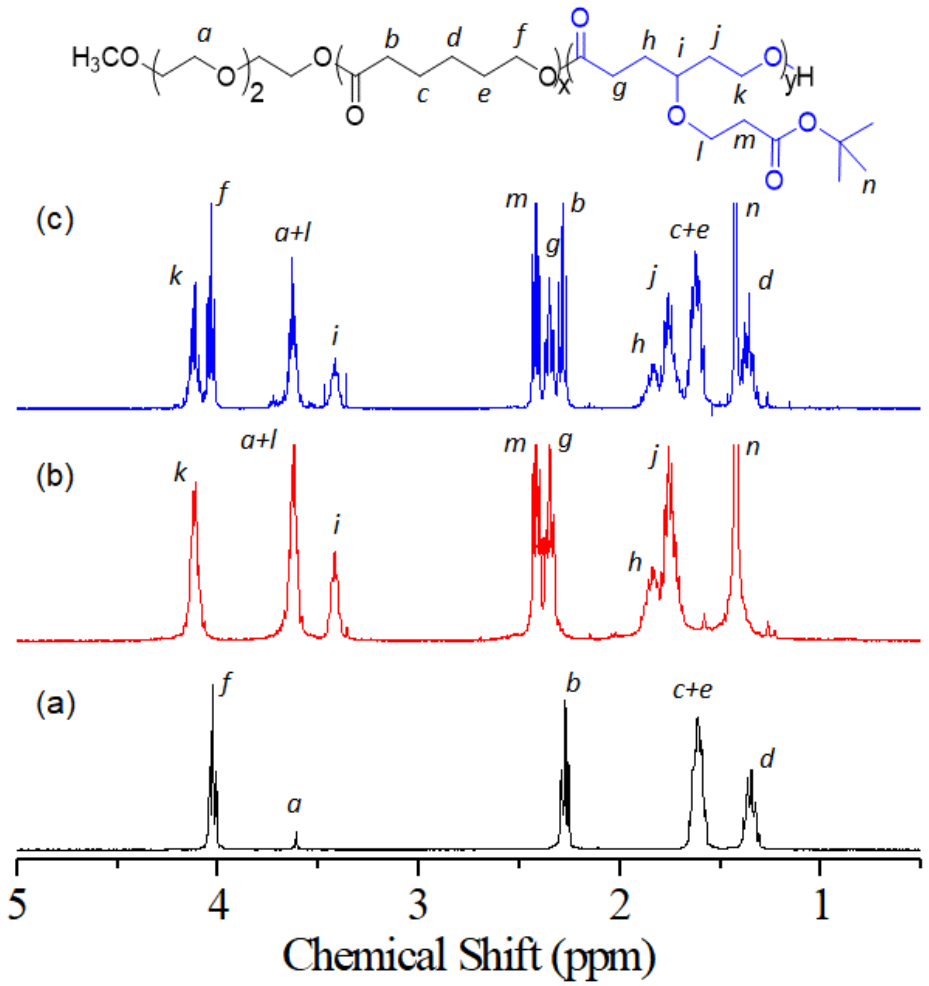

Figure 2.4. *^{1}H NMR spectra of PCL (a), butyl ester BPCL (b), and random copolymer butyl ester BPCL-50 (c) in $CDCl_3$. The spectra were plotted only up to 5.00 ppm for simplicity.*

Molecular weights (NMR and SEC) of random copolymers

S.No.	mTEG-PCL$_x$-BPCL$_y$ Feed		^{1}H-NMR			SEC		
	x	y	x	y	M_n (g/mol)	M_n (g/mol)	M_w (g/mol)	PDI
1	20	80	27	100	28,800	13,900	19,300	1.3
2	30	70	38	75	23,700	14,600	20,700	1.4
3	40	60	37	60	19,700	14,800	20,900	1.4
4	50	50	58	60	22,100	14,100	20,200	1.4
5	60	40	60	40	17,200	14,100	21,400	1.5
6	70	30	66	33.3	16,100	17,100	26,100	1.5
7	80	20	83	23	15,400	18,500	26,000	1.4
8	90	10	104	11.6	14,800	13,500	21,800	1.6

Table 2.1. *Tabulated molecular weights of all random copolymers from ^{1}H NMR and SEC.*

The composition of the BPCL-x units incorporated in the random copolymer was plotted against the monomer **3** in feed and shown in figure 2.5a. The linear trend revealed that the reactivity of the caprolactone and carboxylic caprolactone monomer **3** were almost identical in the ROP process for the incorporation of expected amount of PCL and BPCL units in the random copolymer. Further, the ratio of proton 'a' versus proton 'f' and proton 'a' versus proton 'k' yielded the number average degree of polymerization (DP_n) for PCL and BPCL, in the random copolymer units respectively. From these values, the number average molecular weights of the random copolymers were determined by $M_n = DP_n \times M_o$ (where M_o is the repeating units mass). The plot of M_n versus BPCL-x in the random copolymer (determined by ^{1}H NMR) is shown in figure 2.5b. The linear trend revealed that the random copolymers indeed followed the controlled ROP process. The molecular weights of the polymers were determined by size exclusion chromatography (SEC) and the weight average (M_w), number average (M_n) molecular weights and their polydispersity are summarized in table 2.1 for the random copolymers. The SEC chromatograms of the random copolymers (in figure 2.5c) showed monomodal distribution with narrow polydispersity (~ 1.5) for all the polymers.

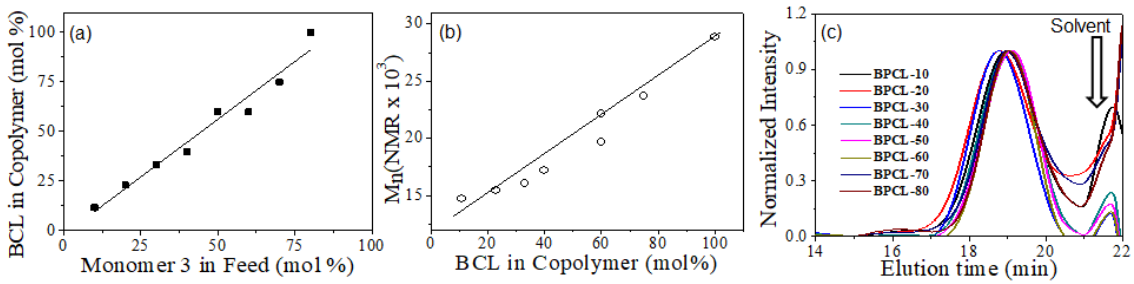

Figure 2.5. *(a) Plot of BPCL incorporation in the copolymers versus monomer 3 in the feed. (b) Plot of M_n (determined by NMR) versus the actual incorporation of BPCL units in the copolymer. (c) Size exclusion chromatography (SEC) plot of random copolymers BPCL-x.*

The ^{1}H NMR spectra for other random copolymers and the homopolymers were arranged in a stack plot, as can be seen in figure 2.6. The number average degree of polymerization, DP_n for the BPCL and PCL backbone was calculated in the same manner as explained above for all the random copolymers. The number average molecular weights were

determined using the formula, $M_n = DP_n \times M_0$ and are tabulated in table 2.1. The peaks corresponding to both PCL and BPCL appeared in the random copolymers.

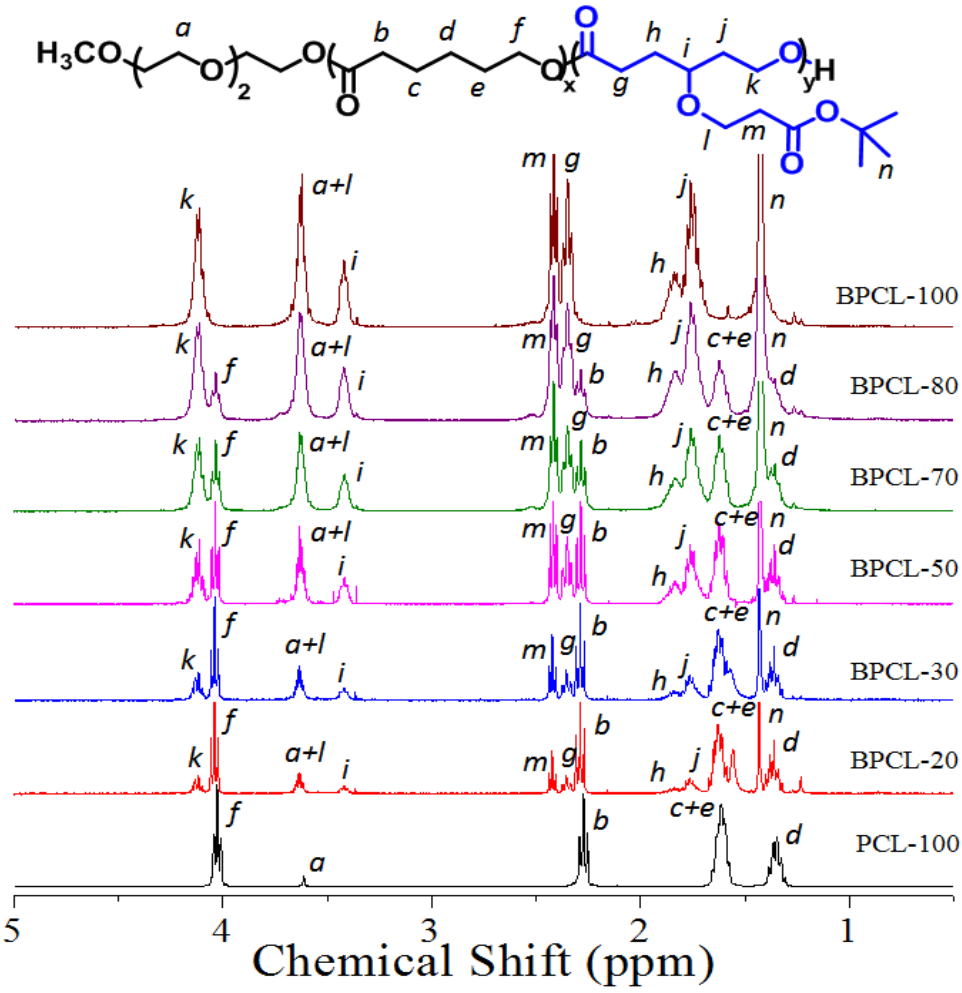

Figure 2.6. *Stack plot of ^1H NMR of random copolymers and homopolymers.*

2.3.2 Synthesis of Amphiphilic PCL Block Copolymers

The block copolymers were made by sequential addition in which the first synthesized PCL macro-initiator (MI) was employed for the ROP of the second monomer **3**. The number of the units in both initiator PCL block and the second BPCL block were varied by controlling their M/I ratio in the feed; however, the total concentration of two monomers together to initiator was retained as 100. These blocks are named as PCL_m-*b*-$BPCL_n$ (or) PCL_m-*b*-$CPCL_n$ where m and n are number of repeating units in the PCL and carboxylic PCL blocks, respectively. By this method, two block copolymers PCL_{75}-*b*-$BPCL_{25}$ and PCL_{50}-*b*-$BPCL_{50}$

were made and they were de-protected to yield their corresponding carboxylic acid derivatives PCL_{75}-*b*-$CPCL_{25}$ and PCL_{50}-*b*-$CPCL_{50}$, respectively (see scheme 2.3).

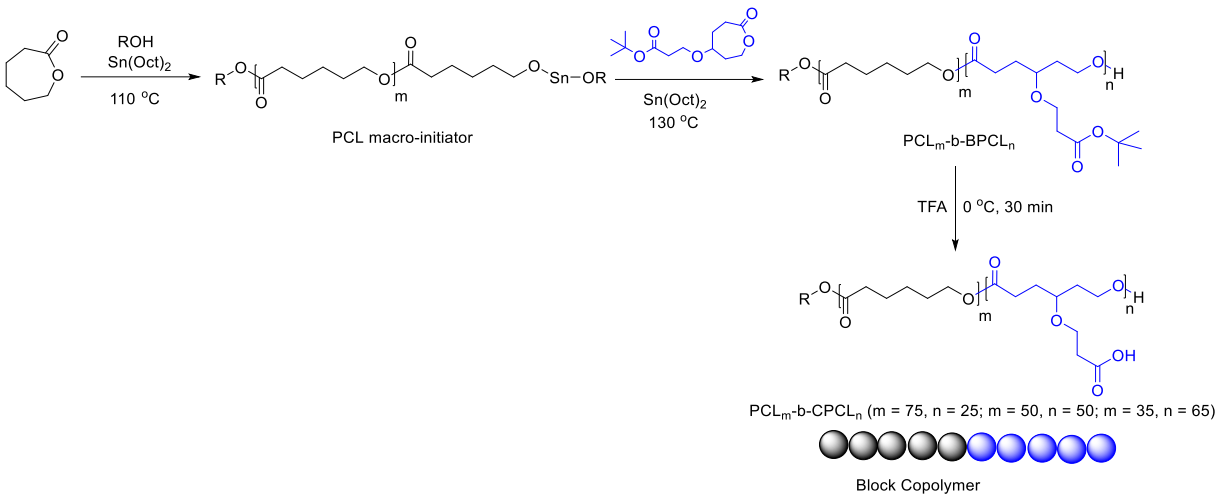

Scheme 2.3. *Synthetic scheme of substituted caprolactone monomer and PCL block copolymers via sequential ring-opening polymerization methodology.*

The structures of block copolymers were confirmed by comparing the ^{1}H NMR spectra of PCL macro-initiator and their resultant diblock. For this purpose, two polymerization reactions were setup simultaneously with required M/I ratio in PCL macro-initiator. One of the polymerization reactions was stopped and the second reactor was charged with monomer **3** (with appropriate M/I ratio) and the ROP process was continued. By this process, we were able to isolate the PCL macro-initiator (from the first reactor) for determining its actual chain length. ^{1}H NMR spectra of PCL_{50}-*b*-$BPCL_{50}$ block and its macro-initiator are shown in figure 2.7 (see the details for PCL_{75}-*b*-$BPCL_{25}$ block in Appendix). The comparison of the spectra of PCL macro-initiator and the resultant PCL_m-*b*-$BPCL_n$ polymer clearly indicated the formation of expected block copolymer structure. For example, the peaks corresponding to the BPCL-x blocks seen in figure 2.7b were completely absent in its macro-initiator in figure 2.7a. The comparison of the peak intensities corresponding to protons 'a' and protons 'f' gave the degree of polymerization (DP_n) for the PCL block. Similarly, the newly formed ester peak in the BPCL block at 4.10 ppm (protons 'k') was compared to the protons 'a' belonging to the TEG part (calculated by subtracting the protons 'a+l-k'; as explained in detail for the random copolymers) that eventually gave the DP_n values for the BPCL block. The number average

molecular weight M_n for the diblock was then calculated using the formula mentioned above and the values are summarized in table 2.2.

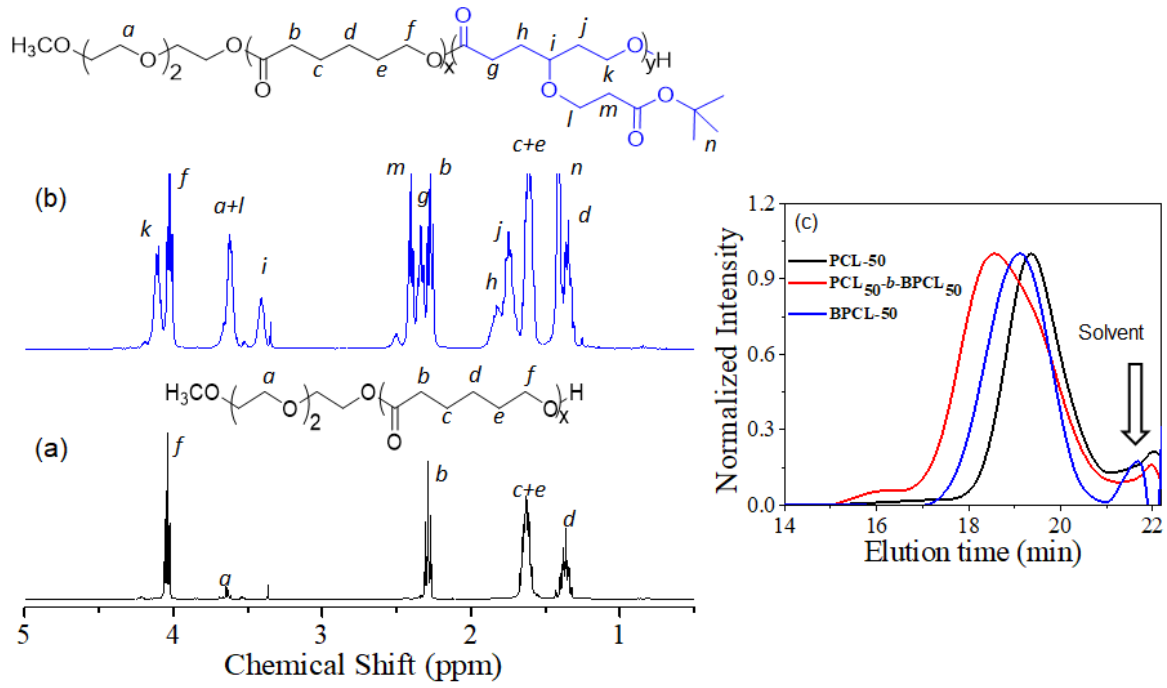

Figure 2.7. *^{1}H NMR spectra of macro-initiator PCL (a) and block copolymer butyl ester PCL_{50}-b-$BPCL_{50}$ (b) in $CDCl_3$.The spectra were plotted only up to 5.00 ppm for simplicity. (c) SEC plots of the random and block copolymer and the macro-initiator.*

S.No.	mTEG-PCL_x-b-$BPCL_y$ Feed		^{1}H-NMR			SEC		
	x	y	x	y	M_n (g/mol)	M_n (g/mol)	M_w (g/mol)	PDI
1	70	30	75	25	15,000	6,350	13,300	2.1
2	50	50	50	50	18,600	13,400	38,200	2.8

Table 2.2. *Molecular weights (NMR and SEC) of diblock copolymers*

The SEC chromatogram of the block copolymer PCL_{50}-*b*-$BPCL_{50}$ showed significant difference with respect to its PCL macro-initiator (see figure 2.7c). The comparison of the SEC of the BPCL-50 random copolymer and the PCL_{50}-*b*-$BPCL_{50}$ (see figure 2.7c) exhibited significant difference in their retention time. Both random and block copolymer have identical

molar mass; however, they exhibited large difference in their hydrodynamic volume in SEC plots with respect to difference in the sequential arrangements in their backbones.

The random copolymer BPCL-x and blocks PCL_m-*b*-$BPCL_n$ copolymers were then hydrolyzed into carboxylic acid substituted polymers. ^{1}H NMR and FT-IR spectra of the polymers confirmed the occurrence of the deprotection of the butyl ester into carboxylic acids without altering the copolymer backbone structure (see figure 2.8). The complete disappearance of the t-butyl peak at 1.45 ppm confirmed the formation of carboxylic acid-substiuted copolymers.

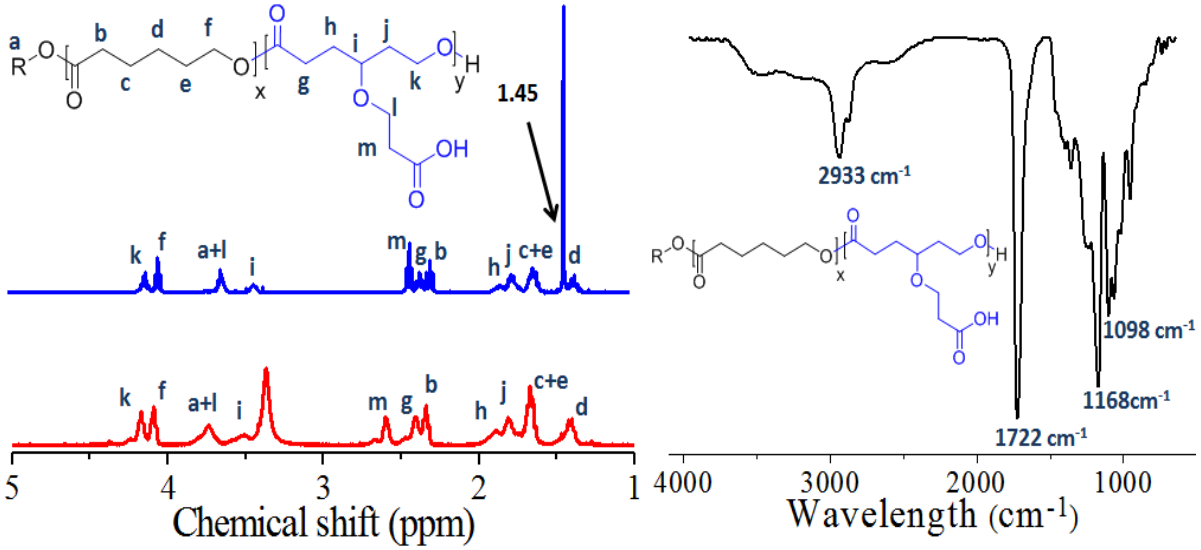

Figure 2.8. *^{1}H NMR and FTIR profile of carboxylic substituted random copolymer CPCL-50.*

2.3.3 Polymerization kinetics

To further prove the controlled ROP process in both random copolymer and block copolymer; ROP kinetics was performed for BPCL-50 and PCL_{50}-*b*-$BPCL_{50}$. Polymer sample aliquots were taken at regular intervals and they were submitted for ^{1}H NMR and SEC. For BPCL-50 polymerization kinetics, the M_n determined by the ^{1}H NMR showed a linear increasing trend over polymerization time confirming the occurrence of the controlled ROP process in BPCL-50 (see figure 2.9a). The actual incorporation of the both PCL and BPCL units were calculated from the ^{1}H-NMR spectra and it was plotted against time (refer to figure 2.9b). These plots showed linear trend and the ratio of their slopes was determined to be 1 :

1.06 for BPCL : PCL units, respectively. Thus, the reactivity ratio of the monomers is typically ~1:1 and confirmed the formation of ideal random copolymer. The SEC chromatogram in figure 2.9c depicts the various aliquots corresponding to the PCL_{50}-*b*-$BPCL_{50}$ block polymerization kinetics, wherein a vivid change was observed in the retention time. The figure 2.9d clearly shows the linear increase in M_n with increase in the reaction time and the polydispersity index values were nearly the same, which reinstated the controlled nature of ring opening polymerization.

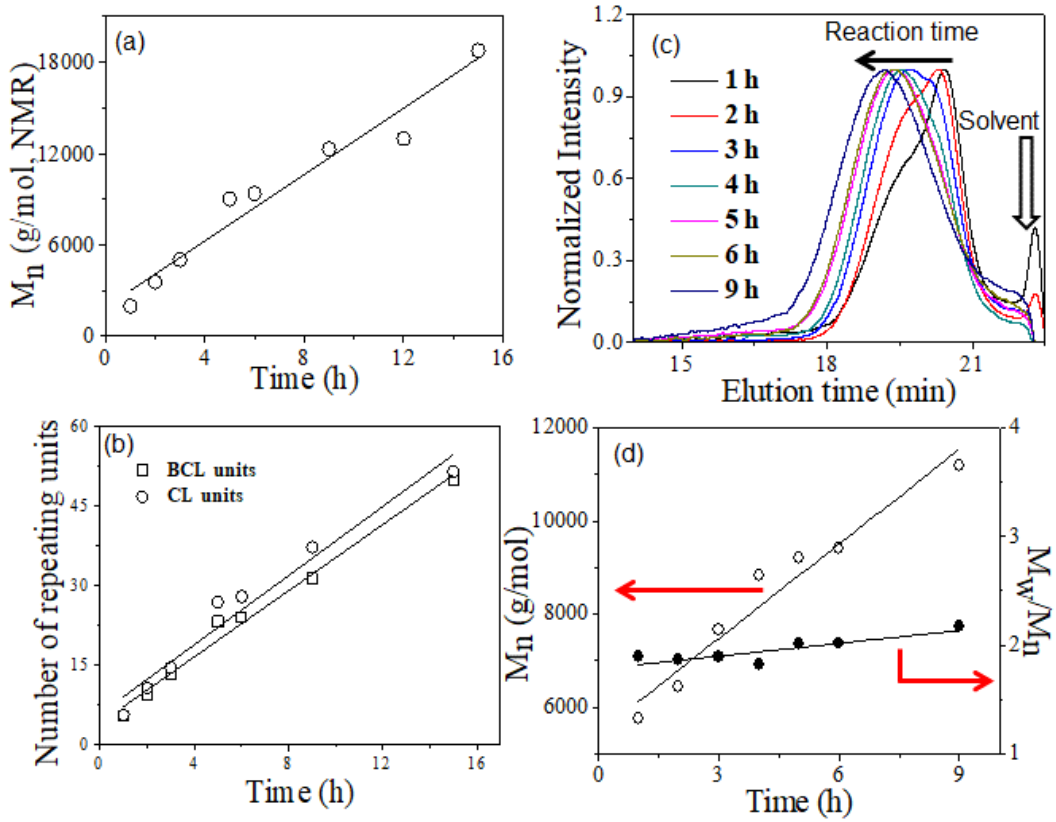

Figure 2.9. *(a) Ring opening polymerization (ROP) kinetics of BPCL-50 monitored with ^1H NMR. (b) Actual Incorporation of CL and BCL monomers in the random copolymer with time. (c) SEC plots depicting the kinetics of block copolymerization PCL_{50}-b-$BPCL_{50}$. (d) Plot of M_n and M_w/M_n from SEC vs. time for block copolymerization kinetics.*

The synthesis of the diblocks sequence was reversed by first creating the t-butyl ester substituted BPCL macro-initiator followed by addition of the CL monomer to build the second PCL block (see the scheme in figure 2.10). The polymerization kinetics was followed by SEC and the chromatograms of this block copolymer synthesis exhibited a clear decrease in the elution time, which implies an increase in the molecular weight with reaction time, as shown in figure 2.10a. The plot of M_n versus time exhibited a linear fit with respect to living

polymerization (figure 2.10b). This unique trend was attributed to the 1:1 reactivity ratio of both monomers. Thus, the caprolactone monomer and the newly designed carboxylic CL monomer **3** have identical reactivity and they are very unique systems to produce block copolymers by controlled ROP process irrespective of the sequence of the initiation process.

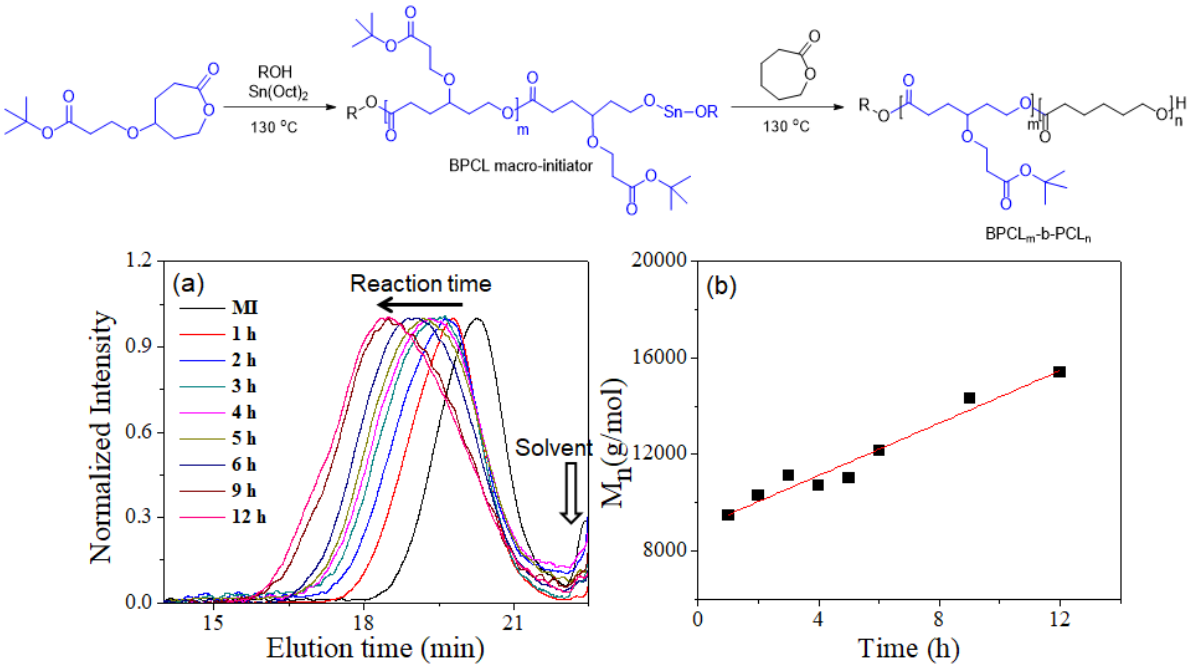

Figure 2.10. *Synthetic scheme of the reverse diblock $BPCL_{50}$-b-PCL_{50}. SEC chromatogram depicting the polymerization kinetics of $BPCL_{50}$-b-PCL_{50} diblock (a). Plot of M_n (SEC) vs. time (b).*

2.3.4 Thermal Properties

Thermal stability of the polymers were studied using thermogravimetric analysis (TGA) and the results indicated that polymers were stable up to 250 °C (see figure 2.11a). Differential scanning calorimeter (DSC) was employed to study the semi-crystalline and amorphous nature of the random and block copolymers. DSC thermograms (in the heating cycle) of butyl ester BPCL-x random polymers (see figure 2.11b) showed a clear transformation from semi-crystalline to amorphous nature upon increasing the BPCL content in the backbone. This trend was almost identical to its counterpart carboxylic acid substituted copolymers CPCL-x in the heating cycle (see figure 2.11c). The polymer CPCL-10 showed a melting transition at T_m = 47 °C which was much lower than that for the PCL (T_m = 55 °C). CPCL-20 polymer exhibited cold crystallization peak followed by the melting transition at 30

°C. With increase in the number of carboxylic units in the random copolymers; the polymers turned completely amorphous. Thus, it may be concluded that the carboxylic acid substitution in the PCL backbone (or its butyl ester) induced steric hindrance and disturbed the chain packing of PCL backbone. The glass transition temperatures (T_g) of the butyl ester BPCL-X and carboxylic CPCL-X were obtained in the range of -48 to -18 °C.

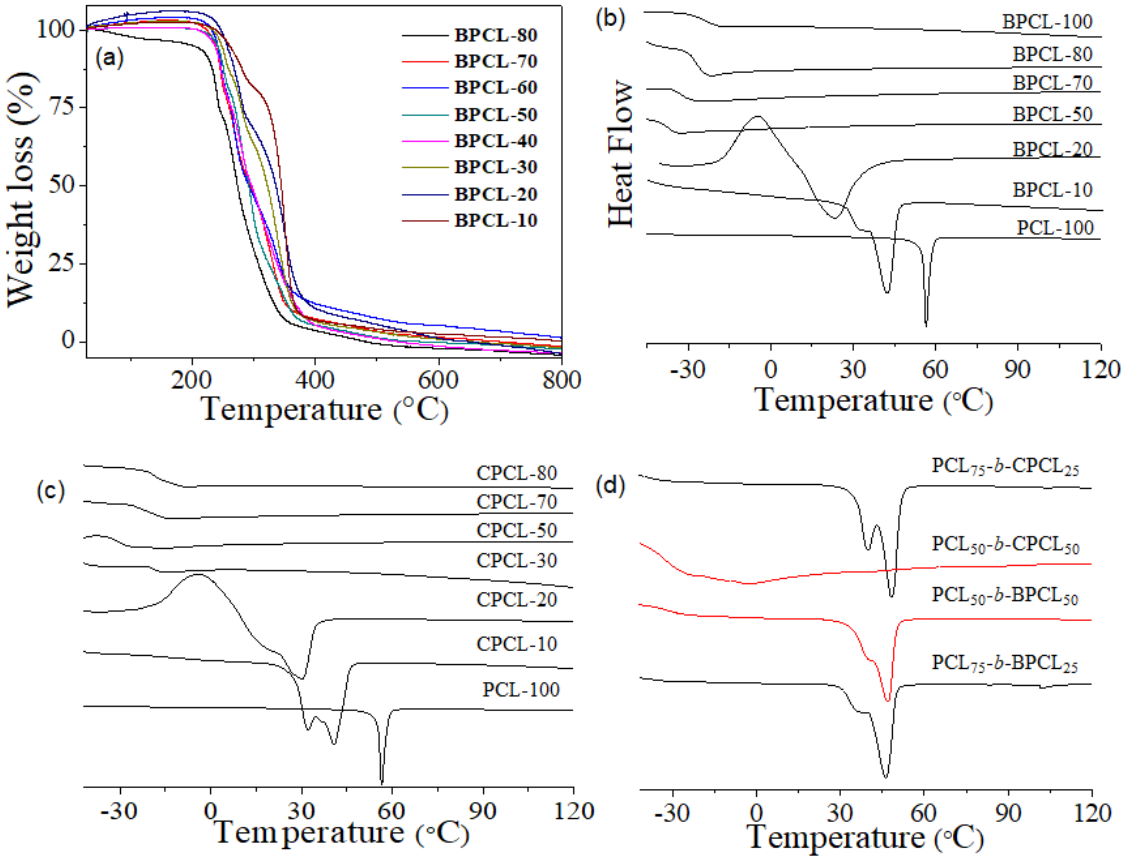

Figure 2.11. *(a) TGA profiles of random copolymers. (b) DSC thermograms of butyl ester substituted random copolymers and homopolymers at 10 °/min in the heating cycle. (c) DSC thermograms of carboxylic substituted random copolymers CPCL-X at 10 °/min in the heating cycle. (d) DSC thermograms of butyl ester and carboxylic acid block copolymers PCL_m-b-$CPCL_n$ at 10 °/min in the heating cycle.*

DSC thermograms of block copolymers are shown in figure 2.11d. Both block copolymers showed semi-crystalline nature and exhibited melting transition for their butyl ester substitution. The comparison of the DSC plots of random copolymer BPCL-50 and block copolymer PCL_{50}-*b*-$BPCL_{50}$ revealed that the block copolymer topology exhibited semi-crystalline properties whereas the random copolymer structure was found to be sluggish to

crystallize. Upon de-protection into carboxylic acid derivatives, the block with the higher PCL content PCL_{75}-*b*-$CPCL_{25}$ still retained the semi-crystalline nature whereas the block with less PCL content PCL_{50}-*b*-$CPCL_{50}$ turned into amorphous (see figure 2.11d). These results suggest that the block copolymers could retain the semi-crystalline properties at lower carboxylic acid substitutions; however, the increase in the carboxylic content resulted both random and block copolymers into amorphous. Transition temperature and their enthalpies of the transitions for all random and block copolymers are given in a table in the Appendix.

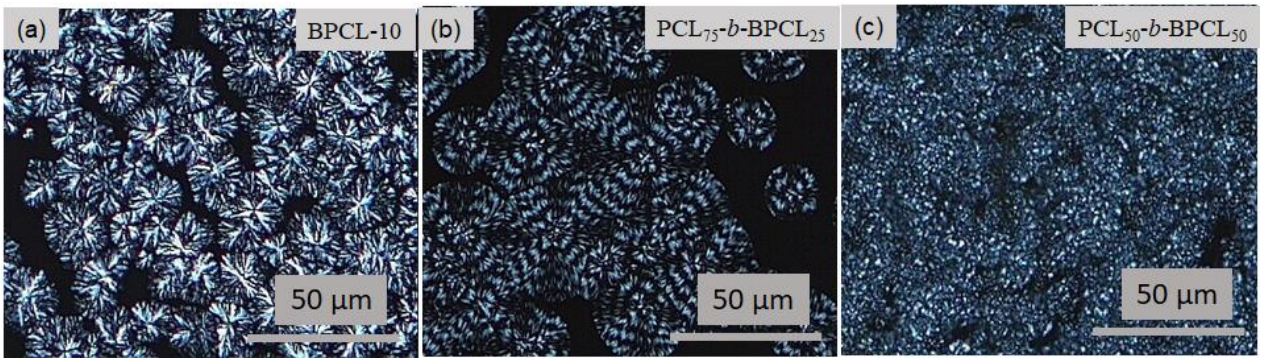

Figure 2.12. *PLM images of BPCL-10 (a), PCL_{75}-b-$BPCL_{25}$ (b), and PCL_{50}-b-$BPCL_{50}$ (c) at 10 °/min cooling from the melt.*

In order to visualize the nature of chain packing in the aforementioned semi-crystalline polymers, they were subjected to polarizing light microscope (PLM). In a typical experiment, the polymer sample was melted and control cooled at a rate of 10 °/min on a hot stage. The crystallization process is recorded by taking images at various time points in the process. As can be seen in figure 2.12a, upon cooling the BPCL-10 polymer slowly crystallized out as spherulites. In the case of PCL_{75}-b-$BPCL_{25}$ block copolymer, exquisite ring-bound spherulites were observed upon crystallization (see figure 2.12b). The PCL_{50}-b-$BPCL_{50}$ block copolymer gave comparatively smaller spherulites as is visible in figure 2.12c. The reasons behind these differences in the crystallization process are not well-understood currently; more detail study on the crystallization process is currently pursued.

2.3.5 Self-assembly and Encapsulation Capabilities

The butyl ester substituted random and block copolymers were hydrophobic and water insoluble. Upon deprotection into carboxylic acid groups; the carboxylic units in the side chain provide hydrophilicity and the resultant polymer structure became amphiphilic in nature. This hydrophilic and hydrophobic balance made the random copolymers and block copolymers to

self-assemble in water as nano-aggregates. To trace the transformation of hydrophobic polymer (in the butyl ester form) into amphiphilic upon de-protection; they were subjected to water contact angle (WCA) measurements. WCA measurement is employed to study the amphiphilicity of the functional random and block copolymers by us[231] and others[267]. WCA of the BPCL-x and CPCL-x were measured for thin films on glass substrate by low bond axisymmetric drop shape analysis (LB-ADSA method). The photographs of the water droplet for BPCL-50 and CPCL-50 films are shown in figure 2.13a (for other polymers, see Appendix). It is very clear from the photographs and the WCA plot against the copolymer content that the BPCL-x showed WCA in the range of 68 to 72 ° with respect to highly hydrophobic nature. On the other hand, the carboxylic acid copolymers CPCL-x exhibited WCA < 15 ° with respect to their highly hydrophilic nature. The PCL_{50}-b-$BPCL_{50}$ block copolymer also exhibited WCA in the similar range, i.e. 76 ° owing to the hydrophobic nature. The deprotected block gave WCA as 43 °, which is higher compared to the carboxylic substituted random copolymers. Thus, based on the WCA data; it may be concluded that the custom designed carboxylic PCL random polymers are amphiphilic in nature.

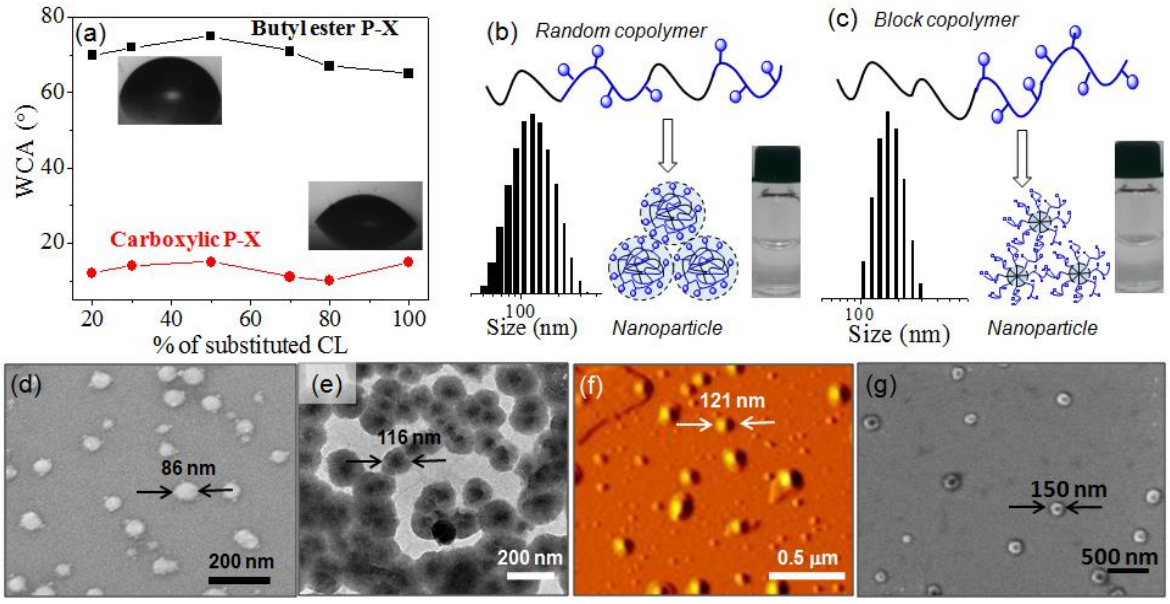

Figure 2.13. *Water Contact Angle of BPCL-x and CPCL-x (a). DLS histograms of CPCL-50 (b) and PCL_{50}-b-$CPCL_{50}$ (c) at 0.2 mg/mL concentration in water. FESEM image (d), HR-TEM image (e), and AFM image (f) of CPCL-50 polymer. FESEM image of PCL_{50}-b-$CPCL_{50}$ polymer (g). The images were recorded at 0.05 mg/mL concentration in water.*

In order to study the aqueous self-assembly of the amphiphilic random and block copolymers; the polymers were dissolved in DMSO and water mixture and the polymer solutions were transferred to a semi-permeable membrane of MWCO = 1000. The polymer samples were dialyzed against large amount of milli Q water for 48 h and fresh water was replenished periodically to remove DMSO completely. At the end of the dialysis, clear, transparent and stable aqueous polymer solution was obtained (see the photographs of sample vials in figures 2.13b and 2.13c). To study the size of the aqueous polymer assemblies, the dialyzed sample was subjected to dynamic light scattering and the histograms for the polymers CPCL-50 and PCL_{50}-*b*-$CPCL_{50}$ are shown in figures 2.13b and 2.13c, respectively. The samples showed uniform mono-modal distribution of aggregates with average sizes 120 ± 5 nm and 160 ± 5 nm for random and block copolymers, respectively. To visualize the morphology of these aqueous nano-aggregates, the sample was subjected to field emission scanning electron microscope (FE-SEM), high resolution transmission electron microscope (HR-TEM) and atomic force microscope (AFM) analysis. FE-SEM images of CPCL-50 sample showed spherical morphology with nanoparticles of size 86 ± 10 nm in water (see figure 2.13d). HR-TEM image (see figure 2.13e) gave clear evidence for the existence of spherical nano-assemblies with dark contrast in the middle and light hydrophilic-kin of layer at the periphery. The sizes of the nanoparticles were obtained as 110 ± 10 nm. AFM image of the CPCL-50 sample showed the spherical morphology with sizes in the range of 120 ± 10 nm (see figure 2.13f). FE-SEM image of the block copolymer PCL_{50}-*b*-$CPCL_{50}$ also showed the existence of spherical nanoparticles of size 150 ± 10 nm (see figure 2.13g). The sizes of the nanoparticles obtained from DLS were in good correlation with FE-SEM, AFM and HR-TEM images. DLS histograms of other random copolymer are given in figure 2.14. The morphology characterization was carried out for the other random and block copolymers as well utilizing FE-SEM and the images can be seen in figure 2.15.

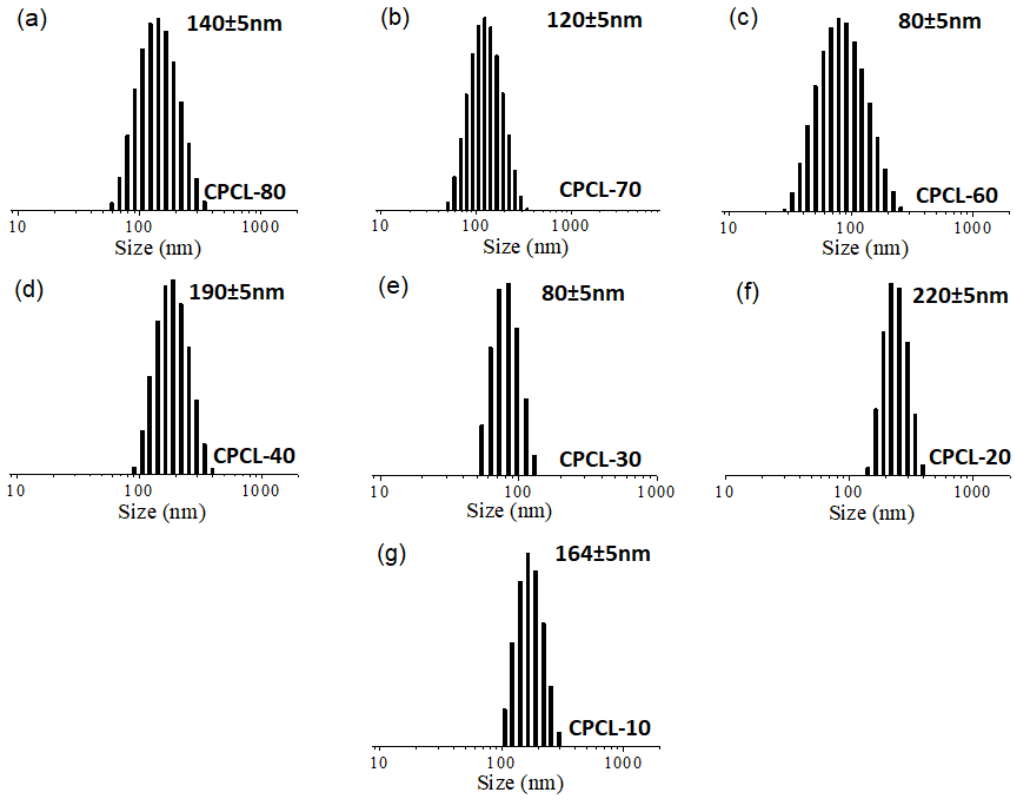

Figure 2.14. *DLS histograms of nascent random copolymer scaffolds at 0.2 mg/mL concentration in water.*

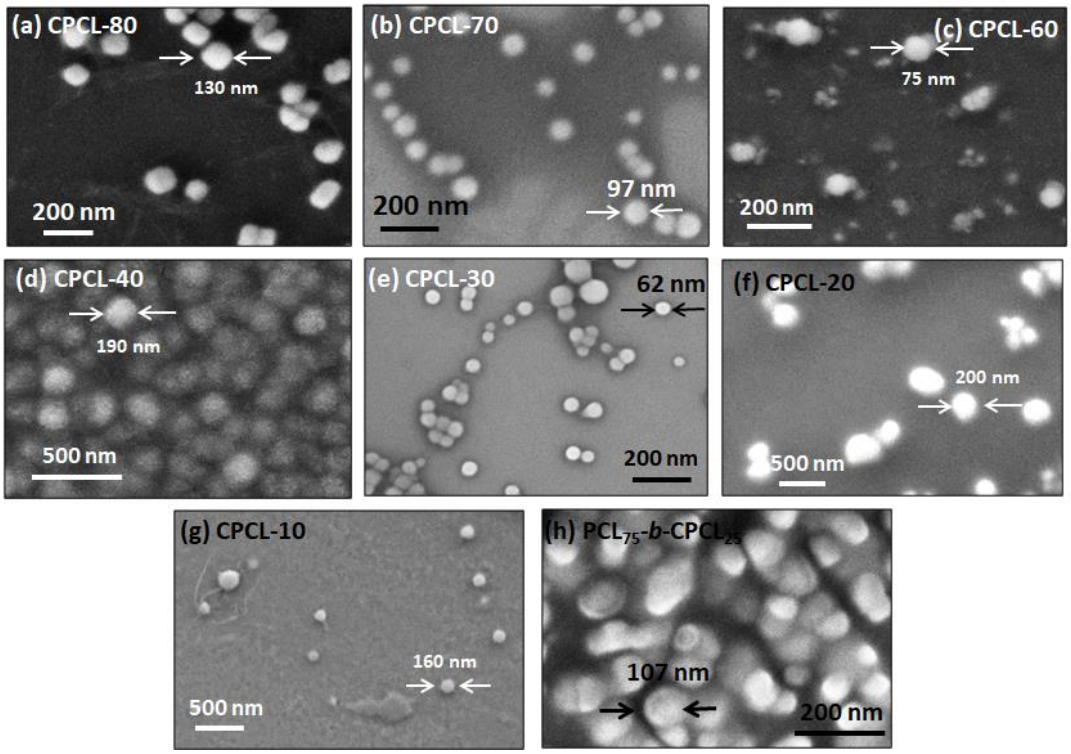

Figure 2.15. *Field emission scanning electron microscopy (FESEM) images depicting spherical morphology of the random and block copolymer nanoparticles. The images were recorded at 0.05 mg/mL concentration in water.*

To determine the critical micellar concentration (CMC) of the polymer aggregates, pyrene was employed as fluoro-probe. The concentration of pyrene was fixed as 0.6 x 10^{-6} M and the concentration of copolymer was varied over a wide range.[268] Pyrene exhibits five distinct vibronic levels in the emission spectra when excited at 337 nm. The respective intensities of the vibronic levels I_1 and I_3 change with respect to the hydrophobic environment around the pyrene molecules. The ratio of fluorescence intensity of I_1 (at 372 nm) and I_3 (at 383 nm) were determined from the emission plot and these values were plotted against Log (conc). From the plot of I_1/I_3 fluorescent peak intensities versus the concentration of polymer (as can be seen in the inset plot in figure 2.16); the CMC of the CPCL-50 polymer was obtained as 6.65 µg/mL. CMC of CPCL-30, CPCL-70 and PCL_{50}-*b*-$CPCL_{50}$ were determined as 7.26, 2.95 and 40 µg/mL (see figure 2.16). The CMCs are in the range of PCL based nano-assemblies reported by us and others in the literature.[269] The polymer aggregates of 120 nm is typically corresponding to micellar aggregates which is represented in figures 2.13b and 2.13c. Thus, the newly designed carboxylic substituted amphiphilic PCL random copolymers and block copolymers were able to self-assemble as stable spherical nanoparticles in water and also capable of loading water insoluble aromatic molecules such as pyrene in the hydrophobic core.

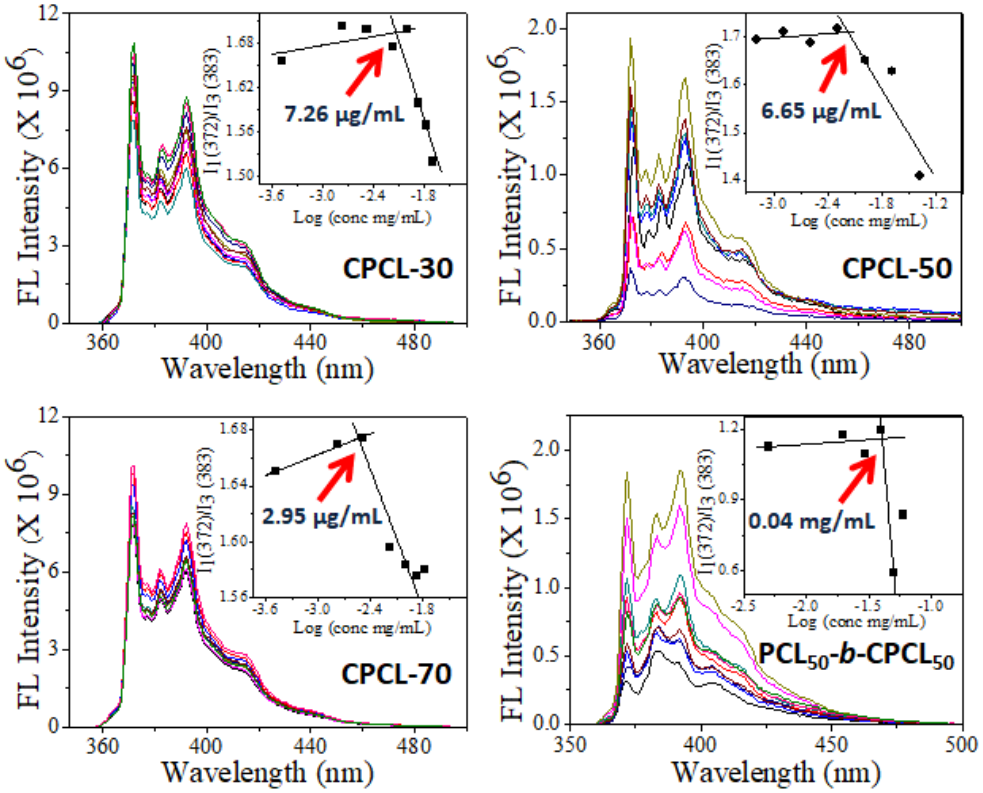

Figure 2.16. *Critical Micelle Concentration (CMC) plots of random and block copolymer scaffolds.*

2.3.6 Drug Encapsulation

The polymers were subjected to encapsulation studies using doxorubicin (DOX) anticancer drug. The polymer and DOX were dissolved in a mixture of water and DMSO (3 mL+2 mL). The mixture was transferred to a semi-permeable membrane of MWCO = 1000 and dialyzed against milli Q water for 24 h. The removal of unencapsulated drug molecules and DMSO was facilitated by periodically replenishing the fresh water for 24 h. The dialyzed solutions were filtered using whatmann filter paper, lyophilized and stored at 4 °C for further studies. The photographs of the vials containing the DOX loaded polymer samples are shown in figures 2.17a and 2.17b for random and block copolymers, respectively. The drug loading content (DLC) was determined using UV-Vis spectroscopy. CPCL-30, CPCL-50 and CPCL-70 random copolymer nanoparticles showed DLC as 1.38 %, 1.47 % and 0.90 %, respectively. The block copolymer nanoparticles PCL_{75}-*b*-$CPCL_{25}$ and PCL_{50}-*b*-$CPCL_{50}$ showed DLC as 1.45 % and 1.53 %, respectively. Drug loading efficiency (DLE) of the random copolymers CPCL-30, CPCL-50 and CPCL-70 was observed to be 27.6 %, 29.5 % and 17.6 %, respectively. For the block copolymers PCL_{75}-*b*-$CPCL_{25}$ and PCL_{50}-*b*-$CPCL_{50,}$ the DLE values were 29 % and 30.7 %, respectively. Rainbolt et al. reported the DLC = 3.0 to 4.9 % and DLE = 30 to 49 % for triethylene glycol substituted PCL random copolymers.[229] Cheng et al. had reported DLC = 1.1 to 2.0 % and DLE = 20 to 55 % for octyl and triethylene glycol substituted PCL block copolymers.[225] Thus, the DLC and DLE of both random and block copolymers reported in the present work are in the same range of other PCL polymer scaffolds.

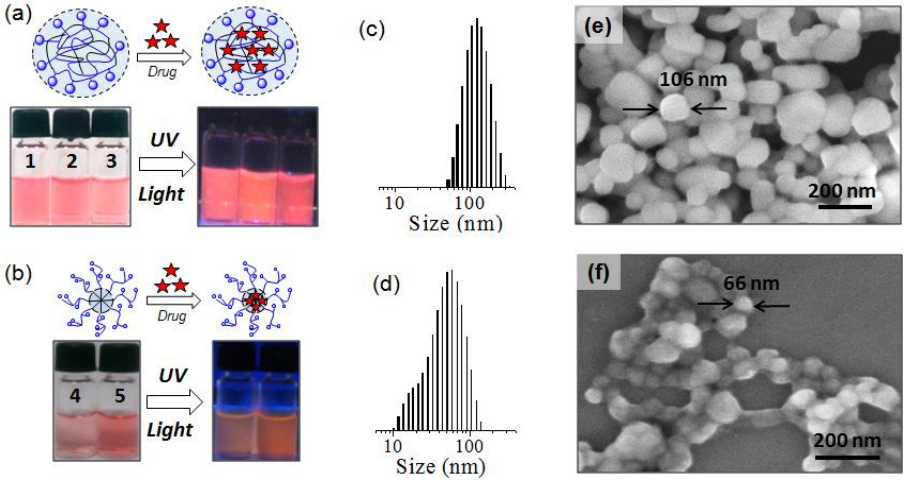

Figure 2.17. *Photograph of vials containing DOX-loaded random (a) and block copolymer (b) nanoparticles [1=CPCL-30, 2=CPCL-50, 3=CPCL-70, 4=PCL_{75}-b-$CPCL_{25}$, 5=PCL_{50}-b-$CPCL_{50}$]. DLS histogram of CPCL-50-DOX (c) and PCL_{50}-b-$CPCL_{50}$-DOX (d), FESEM image of CPCL-50-DOX (e) and PCL_{50}-b-$CPCL_{50}$-DOX (f) nanoparticles.*

These DOX-loaded nanoparticles were subjected to DLS measurements so as to ensure that the scaffolds were stable post DOX loading. The DLS histogram of the DOX loaded nanoparticles CPCL-50-DOX and PCL_{50}-*b*-$CPCL_{50}$-DOX showed a mono-modal distribution with average size of 80 ± 5 nm and 45 ± 5 nm, respectively (see figures 2.17c and 2.17d). FE-SEM images revealed the morphology of homogenous spherical nanoparticles for the DOX loaded samples (see figures 2.17e and 2.17f). The DLS histograms and FESEM images of other DOX loaded nanoparticles are given in figure 2.18.

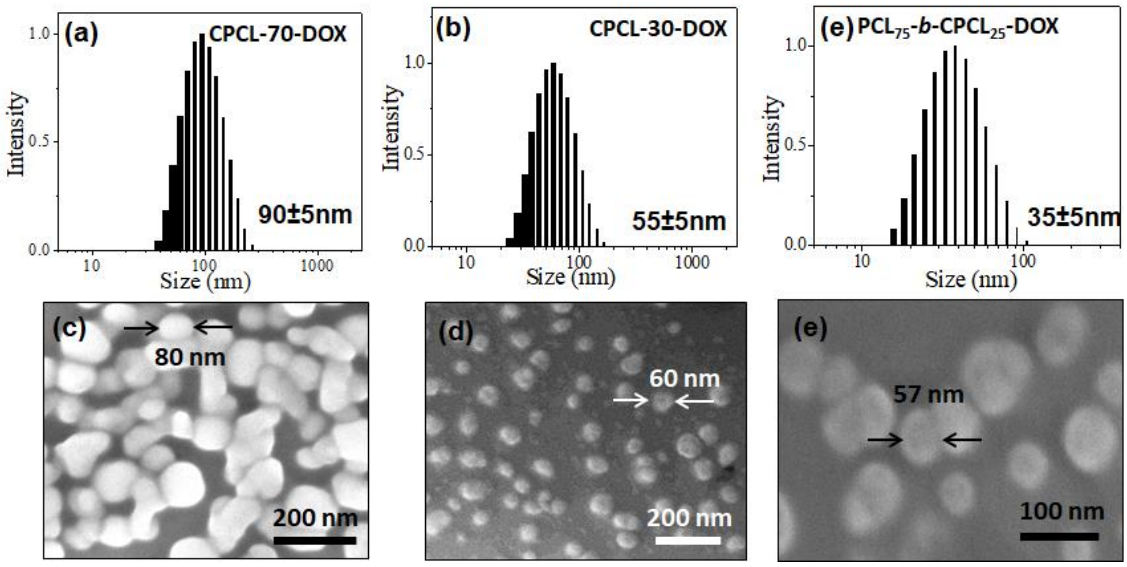

Figure 2.18. *DLS histograms and FESEM images of DOX-loaded random and block copolymer nano-assemblies in milli-Q water.*

The photophysical properties of the DOX loaded nanoparticles were studied by absorbance and fluorescence spectroscopy (see figure 2.19a). The spectra of the DOX loaded nanoparticles were found to be almost identical to free DOX in all the cases indicating the carboxylic PCL random copolymers stabilized the DOX in the nascent form without any disturbance to its photophysical characteristics. The DOX loaded nanoparticles were subjected to fluorescent light microscopy (FLM) analysis (see figure 2.19b). The FLM image revealed the existence of highly red-fluorescent DOX loaded nanoparticles. Thus, based on the above studies it may be concluded that the newly designed random and block copolymer nano-assemblies are efficient drug nano-carrier for anticancer drugs such as doxorubicin.

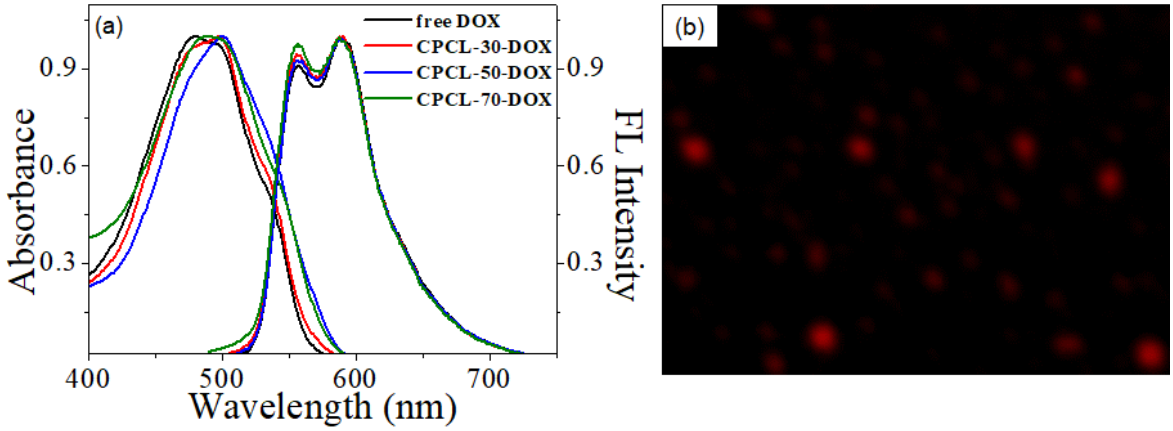

Figure 2.19. *(a) Absorbance and emission plots of free DOX and DOX-loaded nanoparticles. (b) Fluorescense light microsopy (FLM) image of CPCL-50-DOX nanoparticle.*

2.3.7 Enzyme-Responsive Drug Delivery

The PCL backbone is constituted by aliphatic ester linkages; thus, it is highly susceptible to undergo enzymatic biodegradation at the lysosomal compartments of the cells[270–272] when taken up through the endocytosis process (see figure 2.3). It is important to mention that the random and block copolymer scaffolds have different amount of carboxylic PCL units as well as topology in the backbone. They also exhibited significant difference in their chain packing ability as evident from semi-crystalline or amorphous nature in thermal properties (see figures 2.11c and 2.11d). Thus, the difference in the PCL chain packing in the nanoparticles may influence on the enzymatic biodegradation process. For instance, CPCL-30 has 30 mole % carboxylic acid and high amount of PCL units (70 %) which exhibit strong inter-chain interactions and account for the tightly packed domains. On the other hand, the CPCL-70 nanoparticle has large amount of carboxylic PCL; thus, the steric hindrance could hinder the chain packing and result in relatively loosely packed nanoparticle structure. The block copolymer has well defined hydrophilic CPCL chains projected outside and hydrophobic PCL at the core of the nanoparticles. Hence, these inter-chain interactions among the PCL chains are expected to influence on the enzyme-responsive cleavage of the nanoparticles to deliver the DOX.

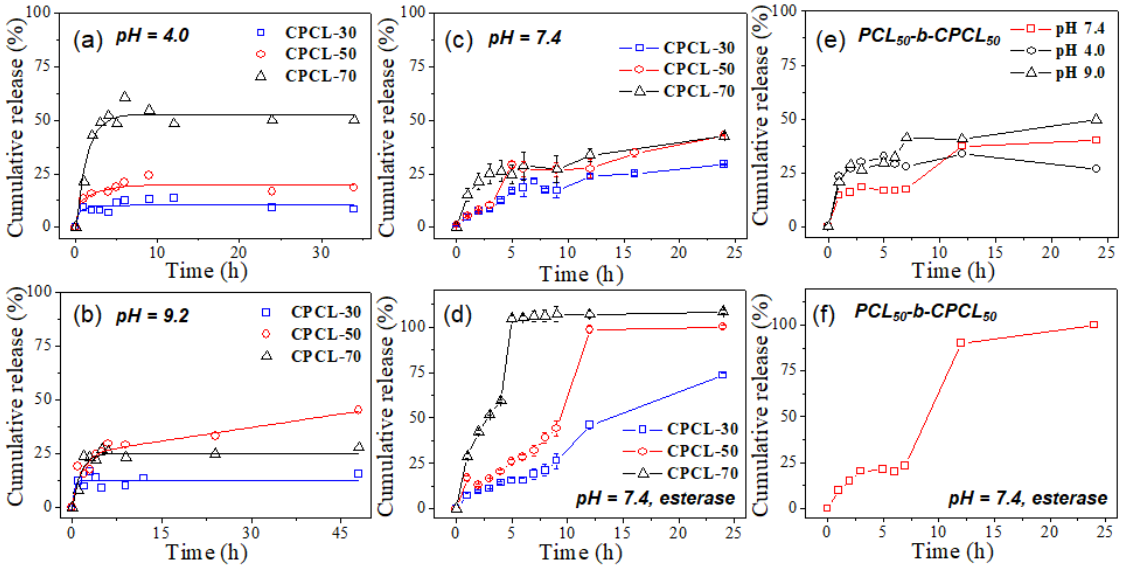

Figure 2.20. *In vitro drug release kinetics of DOX loaded random copolymer CPCL-x nanoparticle at pH 4.0 (a), pH 9.2 (b), pH 7.4 (c) in PBS at 37 °C. (d) Cumulative release of DOX in presence of esterase enzyme in PBS, pH 7.4 at 37 °C. In vitro drug release kinetics of block copolymer PCL_{50}-b-$CPCL_{50}$-DOX in PBS at various pH (e) and in the presence of esterase enzyme in PBS at 37 °C, pH = 7.4 (f).*

The DOX-loaded polymeric nanoparticles were examined for enzyme-responsive drug delivery by carrying out the *in vitro* release studies in the presence of esterase enzyme (horse liver).[232,271] The polymer nanoparticles were initially subjected to stability testing at various pH = 4.0, 7.4 and 9.0 (in PBS at 37 °C) prior to the enzyme-kinetics. The DOX-loaded polymeric nanoparticles were taken in a dialysis tube (MWCO = 1000) and incubated at 37 °C in PBS. The DOX release in the reservoir was subjected to absorbance spectroscopy at regular time intervals to deduce the amount of DOX released from the scaffolds. The cumulative DOX release observed in PBS at 37 °C at various pH for the CPCL-30-DOX, CPCL-50-DOX and CPCL-70-DOX were plotted and shown in figures 2.20a to 2.20c, respectively. The CPCL-70 nanoparticle exhibited higher DOX release up to 50 % at acidic pH (see figure 2.20a). This trend was attributed to both the presence of large amount of the carboxylic units for loosely packed nanoparticle structure as well as their susceptibility for hydrolytic cleavage. On the other hand, CPCL-30 and CPCL-50 nanoparticles exhibited better stability with < 25 % DOX release in PBS at 37 °C for the entire pH range. To study the drug release under the intracellular environment conditions, the DOX loaded CPCL-30, CPCL -50 and CPCL -70 nanoparticles were incubated in the presence of 10 U of esterase enzyme in PBS at 37 °C. The cumulative

DOX release data was plotted and shown in figure 2.20d. This *in vitro* experiment resembles the rupture of the nanoparticles in the intracellular lysosomal environment. An interesting observation here is that the degradation kinetics of the random copolymer was altered upon changing the number of carboxylic PCL units in the random copolymer. Up on increasing the carboxylic PCL units, the esterase-driven polymer cleavage becomes faster. In other words, the polymer nanoparticles with more carboxylic PCL units (CPCL-70-DOX, see figure 17d) exhibited a "burst" (< 3.0 h) release of 90 % drugs whereas "controlled" release (> 8-10 h) was observed in the case of CPCL-50-DOX. In the case of CPCL-30-DOX nanoparticles, the enzymatic cleavage is not well-pronounced and only < 75 % drug was released. Interestingly, the polymer nanoparticles with 50 % hydrophilic carboxylic PCL and hydrophobic PCL possessed optimum geometry and it exhibited controlled release of 90 % drugs in 8-10 h which is good for drug delivery. Thus, the *in vitro* studies revealed that balancing the PCL and carboxylic substituted PCL segment in the random copolymer brought about control in the scaffold degradation and subsequent release of drug. The drug release profiles of the PCL_{50}-*b*-$CPCL_{50}$ block copolymer was studied in PBS at 37 °C at various pH as well as in the presence of 10 U esterase in PBS at pH=7.4 (see figures 2.20e and 2.20f). The block copolymer also exhibited enzyme-responsiveness similar to that of random copolymer CPCL-50 (see figure 2.20d).

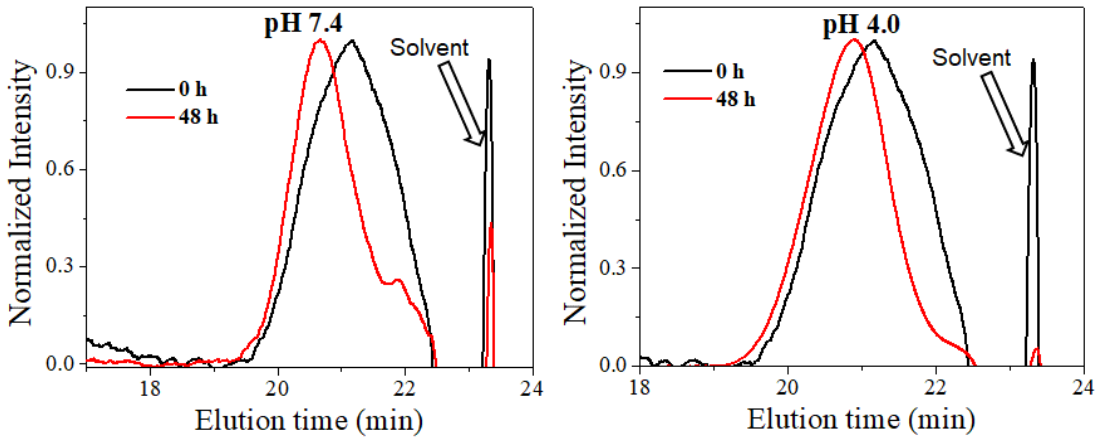

Figure 2.21. *SEC plot of the random copolymer CPCL-50 after 48 h exposure at pH=4.0 and pH=7.4.*

The polymer CPCL-50 was subjected to degradation studies at pH = 4.0 and pH = 7.4 which are corresponding to the lysosomal compartments at the intracellular level and extracellular conditions, respectively. The SEC plots of polymer after 48 h exposure at pH = 4.0 and pH = 7.4 are shown in figure 2.21. The SEC plots of polymer samples treated at pH 4.0 and 7.4 did not show any appreciable change in their SEC plots compared to that of the nascent polymer. Thus, the polymer scaffold is not susceptible to degrade under pH variation and this trend supports the *in vitro* release data showed in figure 2.20.

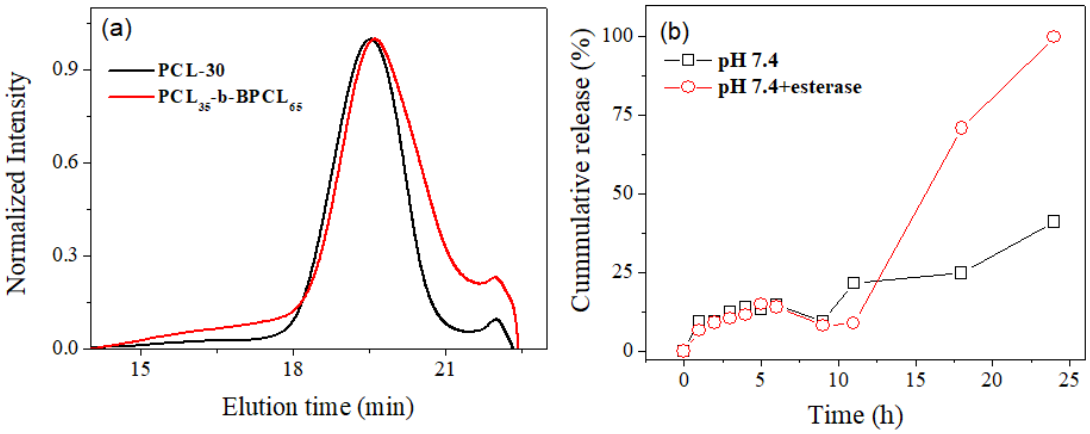

Figure 2.22. *(a) SEC chromatogram of the block copolymer PCL_{35}-b-$BPCL_{65}$ and it's macroinitiator. (b) In vitro release kinetics of the DOX-loaded block copolymer at pH 7.4 in the absence and presence of esterase at 37 °C.*

To confirm the biodegradation of the block copolymer, a new diblock copolymer PCL_{35}-b-$CPCL_{65}$ with higher amount of CPCL content was synthesized and employed for DOX release studies (see figure 2.22). This diblock copolymer showed very good stability in the DOX loaded form with only < 30 % of drug release in PBS at 37 °C. In the presence of esterase enzyme, the diblock nanoparticle readily underwent biodegradation and released more than 95 % drugs in PBS at 37 °C. Hence, it may be concluded that the enzymatic-biodegradation of the block copolymers was not restricted to block copolymer composition in the PCL-*b*-CPCL diblock system.

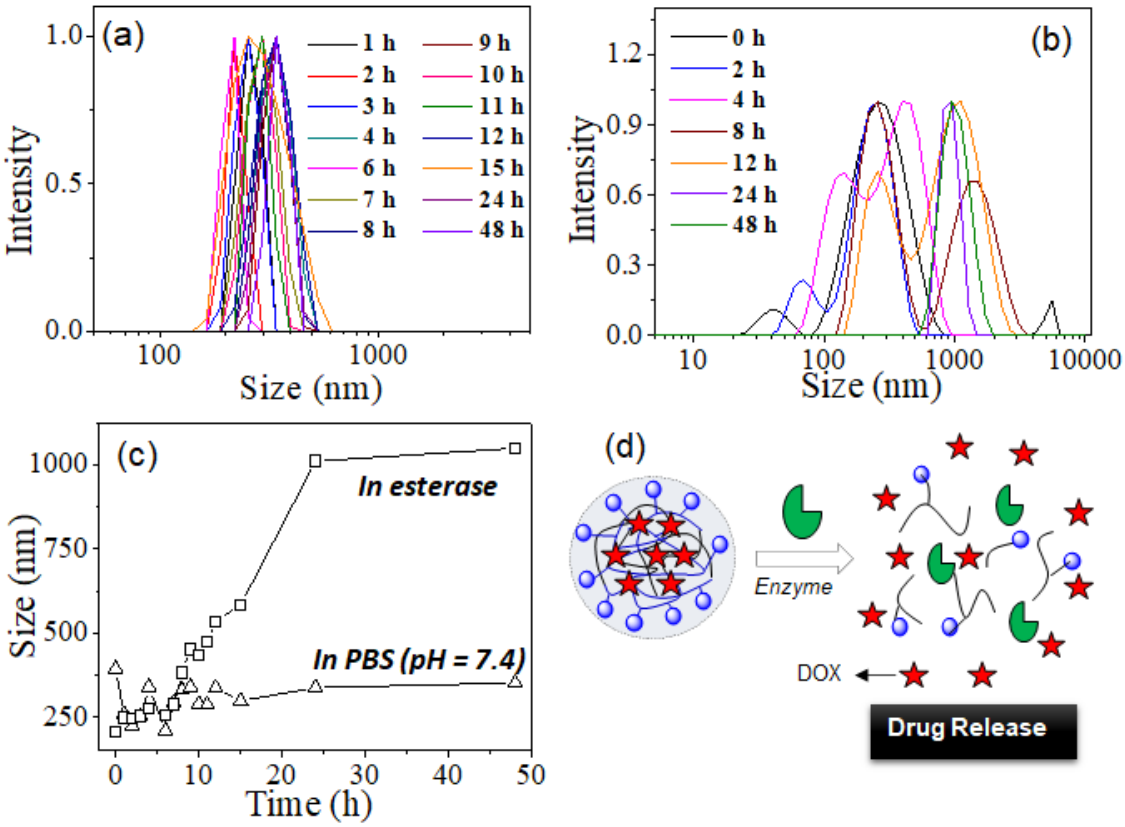

Figure 2.23. *DLS histograms of CPCL-50 polymer incubated in PBS alone (a) and in the presence of 10 U esterase at 37℃ in PBS (b). Average size of the degraded nanoparticles versus incubation time in PBS alone and in the presence of esterase enzyme in PBS at 37 °C (c). Proposed mechanism for the biodegradation of polymer scaffold by esterase enzyme (d).*

In order to substantiate the release data, time-dependent DLS experiment was carried out where the nascent scaffold CPCL-50 was exposed to esterase in PBS and also without enzyme in PBS incubated at 37 °C (see figure 2.23). The sample was subjected to DLS measurements at periodic intervals in order to understand the degradation process. The compiled DLS histograms at different time points can be seen in figure 2.23a and 2.23b for polymer nanoparticle incubated with PBS alone and in the presence of esterase, respectively. The average sizes of the nanoparticles were plotted against incubation time and shown in figure 2.23c. The plot explicitly shows that up to 8 h there is only swelling up of the scaffold that happens in the presence of PBS; however, after 8 h the action of esterase enzyme begins and leads to complete cleavage of the scaffold upto 48 h. The degraded nanoparticles do not possess tightly packed self-assembly; as a result, the particle size increased from nano-meter to micro-meter range. This is evident from the transition of mono to multi-modal size distribution and

then higher size aggregates were observed. On the other hand, in the absence of the esterase enzyme, the size of the nanoparticles did not show any change. This data corroborates with the DOX release data in figure 2.20d and provide direct proof for the enzyme-controlled release of the DOX from the random copolymer scaffolds.

The polymer backbone consists of aliphatic esters that are known to get chopped off in the presence of esterase in the lysosomal compartment. In order to give a proof-of-concept for this and to analyze the degraded polymer product, the CPCL-50 dialyzed sample after 48 h of incubation with esterase in PBS at 37 °C was lyophilized and submitted for MALDI-TOF-TOF analysis. Herein, several peaks were observed corresponding to various subunits of the random copolymer caused by the random chain scission catalysed by esterase enzyme in the polyester backbone. A few peaks have been shown with the possible chain motif (see the appendix). The peaks appeared corresponding to randomly cleaved oligomers such as TEG-PCL, PCL_2-CPCL, TEG-PCL_3 as Na^+ or K^+ ions. Therefore, from the *in vitro* release data it can be concluded that the PCL backbone enzymatic biodegradation can be tuned by varying the ratio of the PCL and carboxylic PCL composition in the random copolymer to release the DOX at the intracellular compartments.

2.3.8 Cytotoxicity and Cellular Uptake

The cytotoxicity studies for free DOX, nascent scaffolds and the DOX-loaded scaffolds were investigated in cervical (HeLa) and breast (MCF 7) cancer cell lines. For this purpose CPCL-50 and PCL_{50}-*b*-$CPCL_{50}$ polymer nanoparticle and their DOX loaded nanoparticle were chosen. The cytotoxicity of the nascent polymers was tested in both cell lines by varying the concentration and the histograms are shown in figures 2.24a to 2.24c.The nascent polymers CPCL-50 and PCL_{50}-*b*-$CPCL_{50}$ were non-toxic to cells up to the concentration of 60 μg/mL which lies in the acceptable range for PCL based nano-carriers. The DOX-loaded nanoparticles and free DOX were also fed to HeLa and MCF 7 cell lines and the concentrations were varied over a range from 0.1 to 1.0 μg/mL and respective histograms are provided in figures 2.24d to 2.24f. As seen from both histograms, free DOX showed IC_{50} value of ~ 0.4 μg/mL and complete cell killing was observed at 1.0 μg/mL. The DOX-loaded random and block copolymer nanoparticles in HeLa cell showed similar toxicity as free drug with IC_{50} value of ~ 0.5 μg/mL and exhibited complete cell killing at 1.0 μg/mL (see figures 2.24d and 2.24e).

The cytotoxicity data for the DOX loaded random copolymer CPCL-50 nanoparticle in breast cancer cell line (MCF 7) is shown in figure 2.24f. It is clearly evident from the histogram that free DOX and DOX loaded nanoparticles exhibited almost similar cell killing with IC_{50} of 0.4 μg/mL.[270] At a higher drug concentration (> 0.8 μg/mL), the DOX-loaded random copolymer scaffolds were found to be killing more than 90 % of the cells. These results explain that the DOX-loaded PCL based random and block copolymer nanoparticles showed excellent cell killing ability in both HeLa and MCF 7 cell lines. Hence, from the above results it can be concluded that the random and block copolymers are non-toxic to cells and their DOX loaded nanoparticles can accomplish apoptosis in cancer cells.

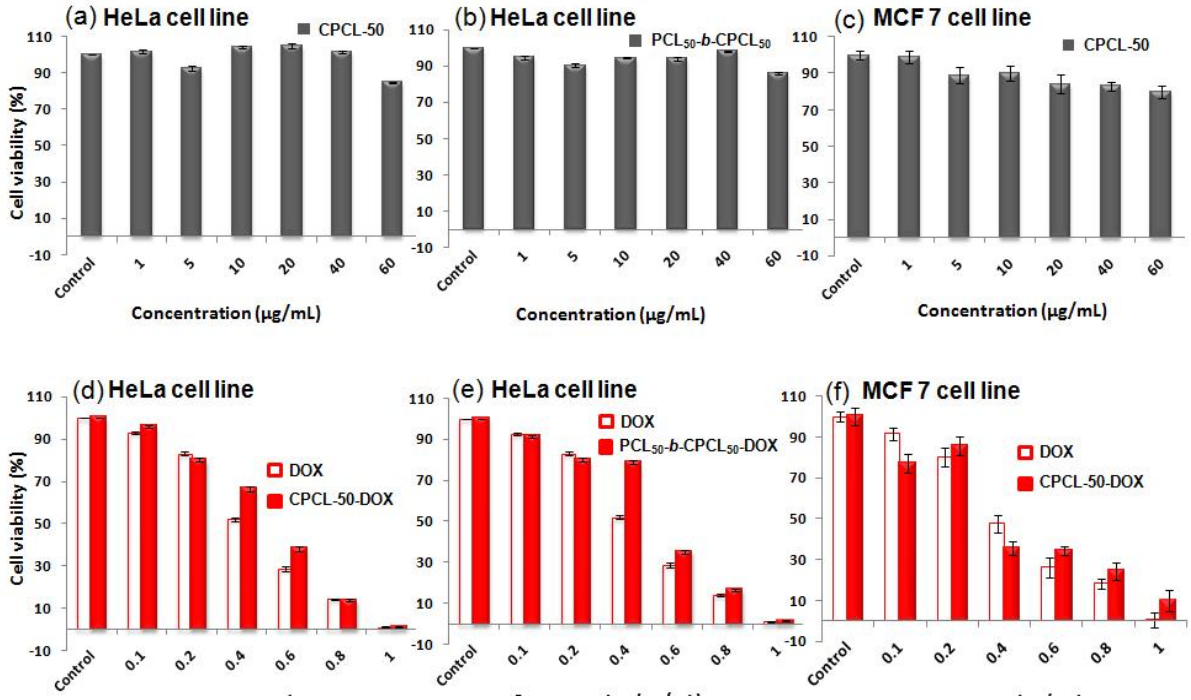

Figure 2.24. *Histogram depicting the cytotoxicity of nascent polymer scaffolds CPCL-50 (a) and* PCL_{50}-*b*-$CPCL_{50}$ *(b) in HeLa cell lines at various concentrations. (c) Cytotoxicity of nascent polymer scaffold CPCL-50 in MCF 7 cell line at various concentrations. The cytotoxicity of free DOX and DOX-loaded nanoparticle CPCL-50-DOX (d) and* PCL_{50}-*b*-$CPCL_{50}$-*DOX (e) in HeLa cell lines at various concentrations. (f) Cytotoxicity of DOX-loaded CPCL-50 in MCF 7 cell lines at different concentrations.*

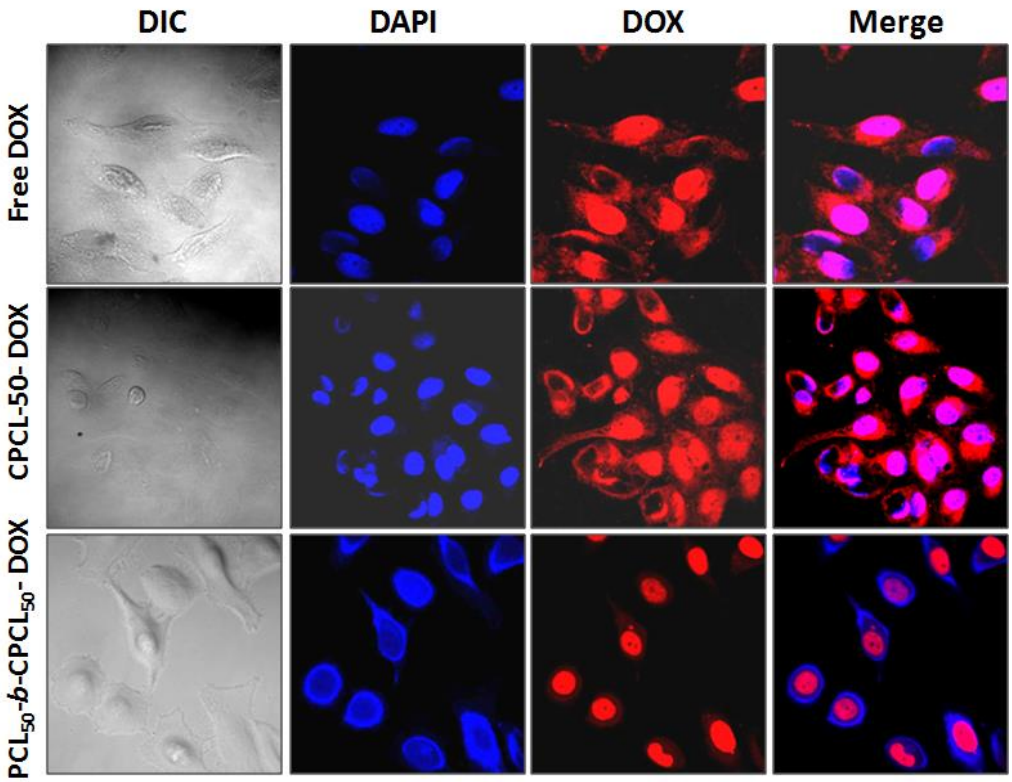

Figure 2.25. *CLSM images of HeLa cells incubated with free DOX (first panel), CPCL-50-DOX (second panel) and PCL_{50}-b-$CPCL_{50}$-DOX (third panel). The cells were counterstained with DAPI (blue). The red fluorescence of the DOX was visualized using the red channel.*

In order to confirm the uptake of the drug-loaded polymeric nanoparticles, CPCL-50-DOX, PCL_{50}-*b*-$CPCL_{50}$-DOX and free drug were subjected to cellular uptake in HeLa and MCF 7 cell lines. Confocal laser scanning microscopy (CLSM) images for free DOX, DOX-loaded nanoparticle, DAPI stained nuclei and phalloidin stained actins (or filaments) were visualized at red ($\lambda = 561$ nm), blue ($\lambda = 405$ nm) and green ($\lambda = 488$ nm) channels, respectively. The CLSM images are shown in figures 2.25 and 2.26 for HeLa and MCF 7 cell lines, respectively. The first panel in figure 2.25 vividly demonstrates the red fluorescence corresponding to free DOX predominately at the nucleus and partially in the cytoplasm. Similar trend can be seen in the CPCL-50-DOX loaded nanoparticle which showed sharp red florescence in the nuclei as well as the cytoplasm. The PCL_{50}-*b*-$CPCL_{50}$-DOX nanoparticle showed a prominent magenta colour in the nuclei of the merged image due to the overlapping of DAPI stained blue colour and the strong red fluorescence of the DOX nanoparticle. The differential interference contrast (DIC) image clearly shows the cellular morphology with contrasting nuclei within for all the images. As can be seen in the first-row images in the figure 2.26, the red fluorescence corresponding to free DOX can be seen at both the nucleus and the

cytoplasm. On the other hand, the CPCL-50-DOX loaded nanoparticle showed strong red florescence in the nuclei compared to the cytoplasm due to the exorbitant DOX uptake by the nucleus mediated by the polymer scaffold. It can also be seen by the intense magenta colour in the merged image corresponding to the amalgamation of DAPI stained nuclei (blue) and DOX particles (red). Alexa fluor-conjugated phalloidin is known to stain the actins or filaments present in the cytoplasm as well as in the nuclei. As can be seen in the images, the stain clearly demarcates the filaments present at the cell wall. Hence, it can be concluded that the newly designed PCL based random and block copolymers are efficient enzyme-responsive nano-carriers for the delivery of anticancer drugs like DOX at the nuclear site leading to effective death in cancer cells. Cellular internalization of DOX-loaded nanoparticles and free DOX was corroborated using flow cytometry analysis. The fluorescence histogram vividly showed that the DOX internalization in HeLa cell lines was 20-fold higher for CPCL-50-DOX random copolymer nanoparticles in comparison to free DOX (see figure 2.27). The block PCL_{50}-*b*-$CPCL_{50}$-DOX copolymer nanoparticles exhibited a 3.3-fold higher cellular uptake compared to free DOX. Among the random and block copolymer nanoparticles, the random copolymer nanoparticle exhibited 6-fold higher DOX uptake in the cells. Thus, the CPCL-50-DOX loaded nanoparticle exhibited to be the most promising nano-carrier for delivery of DOX to cervical cancer cells. The flow cytometry data was in accordance to the confocal microscopy images.

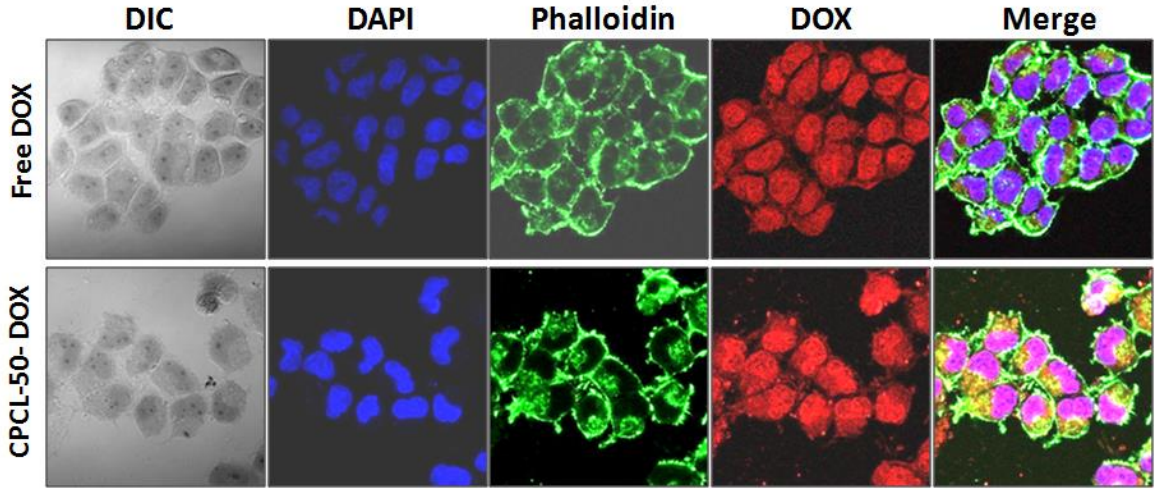

Figure 2.26. *CLSM images of MCF 7 cells incubated with free DOX (first panel) and CPCL-50-DOX (second panel). The cells were counterstained with DAPI (blue) and phalloidin (green). The red fluorescence of the DOX was visualized using the red channel.*

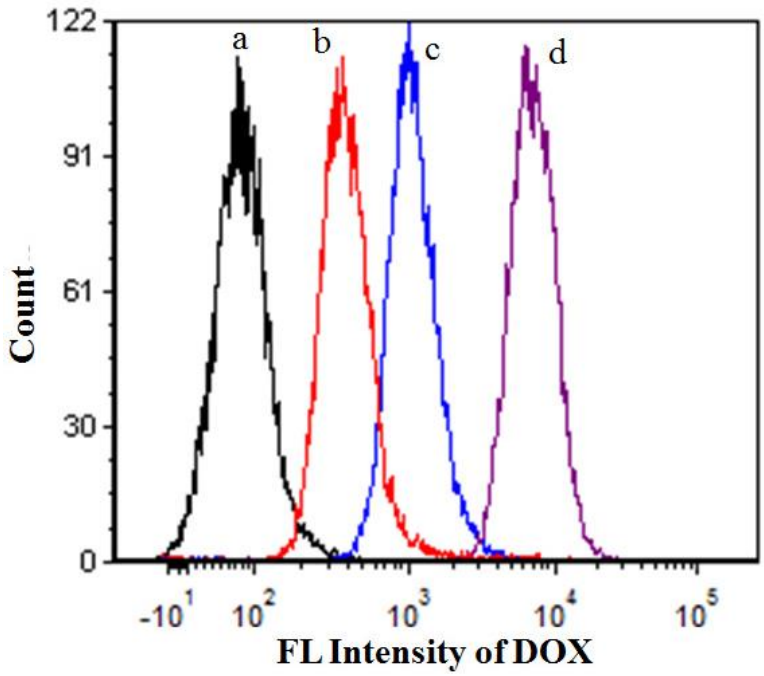

Figure 2.27. *Flow cytometry plots for control (a), free DOX (b), PCL_{50}-b-$CPCL_{50}$-DOX (c) and CPCL-50-DOX (d) in HeLa cell lines after 9 h incubation (DOX concentration = 1 μg/mL and 10000 cells are used).*

In the present investigation, the polymer with equal composition of PCL and carboxylic substituted PCL in both the random and block copolymer arrangement exhibited 'controlled' DOX release. Thus, the current polymer design allows one to precisely fine-tune the enzymatic biodegradation of PCL nano-scaffolds by simply varying the carboxylic acid content in the backbone. The block copolymer and random copolymer design principle is not restricted only to the present example, in general, it may be applicable to wide ranges of other PCL based substituted systems. Further, the carboxylic acid functionality in the present copolymer is also capable of anchoring drug molecules, targeting agents and stimuli responsive units for improved cellular uptake and delivery. Wide ranges of other anticancer drugs could also be loaded and delivered in these block copolymers and the research work is currently being pursued to address these drug delivery challenges.

2.4 Conclusion

In summary, new classes of fully biodegradable and amphiphilic carboxylic functionalized polycaprolactone-co-polycaprolactone random and block copolymers were custom designed via ring opening polymerization methodology. The amphiphilic polymers were self-assembled as nanoparticles of < 200 nm size in water and they also exhibited excellent tendency for loading and delivering anticancer drugs to cervical and breast cancer cells. The random copolymers were found to transform from semi-crystalline into completely amorphous up on increasing the carboxylic acid substituted PCL content in the polymer backbone. On the other hand, the block copolymers displayed completely different topology wherein they retained their semi-crystalline nature upon increasing the butyl ester PCL in the backbone. Upon de-protection, the block with higher ratio of carboxylic PCL became sluggish to crystallize. Water contact angle (WCA) measurements suggested the polymers with butyl ester substitution were hydrophobic with WCA > 70 ° whereas it's hydrolyzed carboxylic acid random copolymer turned into highly hydrophilic having WCA < 15 °. *In vitro* enzymatic-biodegradation and drug release kinetics analysis of the DOX loaded polymer nanoparticles revealed that their drug delivering ability was directly controlled by the amount of carboxylic acid units present in the random copolymers and their chain packing abilities. The nanoparticles with less number of carboxylic units in the backbone exhibited tightly packed chains as evident from their semi-crystallinity and exhibited 'slow' release of drugs as a result of restricted enzymatic cleavage on the polymer scaffold. On the other hand, random copolymers with high carboxylic content restricted the chain alignment (amorphous) and the loosely packed domains provided enhanced enzymatic-biodegradation for 'burst' drug delivery. *In vitro* cytotoxicity studies in cervical and breast cancer cells revealed that the nascent polymer scaffolds were non-toxic to cells. The DOX loaded nanoparticles exhibited excellent cell killing ability in cervical and breast cancer cells and accomplished more than 90 % cell death at 1.0 μg/mL. Confocal microscopic analysis elucidated that the polymer loaded drugs are predominantly internalized at the nucleus of the cells and support their enzymatic-biodegradation pathway of drug delivery and their excellent cell killing ability. Flow cytometry analysis revealed that the random and block copolymer nanoparticles were more efficiently taken up by the cells as compared to free DOX. Amongst these, CPCL-50-DOX nanoparticle exhibited the highest cellular internalization in HeLa cell lines. The current polymer design opens up new opportunities for

fully enzymatic-biodegradable amphiphilic random and block copolymer concept in carboxylic PCL nano-scaffolds and successfully demonstrates their ability to deliver the drugs at the intracellular compartments and accomplish apoptosis in cervical and breast cancer cells.

3

Development of Star block copolymer Unimolecular Nano-carriers: In vitro Cellular Uptake

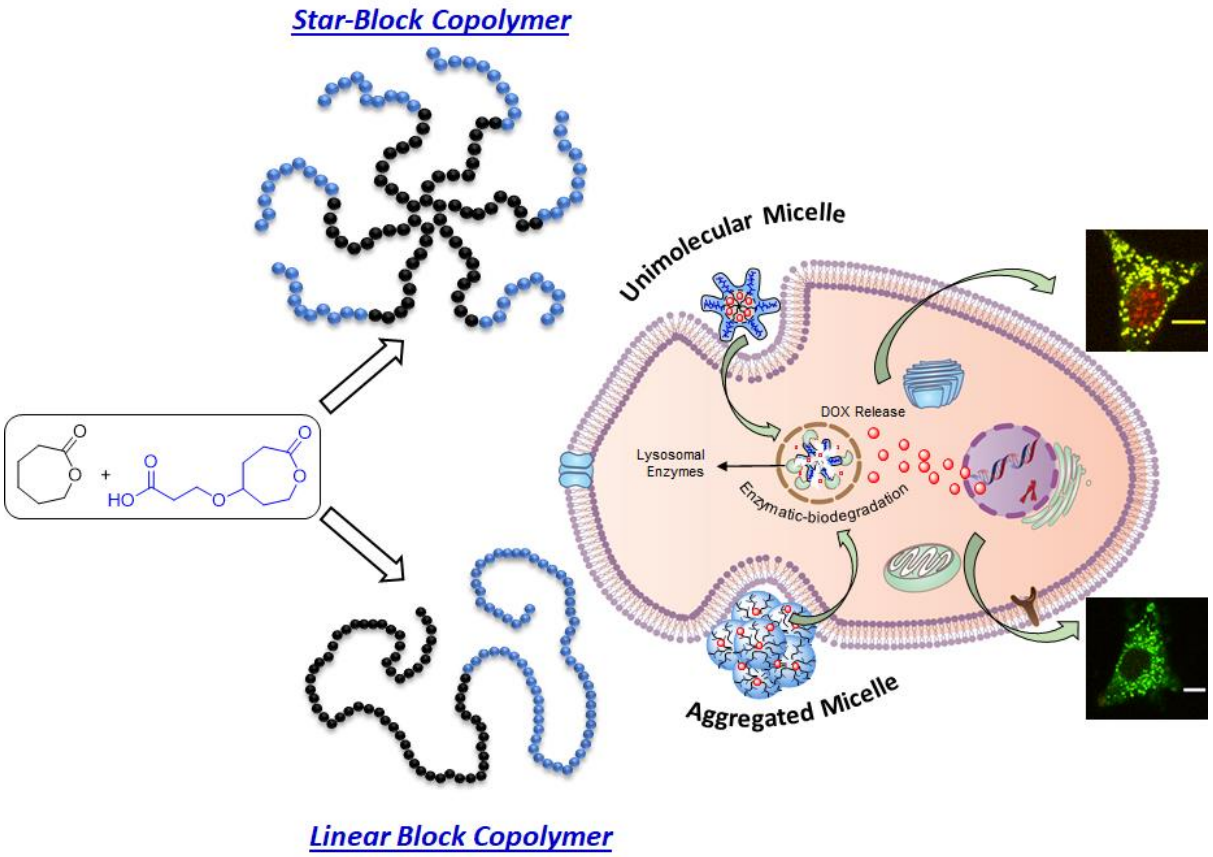

Abstract

Investigating the impact of polymer architecture on macromolecular self-assembly and the ability to cross biological barriers can help devise efficient nano-carriers to overcome the bottlenecks in the field of Polymer therapeutics. The idea was to understand if topological tweaks in architecture did in fact transcend directly onto their drug loading capability, self-assembly and *in vitro* cellular uptake kinetics of anticancer drug Doxorubicin. In order to accomplish this task, we opted to draw a comparison between the star and linear polymer topology by maintaining similar chemical composition and molecular weight. Herein, fully biodegradable amphiphilic caprolactone based star and linear block polyesters were designed using an in-house tailor-made melt reactor set up. The 6-arm star block copolymers self-assembled in water to result in unimolecular micelles (UMs) in the size range of 18-30 nm as opposed to the multimolecular micelle formation of ~ 200 nm size for the linear block counterpart. The topology difference influenced the drug loading content capability of these nano-carriers wherein the star-shaped unimolecular micelles exhibited a 7-fold higher loading of the anticancer drug Doxorubicin with a DLC of ~ 14 %. The polyester backbone of the star block copolymer underwent complete degradation in the presence of esterase enzyme replicating the intra-cellular lysosomal compartment *in vitro*. The star block copolymer was found to be highly cyto-compatible and non-toxic to the Wild-type mouse embryonic fibroblast (WT-MEF) cell lines up to a concentration of 500 µg/ml. The DOX-loaded nano-carriers exhibited higher cell viability in comparison to free DOX after a 72 h incubation with WT-MEF cells. The live cell experiment in WT-MEF cells demonstrated the cellular uptake pathway of the UMs to be via endocytosis followed by lysosomal degradation and release of DOX into the nucleus. The unimolecular micelle cellular uptake was significantly higher than the linear polymer and the free DOX. Thus, the star-shaped unimolecular micelles proved to be excellent drug delivery candidates *in vitro* and should be exploited for *in vivo* applications.

3.1 Introduction

Conventional chemotherapeutic drugs available in the market are all small molecules that are rendered ineffective due to their poor biodistribution, target specificity, short half-life and consequential side effects like cardiotoxicity, nephrotoxicity and neurotoxicity.[4,10,273] This obstacle in cancer treatment led to the development of "Polymer therapeutics" wherein polymers served as the nano-carriers for efficient delivery of drug molecules to the target site with reduced side effects and prolonged half-life.[274] They offer the advantage of passive selectively targeting the tumor tissue via the Enhanced Permeability and Retention (EPR) effect along with increased blood circulation time due to reduced renal clearance that alleviates the residence time in tumor micro-environment.[61] In addition to this, polymer drug delivery vehicles face numerous other challenges in the body. The ultimate fate of these polymeric carriers is to be eliminated from the body, however, there needs to be a balance between the elimination of polymer from the body via kidney, liver or spleen and the extravasation of polymers from the blood stream into the tumor tissue.[65,76,275] The various factors that influence this balance are the molecular architecture of the polymer, molecular weight, size, shape, chain flexibility and branching.[273] This is where topological tweaks in the polymer architecture could play a significant role in altering properties such as the size, self-assembly, and further the biodistribution *in vivo*.

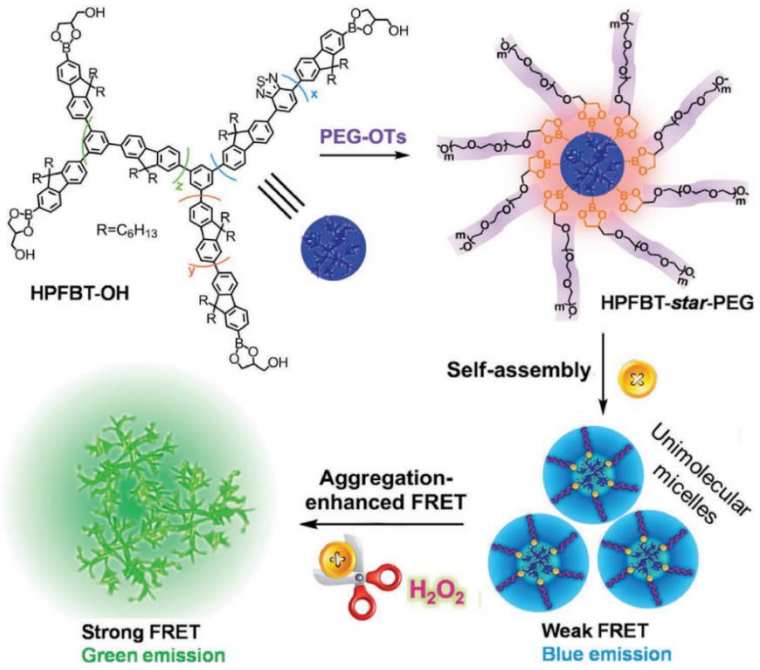

Figure 3.1. *Synthetic design of HPFBT-star-PEG unimolecular micelle depicting H_2O_2-activatable blue-to-green conversion (adapted from Huang et al. Small,* **2017**, *13*, 1604062*)*

This unfathomable task has been addressed by scientists in the past by exploiting various complex three-dimensional architectures like dendrimers, hyperbranched, brush-type and star polymers for various applications including *in vitro* and *in vivo* drug delivery[276–280], gene delivery[281–283], bioimaging[139,143,284–286], catalysis[152,287,288] etc. Gong et al. developed an amphiphilic star polymer based on the PAMAM dendrimer conjugated with the targeting ligand KE108 peptide and Cy5 dye, PAMAM-PVL-PEG-OCH_3/KE108/Cy5 for medullary thyroid cancer treatment studies *in vivo*.[141] Zhu and coworkers designed a H_2O_2-activatable color-convertible fluorescent nanoprobe composed of a hyperbranched core HPFBT and a hydrophilic PEG shell used to differentiate between normal and tumor cells (see figure 3.1).[289] Dendrimers and hyperbranched topologies have been the most prominently studied systems for drug delivery applications, however, their multi-step synthesis makes them quite tedious. This limitation was overcome by the star polymers that offer extreme structural control along with a facile synthetic approach whilst providing all the aforementioned advantages as dendrimers or hyperbranched architectures. Well-defined star architectures with low polydispersity can be attained with one-step polymerization approach resulting in compact structures.[165] Star polymers are exceptionally stable at infinite dilution as opposed to their linear block counterparts that self-assemble via a thermodynamically driven process into multimolecular (or aggregated) micelles.[110] Thus, the unimolecular micelles can overcome the limitation of premature drug release in the blood posed by the disintegration of aggregated micelles. Star-shaped polymers exhibit higher drug loading content, sustained drug release, prolonged blood circulation and their relatively small sizes prevent RES uptake as compared to the linear polymers having the same molecular weight.[110,116,165]

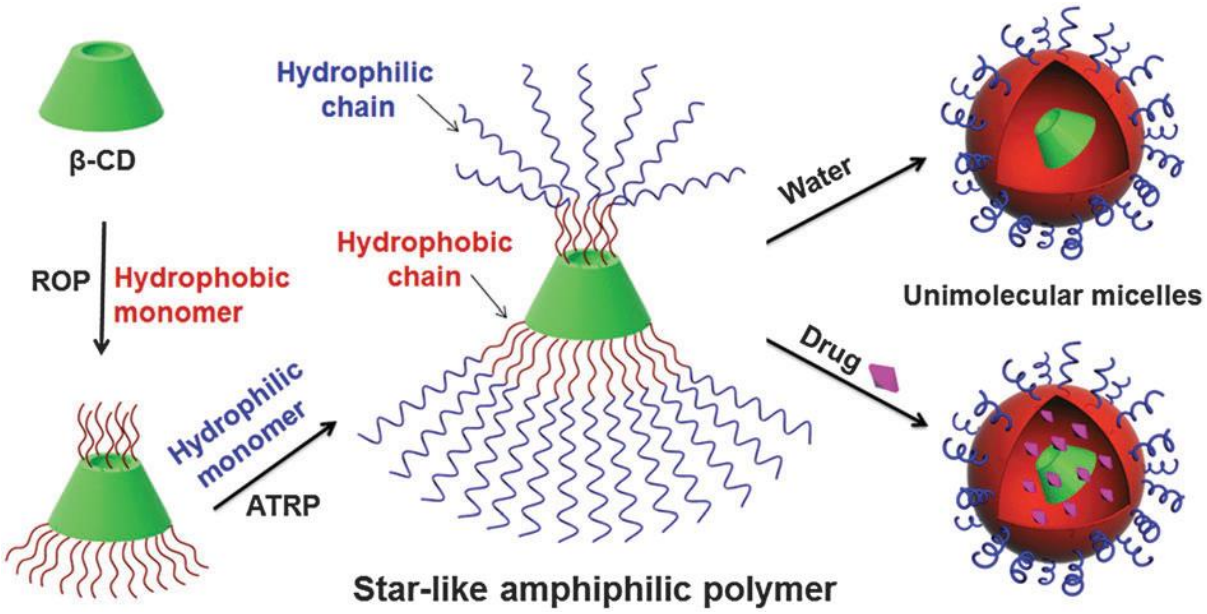

Figure 3.2. *Schematic representation of the β-CD based star polymer PLA-POEGMA synthesized using ROP and ATRP polymerization and employed for drug delivery application. (adapted from Xu et al. Chem. Commun.* **2015**, *51*, 15768-15771)

These architectures have been explored at length in the literature with a plethora of synthetic approaches and applications of star polymers. Wang and coworkers developed a 21-arm PLA-POEGMA star polymer using β-cyclodextrin as the macroinitiator employing ROP and ATRP polymerization routes that resulted in a unimolecular micelle with high DOX loading content (6-10 %) and was used for drug delivery *in vitro* (see figure 3.2).[172] Qiao et al. synthesized PEG-b-PCL core crosslinked unimolecular micelles that exhibited 11-18 % loading content for hydrophobic drugs DOX and pirarubicin with higher cellular uptake.[290] Davis and coworkers utilized RAFT polymerization for designing POEGA star polymers to be used as drug delivery vehicles *in vivo*.[291] In all the reports known so far to the best of our knowledge, all the polymer designs emanated non-biodegradable backbones and the ability to degrade *in vivo* after payload delivery to undergo renal filtration is an extremely important attribute of a drug delivery vehicle to avoid systemic toxicity.

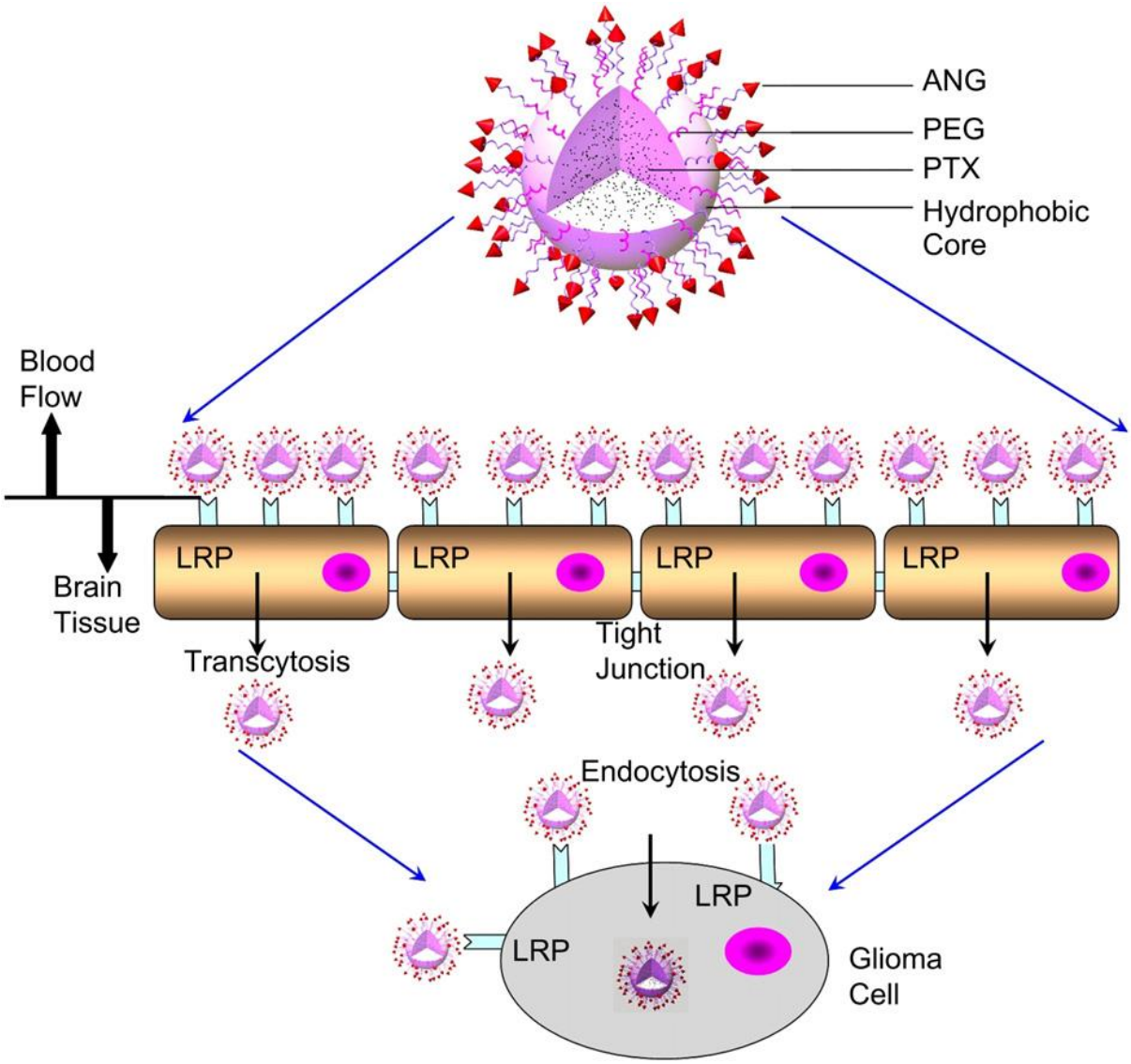

Figure 3.3. *Schematic description of the Angiopep conjugated PEG-PCL nanoparticle loaded with paclitaxel for glioblastoma treatment via LRP-mediated targeted delivery. (adapted from Xin et al. Biomaterials,* **2012**, *33,* 8167-8176*)*

Amongst the biodegradable polymers, polycaprolactones are the most prominently used for biomedical applications owing to their environmental stability, blend compatibility, mechanical robustness etc.[217] Most of the PCL based star-block copolymers known in literature have been produced using polyethylene glycol (PEG) as the macroinitiator-cum-hydrophilic block (see figure 3.3).[292] In these star-block copolymers, the biocompatible PEG-part was

primarily introduced for appropriate hydrophilicity; however, the polyether backbone in PEG was completely inert towards biodegradation by enzymes.[242,293] Hence, there is a need for the development of non-PEGylated and fully biodegradable amphiphilic PCL star-block polymers exclusively using caprolactone monomer resources. In our previous chapter, we developed new classes of fully biodegradable and amphiphilic carboxylic functionalized polycaprolactone-co-polycaprolactone random and block copolymers via ring opening polymerization methodology.[294]

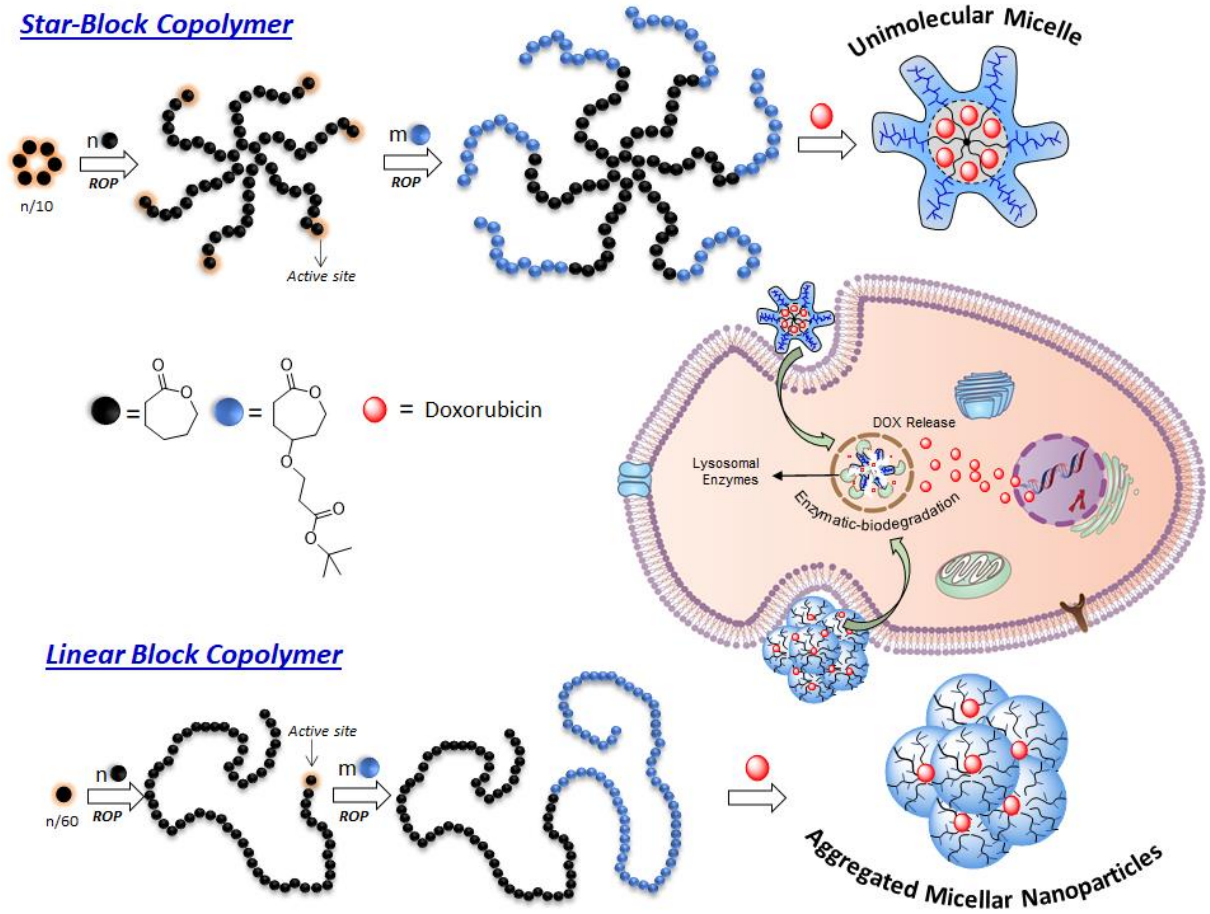

Figure 3.4. *Design and development of star and linear block copolymer to understand the role of topology on the in vitro cellular uptake.*

Building up on the same ideology, in this chapter we designed novel fully biodegradable amphiphilic 6-arm star-shaped PCL block copolymers. The aim of the study was understanding the role of polymer topology on the self-assembly, drug loading, and *in vitro* cellular uptake of nanoparticles. The most ideal way to compare topologies, in this case star

and linear polymer, was to design polymers with the same chemical composition of the backbone and molecular weight with only the exception of architecture (see figure 3.4). Herein, star and linear block copolymers were synthesized utilizing ε-caprolactone as the hydrophobic core and ɣ-substituted tertiary butyl caprolactone as the hydrophilic shell (upon hydrolysis to carboxylic acid). Our last one-decade experience in biodegradable polycaprolactone in cancer treatment,[231–233,261,294] bio-imaging[234–236] and antimicrobial research[237] has enabled us in choosing the appropriate geometry to address the above task. The star-shaped polymers self-assembled into unimolecular micelles of sizes in the range of 18-30 nm as determined using DLS, SAXS and microscopy techniques such as FESEM, HR-TEM, AFM. Their unimolecular nature was reinstated from the pyrene experiment wherein there was no change in the I_1/I_3 value. Their unimolecular property renders them exceptional stability even at infinite dilution, whereas the linear block copolymer self-assembled into aggregated micelles with a CMC of 1 µg/mL. The *in vitro* studies carried out in Wild-type mouse embryonic fibroblasts (WT-MEF) cell lines gave proof of the cyto-compatibility of the polymeric micelles upto a concentration of 500 µg/mL. The live cell experiment established the uptake pathway of the unimolecular micelles to be via endocytosis as opposed to the diffusion mechanism followed by free DOX. The cellular uptake was significantly higher in the case of the star-shaped unimolecular micelles and they exhibited a faster kinetics when compared to free DOX and the linear block DOX loaded micelle which displayed a slower time-dependent increase. We were able to successfully demonstrate that tweaking the polymer architecture had a cascade effect on all the properties of the nano-scaffolds translating directly to their cellular uptake kinetics *in vitro*. The aforementioned attributes of the star-shaped unimolecular micelles make them ideal for *in vivo* drug delivery applications and extremely suitable for tasks requiring tiny particles such as the breach of BBB.

3.2 Experimental Methods

3.2.1 Materials

Cis, trans-1,4-Cyclohexanediol, potassium t-butoxide, tertiary butyl acrylate, pyridinium chlorochromate (PCC), molecular sieves (4Å), m-chloroperbenzoic acid (m-CPBA), dipentaerythritol, tin(II) 2-ethylhexanoate ($Sn(oct)_2$), caprolactone (CL), pyrene, nile red,

horse-liver esterase and α-Chymotrypsin were acquired from Sigma Aldrich. Doxorubicin hydrochloride was purchased from Alfa Aesar. All the salts were purchased locally (Rankem). Wild-type mouse embryonic fibroblast cells (WT-MEF) and MCF 7 cells were maintained in DMEM (phenol red free medium: Gibco) containing 10 % (v/v) fetal bovine serum (FBS) and 1 % (v/v) penicillin–streptomycin at 37 °C under a 5 % CO_2 humidified atmosphere. Cells were trypsinised using 0.05 % trypsin (Gibco) and seeded in 96 well or 4-well live cell chamber (as per experiment) flat bottomed plastic plates (Eppendorf) for all assays. Tetrazolium salt, 3-(4, 5 dimethylthiazolyl)-2,5 diphenyltetrazolium bromide (MTT), DAPI and paraformaldehyde were obtained from Sigma Aldrich chemicals. Lysotracker Red DND-99 (1mM) was procured from Thermofischer Scientifc. Acetonitrile (ACN), methanol, hexane, dimethyl sulfoxide, diethyl ether and trifluoroacetic acid (TFA) solvents were are all HPLC grade.

3.2.2 Methods

Jeol 400 MHz spectrophotometer was used for recording NMR samples in $CDCl_3$, CD_3OD and $(CD_3)_2SO$ solvent using TMS as the standard. Gel Permeation Chromatography (GPC, also referred to as Size Exclusion Chromatography) data acquisition was carried out by a Viscotek VE 1122 pump, Viscotek VE 3580 RI, 3210 UV-Vis and Light scattering detectors. Samples for GPC were prepared in HPLC tetrahydrofuran (THF) and executed from method files obtained after calibration using polystyrene standards. The Perkin-Elmer thermal analyzer STA 6000 model was used to determine the polymer's thermal stability at 10 °/min heating rate under nitrogen atmosphere. Thermal properties of polymers were analyzed using a TA Q20 differential scanning calorimeter (DSC), wherein the polymers were first heated to melt in order to remove any pre-thermal history and then subsequent heating-cooling cycles were recorded at 10 °/min under inert conditions to generate the respective thermograms. Perkin-Elmer Lambda 45 UV-Visible Spectrophotometer was used for the absorption studies. Emission spectra for determining the Critical Micelle Concentration (CMC) and nile red encapsulation were recorded using a SPEX Fluorolog HORIBA JOBIN VYON fluorescence spectrophotometer. A 450 W Xe lamp serves as the source of excitation at room temperature. Pyrene was used as the fluorophore for CMC studies, which has excitation maxima at 337 nm. The emission spectrum gives five distinct vibronic levels, amongst which the intensity of levels I_1 and I_3 are known to be extremely sensitive of the hydrophobic environment. As a result, pyrene when encapsulated within a micelle will give different I_1 and I_3 values. The ratio of I_1/I_3

v/s polymer concentration is plotted in order to determine the critical aggregate concentration (CAC), which in the case of a unimolecular micelle gives a line with zero slope. Dynamic light scattering (DLS) was performed using Nano ZS-90 setup (Malvern instruments). DLS utilizes a 633 nm laser as the light source, and the detector collects the scattered light at 90° angle. This gives information about the correlation function [$g^2(t)$], from which the diffusion coefficient (D) is calculated using cumulant method and further the diameter of the particle is determined using the Stokes-Einstein equation. The experiment was performed thrice with independent amphiphilic solutions to yield reproducible data. SAXS was caried out on the Nanoviewer instrument (made in Rigaku, Japan) that is calibrated with silver behenate. It comprises of a rotating anode X-ray source Micromax 007 of 40 kV and 30 mA, HyPix 3000 photon-counting detector and an X-ray collimator system (3-pin hole with an evacuated beam path). FE-SEM analysis requires the sample to be drop casted on silicon wafer and the experiment was done on a Zeiss Ultra Plus scanning electron microscope. Polymer solutions were drop casted on mica plates for carrying out atomic force microscopic (AFM) analysis using Agilent instruments. HR-TEM samples were prepared by drop-casting the dialyzed polymer solutions on copper TEM grids and the images were recorded using Jeol JEM2200FS 200 KeV systems. Again the reproducibility of the data was confirmed using three independent polymer solutions. Confocal microscopic analysis was done using Leica SP8 microscope. The cell viability determination was done by measuring the absorbance of the formazan crystals on a microplate reader (Varioskan Flash).

3.2.3 Synthesis Procedures

Synthesis of S-Y Macroinitiator (MI): A specially designed melt reactor set up with an overhead stirrer and was employed in order to carry out ring opening polymerization over a multi-arm initiator (6-arm). The polymerization protocol of ε-caprolactone using dipentaerythritol as the initiator and tin (II) 2-Ethylhexanoate [$Sn(Oct)_2$] as the catalyst, which generates the active initiator *in situ*, has been explained here for the **S-60** MI. The degree of polymerization was varied by controlling the [Monomer]/[Initiator] ([M]/[I]) ratio. The catalyst equivalents were calculated such that for every equivalent of the initiator, three equivalents of the catalyst were fed to the reactor. Dipentaerythritol (37.2 mg, 0.1462 mmol) and the catalyst $Sn(Oct)_2$ (177.7 mg, 0.4386 mmol) were weighed in a flame dried tailor-made schlenk tube followed by addition of the caprolactone monomer (1.0 g, 8.7719 mmol). The schlenk tube was

evacuated under high vacuum (0.01 mbar) prior to the start of the polymerization for 45 mins. The polymerization reaction was continued at 110 °C under neat conditions for 8 h with constant overhead stirring set at 130 rpm. The polymer was dissolved in acetonitrile (HPLC) and precipitated in cold methanol. The precipitation was repeated thrice in order to obtain highly pure polymer. Yield = 0.85 g (85 %). ^{1}H NMR (400 MHz, $CDCl_3$) δ ppm: 4.05 (t, 2.00 H), 3.64 (t, 0.19 H), 3.38 (s, 0.06 H), 2.30 (t, 1.99 H), 1.64 (m, 4.04 H), 1.37 (m, 2.03 H). ^{13}C NMR (100 MHz, $CDCl_3$) δ ppm: 173.6, 64.2, 62.6, 34.1, 32.3, 28.3, 25.5, 24.6. FT-IR (cm^{-1}): 2953.57, 2869.63, 1728.41, 1644.79, 1459.08, 1418.07, 1392.87, 1366.46, 1277.23, 1235.36, 1187.44, 1162.94, 1065.67, 1037.24, 964.50, 927.11, 846.51, 743.08, 564.83, 520.43. SEC molecular weights: M_w = 12,000 g/mol, M_n = 10,000 g/mol, M_w/M_n = 1.2.

S-110 MI: Dipentaerythritol (18.6 mg, 0.0731 mmol), $Sn(Oct)_2$ (88.8 mg, 0.2193 mmol), caprolactone (1.0 g, 8.7719 mmol). The polymerization was carried out for 8 h at 110 °C. Yield = 0.75 g (75 %). ^{1}H NMR (400 MHz, $CDCl_3$) δ ppm: 4.05 (t, 2.00 H), 3.63 (t, 0.11 H), 3.38 (s, 0.04 H), 2.29 (t, 2.00 H), 1.64 (m, 4.00 H), 1.37 (m, 2.00 H). ^{13}C NMR (100 MHz, $CDCl_3$) δ ppm: 173.6, 64.2, 62.7, 34.2, 32.4, 28.4, 25.6, 24.6. FT-IR (cm^{-1}): 2952.19, 2868.82, 1728.69, 1459.78, 1418.77, 1391.53, 1363.48, 1275.02, 1234.41, 1162.74, 1066.93, 1039.11, 965.35, 929.70, 847.71, 740.46, 561.76, 514.61. SEC molecular weights: M_w = 20,200 g/mol, M_n = 16,700 g/mol, M_w/M_n = 1.2.

S-35 MI: Dipentaerythritol (74.4 mg, 0.292 mmol), $Sn(Oct)_2$ (355.4 mg, 0.8772 mmol), caprolactone (1.0 g, 8.7719 mmol). The polymerization was carried out for 6 h at 110 °C. Yield = 0.7 g (70 %). ^{1}H NMR (400 MHz, $CDCl_3$) δ ppm: 4.05 (t, 2.00 H), 3.63 (t, 0.34 H), 3.36 (s, 0.11 H), 2.30 (t, 1.98 H), 1.64 (m, 3.99 H), 1.37 (m, 2.00 H). ^{13}C NMR (100 MHz, $CDCl_3$) δ ppm: 173.7, 64.2, 62.7, 34.2, 32.4, 28.4, 25.6, 24.6. FT-IR (cm^{-1}): 2952.36, 2868.90, 1728.53, 1459.75, 1419.32, 1363.71, 1233.85, 1161.63, 1066.32, 1039.20, 965.21, 929.68, 847.76, 740.19, 564.54, 514.34. SEC molecular weights: M_w = 9,000 g/mol, M_n = 6,900 g/mol, M_w/M_n = 1.3.

L-60 MI: Triethyleneglycol monomethylether (23 mg, 0.14 mmol), $Sn(Oct)_2$ (28.4 mg, 0.0701 mmol), caprolactone (1.12 g, 9.8245 mmol). The polymerization was carried out for 8 h at 110 °C. Yield = 0.80 g (71 %). ^{1}H NMR (400 MHz, $CDCl_3$) δ ppm: 4.05 (t, 2.00 H), 3.65 (t, 0.20 H), 3.37 (s, 0.05 H), 2.30 (t, 2.00 H), 1.64 (m, 4.08 H), 1.37 (m, 2.03 H). ^{13}C NMR (100 MHz,

$CDCl_3$) δ ppm: 173.6, 64.2, 62.7, 34.2, 28.4, 25.6, 24.6. FT-IR (cm^{-1}): 2952.99, 2869.31, 1728.64, 1459.65, 1419.16, 1364.04, 1275.63, 1234.61, 1162.68, 1066.55, 1038.73, 964.93, 929.28, 847.53, 741.08, 561.14, 516.07. SEC molecular weights: M_w = 10,200 g/mol, M_n = 6,600 g/mol, M_w/M_n = 1.5.

Synthesis of star-shaped block copolymers SB-X: The typical synthetic protocol for the block copolymer has been outlined here for **SB-60**. The purified **S-60** polymer served as the macro-initiator for polymerization of tertiary butyl ester substituted caprolactone monomer (BPCL). The melt reactor was charged with the S-60 MI (307.5 mg, 0.0419 mmol) and $Sn(Oct)_2$ (51.03 mg, 0.126 mmol) in a 1:3 ratio followed by the addition of the BPCL monomer (650 mg, 2.5194 mmol). The schlenk tube was evacuated under high vacuum (0.01 mbar) prior to the start of the polymerization for 45 mins and the reaction was continued for 12 h at 130 °C with constant overhead stirring set at 130 rpm. The polymer was dissolved in minimum amount of acetonitrile and precipitated in cold 20% hexane/diethyl ether. This precipitation was repeated thrice in order to obtain polymer in high purity. Yield = 0.6 g (63 %). ^{1}H NMR (400 MHz, $CDCl_3$) δ ppm: 4.12 (m, 2.00 H), 4.05 (t, 2.00 H), 3.64 (m, 2.19 H), 3.43 (m, 0.97 H), 3.38 (s, 0.06 H), 2.43 (t, 2.00 H), 2.36 (t, 2.01 H), 2.29 (t, 2.01 H), 1.84 (m, 1.98 H), 1.77 (m, 1.98 H), 1.64 (m, 4.00 H), 1.44 (s, 8.45 H), 1.37 (m, 2.03 H). ^{13}C NMR (100 MHz, $CDCl_3$) δ ppm: 173.6, 173.5, 170.9, 80.6, 75.5, 64.8, 64.2, 61.2, 36.5, 36.3, 34.1, 32.9, 29.7, 28.9, 28.3, 28.1, 25.5, 24.6. FT-IR (cm^{-1}): 2954.68, 1727.50, 1457.89, 1418.25, 1392.41, 1366.87, 1254.04, 1158.22, 1102.28, 1064.60, 964.60, 928.40, 845.68, 752.09, 559.84, 512.86. SEC molecular weights: M_w = 42,000 g/mol, M_n = 30,200 g/mol, M_w/M_n = 1.4.

SB-100 block copolymer: S-110 MI (309.9 mg, 0.0242 mmol), $Sn(Oct)_2$ (29.4 mg, 0.0726 mmol), BPCL monomer (750 mg, 2.9069 mmol). The polymerization was carried out for 12 h at 130 °C. Yield = 0.7 g (66 %). ^{1}H NMR (400 MHz, $CDCl_3$) δ ppm: 4.12 (m, 1.86 H), 4.05 (t, 2.00 H), 3.64 (m, 1.96 H), 3.43 (m, 0.93 H), 3.38 (s, 0.04 H), 2.43 (t, 1.84 H), 2.36 (t, 1.91 H), 2.30 (t, 2.00 H), 1.85 (m, 1.90 H), 1.77 (m, 1.90 H), 1.64 (m, 4.00 H), 1.44 (s, 8.75 H), 1.37 (m, 2.02 H). ^{13}C NMR (100 MHz, $CDCl_3$) δ ppm: 173.7, 173.6, 170.9, 80.7, 75.5, 64.9, 64.2, 61.3, 36.5, 36.4, 34.2, 33.0, 29.8, 29.0, 28.4, 28.2, 25.6, 24.6. FT-IR (cm^{-1}): 2955.32, 1726.52, 1457.53, 1366.52, 1253.48, 1159.15, 1101.68, 1064.58, 964.63, 929.05, 845.47, 752.03, 554.74, 515.39. SEC molecular weights: M_w = 60,200 g/mol, M_n = 44,800 g/mol, M_w/M_n = 1.3.

SB-35 block copolymer: S-35 MI (281.9 mg, 0.0664 mmol), $Sn(Oct)_2$ (80.8 mg, 0.1993 mmol), BPCL monomer (600 mg, 2.3256 mmol). The polymerization was carried out for 12 h at 130 °C. Yield = 0.55 g (62 %). ^{1}H NMR (400 MHz, $CDCl_3$) δ ppm: 4.13 (m, 2.01 H), 4.05 (t, 2.00 H), 3.65 (m, 2.34 H), 3.43 (m, 0.99 H), 3.37 (s, 0.11 H), 2.43 (t, 2.02 H), 2.37 (t, 1.99 H), 2.30 (t, 1.98 H), 1.85 (m, 2.06 H), 1.78 (m, 2.00 H), 1.64 (m, 4.06 H), 1.44 (s, 9.02 H), 1.37 (m, 2.04 H). ^{13}C NMR (100 MHz, $CDCl_3$) δ ppm: 173.6, 173.5, 170.9, 80.7, 75.5, 64.9, 64.2, 61.3, 36.5, 36.4, 34.2, 33.0, 29.8, 29.0, 28.4, 28.2, 25.6, 24.6. FT-IR (cm^{-1}): 2955.84, 2926.20, 1727.04, 1458.18, 1366.74, 1253.88, 1159.58, 1101.96, 1064.45, 963.83, 928.45, 845.80, 751.71, 565.11, 517.31. SEC molecular weights: M_w = 43,300 g/mol, M_n = 20,900 g/mol, M_w/M_n = 2.1.

LB-60 block copolymer: L-60 MI (294.1 mg, 0.0419 mmol), $Sn(Oct)_2$ (8.5 mg, 0.0209 mmol), BPCL monomer (650 mg, 2.5194 mmol). The polymerization was carried out for 12 h at 130 °C. Yield = 0.65 g (69 %). ^{1}H NMR (400 MHz, $CDCl_3$) δ ppm: 4.13 (m, 1.67 H), 4.05 (t, 2.00 H), 3.65 (m, 1.87 H), 3.44 (m, 0.80 H), 3.38 (s, 0.05 H), 2.43 (t, 1.67 H), 2.37 (t, 1.64 H), 2.30 (t, 2.06 H), 1.85 (m, 1.75 H), 1.78 (m, 1.75 H), 1.64 (m, 4.06 H), 1.44 (s, 7.49 H), 1.37 (m, 2.02 H). ^{13}C NMR (100 MHz, $CDCl_3$) δ ppm: 173.6, 173.5, 170.9, 80.6, 75.5, 64.8, 64.2, 61.2, 36.5, 34.1, 32.9, 29.7, 28.9, 28.4, 28.1, 25.5, 24.6. FT-IR (cm^{-1}): 2955.55, 2923.18, 1727.32, 1644.59, 1457.86, 1418.50, 1367.34, 1280.78, 1254.76, 1161.16, 1065.58, 965.05, 928.19, 845.62, 749.67, 563.10. SEC molecular weights: M_w = 21,100 g/mol, M_n = 12,700 g/mol, M_w/M_n = 1.7.

Synthesis of the carboxylic acid substituted star-block copolymers SB-X: Deprotection of the tertiary butyl group in the polymer SB-60 (214 mg) was carried out using trifluoroacetic acid (TFA) at 0 °C for 30 min. TFA (2.0 mL) was added slowly along the sides of the round bottom flask containing the polymer solution (in DCM) and the reaction was continued at 0 °C for 30 min with constant stirring. TFA was removed by repeated washings with DCM and then the polymer was dissolved in DCM followed by precipitation in cold 20% hexane/diethyl ether. The solution was vortexed at 1000 rpm and then the supernatant solution was decanted. This procedure was repeated thrice in order to ensure the complete removal of TFA. Yield = 150 mg (82 %). ^{1}H NMR (400 MHz, $(CD_3)_2SO$) δ ppm: 4.03 (m, 2.01 H), 3.98 (t, 2.00 H), 3.55 (m, 2.18 H), 2.39 (t, 2.01 H), 2.31 (t, 1.97 H), 2.27 (t, 2.01 H), 1.70 (m, 3.99 H), 1.54 (m, 4.06 H), 1.29 (m, 2.02 H). ^{13}C NMR (100 MHz, $(CD_3)_2SO$) δ ppm: 173.3, 173.1, 75.3, 64.7, 63.9, 61.2,

35.4, 33.8, 32.8, 29.7, 29.1, 28.3, 25.3, 24.5. FT-IR (cm^{-1}): 2253.15, 2126.47, 1727.73, 1657.83, 1550.29, 1226.44, 1048.82, 1023.57, 1000.01, 822.81, 760.38, 617.53, 512.85.

SB-100 block copolymer: SB-100 butyl ester substituted polymer (150 mg), TFA (1.5 mL). Yield = 100 mg (78 %). ^{1}H NMR (400 MHz, CD_3OD) δ ppm: 4.15 (m, 1.86 H), 4.06 (t, 2.00 H), 3.69 (m, 1.96 H), 3.49 (m, 0.92 H), 2.50 (t, 1.87 H), 2.40 (t, 1.83 H), 2.32 (t, 2.02 H), 1.86 (m, 1.83 H), 1.79 (m, 1.84 H), 1.63 (m, 4.02 H), 1.38 (m, 2.03 H). ^{13}C NMR (100 MHz, CD_3OD) δ ppm: 173.6, 173.5, 75.5, 64.9, 64.2, 61.3, 35.4, 33.9, 33.0, 29.7, 29.0, 28.3, 25.6, 24.6. FT-IR (cm^{-1}): 2251.29, 2124.31, 1726.87, 1656.91, 1514.46, 1050.43, 1024.08, 1002.39, 821.67, 758.95, 617.52.

SB-35 block copolymer: SB-35 butyl ester substituted polymer (105 mg), TFA (1.0 mL). Yield = 60 mg (67 %). ^{1}H NMR (400 MHz, $(CD_3)_2SO$) δ ppm: 4.04 (m, 2.00 H), 3.98 (t, 2.00 H), 3.56 (m, 2.36 H), 2.39 (t, 2.06 H), 2.32 (t, 2.07 H), 2.27 (t, 2.04 H), 1.69 (m, 4.01 H), 1.54 (m, 4.01 H), 1.29 (m, 1.98 H). ^{13}C NMR (100 MHz, $(CD_3)_2SO$) δ ppm: 173.4, 173.2, 75.5, 64.7, 64.0, 61.1, 35.4, 33.8, 32.8, 29.7, 29.1, 28.3, 25.3, 24.5. FT-IR (cm^{-1}): 2251.24, 2124.63, 1725.97, 1657.18, 1514.26, 1201.78, 1050.55, 1023.98, 1002.54, 821.61, 758.84, 618.29.

LB-60 block copolymer: LB-60 butyl ester substituted polymer (220 mg), TFA (2.0 mL). Yield = 130 mg (70 %). ^{1}H NMR (400 MHz, $(CD_3)_2SO$) δ ppm: 4.04 (m, 1.68 H), 3.98 (t, 2.00 H), 3.56 (m, 1.87 H), 2.39 (t, 1.74 H), 2.32 (t, 1.65 H), 2.26 (t, 2.03 H), 1.69 (m, 3.38 H), 1.52 (m, 3.99 H), 1.28 (m, 2.02 H). ^{13}C NMR (100 MHz, $(CD_3)_2SO$) δ ppm: 173.4, 173.2, 75.3, 64.7, 63.9, 61.2, 35.4, 33.8, 32.8, 29.7, 29.1, 28.3, 25.3, 24.5. FT-IR (cm^{-1}): 2253.01, 2126.38, 1656.71, 1515.18, 1049.08, 1023.53, 1000.23, 822.67, 760.13, 616.11, 520.82.

3.2.4 Self-assembly of copolymers

The polymer **SB-60** (0.5 mg) was dissolved in 0.8 mL DMSO and this solution was then added dropwise to 4.2 mL milli-Q water with constant stirring for 4 h at 25 °C. The solution was then transferred to a semi-permeable membrane of MWCO = 3.5 kD and dialyzed against milli-Q water for 24 h. The water was replenished at regular intervals in order to substantiate the removal of DMSO. Similar protocol for self-assembly was adapted for all the carboxylic acid substituted star and linear block copolymers.

3.2.5 Photophysical studies

The self-assembled star and linear block copolymer micelles were subjected to the critical micelle concentration (CMC) study using pyrene as the probe employing fluorescence spectroscopy. Herein, a pyrene stock was prepared in acetone (HPLC) and 1 mL of this stock was added to each sample vial such that the final pyrene concentration turned out to 0.6 µM (for 3 mL of the sample). The solvent was evaporated completely followed by addition of different concentrations of polymer dialyzed solutions ranging from 10^{-6} mg/mL to 0.5 mg/mL maintaining the overall volume to 3ml. These sample vials were then sonicated for 3 h followed by equilibration at room temperature for 12 h. Prior to acquiring the samples, all the vials were purged with nitrogen in order to eliminate all the dissolved oxygen. The fluorescence measurements were carried out by exciting the pyrene molecule at 337 nm and the emission was collected at 347-500 nm. The I_1 and I_3 vibronic levels were monitored and these values helped determine the CMC for all the dialyzed solutions.

3.2.6 Drug Encapsulation in the Copolymer Scaffolds

Typical encapsulation procedure is given for the star-block polymer. **SB-60** (0.5 mg) and DOX (0.2 mg, DOX.HCl pre-treated with triethylamine) were dissolved in 0.8 mL DMSO followed by dropwise addition of the cocktail to 4.2 mL water with continuous stirring for 4 h. The dialysis was carried out in a dialysis tube of MWCO = 3.5 kD against large amount of milli-Q water for 48 h. At regular intervals the water was changed in order to facilitate the removal of un-encapsulated DOX and DMSO.

The drug loading efficiency (DLE) and drug loading content (DLC) were determined by UV-Visible spectroscopy using the following equations:

DLE (%) = {weight of drug in micelles/weight of drug in feed} X 100%

DLC (%) = {weight of drug in micelles/weight of drug-loaded nanoparticles} X 100%

3.2.7 *In vitro* DOX Release kinetics

The star-block copolymers comprise of a complete polyester backbone that is known to cleave in the presence of enzymes in the lysosomal compartment rendering these nano-assemblies enzyme-responsive. This investigation was carried out by incubating SB-60+DOX nano-assemblies with two lysosomal enzymes, i.e. horse-liver esterase (10U) and α-Chymotrypsin (8U). The enzyme containing DOX solutions were taken in a dialysis tube of MWCO = 1kD

and this tube was then immersed in 4 ml of 1X PBS (pH = 7.4) maintained at 37 °C with constant stirring. In another control setup, the dialyzed solution was taken alone in the tube and exposed to pH = 7.4 (1X PBS) at 37 °C. The nanoparticle degradation was monitored in terms of the amount of DOX released from the tube into the outside 1X PBS solution and these values were determined using absorbance spectroscopy at various time points up to 48 h. Comparing these values with the amount of DOX inside the dialysis tube at time t = 0 h, resulted in the cumulative drug release values.

Cumulative release (%) = $C_n \times V_0/m \times 100$

where C_n represents the amount of DOX in the n^{th} sample, V_0 is the total volume of 1X PBS in the container, and m is the total amount of DOX loaded in nanoparticles taken inside the dialysis tube.

3.2.8 Cell Viability Assay (MTT Assay)

The biocompatibility of the star and linear block copolymers along with their DOX loaded nano-formulations was investigated via the cell viability assay in wild type mouse embryonic fibroblast cell lines (WT-MEF) employing the tetrazolium salt, 3-(4,5 dimethylthiazolyl)-2,5-diphenyl tetrazolium bromide (MTT). In a typical experiment, 10^3 cells were seeded in each well of a 96-well plate (Eppendorf) in 100 µL of complete DMEM containing 1 % penicillin streptomycin and 10 % FBS (fetal bovine serum). The cells were incubated at 37 °C in a 5 % CO_2 humidified atmosphere for 16 h allowing the cells to adhere following which media aspiration was carried out from each well. The desired concentrations of the nascent polymers, free DOX and the DOX loaded nano-scaffolds were then added to each of the wells for the cell treatment and all of these were done in triplicates. For each of these experiments, there was a control without any compound containing only the complete DMEM and the cells were then incubated at conditions mentioned before for 72 h. At the end of the incubation, the compound containing media was replaced with a freshly prepared MTT solution (0.5 mg/mL) in complete DMEM followed by 4 h incubation at 37 °C, 5% CO_2. The mitochondrial dehydrogenase enzyme present in the viable cells reduces the tetrazolium salt into formazan crystals, whose purple colour gives the read out for number of viable cells. At the end of 4 h, the MTT containing media was aspirated and the purple formazan crystals were dissolved in 100 µL DMSO; the plate was then subjected to absorbance measurements at 570 nm using the

Varioskan flash microplate reader. The absorbance values from the sample treated wells were compared with the control wells considering the control value to be 100 % and thus, the cell viability % was determined for all the samples as mean ± SEM.

3.2.9 Monitoring Cellular Uptake of DOX-loaded Polymeric Nanocarriers by Live cell experiment

The cellular uptake of free DOX, SBC-60+DOX and LBC-60+DOX was monitored with the aim of understanding the uptake mechanism and kinetics. To this effect, live cell experiment was devised with Lysotracker staining (stains the lysosomal compartment) in a time-dependent manner in WT-MEF cells. The 4-well live cell chamber plates were seeded with 25,000 cells per well in 1 mL of complete DMEM containing 10 % FBS and 1 % antibiotic followed by incubation at 5 % CO_2 at a temperature of 37 °C for 16 h. The requisite concentrations of free DOX and DOX loaded polymeric micelles (DOX concentration = 5 μg/ml) were added to separate wells and then incubated for two time points, i.e. 90 min and 180 min. At the end of the time point, the compound containing media was removed followed by addition of 50 nM lysotracker red DND-99 solution in DMEM and these were then imaged within 10 min using Leica SP8 while being incubated in a chamber maintained at 37 °C and 5 % CO_2 humidified atmosphere. For the time scan experiment, the compounds were added to individual wells just before the start of microscopy with the lysotracker solution (50 nM) and imaged using similar settings as used for the other time points in the same chamber. The confocal imaging was done on a Leica SP8 system with a sequential scan setting using the lasers λ = 488 nm for DOX excitation and λ = 561 nm for excitation of the lysotracker red dye followed by the imaging analysis done using Fiji software.

3.3 Results and Discussion

3.3.1 Synthesis and structural characterization of PCL based Star architecture block copolymers

The synthesis of the star and linear block polycaprolactone (PCL) copolymers is outlined in scheme 3.1. Solvent-free ring opening polymerization (ROP) was employed as the tool to synthesize high molecular weight polymers with narrow polydispersity in melt (under neat conditions). This was attainable owing to the in-house specially designed melt reactor with an overhead stirrer, essential for the polymerization of star-shaped or other higher order architectures (see figure 3.5). In the regular schlenk tube set-up, the extensive viscosity build-up in higher order structures deters the polymerization process and results in low molecular weight polymer with high polydispersity. The melt reactor was able to overcome this hurdle because of the overhead stirrer that maintains constant stirring throughout the polymerization, irrespective of the viscosity build-up resulting in high molecular weight star-shaped polymers with narrow polydispersity. Star-block copolymers were constituted with simple PCL core and ɣ-tert butyl ester substituted PCL segments at the periphery as shown in scheme 3.1a.

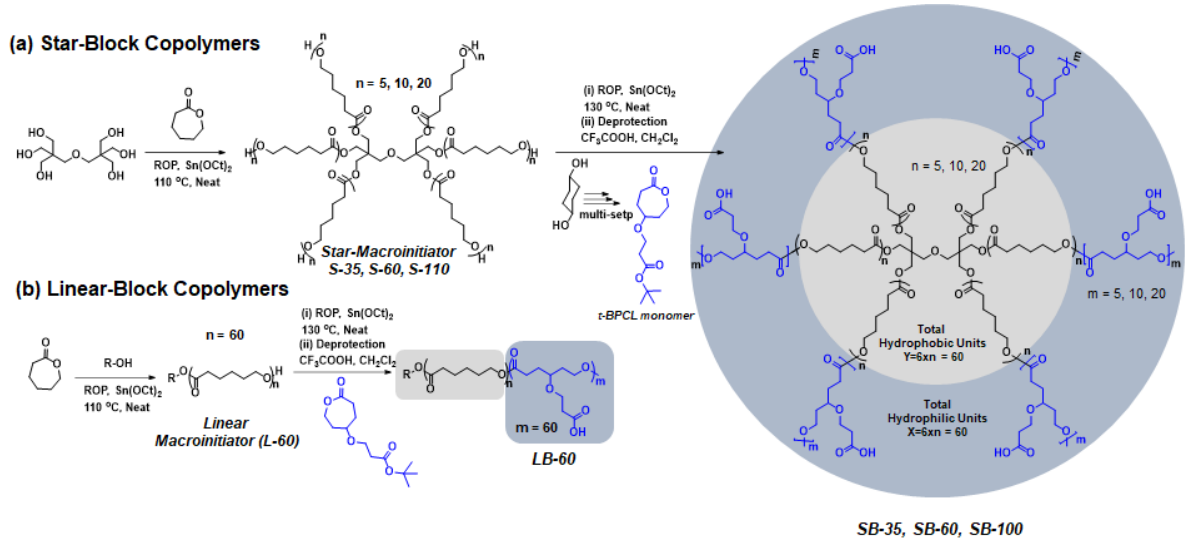

Scheme 3.1. *Synthetic scheme of ring opening polymerization of ε-caprolactone and ɣ-substituted tert-butyl caprolactone monomers to yield star (a) and linear block copolymers (b).*

Upon post polymerization de-protection, the ester was converted into carboxylic acid functionality; thus, imparting the required amphiphilic balance having hydrophobic core and hydrophilic shell in star-block architectures. Star-block copolymers were synthesized in a sequential ROP process in which initial polymerization of ε-caprolactone (CL) yielded six-arm macroinitiator (MI). A 6-arm dipentaerythritol was chosen as the initiator and tin (II) 2-ethylhexanoate ($Sn(Oct)_2$) was employed as the catalyst wherein the initiator to catalyst ratio was maintained as 1:3 in order to generate the active initiator *in situ*. The CL monomer to dipentaerythritol ratio was taken to be, [M]/[I] = 60 in order to afford 6-arm star-shaped polycaprolactone with statistically 10 CL units per arm. It was then employed for the ROP of t-butyl ester substituted caprolactone monomer (t-BPCL monomer), designed following the procedure reported in chapter 2. The macroinitiator was used to ring open the t-BCL monomer such that the feed [M]/[MI] was taken to be 60 and $Sn(Oct)_2$ was the catalyst (as can be seen in scheme 3.1a). A linear block copolymer was also synthesized by ROP process wherein triethyleneglycol monomethyl ether (TEG) was used as the initiator (see scheme 3.1b). This linear PCL macroinitiator was used for the ROP of t-BCL monomer to yield linear block copolymer (see scheme 3.1b). Two more star block copolymers were also synthesized having 30/30 and 120/120 units in the feed for PCL and t-butyl ester PCL and the details are shown in scheme 3.1a. Our attempts to make higher analogue of the star-blocks with total 180/180 units was not successful due to very high viscosity in the reactor and inhomogeneity in the chain formation. The star (S) and linear (L) macroinitiator are referred to as S-Y and L-Y (Y = number of PCL units); the t-butyl ester functionalized star block (SB) and linear block (LB) copolymers are referred to as SB-X and LB-X respectively (B = t-butyl ester group) where "X" refers to the number of repeating units in the carboxylic PCL part.

Figure 3.5. *Representative image of the in-house specially designed melt reactor set-up with an overhead stirrer and thermocouple*

The structural characterization of the star-macroinitiators and star-block copolymers was carried out using ^{1}H-NMR as can be seen in figures 3.6 to 3.8. In order to determine the degree of polymerization (X_n), the integration of the peak intensities from the initiator were compared to those of the polymer backbone in ^{1}H-NMR. As can be seen in lowest panel of figure 3.6 corresponding to the S-60 macroinitiator, the dipentaerythritol initiator peaks appeared at 3.64 ppm corresponding to the 12 protons adjacent to the ester and at 3.39 ppm for the 4 ether protons. The newly formed ester peaks in the polycaprolactone part were found to appear at 4.06 ppm and 2.30 ppm. The initiator peak at 3.64 ppm was chosen as the reference peak and given an integration of 12, corresponding to which the integration of the PCL part at 4.06 ppm was determined and hence, comparing the intensities of the aforementioned peaks gave the incorporated degree of polymerization (X_n). For feed [M]/[I] = 60 in the star

macroinitiator: the actual incorporation as determined from the ^{1}H-NMR was 64 ± 3 repeating units confirming the statistical distribution of 10-11 units per arm.

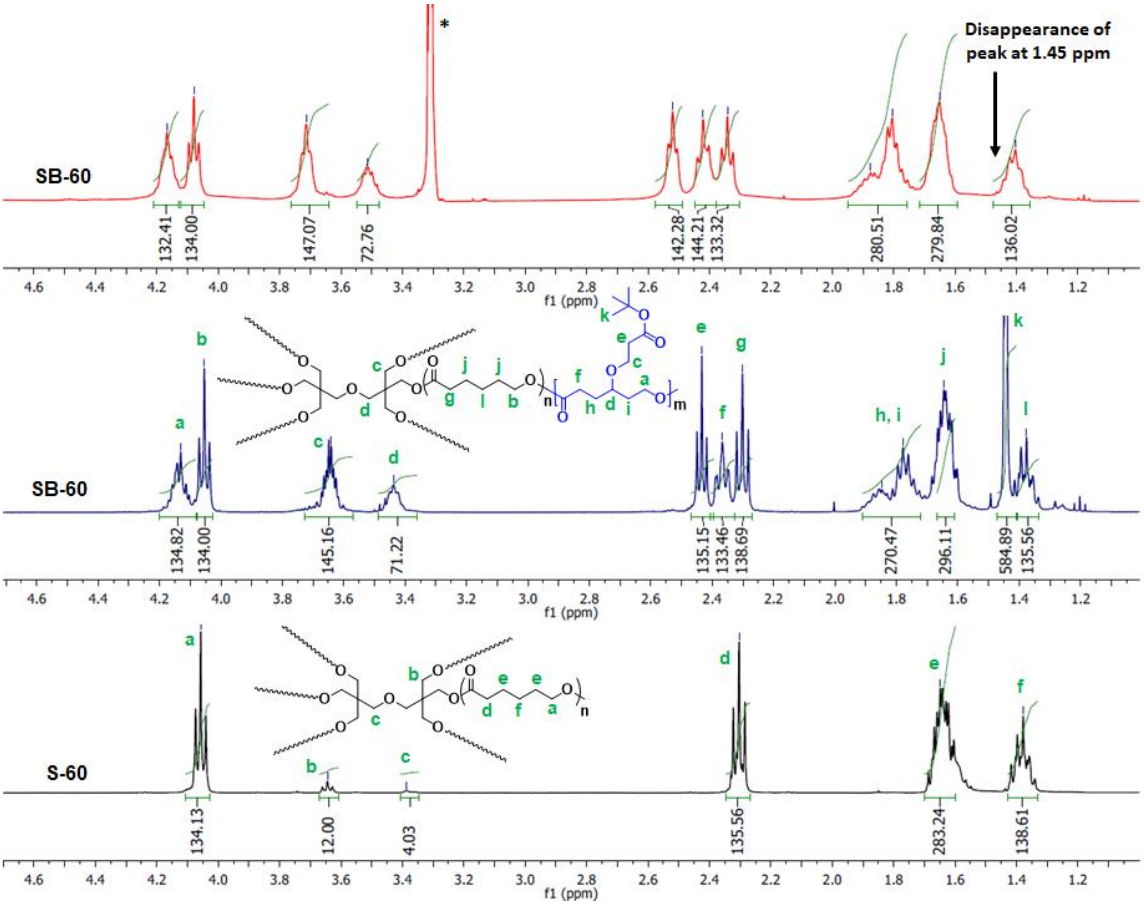

Figure 3.6. *^{1}H NMR stack plot of S-60, SB-60 and carboxylic substituted SB-60 in $CDCl_3$ and CD_3OD. The spectra are plotted up to 4.70 ppm for simplicity.*

.

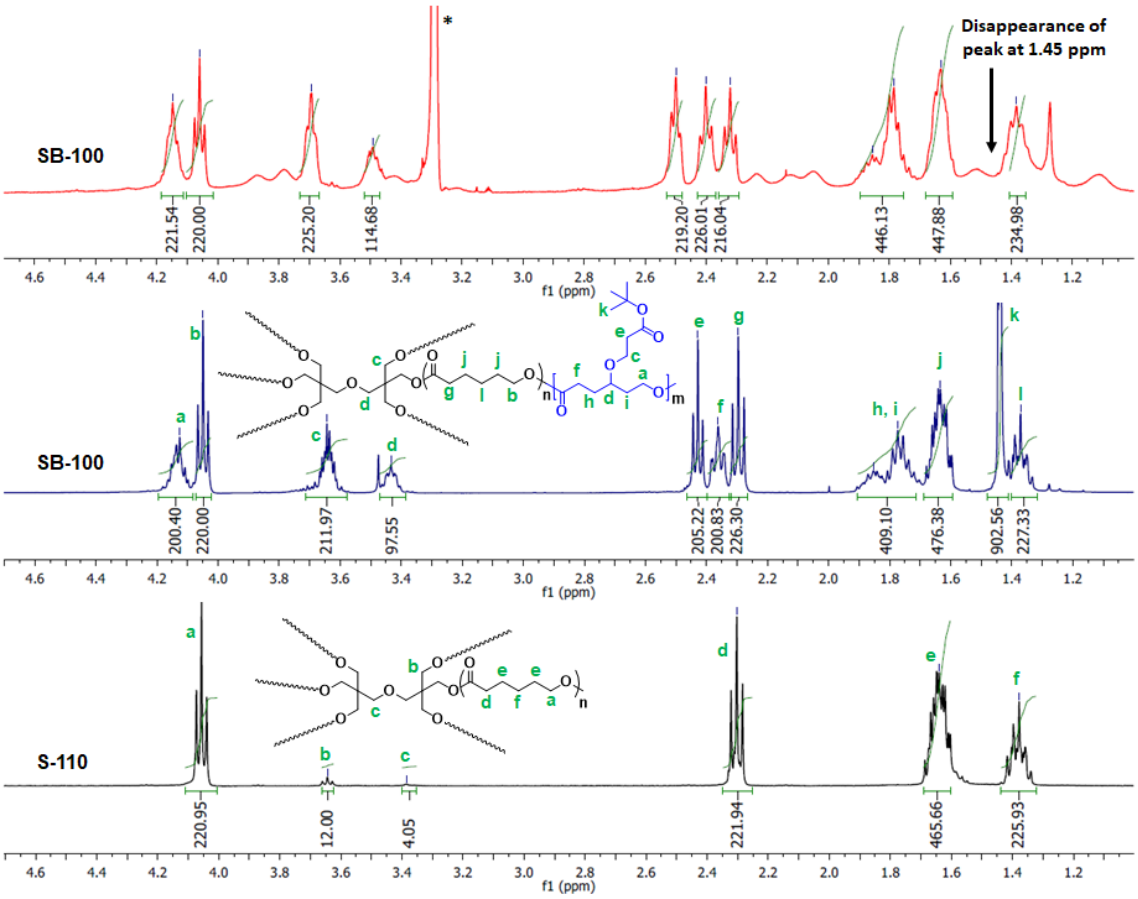

Figure 3.7. *^{1}H NMR stack plot of S-110, SB-100 and carboxylic substituted SB-100 in $CDCl_3$ and CD_3OD. The spectra are plotted up to 4.70 ppm for simplicity.*

To estimate the degree of polymerization in star-block copolymer; the appearance of new peak corresponding to t-butyl ester PCL was compared with macroinitiator PCL units. In case of the polymer SB-60 (second panel in figure 3.6), additional peaks corresponding to the BPCL part were seen when compared to the S-60 NMR, wherein the new ester peaks appeared at 4.13 ppm and 2.37 ppm reiterating the formation of the star-block copolymer. Since the S-60 macroinitiator was employed to yield the star-block copolymer, hence comparing the intensities of the two ester peaks at 4.06 ppm (PCL part) and 4.13 ppm (BPCL part) gave us the number of repeating units for the BPCL unit. The number average degree of polymerization (X_n) for the t-butyl ester PCL block was estimated to be 64 ± 3 (for feed [M]/[MI] = 60) indicating the formation of average 10-11 substituted PCL units per arm. Similarly, ^{1}H-NMR analysis of other star macroinitiators and block copolymers were carried out and the details are

shown in figures 3.7 and 3.8. The star block copolymers were then subjected to hydrolysis using trifluoroacetic acid to result in the deprotection of the tertiary butyl group and formation of carboxylic acid substituted amphiphilic star block copolymers. These carboxylic acid derivatives were characterized using ^{1}H-NMR that was used to confirm the deprotection by the complete disappearance of the tertiary butyl group peak at 1.45 ppm without any alterations in the structural integrity of the polymer (see third panel in the figures 3.6 to 3.8).

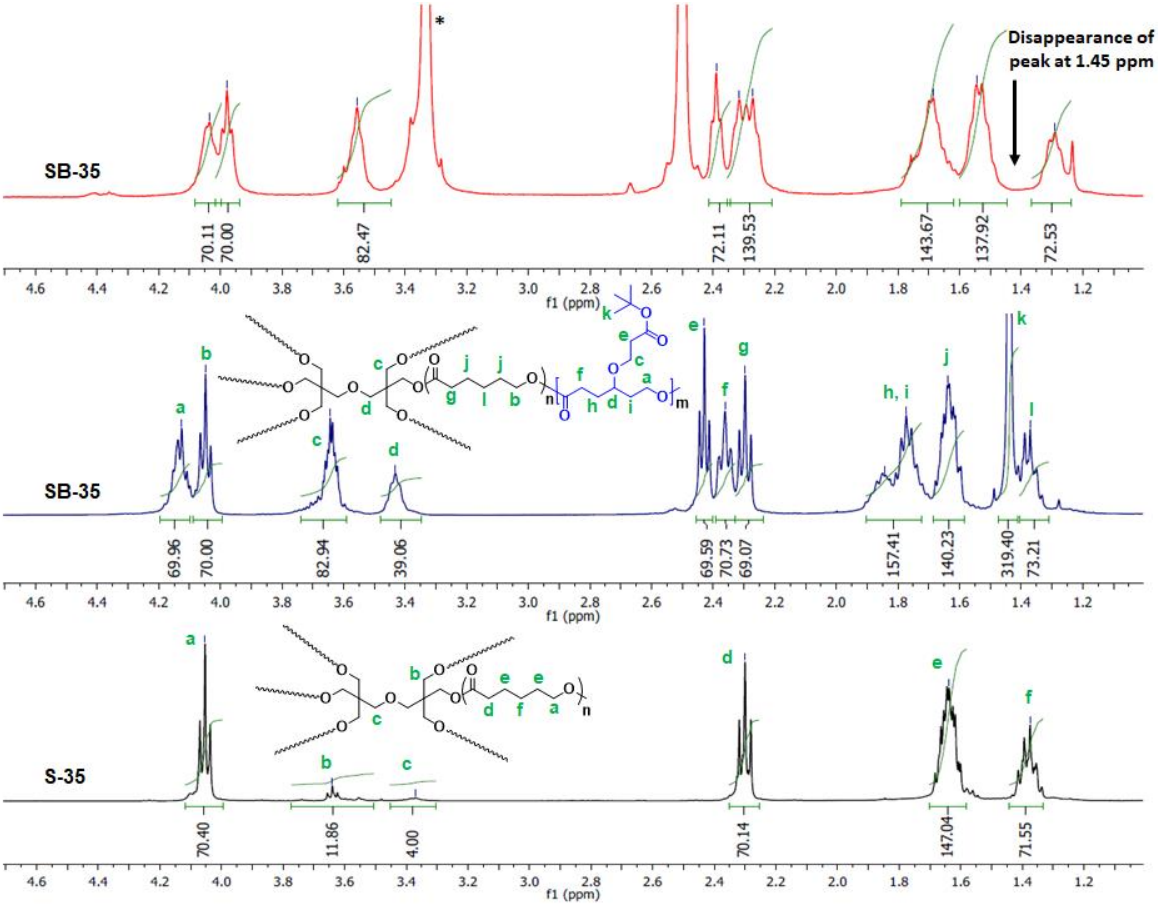

Figure 3.8. *^{1}H NMR stack plot of S-35, SB-35 and carboxylic substituted SB-35 in $CDCl_3$ and $(CD_3)_2SO$. The spectra are plotted up to 4.70 ppm for simplicity.*

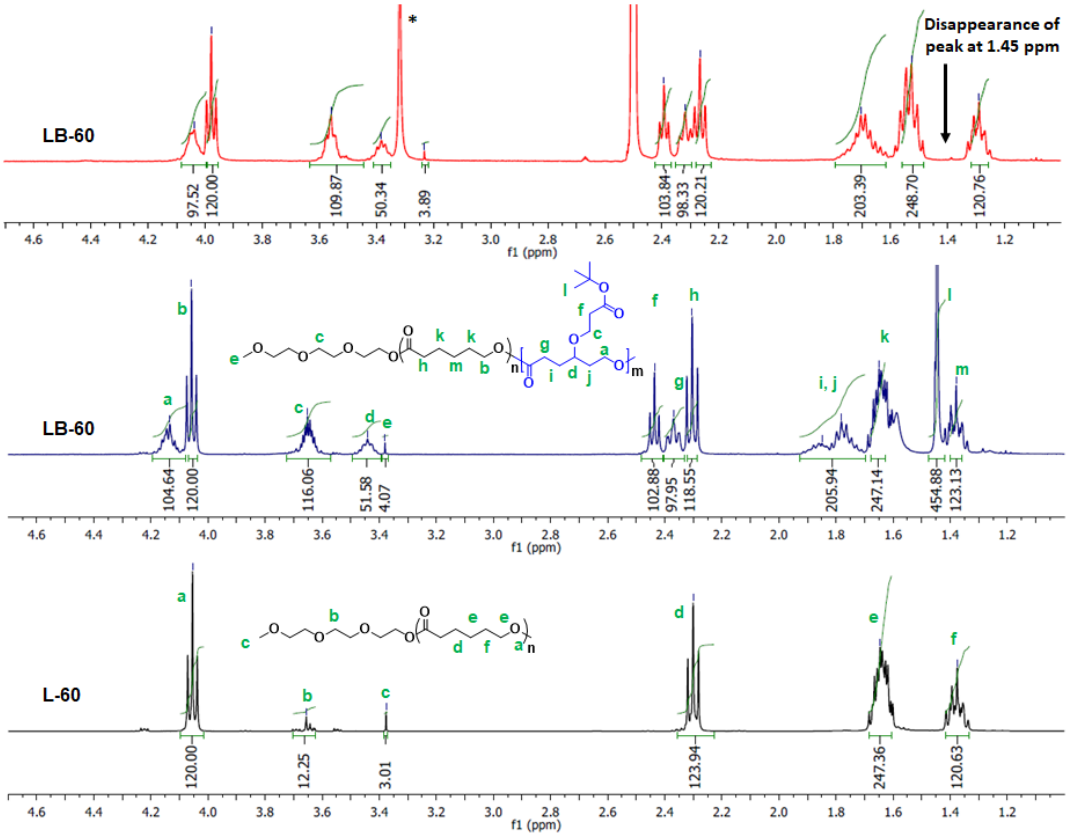

Figure 3.9. *^{1}H NMR stack plot of the L-60, LB-60 and carboxylic substituted LB-60 in $CDCl_3$ and $(CD_3)_2SO$. The spectra are plotted up to 4.70 ppm for simplicity.*

In case of the linear macroinitiator L-60, the peak corresponding to the TEG part at 3.63 ppm was compared to the ester peak of PCL unit at 4.06 ppm in order to give the $X_n = 60 \pm 2$. Similarly the X_n for the linear block copolymer was determined by comparing the intensities of the ester peak in the PCL unit at 4.06 ppm to the new ester peak at 4.13 ppm corresponding to the BPCL part (see the ^{1}H-NMR spectra of L-60 (first panel) and LB-60 (second panel) in figure 3.9). The linear block copolymer was deprotected following the same protocol as mentioned before for the star block copolymers and the formation of carboxylic acid substituted linear block was confirmed by the vanishing of the peak at 1.45 ppm (see third panel in figure 3.9). The number average molecular weight of all these polymers was determined using the formula, $M_n = X_n \times M_o$ (where M_o represents the mass of each repeating unit) and these values have been tabulated in table 3.1.

Molecular Weights

Sample	M/I ratio (Feed) PCL Arm	M/I ratio (Feed) SPCL Arm	n (^{1}H NMR)	M_n (^{1}H NMR) (g/mol)	M_n (GPC) (g/mol)	M_w (GPC) (g/mol)	PDI
S-35	5 (x6 arms)	-	35 ± 2	4200	6900	9000	1.3
S-60	10 (x6 arms)	-	64 ± 3	7900	10000	12000	1.2
S-110	20 (x6 arms)	-	105 ± 5	12800	16700	20200	1.2
L-60	60 (1 arm)	-	60 ± 2	7000	6600	10200	1.5
SB-35	Initiator S-35	5 (x6 arms)	35 ± 2	13200	20900	43300	2.1
SB-60	Initiator S-60	10 (x6 arms)	64 ± 3	25200	30200	42000	1.4
SB-100	Initiator S-110	20 (x6 arms)	95 ± 5	38600	44800	60200	1.3
LB-60	Initiator L-60	60	50 ± 5	19900	12700	21100	1.7

[a]Monomer/Initiator feed ratio was maintained for each arm. [b]Expected molecular weights were calculated based on feed ratio in the ROP. [c]Degree of polymerization (n) and molecuclar weights were estimated by ^{1}H-NMR analysis. [d]Molecular weights were determined by GPC in THF solvent using polystyrene standards for calibration.

Table 3.1. *Molecular weights of the polymers obtained from ^{1}H NMR and SEC are given in the table.*

Size exclusion chromatography (SEC) was employed to determine the molecular weights, polydispersity and purity of the polymers. The SEC chromatograms gave us the number-average (M_n) and weight-average molecular weight (M_w) along with the polydispersity (PDI) of the polymers, all of which have been summarized in the table 3.1. There was a significant shift in the retention time of the star and linear block copolymers compared to their respective macroinitiators (for all the SEC chromatograms see figure 3.10) depicting a clear increase in molecular weight for the block copolymers. All the polymers exhibited a monomodal distribution with narrow polydispersity (PDI) reinstating the purity of the polymers and the presence of chains with statistically similar number of repeating units. The n and M_n values from ^{1}H-NMR analysis along with the M_n and M_w values from SEC are summarized in table 3.1. This supports that the melt reactor set-up allows for the formation of higher order architectures like the star-block copolymers with molecular weights as high as 50 kDa while still maintaining narrow PDI by overcoming the viscosity build-up.

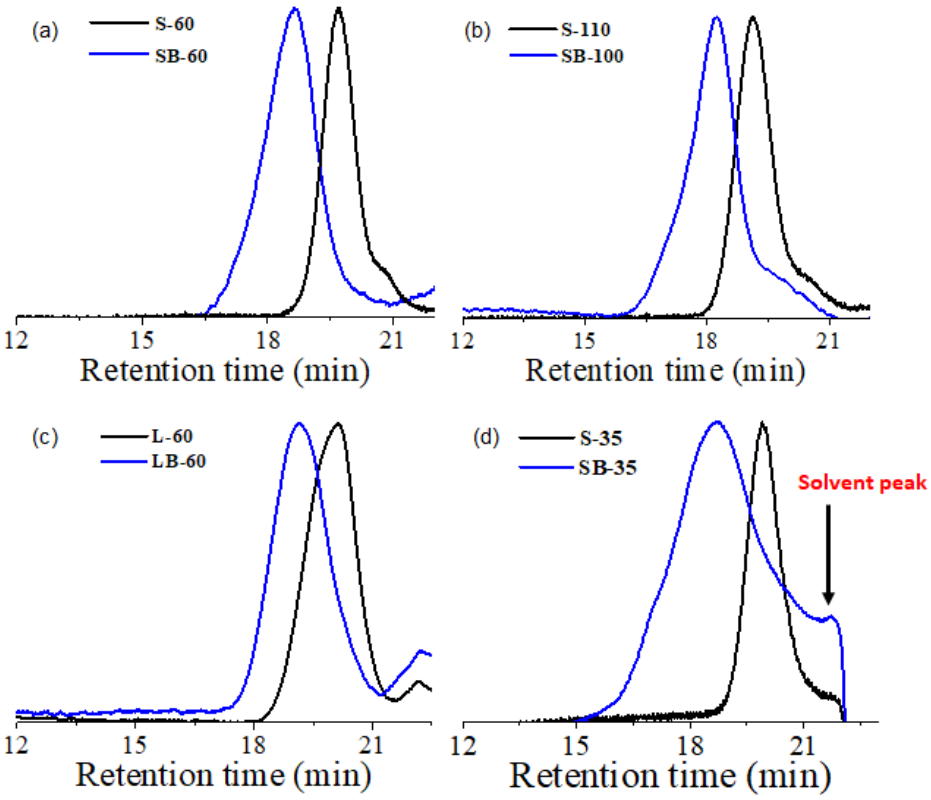

Figure 3.10. *Gel permeation chromatograms of star and linear polymers alongwith their corresponding macroinitiators.*

Thermo gravimetric analysis (TGA) was employed as the tool to study the thermal stability of the polymers and as can been from the figure 3.11a, the polymers exhibited stability up to ~280 °C. Having determined the decomposition temperature (T_d) of the polymers, the next step was to understand the solid-state packing of these higher order architectures by subjecting them to Differential scanning calorimetry (DSC) analysis. DSC thermograms give us information about whether the sample is semi-crystalline or amorphous in nature, their glass transition temperatures (T_g), melting and cooling transition temperatures (T_m and T_c, respectively) and the corresponding enthalpy of melting and cooling (ΔH_m and ΔH_c). As can be seen from figure 3.11b and 3.11c, both the macroinitiators S-60 and S-110 exhibited semi-crystalline behavior with their respective melting transitions at 45.6 °C and 48.6 °C. There was a clear transformation to amorphous nature in the star-block copolymer SB-60 implying that the addition of the BPCL unit in the backbone made the polymer chains sluggish to crystallize

and the polymer displayed glass transition (T_g) at -42.5 °C. On the other hand, the SB-100 polymer exhibited a cold crystallization peak at 10.5 °C followed by a melting transition at 34.4 °C. Upon deprotection of the tert-butyl group, both the carboxylic acid substituted star-block copolymers SB-60 and SB-100 exhibited semi-crystalline behavior wherein both the glass transition as well as the melting transitions were observed (see figure 3.11b and 3.11c). The thermal properties of the linear macroinitiator and block copolymer have already been reported previously (in Chapter 2).

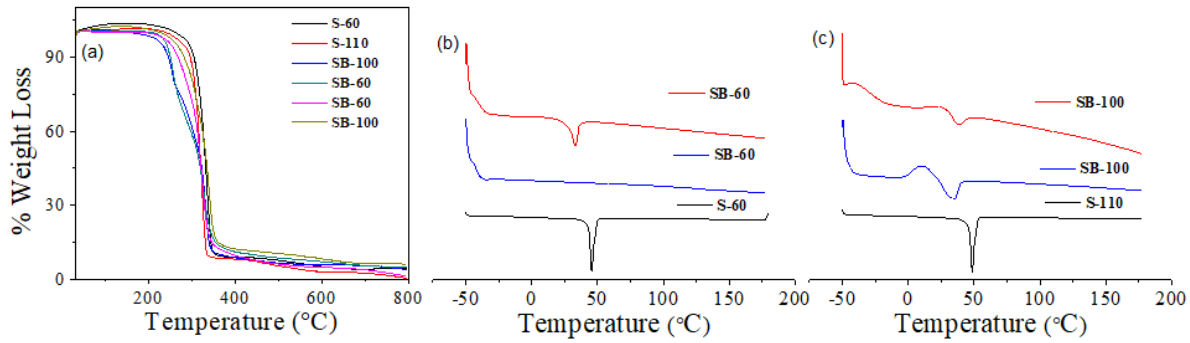

Figure 3.11. *Thermogravimetric Analysis (TGA) plot (a) and Differential Scanning Calorimetry (DSC) thermograms (heating cycle) of star macroinitiators and block copolymers (b,c).*

3.3.2 Self-assembly and Photophysics

The amphiphilicity in the carboxylic acid substituted star and linear block copolymers allows them to self-assemble in an aqueous medium into nanoparticles (or nano-aggregates). The macroinitiators were completely water insoluble and only upon addition of the carboxylic acid counterpart the polymers became water dispersible. The self-assembly of these star **SB** and linear block **LB** copolymers was studied using the dialysis method, wherein the polymers were dissolved in an organic solvent (DMSO) followed by their dropwise addition into water and then dialysed in a semi-permeable membrane (MWCO = 3.5 kD) against water for 24 h. The water in the container was replaced with fresh water at regular intervals in order to facilitate the removal of DMSO and thus drive the formation of polymeric nanoparticles. After the dialysis, the transparent polymer solutions obtained via filtration were lyophilized into stable nano-formulations that were stored at 4°C and these formulations exhibited a long shelf-life. The foremost investigation carried out was to determine the size of these stable nano-

formulations, for which Dynamic light scattering (DLS) and Small-Angle X-ray scattering (SAXS) were employed. DLS provides information about the hydrodynamic radius (R_h) by exploiting the Brownian motion of particles and then using the Stokes-Einstein equation gives us the correlation coefficient (g^2t). Freshly dialyzed solutions of the star and linear block copolymers were first subjected to Dynamic light scattering in order to determine the hydrodynamic radius (R_h) of these nano-formulations. The hydrodynamic radius of the star-block copolymer SB-60 was determined to be 12 ± 3 nm, as can be seen from the histogram in figure 3.12a. The histograms of the other star-block copolymer formulations are also given in the figure 3.12a.

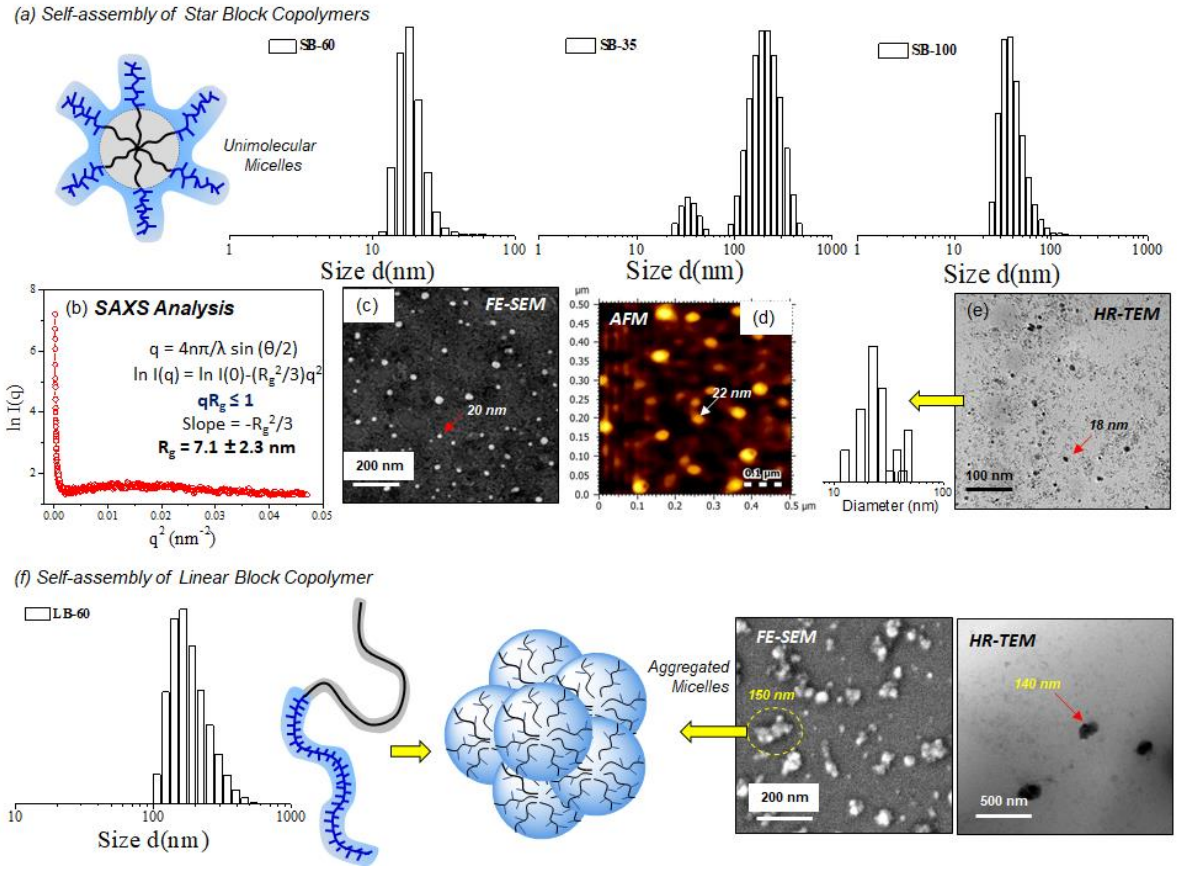

Figure 3.12. *Hydrodynamic diameter of self-assembled star block copolymers SB-60, SB-35 and SB-100 (a) at 0.1 mg/mL concentration in water. (b) Small Angle X-ray Scattering (SAXS) analysis and determination of radius of gyration (R_g) for the star block copolymer SB-60. FESEM (c), AFM (d) and HR-TEM (e) images for SB-60 were recorded at 0.05 mg/mL concentration in water. (f) Self-assembly of linear block copolymer LB-60 depicted via DLS histogram at 0.1 mg/mL concentration and FESEM, HR-TEM images at 0.05 mg/mL concentration in water.*

SAXS technique gives us enormous amount of information related to size, shape, structure and aggregation properties of the nanoparticles based on the scattering intensity of X-rays. The scattering intensity, I is determined as a function of the scattering vector "q" and according to the Guinier approximation, the value of I depends on the Radius of gyration R_g as per the equation given in figure 3.12b. The Guinier approximation focusses on the lower q values of the SAXS scattering curve and the plot of ln I(q) vs q^2 is what is referred to as the Guinier plot, whose slope gives us the value of R_g (under the condition that $qR_g \leq 1$). The ratio of R_g/R_h provides indispensable information on the architecture and structure of the polymeric nanoparticles in solution. The SB-60 aqueous assemblies were subjected to Small Angle X-ray scattering (SAXS) analysis in a quartz capillary and using the Guinier approximation the radius of gyration (R_g) was determined from the slope of the Guinier plot to be 7.1 ± 2.3 nm (see figure 3.12b). The R_g/ R_h ratio for the SB-60 unimolecular nano-formulation was calculated to be 0.77, which is the ideal value for micelles as per the literature reports (ref). In order to visualize the size and morphology of these self-assembled nanoparticles, techniques such as FESEM, AFM and HR-TEM were employed. As can be seen in figure 3.12c, FESEM image of SB-60 revealed the formation of spherical nanoparticles with average size in the range of 23 ± 3 nm. The spherical morphology of these nanoparticles was reiterated from the AFM and HR-TEM images, wherein the sizes obtained were in coherence with the FESEM and DLS data. A histogram generated from more than 50 particles in the HR-TEM image (see figure 3.12e, next to HR-TEM image) gave an average value of 28 ± 4 nm which is in good agreement to the DLS histogram with the average D_h = 26 nm. On the other hand, the linear block counterpart LB-60, having the same repeating units as SB-60, exhibited the R_h to be 100 ± 5 nm (see figure 3.12f). This extensive difference in the hydrodynamic radii of the SB-60 and LB-60 nano-formulations was the first proof in favour of our hypothesis that polymer topology played a crucial role in every aspect of the macromolecular self-assembly. The LB-60 nano-assemblies exhibited higher R_h due to the formation of aggregated micelles, as can be seen clearly from the schematic in figure 3.12f. The FESEM and HR-TEM images for the LB-60 polymeric assemblies clearly exhibited the spherical aggregate morphology with sizes in the range of 150 ± 10 nm and 140 ± 10 nm, respectively and were coherent with the DLS data (see figure 3.12f). It is important to note that the SB-60 and LB-60 have identical molecular weights; however, they largely differ in their self-assembly due to variation in their topology.

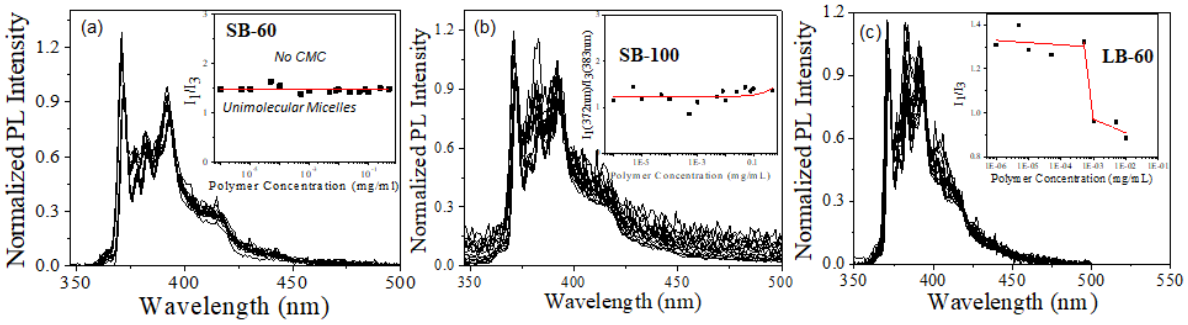

Figure 3.13. *Critical Micelle Concentration (CMC) determination of star and linear block copolymers SB-60 (a), SB-100 (b) and LB-60 (c) using pyrene as the fluorescent probe. The inset plot represents I_1/I_3 vs polymer concentration (mg/mL).*

The yardstick experiment that is most frequently done to substantiate the formation of unimolecular micelles is the determination of critical micellar concentration (CMC) of the polymer nanoparticles, wherein pyrene is used as the fluorescent probe. The peculiar characteristic of pyrene that makes it the most sought dye for CMC determination is its signature I_1 (372 nm) and I_3 (383 nm) vibronic levels that change drastically upon change in the environment of the pyrene molecule from hydrophilic (in water) to hydrophobic (in micellar cavity). Typical amphiphiles undergo concentration dependent self-assembly to exhibit breakpoint in the I_1/I_3 plot above the critical micelle concentration whereas unimolecular micelles are rather unperturbed by the concentration gradient and thus exhibit a plot with zero slope. Herein, the concentration of star and linear block copolymers was varied over a wide range from 10^{-6} mg/mL to 0.5 mg/mL while keeping the pyrene concentration fixed at 0.6 x 10^{-6} M. The photoluminescence spectra were obtained upon excitation at 337 nm; and the ratio of the intensity of I_1/I_3 peaks were plotted against the concentration and shown as inset in figure 3.13a for SB-60. As is evident from the inset plot, there was no change in the ratio of I_1/I_3 at different polymer concentrations depicting the absence of a critical micelle concentration (CMC) for the star-block copolymer. The absence of CMC was a direct evidence towards the existence of unimolecular micelles in the system, which remain stable at infinite dilution and are independent of concentration, characteristics vital for *in vivo* experiments. Similar results were derived in case of the star-block copolymer SB-100 (see figure 3.13b), however, the CMC determination could not be carried out for the lower star analogue SB-35 because the polymer was not dispersible in water as has been mentioned before about the turbidity in the dialyzed

solution. Also, the typical values of I_1/I_3 for pyrene in aqueous medium and hydrophobic environment are 1.8 and 1.0-1.4, respectively as per the literature reports (ref). As can be seen from the inset plots of both the star-block copolymers SB-60 and SB-100, the I_1/I_3 values remained constant in the range of 1.0-1.4 which affirms the presence of pyrene in the hydrophobic cavity of these unimolecular micelles. On the other hand, the linear diblock copolymer LB-60 exhibited break point with respect to critical micellar concentration at 1 µg/mL (figure 3.13c) which is similar to that of typical CMC values reported for aggregated micelles (ref). The determination of CMC was a key experiment to justify the claim of star-block copolymers self-assembling in water to result in the formation of unimolecular micelles. Polymer topology played a significant role here as well, wherein two polymers having the same molecular weight, i.e. SB-60 and LB-60 resulted in the formation of two radically opposite self assemblies - unimolecular micelles and aggregated micelles, respectively. Based on the DLS, SAXS, morphology and pyrene fluorescent experiments; it may be summarized that the star-block copolymers were indeed self-assembled as tiny < 30 nm sized unimolecular micelles (single nano-vector) whereas its linear counterpart produced large >100 nm sized aggregated micelles.

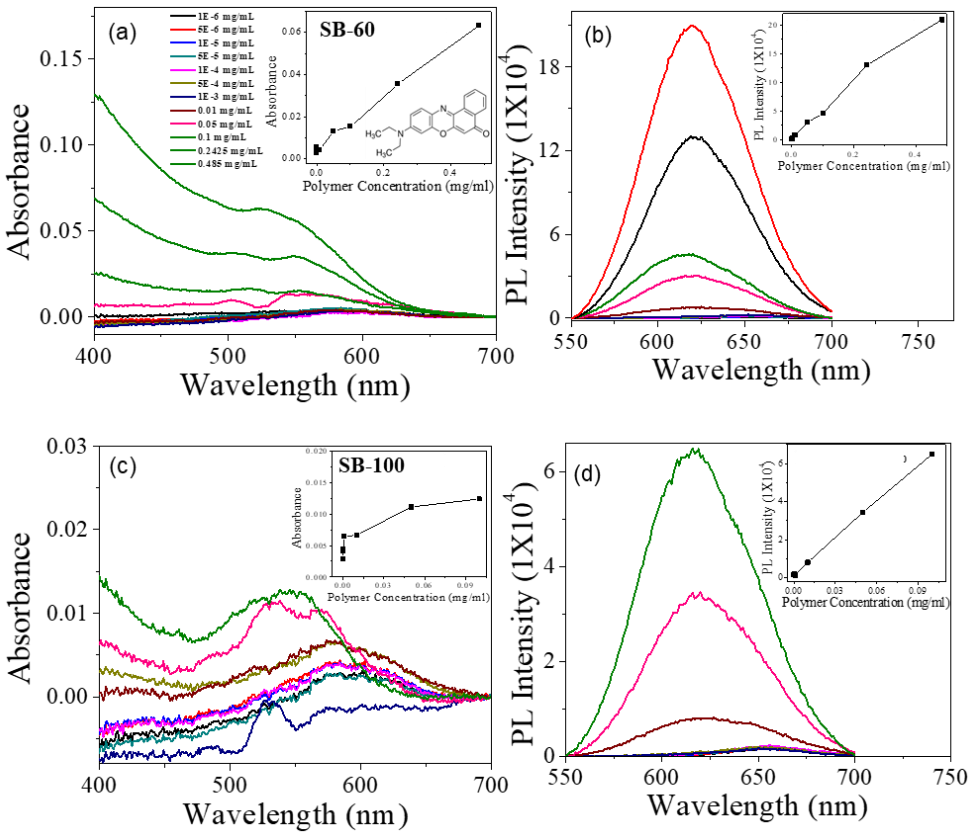

Figure 3.14. *Encapsulation study carried out for star block copolymers SB-60 (a), (b) and SB-100 (c), (d) using Nile red as the fluorescent probe employing absorbance and fluorescence*

spectrophotometer, respectively. The inset plot represents absorbance or PL intensity values vs polymer concentration (mg/mL).

Another important study was to determine the encapsulation capability of hydrophobic dyes in these unimolecular micelles (SB-60 and SB-100) and for the aforementioned study, both absorbance and fluorescence techniques were employed using Nile red as the probe. Herein, the concentration of Nile red was maintained constant and the polymer concentration was changed from 10^{-6} mg/mL to 0.5 mg/mL following which their respective absorbance and fluorescence were determined. As can be seen in the insets of figure 3.14 (a), (b), (c) and (d), the absorbance and PL intensity values increased in a linear fashion with increasing polymer concentration for both the star-block copolymers. This is yet another hallmark characteristic of unimolecular micelles, wherein the number of dye molecules encapsulated in the hydrophobic core of UMs increases linearly with increase in polymer concentration since they form single polymer chain nanocarriers and not the typical aggregated micelles. Thus, the formation of unimolecular micelles of both the star-block copolymers SB-60 and SB-100 was effectively proven by the absence of CMC and the linear increase in the concentration of dye encapsulated by the UMs.

3.3.3 DOX Encapsulation and Enzymatic Degradation

Star and linear block copolymers were subjected to clinically important and fluorescent (red) chemotherapeutic drug doxorubicin (DOX). The drug loading was accomplished by dialysis method as mentioned before wherein the polymer and the anticancer drug DOX were dissolved in DMSO and added to water in a dropwise manner with constant stirring followed by dialysis against water in a semi-permeable membrane of MWCO = 3.5 kDa for 48 h. The removal of DMSO and unencapsulated DOX molecules was facilitated by regularly replacing the outside water in the container and at the end of 48 h, these dialyzed solutions were filtered using a Whatman paper, lyophilized and stored at 4 °C for further use. Before lyophilization,

the freshly dialyzed solutions were subjected to the Absorbance spectroscopic analysis in order to determine the drug loading content (DLC) and drug loading efficiency (DLE). The DLC values are plotted and shown for different polymer topologies in figure 3.15a. The DLC for SB-60 UMM was obtained as 14.2 % which is to be the highest DLC achieved for DOX loading in any type of unimolecular micelles. The aggregated micelles of the linear di-block LB-60 displayed a DLC = 2 % which is almost 7-fold lower compared to the star-block UMM. The other star block copolymer SB-100 exhibited DLC = 13.1 %. DOX loading in lower star block analogue SB-35 having statistically 35/35 units showed DLC < 1%. This is reiterating the importance of topology and size of the star-block on the extremely crucial property of DLC of a nano-carrier. The DLS histograms of DOX-loaded star and linear block copolymer formulations are given in figures 3.15b to 3.15e and their hydrodynamic diameter have been tabulated in figure 3.15f. All the nano-formulations showed monomodal size distribution with narrow polydispersity (PDI) values. The SB-35 polymer resulted in a turbid solution after dialysis and that reflected on the R_h value that was equal to 78 ± 2 nm, much higher compared to the two higher analogues. The sizes for the star-block copolymers SB-60 and SB-100 were retained almost identical both in the nascent and DOX-loaded form indicative of their tendency to form unimolecular nano-assemblies. The nascent and DOX loaded micelles were also subjected to Zeta potential measurements; the values have been listed in the table in figure 3.15f. The zeta potential of star and linear lock copolymer and their DOX loaded nanoparticles were determined in the range of -3 mV to -26 mV, which implies the formation of neutral to slightly negatively charged nano-formulations. Both SB-60 and LB-60 have identical molecular weights and significantly differ in size (25 nm and 150 nm), and their self-assembly (unimolecular micelle vs. aggregated micelle), and topology (branched and linear); hence these two candidates were chosen to study their biological activity both *in vitro* and *in vivo*. Their DOX loaded samples are referred to as SB-60+DOX and LB-60+DOX; and free DOX was used as control wherever required.

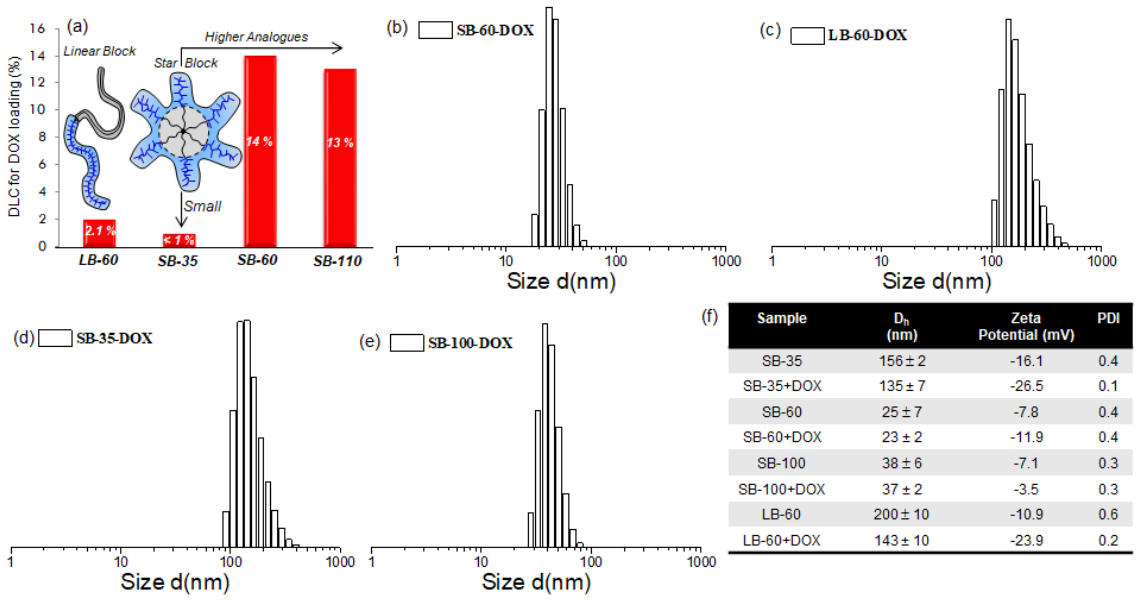

(f)

Sample	D_h (nm)	Zeta Potential (mV)	PDI
SB-35	156 ± 2	-16.1	0.4
SB-35+DOX	135 ± 7	-26.5	0.1
SB-60	25 ± 7	-7.8	0.4
SB-60+DOX	23 ± 2	-11.9	0.4
SB-100	38 ± 6	-7.1	0.3
SB-100+DOX	37 ± 2	-3.5	0.3
LB-60	200 ± 10	-10.9	0.6
LB-60+DOX	143 ± 10	-23.9	0.2

Figure 3.15. *(a) Doxorubicin loading content (DLC) represented for all the nanoparticles. DLS histograms depicting the size of DOX loaded nanoparticles SB-60+DOX (b), LB-60+DOX (c), SB-35+DOX (d) and SB-100+DOX (e). (f) Tabulated the size and zeta potential of nascent and DOX loaded star and linear block copolymers.*

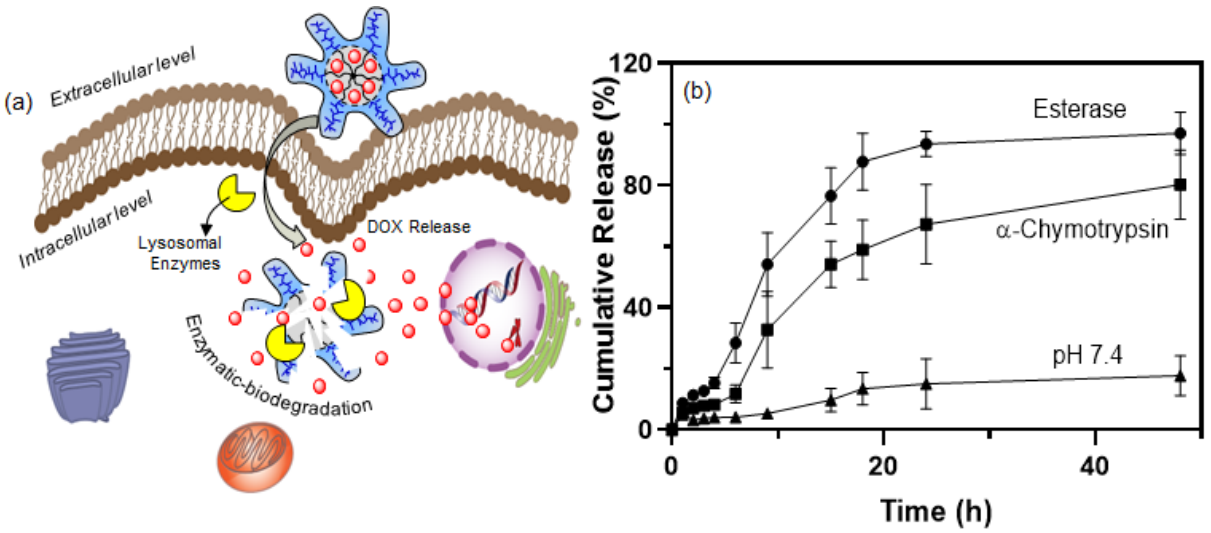

Figure 3.16. *(a) Schematic illustrating the enzymatic biodegradation of the DOX-loaded unimolecular micelle in the lysosomal compartment. (b) In vitro DOX release kinetics of SB-60+DOX nanoparticle in PBS alone and in presence of esterase (10U) and α-Chymotrypsin (8U) at pH 7.4 incubated at 37 °C.*

An important aspect of these newly synthesized amphiphilic star-block copolymers is that they are composed of a polyester backbone that makes them fully biodegradable and extremely suitable for *in vitro* as well as *in vivo* applications. Biodegradability implies the complete breakdown of polymeric micelles into smaller molecules that can be excreted out of the system easily; in this particular case the degradation can be achieved by the esterase enzyme present in the lysosomal compartment of the cells, as has been explained schematically in figure 3.16a. In order to study the biodegradation of the novel star-block copolymers, an *in vitro* experiment was set up wherein SB-60+DOX were exposed to two lysosomal enzymes: horse-liver esterase enzyme (10 U) and α-chymotrypsin (8 U) at pH 7.4 and incubated at 37 °C for 48 h. Both the enzymes are very well known to cleave aliphatic polyester backbone resulting in the biodegradation of the scaffold to release DOX that gives a direct read-out of the degradation which can be monitored using absorption spectroscopy. In such an atypical experiment, the SB-60+DOX dialyzed solution containing the enzyme (esterase or α-Chymotrypsin) was taken in a dialysis tube of MWCO = 1000 Da which was immersed in 4 mL 1X PBS buffer (pH = 7.4) and incubated at 37 °C. In a control experiment, the SB-60+DOX dialyzed solution was taken alone, without the enzyme, at pH = 7.4 and 37 °C. For all the aforementioned three conditions, the absorbance of the outside solution was measured at hourly intervals in order to determine the amount of DOX released that directly pointed out to the degradation of the nano-carrier. The amount of DOX released was used to calculate the % cumulative release by comparing with the amount of DOX inside the dialysis tube at time t = 0 min. This *in vitro* DOX release experiment was repeated three times and incorporating all the values, the cumulative release (%) was plotted against incubation time (h) for the SB-60+DOX polymer, as can be seen in figure 3.16b. In the presence of esterase enzyme, > 95 % drug release was observed within 24 h. The enzymatic cleavage by α-Chymotrypsin resulted in the release of only 60 % DOX molecules. In the control, the percentage release was substantially lower at a value of ~ 15 % indicating that the degradation of the unimolecular micelle only occurred in

the presence of the lysosomal enzymes. Horse-liver esterase enzyme seemed to be the most suitable for complete degradation of the nano-assemblies, as can be seen from figure 3.16b.

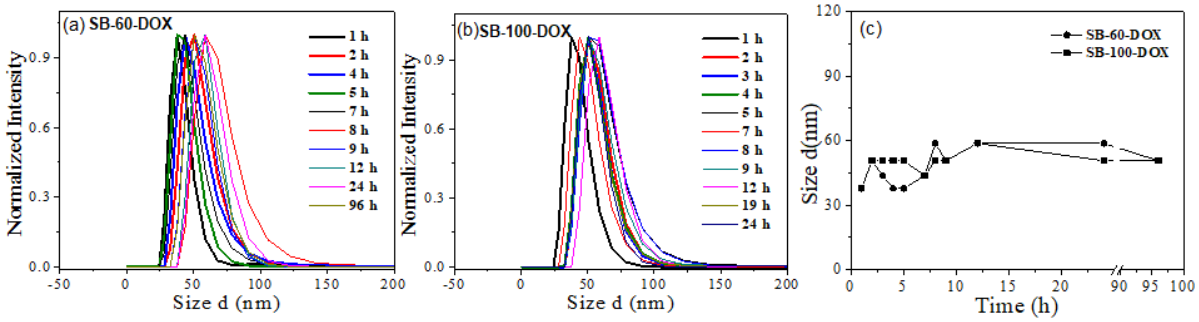

Figure 3.17. *DLS histograms depicting the stability of the star block copolymer scaffolds SB-60 (a) and SB-100 (b) in the presence of PBS buffer at 37 °C at different time points up to 96 h. (c) Plot of size d(nm) vs. time for SB-60 and SB-100 incubated with PBS buffer at 37 °C obtained from DLS histograms.*

Another important experiment to determine the stability of the star-block copolymer nano-formulations at pH = 7.4 (1X PBS) was to monitor the change in size, if any, via the DLS instrument. Herein, the nano-formulations SB-60 and SB-100 were incubated with 1X PBS buffer (pH = 7.4) at 37 °C and at regular intervals, the aliquots were subjected to DLS analysis, using which the size of these nano-assemblies was monitored for 96 h (4 days). The plot of normalized intensity vs size (d. nm) for all the time points can be seen in figure 3.17a and 3.17b for SB-60+DOX and SB-100+DOX, respectively. The conclusion drawn from both the plots was that there was no significant change in the hydrodynamic diameter with change in time up to 96 h (see the compiled plot in figure 3.17c). This experiment depicted the stability of these formulations in PBS buffer that makes them extremely suitable for *in vivo* applications, wherein nano-carriers used for drug delivery are most often given intravenously in a saline solution.

3.3.4 Cytotoxicity and Cellular Uptake

Prior to using the polymeric nanoparticles for *in vivo* experiments, it was essential to determine the cyto-compatibility of these nano-carriers in healthy wild-type mouse embryonic fibroblast (WT-MEF) cell lines. For this purpose, varying concentrations of the nascent star

block copolymer scaffold SB-60 were incubated with WT-MEF cells for 72 h and the cell viability was determined by means of the MTT assay (see histogram in figure 3.18a). As is evident from the histogram, the polymer scaffold displayed 100 % biocompatibility up to 100 µg/mL and about 70-80 % cells were viable up to 200-500 µg/mL. This implied that the SB-60 nano-carrier was non-toxic to cells up to concentrations as high as 500 µg/mL and hence, were ideal for use as drug delivery vehicles *in vivo*. Further, the cytotoxicity of the DOX loaded scaffolds SB-60+DOX, LB-60+DOX and free DOX was investigated in WT-MEF cell lines by varying the concentration of DOX from 0.1 µg/mL to 1 µg/mL. As can be seen from the histogram in figure 3.18b, the cell viability in the case of free DOX was < 10 % at a concentration of 1 µg/mL, that was lower compared to the DOX loaded nano-scaffolds. Hence, free DOX was more toxic to cells compared to their delivery from the polymer platform (see figure 3.18b). MTT assay was also studied in breast cancer MCF 7 cells and is shown in figure 3.19. Herein, a time dependent cytotoxicity assay was carried out wherein the MCF 7 cells were incubated with free DOX and DOX loaded star block copolymers SB-60+DOX and SB-100+DOX for 24, 48 and 72 h. As can be seen from figure 3.19, the star block DOX loaded nanoparticles exhibited cell killing ability similar to free DOX at 1 µg/mL after 72 h.

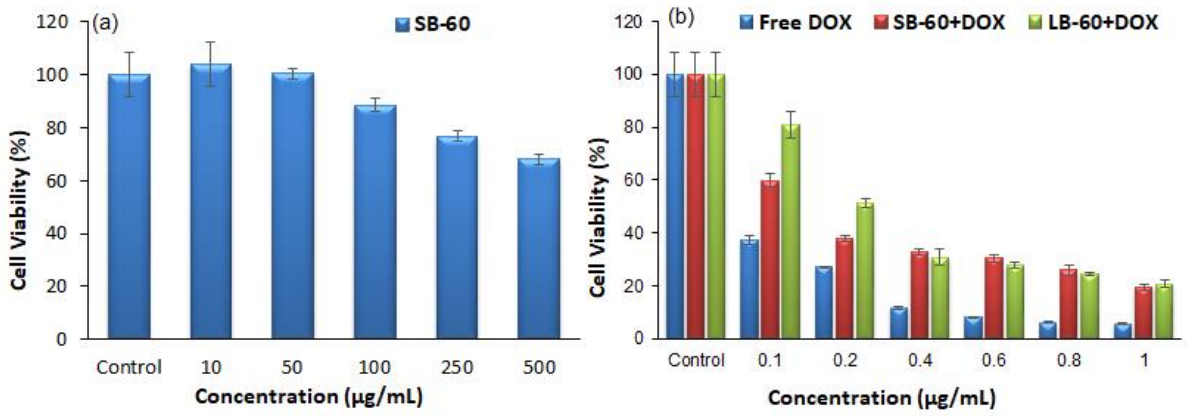

Figure 3.18. *(a) MTT plot depicting the cytocompatibility of the star block copolymer SB-60 upto a concentration of 500 µg/mL. (b) Cytotoxicity of free DOX, SB-60+DOX and LB-60+DOX in WT-MEF cell lines at concentrations up to 1 µg/mL.*

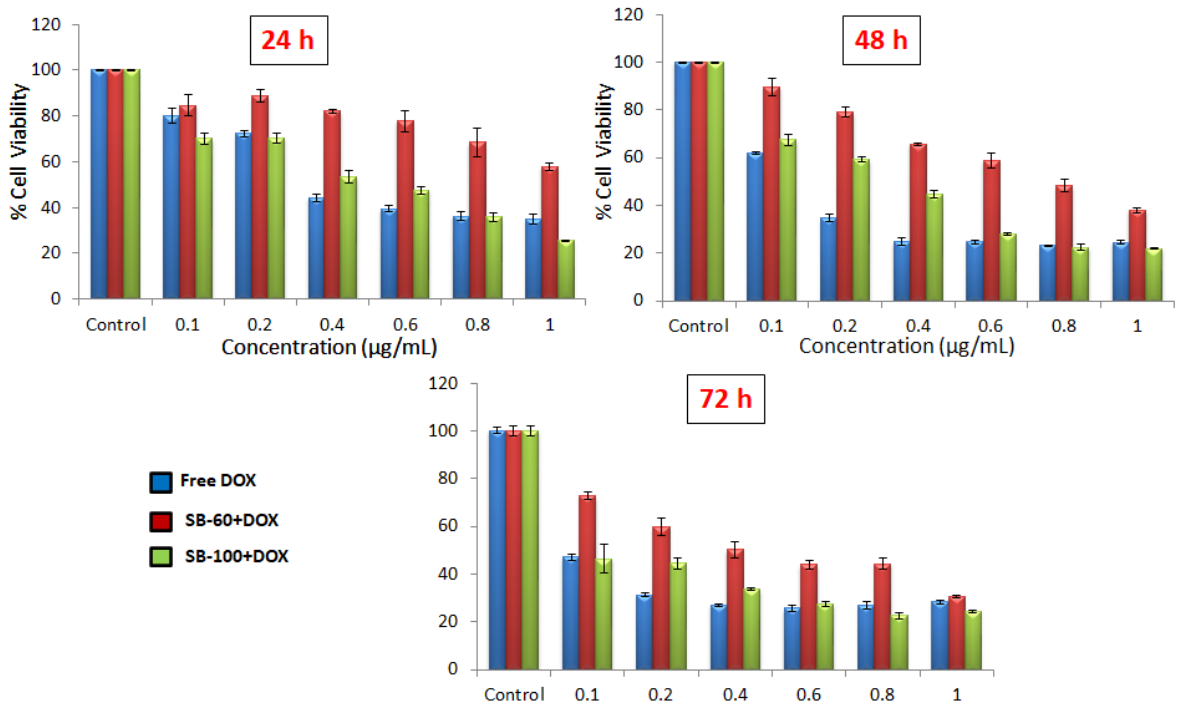

Figure 3.19. *MTT plot depicting the time-dependent cytotoxicity of the star block copolymers SB-60+DOX and SB-100+DOX in MCF 7 (breast cancer) cell lines up to a concentration of 1 µg/mL.*

Having established that the DOX loaded polymer scaffolds were biocompatible, the next investigation carried out was the cellular uptake study in WT-MEF cells in a time dependent manner. Herein, a live cell experiment was carried out with free DOX, SB-60+DOX and LB-60+DOX using Confocal laser scanning microscopy (CLSM) on a Leica SP8 system. This experiment was carried out in two parts; In the first experiment all the three compounds (concentration of DOX = 5 µg/mL) were added in one well of three separate 4-well live cell chambers following which they were stained with the Lysotracker Red DND-99 dye (concentration = 50 nM). The cells were then imaged in a time scan mode wherein an image was captured every 5 min for a duration of 60 min whilst the cells were incubated in a chamber maintained at 37 °C in a 5 % CO_2 humidified atmosphere throughout the imaging process.

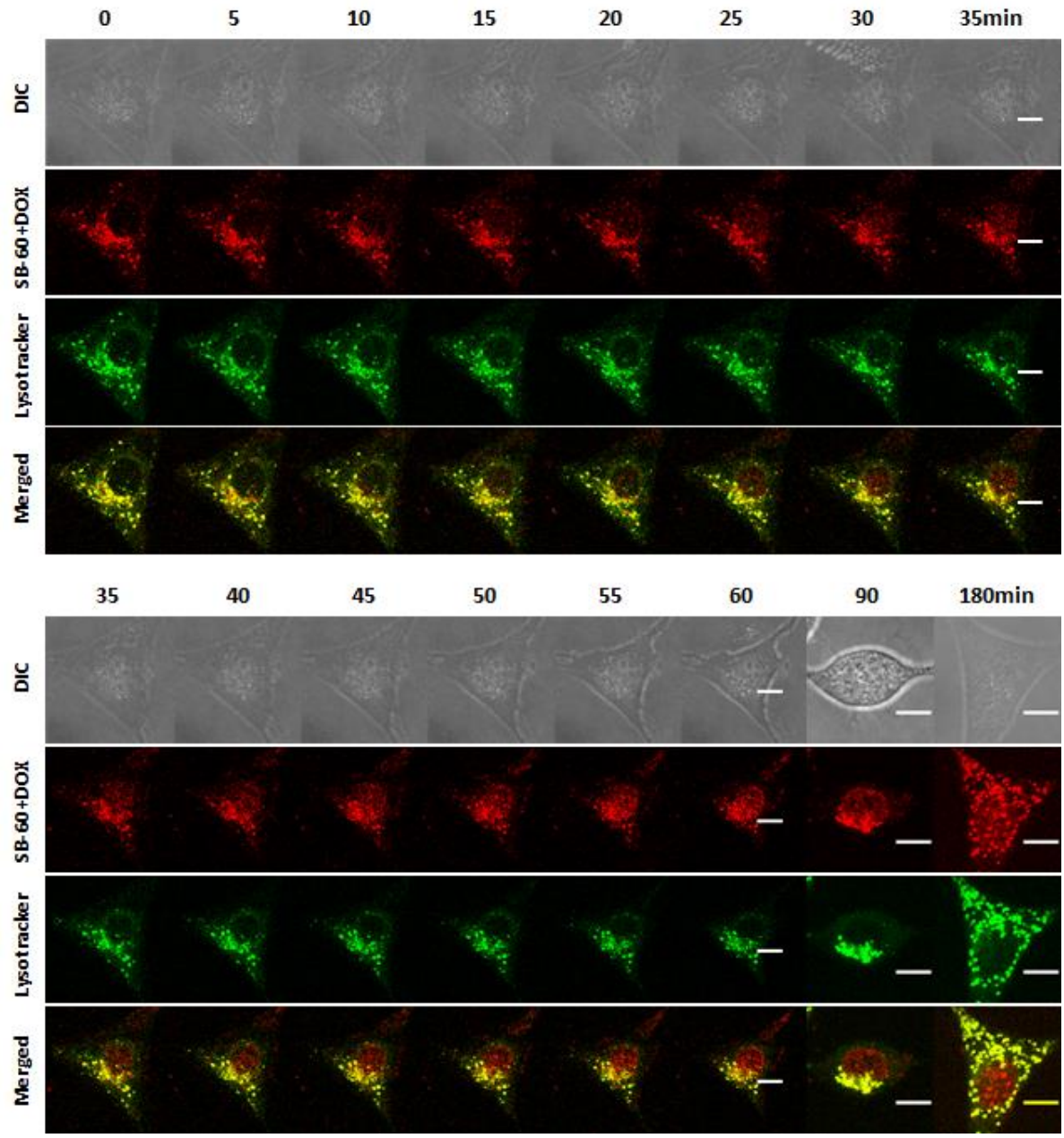

Figure 3.20. *CLSM images of a time-dependent live cell experiment done with SB-60+DOX unimolecular micelle in WT-MEF cells (DOX concentration = 5 µg/mL) and employed Lysotracker Red DND-99 to stain the lysosomes. DOX was excited using the 488 nm laser and the lysotracker excitation was done using the 561 nm laser. Scale bar = 10 µm.*

In the second experiment, compounds were incubated with the cells at two higher time points, i.e. 90 min and 180 min and then stained with the lysotracker dye followed by imaging on the Leica SP8 system maintaining the same laser power, gain and offset as in the previous experiment and same throughout all the three groups. One of the well per plate represented the

control well that contained only cells with no compound and were also stained with the Lysotracker dye. Confocal laser scanning microscopy (CLSM) images for free DOX plus the DOX-loaded nanoparticles and Lysotracker DND-99 dye stained lysosomes were visualized at red (λ = 488 nm) and green (λ = 561 nm) channels, respectively (red colour was chosen for the DOX channel and green for the Lysotracker channel). The λ_{em} for the DOX channel was 490-620 nm and that for the Lysotracker channel was 570-700 nm. The Lysotracker staining was crucial in this live cell experiment to help visualize the uptake of nanoparticles by the cells and co-localization of the DOX signal with that of the lysotracker signal affirms the endocytosis pathway of uptake of the polymeric micelles. As can be seen in figure 3.20, CLSM images captured for cells incubated with SB-60+DOX unimolecular micelle have been shown for all the time points recorded every 5 min up to 60 min and the higher time points, i.e. 90 and 180 min. At initial time points (up to 15 min), there was strong red florescence observed in the lysosomes as can be seen by the intense yellow colour in the merged image corresponding to the amalgamation of Lysotracker stained lysosomes (green) and SB-60+DOX particles (red). The initial DOX fluorescence was restricted to the lysosomal compartment and the cytoplasm, however, by the end of 60 min there was gradual accumulation of these unimolecular micelles in the nuclei. The differential interference contrast (DIC) image clearly shows the cellular morphology with contrasting nuclei within for all the images. This trend attributes that the star-nanocarrier is readily taken up by the cells via endocytosis and internalized at the lysosomal compartment for biodegradation. Once the nanocarrier is digested by the lysosomal enzymes (as seen in Figure 3.16a), the DOX gets released and readily accumulate in the nuclei for binding to DNA. A control experiment with free DOX (in figure 3.21) exhibited no colocalization with lysotracker indicating that DOX being a small molecule is taken up by the cells via diffusion rather than through the lysosomal pathway. The nanoparticle LB-60+DOX exhibited poor cellular uptake even after 180 min as is clearly visible from the CLSM images in figure 3.22. The representative CLSM images showing higher number of cells for free DOX, SB-60+DOX and LB-60+DOX can be seen in figures 3.24 to 3.26.

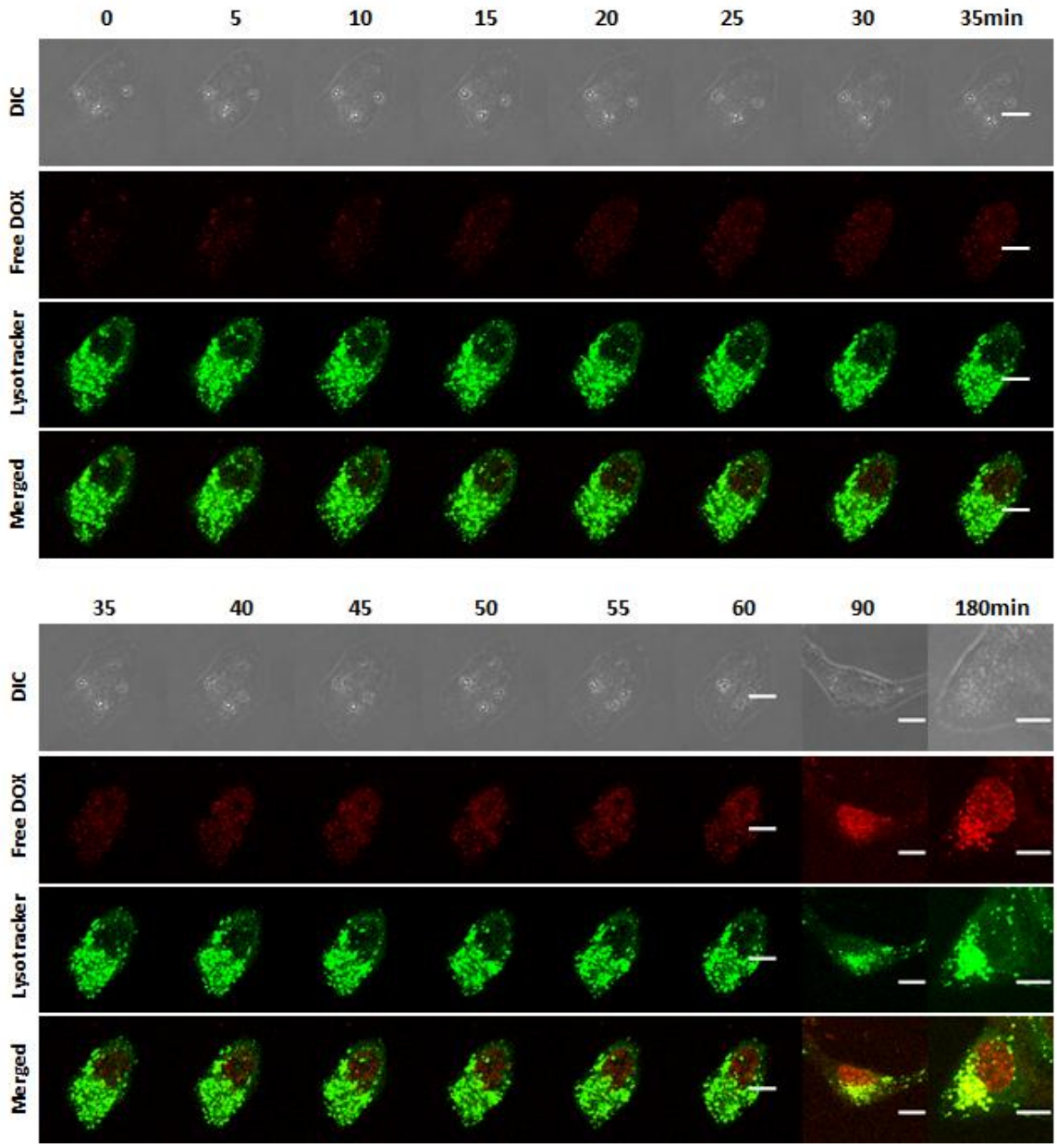

Figure 3.21. *Time-dependent live cell CLSM images depicting the uptake of free DOX by WT-MEF cells. Scale bar = 10 µm*

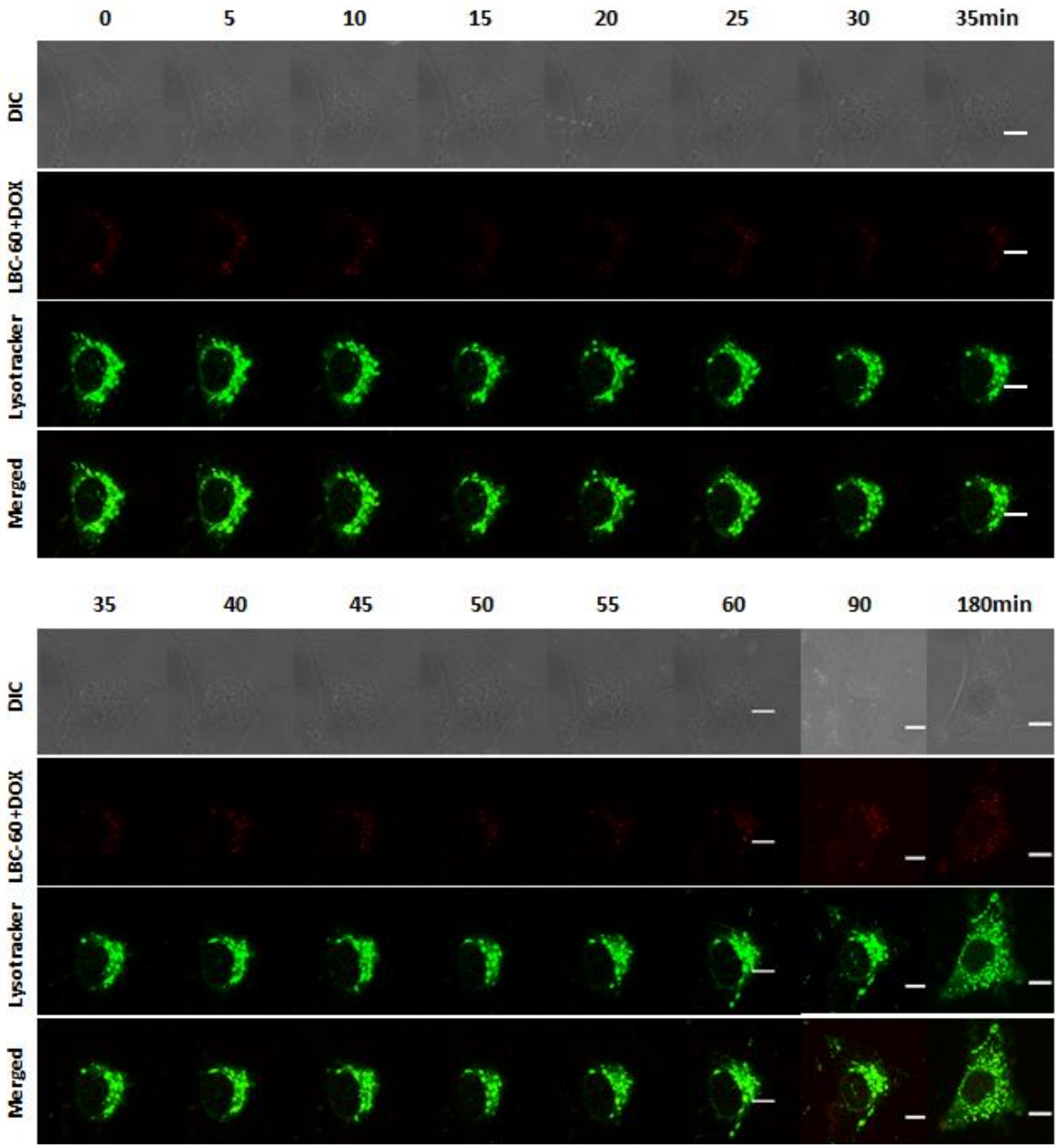

Figure 3.22. *Time-dependent live cell CLSM images of LB-60+DOX in WT-MEF cells. Scale bar = 10 µm*

In order to quantify the uptake of free DOX, SB-60-DOX and LB-60-DOX, the mean corrected total cell fluorescence (CTCF) values were determined by selecting three different regions of interest (ROIs) from each image and these values were then plotted against time (min). As is clearly evident from figure 3.23, the cellular uptake of free DOX gradually increased with time and saturated at 90 min itself, whereas the SB-60+DOX unimolecular

micelle was taken up by the cells within 5 mins of addition and it was much higher compared to the other two samples. The Mean CTCF values for the unimolecular micelle remained unaltered up to 90 min and then exhibited substantial increase in cellular uptake by 180 min (see figure 3.23), which means that the cellular uptake of the micelles did not change over the 90 min window. However, the trajectory of the uptake started with entry via endocytosis, followed by lysosomal localization where esterase aided the cleavage of the unimolecular micelle to release DOX molecules that further accumulated in the nucleus (see the time scan experiment in figure 3.20). The linear block copolymer LB-60+DOX manifested a rather slow cellular uptake kinetics over 180 min and substantially lower cellular uptake as is evident from the mean CTCF values. This live cell experiment reinstated the impact of polymer topology on the ability to permeate the cellular barriers and the star-shaped unimolecular micelle out-performed its linear polymer counterpart as well as the small molecule DOX.

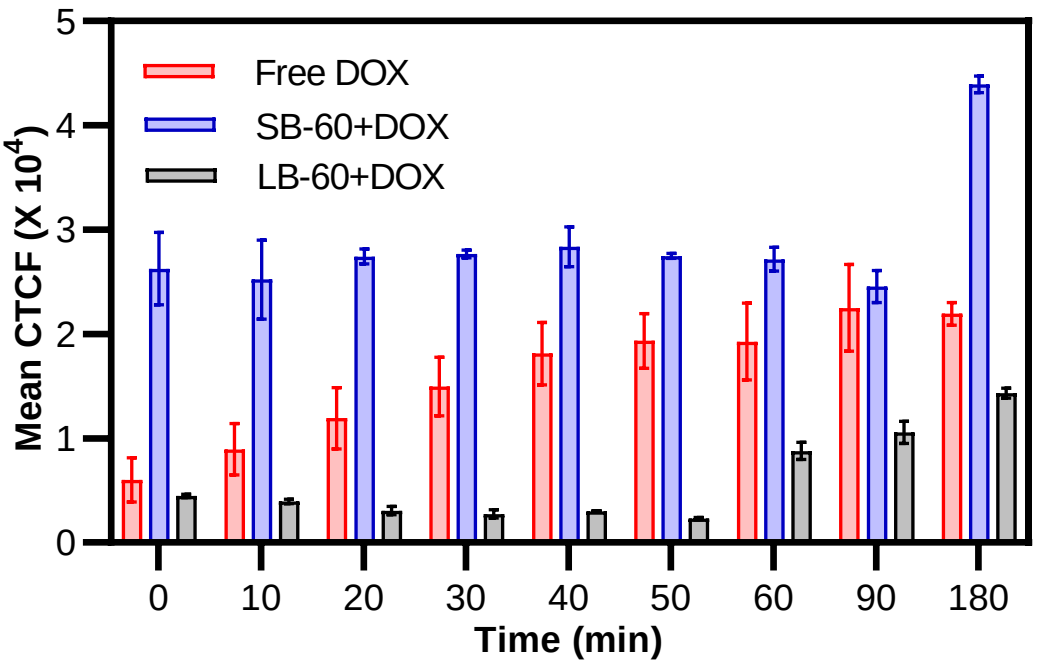

Figure 3.23. *Quantified the cellular uptake of free DOX, SB-60+DOX and LB-60+DOX in WT-MEF cells and represented as the plot of mean corrected total cell fluorescence (CTCF) vs. time (min).*

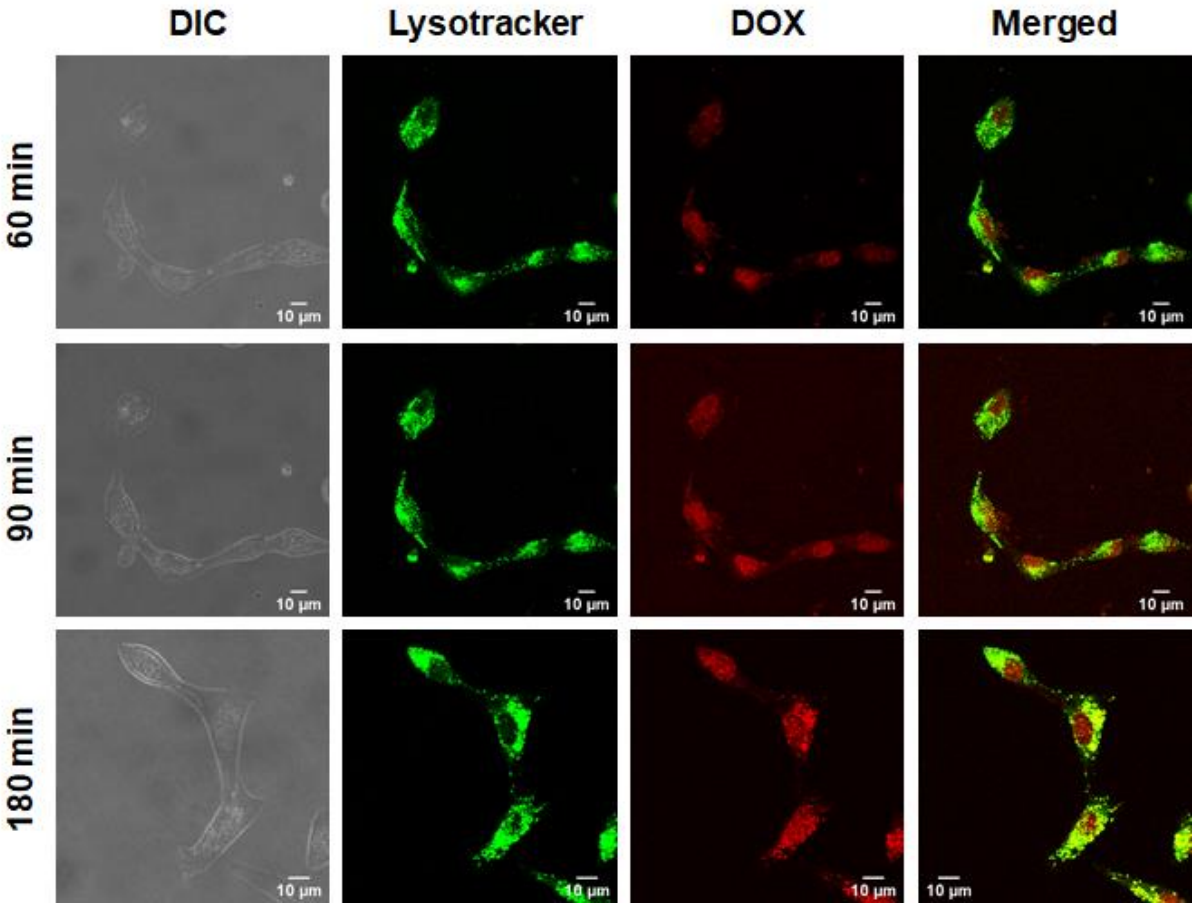

Figure 3.24. *Representative CLSM images depicting cellular uptake of free DOX at different time points 60, 90 and 180 min in WT-MEF cells (showing higher number of cells).*

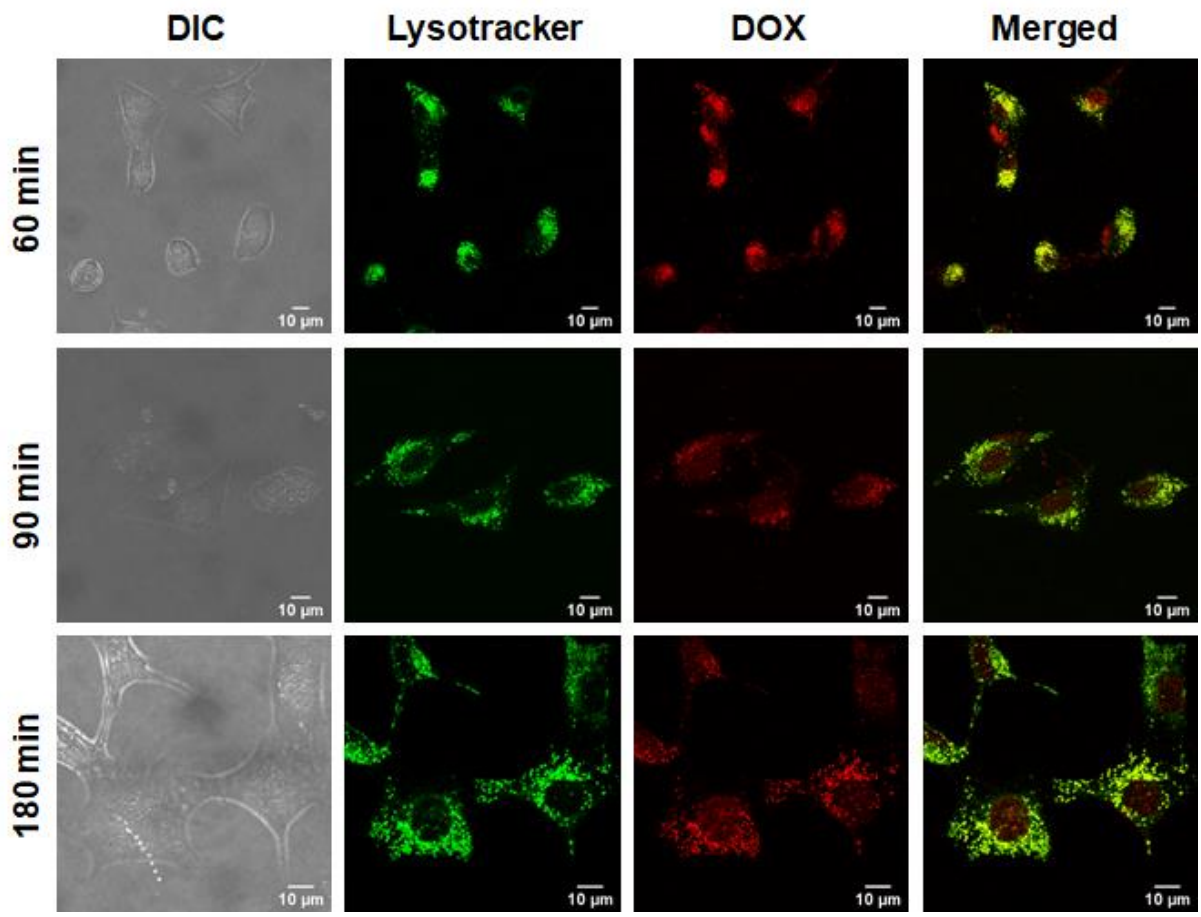

Figure 3.25. *Representative CLSM images depicting cellular uptake of SB-60+DOX at different time points 60, 90 and 180 min in WT-MEF cells (showing higher number of cells).*

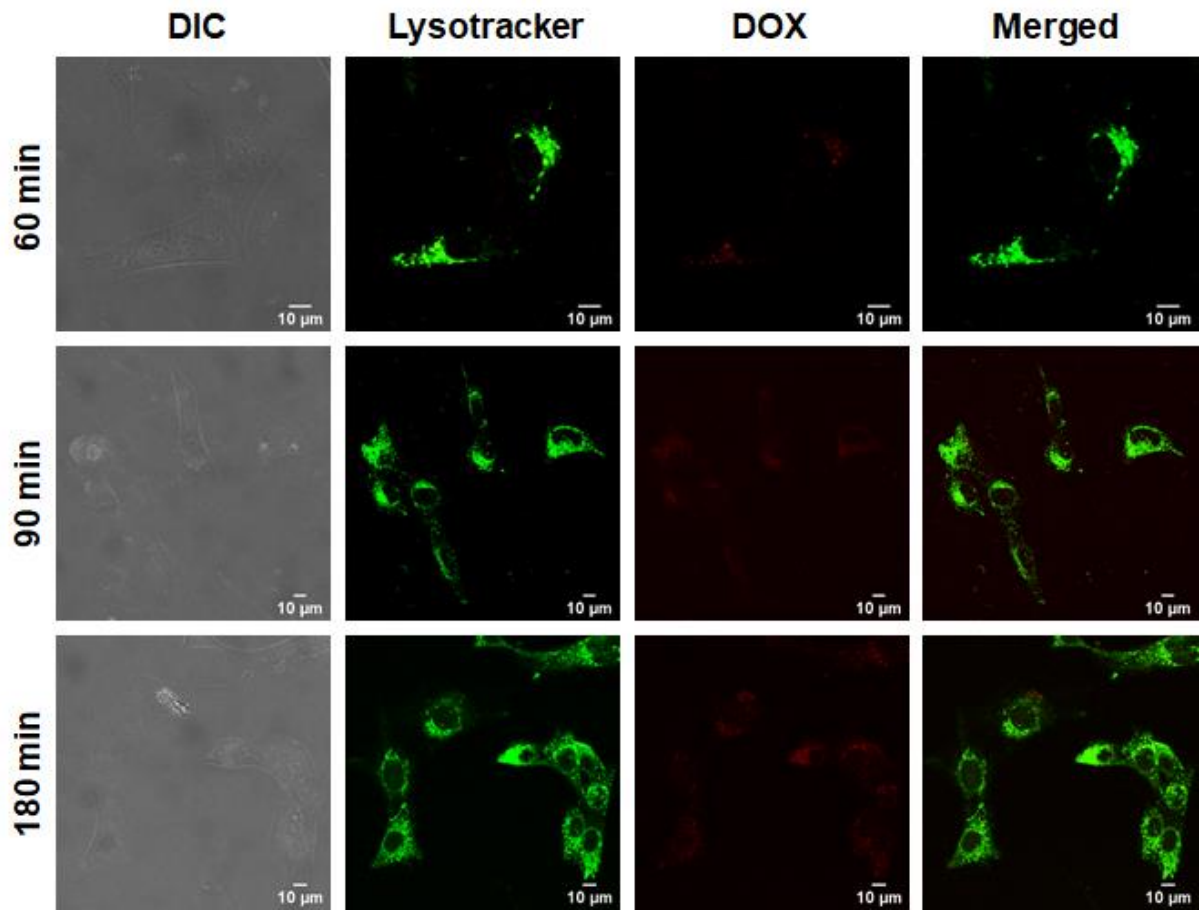

Figure 3.26. *Representative CLSM images depicting cellular uptake of LB-60+DOX at different time points 60, 90 and 180 min in WT-MEF cells (showing higher number of cells).*

3.4 Conclusion

Novel star-shaped fully biodegradable and amphiphilic carboxylic functionalized polycaprolactone-based block copolymers were designed via ring opening polymerization methodology in a custom-made melt reactor set up with an overhead stirrer. The polymerization methodology involved the synthesis of the star macroinitiator followed by the synthesis of the star-block copolymer. The star polymers and their linear counterparts were characterized using NMR and SEC to determine the molecular weights and their polydispersity. The melt reactor set up afforded the formation of high molecular weight up to 50 kDa star

architectures with narrow polydispersity (< 1.4). The star block copolymers resulted in the formation of 18 to 30 nm size unimolecular micelles as corroborated by DLS, FESEM, AFM and HRTEM. SAXS technique gave insight into the radius of gyration of the SB-60 polymer to be 7.1 ± 2.3 nm resulting in a R_g/R_h ratio of 0.77, that is symbolic of the micellar self-assembly. The linear block copolymer, on the other hand, exhibited aggregated spherical nanoparticles of ~ 200 nm size in water. The pyrene CMC experiment confirmed the formation of unimolecular micelles that were stable under infinite dilution, i.e. their self-assembly process was concentration independent for the star block copolymers SB-60 and SB-100. Whereas, the linear block copolymer exhibited the formation of aggregated micelles with a CMC of 1 µg/mL. The amphiphilic star polymers exhibited excellent loading tendency (DLC = 14%) for anticancer drug DOX that was ~ 7-fold high compared to the DLC of the linear block copolymer (DLC = 2 %). The star-block copolymer SB-60+DOX nano-formulations demonstrated extreme stability in the presence of PBS buffer and underwent complete biodegradation upon exposure to the horse-liver esterase enzyme. Cytotoxicity assay in WT-MEF cells showed the cyto-compatibility of the star block copolymer up to 500 µg/mL concentration. Their DOX-loaded counterparts were less toxic to the WT-MEF cells compared to free DOX up to a concentration of 1 µg/mL after 72 h. Confocal microscopic analysis demonstrated that the polymer loaded drugs internalized at the lysosomal compartment of the cells. Herein, the unimolecular star block SB-60+DOX micelle surpassed it's linear block copolymer analogue LB-60+DOX in terms of the cellular uptake via endocytosis as was visualized from the live cell experiment in WT-MEF cells. Thus, these unique star-shaped macromolecular architectures have depicted their ability to load and successfully deliver the chemotherapeutic drug DOX intracellular and opened avenues to exploit these for *in vivo* applications.

4

Tweaking Polymer Topology to Breach Blood Brain Barrier Together with Reduced Cardiotoxicity: In Vivo Analysis

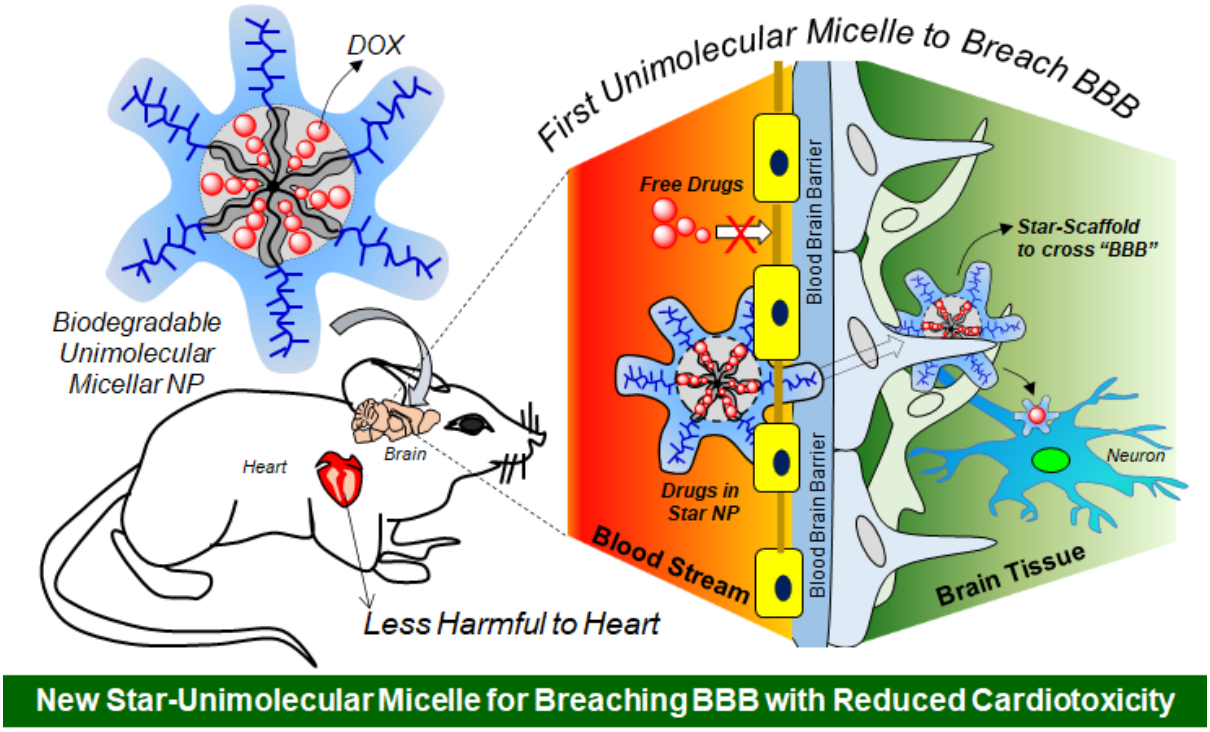

Abstract

Nanocarrier mediated therapeutic delivery across the impermeable blood brain barrier (BBB) remains an impediment till date. The next generation smart BBB crossing nanocarriers are mandatorily designed to be substantially stable to evade disassembly under infinite dilution *in vivo*, tiny-size sub-nanometer objects for penetrating the tightly regulated t-junction, high drug loading content, reduced cardiotoxicity, and most importantly biodegradable under physiological conditions. This multi-task problem has been addressed here by carefully choosing the two radically opposite polymer architectures, i.e. the linear di-block and star-block topologies based on the biodegradable polycaprolactone (PCL) backbone. Amphiphilic linear and star-block PCL copolymers having identical chemical constituents and high molecular weights of 40-60 kDa with narrow polydispersity were structurally engineered using tailor-made functional caprolactone monomers via ring opening polymerization process, as has been explained at length in the previous chapter. The idea was to optimize the new star-shaped unimolecular micelle (UMM) nanocarriers, for the first time, to overcome the bottlenecks in the field of BBB crossing. The star polymer DOX loaded core-shell UMM of 25 ± 2.0 nm size and 14 % drug loading content (DLC) along with the linear polymer DOX-loaded aggregated micelle of 200 ± 10 nm size and 2 % DLC were chosen for comparison. *In vivo* studies established that the DOX loaded UMM exhibited very good stability under blood circulation with $t_{1/2}$ of 4.0 h and together with significant reduction in the cardiotoxicity in heart tissues. The UMM nano-vector has shown remarkable efficiency to breach the blood brain barrier and nearly 8 % of total taken up drug in mice was delivered to brain tissues which is equivalent (or above) to the bench-mark trend in BBB research. Confocal microscopic imaging of brain tissues confirmed that the BBB heterogeneity caused the uptake to decrease on going from the posterior to the anterior parts of the brain and the MAP 2 antibody staining revealed their localization within the mature neurons in the brain tissue. The newly designed star-shaped biodegradable UMM nanocarriers did not exhibit immunogenicity or any necrosis in the tissue highlighting their importance for long term impact in biomedical field including BBB research.

4.1 Introduction

Drug delivery across the tightly regulated vasculature of the blood brain barrier (BBB) in the treatment of tumors and neurodegenerative diseases has been a major bottleneck.[295–297] The BBB maintains the homeostatic balance by regulating the transport of small molecule nutrients and ions through the vasculature into the brain; thus, restricts the transportation of the larger size and extraneous species across this biological barrier.[298] Nano-prodrug development have clearly identified that carriers having < 50 nm in size can impeach the tightly regulated t-junction in the BBB and enable drug accumulation in brain tissues.[299] Emulsifying wax nanoparticles (NP),[300] surface-modified PAMAM dendrimers,[301–304] acid-labile polymer coated Au NP,[305] charge convertible polylysine-Si-RNA nanocomplexes (see figure 4.1),[306] extracellular vesicles,[307] liposomal-DOX formulations,[308] asymmetric polymersomes,[309] PLGA-quantum dot NP,[310] polystyrene nanospheres and rods[46] are some of the most important nano-systems that are explored for BBB research. The penetration of the BBB seems to be highly assisted by the anionic charge on the periphery of these nano-systems. Glomerular renal filtration of the nanocarriers during prolonged circulation in the body by kidney (also liver and spleen) seems to be the major limiting factor in deciding the nano-drug concentration in blood which is crucial for enhanced BBB crossing.[311,312] Important to note that the nano-drugs are exposed to heavy cardiac stress under blood circulation and often encounter premature disassembly in the cardiovascular tissues and enhances the chances of unwanted multiorgan failure following prolonged exposure to chemotherapy.[313] Hence, the next generation BBB nanocarriers are required to be preferably non-cardiotoxic (at least less cardiotoxic) and also have significant stability under blood circulation to overcome the above limitations.

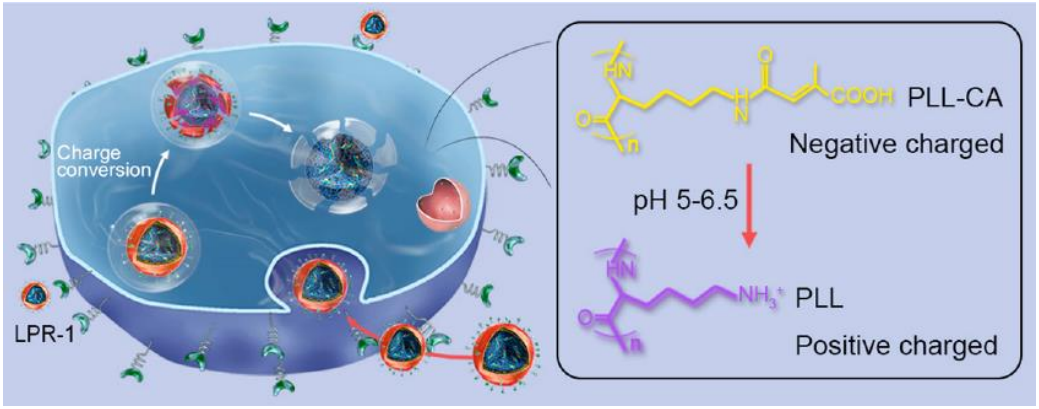

Figure 4.1. *Design principle for the pH responsive charge convertible biomimetic PLL-PEI-SiRNA nanocomplexes for targeted glioblastoma treatment. (adapted from Liu et al. Nano Lett.* **2020**, *20*, 1637-1646).

Review by Szoka and Frechet articulated at length the influence of 1D and 3D molecular architecture, chain flexibility, branching and molecular weight, etc. on renal clearance and blood half-life ($t_{1/2}$) (see figure 4.2).[61] Beyond a certain molecular weight, the sizes of the polymeric nano-carriers increase above 100 nm which leads to their opsonization and further clearance from the body via liver and spleen, referred to as the reticuloendothelial system (RES) uptake. The challenge is to strike a balance so as to have sufficiently high enough molecular weight to avoid fast renal clearance, achieve long blood circulation time yet be able to control the size to sub-100 nm in order to avoid RES uptake.[6,76,314]

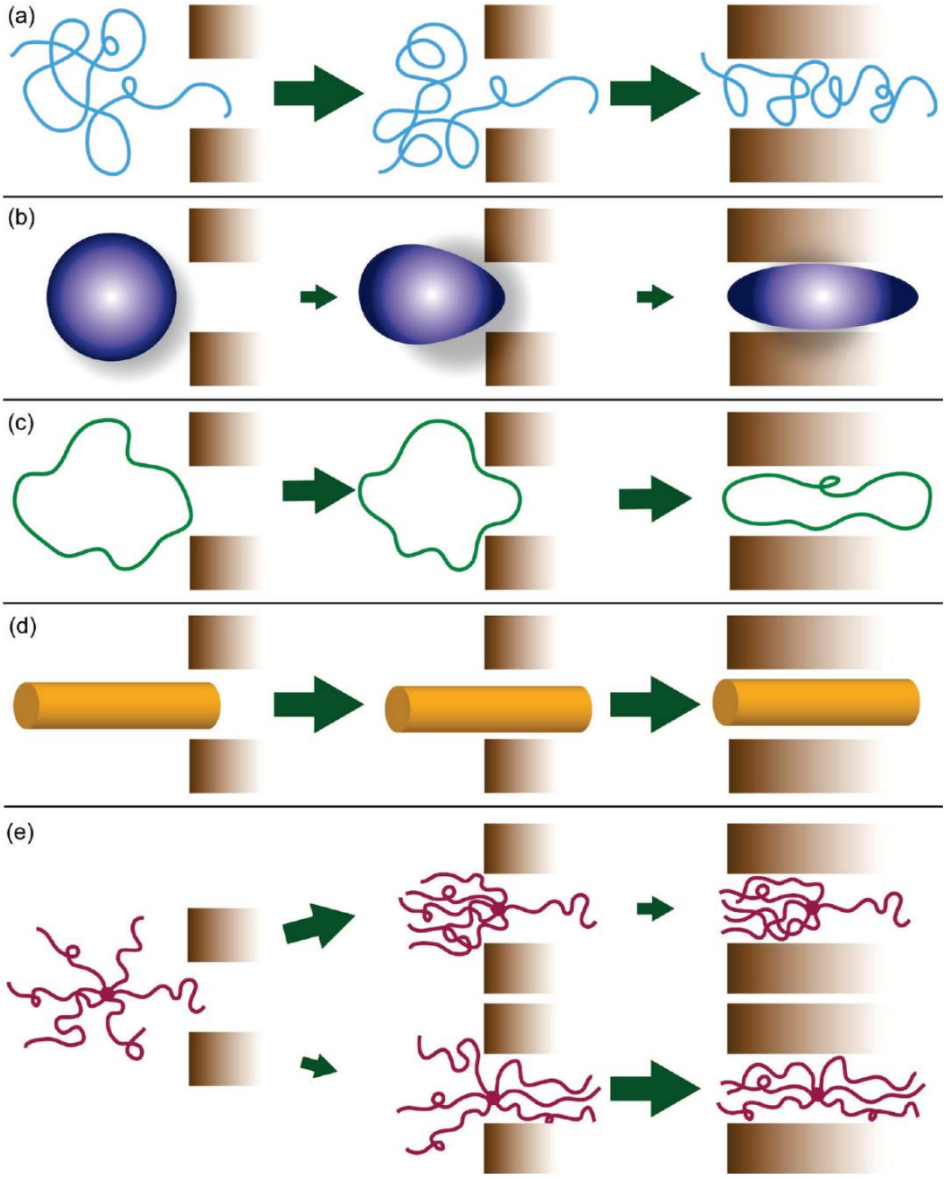

Figure 4.2. *Schematic depicting the various polymer topologies and their ability for pore penetration depending upon factors such as conformational flexibility. (adapted from Fox et al. Acc. Chem. Res.* **2009**, *42*, 1141-1151*)*

Higher order non-linear macromolecular architectures like dendrimers, hyperbranched polymers, brush and star-block copolymers exhibit a myriad of properties ranging from increased $t_{1/2}$ to decreased renal excretion owing to their branched architectures.[116,315] Investigation on the cyclic versus linear block copolymers[316] and length-tunable cylindrical polymer brushes[317] established that the polymer architecture played significant roles on the biodistribution and renal clearance. Among branched macromolecules, star polymers have gained impetus for biomedical applications surpassing its contemporaries owing to its one-pot synthesis, structural control, post-polymerization functionalization and most importantly persistent to their three-dimensional globular core-shell geometry for drug encapsulation.[165,318] Their spatially defined compact structures result in the formation of unimolecular micelles (single polymer nano-assemblies) of < 50 nm sizes that display resilience towards any changes in their self-assembly against concentration gradient.[110,116] Star block copolymers haven been studied for drug and gene delivery,[319–323] and also *in vivo* PET[324] imaging applications.

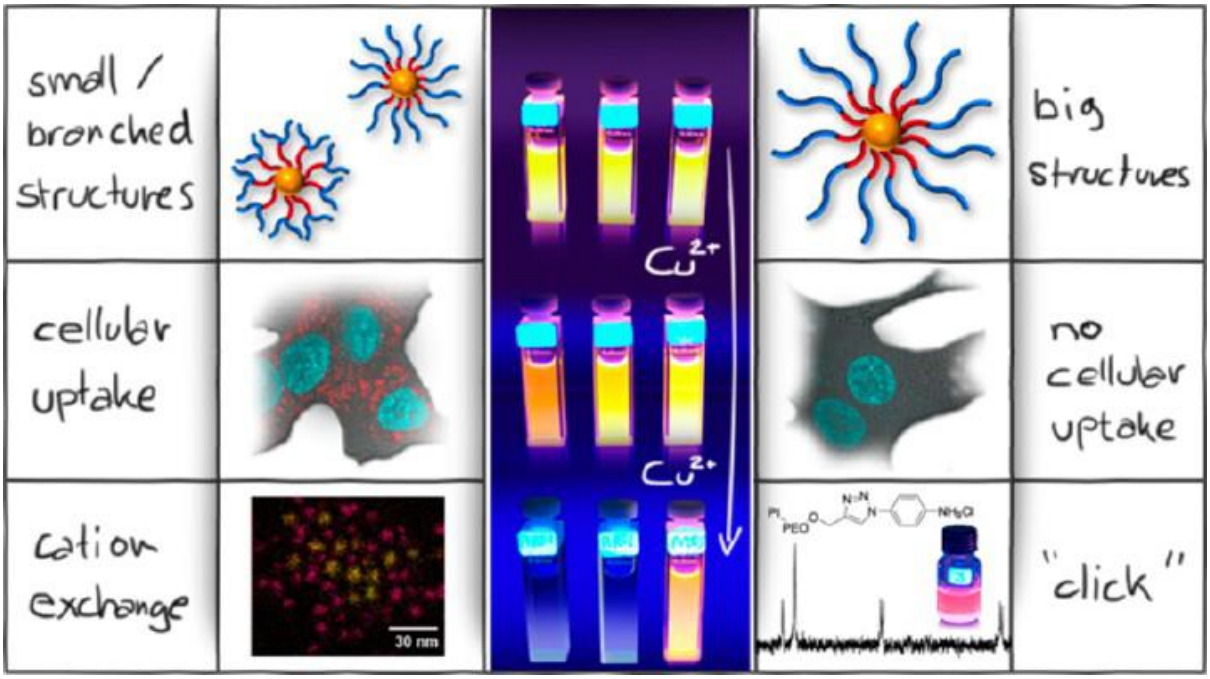

Figure 4.3. *Depicting the role of variation in the physical and biological characteristics of the fluorescent CdSe quantum dots coated with a miktoarm polymer upon variation in the polymer architecture and molecular weight. (adapted from Ostermann et al. ACS Nano,* **2013**, *7,* 9156-9167*)*

However, up to our knowledge, the star-polymer macromolecular architectures or unimolecular micelles have not been explored for BBB research in the literature. Here, we report one of the first attempts on structural engineering of smart unimolecular star-polymer based on biodegradable polycaprolactone (PCL) platform having < 30 nm size unimolecular micelles with outstanding 14 % drug loading content for clinical anticancer drug doxorubicin (DOX). The star-polymer exhibited very good stability under blood circulation, low cardiotoxicity and remarkably capable of impeaching the BBB to deliver drugs to the brain tissues. This new concept for BBB research is shown in Figure 4.4.

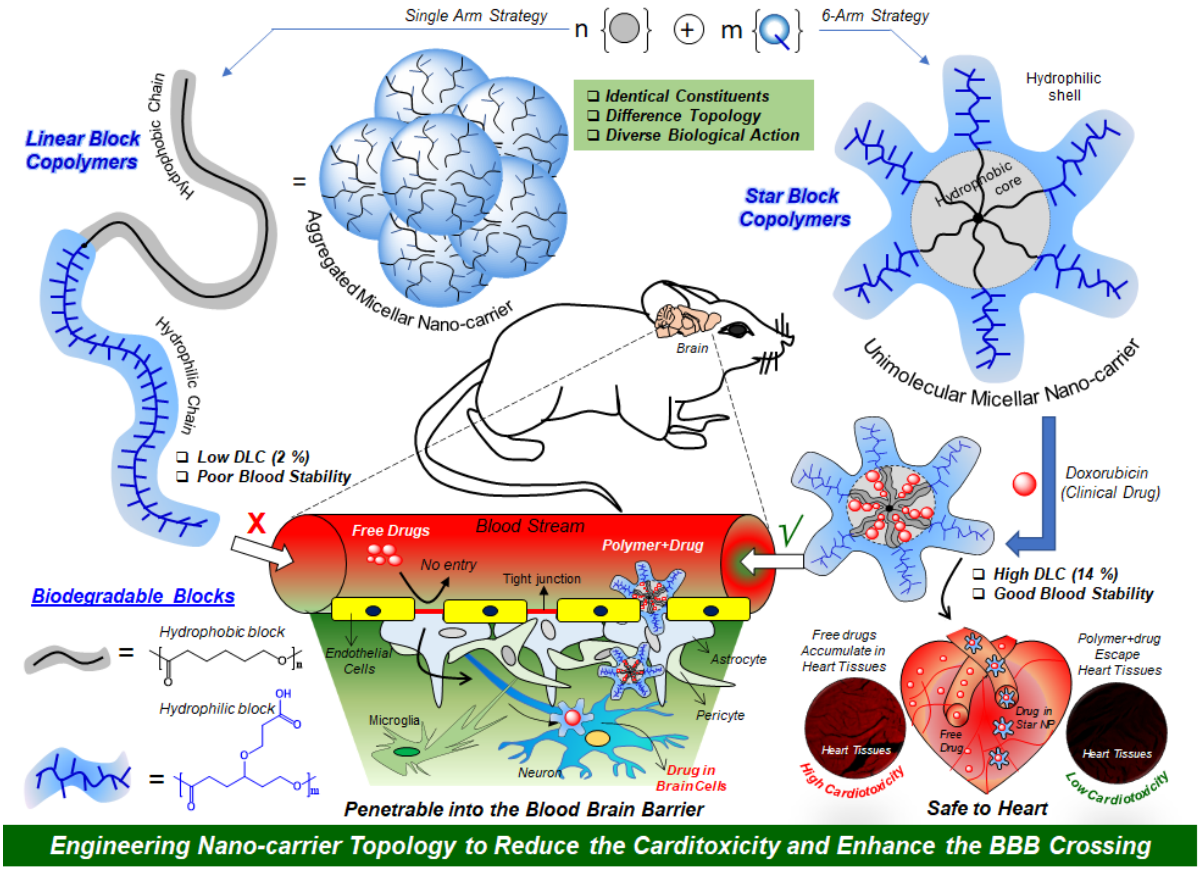

Figure 4.4. *Design and development of star and linear block biodegradable copolymer to study the role of polymer topology on their blood brain barrier crossing ability and also reducing the cardiotoxicity side effects in vivo.*

In the current chapter, the emphasis is to understand if topological tweaks in macromolecular architecture did in fact transcend directly onto their biodistribution, pharmacokinetics, and BBB crossing. For this purpose, two types of macromolecular architectures were structurally engineered having identical chemical composition (repeating

unit structure and number of units) and completely different topology such as linear di-block and star-block copolymers (synthetic details are explained in chapter 3). The newly designed tiny UMM (< 30 nm) has anionic charge at the periphery that makes them ideally suitable for BBB crossing.[300,302,303] The *in vivo* biodistribution data established the supremacy of the UMM over the larger aggregated micelles (> 100 nm) of linear block copolymer of identical composition (or free DOX) by manifesting their ability to cross the blood-brain barrier (BBB). UMM simultaneously significantly diminished the uptake by the heart tissues, thereby overcoming the cardiotoxicity side-effect of DOX. Microtubule assisted protein 2 (MAP 2) immunostaining was employed to mark the differentiated mature neurons in order to ascertain the brain uptake of UMM. The UMM and their DOX-loaded analogues proved to be non-immunogenic as per the cytokine analysis and showed no signs of toxicity to the tissue samples as can be visualized from the H&E staining. The present approach opens up new avenue of research opportunities based on biodegradable star-polymer macromolecules as potential futuristic single molecular (like UMM) nano-vectors for long-term BBB studies.

4.2 Experimental Methods

4.2.1 Materials

DAPI, Doxorubicin, Hemotoxylin, Eosin, paraformaldehyde, sodium azide, trizma base, EDTA, SDS and heparin were obtained from Sigma Aldrich chemicals. The optimal cutting temperature (OCT) medium was purchased from Leica (14020108926). DPX mountant and p-Xylene were procured from Thermo Fischer Scientific. Thiopentone injections (Thiosol sodium) was bought from Neon laboratories (50mg/kg). The primary antibody, i.e. Chicken anti-MAP-2 Antibody (ab92434) was procured from Abcam and the secondary antibody (Goat anti-chicken alexa flour 647) was obtained from Jackson's immunoresearch. Vectashield (Vector labs H-1000) was used as the mounting medium for the MAP2 antibody staining protocol. The cytokine analysis kit used was purchased from BD Life sciences (BD Cytometric Bead array Mouse Th1/Th2/Th17 Cytokine kit). The female balb/c and C57B1/6 male mice were obtained from the IISER Animal House facility, National Facility for Gene function in Health and Disease (NFGFHD).

4.2.2 Methods

The tissue samples were embedded in the tissue freezing medium (Leica) and sectioned using a cryotome. Confocal microscopic analysis of the DAPI stained tissue sections was done using Leica SP8 microscope. H&E stained tissue sections were imaged using the bright field microscope (Carl Zeiss) for histological analyses. Biodistribution assay to determine the amount of DOX in the tissue and plasma samples was performed on the microplate reader (Varioskan Flash) in triplicates. Cytokine Analysis was carried out on the BD Celesta Flow Cytometer at the BD Biosciences FACS facility at IISER, Pune. Cell Lysis buffer (200 mL), used for the dissolution of the tissue samples, was prepared from 2 mL of 1 M Tris-HCl (pH = 8), 0.4 mL of 0.5 M EDTA and 2 mL of 10 % SDS in 150 mL distilled water (volume made up to 200 mL).

4.2.3 Mice handling and injection of nano-vehicles

Female balb/c mice of 8-12 weeks old (~ 25g in weight) were chosen for the *in vivo* experiments and these were divided into 5 groups of n = 6 each, namely free DOX, SB-60+DOX, LB-60+DOX, SB-60 and LB-60. The aim behind the *in vivo* study was to unravel the effect of polymer topology on the biodistribution and pharmacokinetics parameters whilst comparing the same against the small molecule DOX, hence the three groups constituted were free DOX, SB-60+DOX and LB-60+DOX. The other two groups corresponded to nascent polymer scaffolds as control to their DOX-loaded counterparts to help evaluate the immunogenicity and cytotoxic effects, if any, of polymer alone. One mouse was injected with phosphate buffer saline only without any compound; the organs and plasma procured from this mouse served as the control. For all the experiments, the PBS, free DOX and all the nano-formulations were delivered using intraperitoneal injection. The DOX dosage for the biodistribution study was fixed at 2 mg/kg mice, which in this case translated to 50 µg DOX corresponding to 25 g mice and the concentration of DOX-loaded nano-formulations were determined using the drug loading content. Mice from group 1 were injected with 175 µL of DOX alone, group 2 mice were injected 184 µL of unimolecular SB-60+DOX and group 3 mice were injected 221 µL of linear block LB-60+DOX. The aforementioned calculation helped us determine the polymer amount required to inject 50 µg DOX and the same polymer concentration was injected into the mice in the nascent polymer groups. Collection of blood sample was done from retro-orbital sinus, alternating between the sinuses during the sequential collection. Blood was collected at

2, 4, 8 and 24 h after the injection. Absorbable hemostatic gelatin sponge (AbGel) was used if the bleeding did not stop on its own. Animals were left undisturbed, maintained *ad libitum* in between the time points of blood collection. Mice were sacrificed at the end of 24 h post injection by transcardial perfusion and organs were collected to be further utilized either for biodistribution or biochemical analysis. All animal care and procedures were in accordance with the Institutional Animal Ethics Committee (IAEC) at IISER Pune and the Committee for the Purpose of Control and Supervision of Experiments on Animals (CPCSEA), Government of India.

4.2.4 Biochemical analysis of organs and blood samples

Blood sample was collected from each animal (all 5 groups) in heparin coated vials. For each time point, approximately 15 µL of blood was withdrawn from one of the retro-orbital sinuses. The blood was then centrifuged immediately for 20 minutes at 10000 rpm at 4°C to separate plasma from RBCs. The plasma in the supernatant was collected separately in new heparin coated vials and were stored at -80°C until the biochemical assay was carried out. After procuring all the plasma samples, DOX estimation per mL plasma was carried out. Prepared the main DOX stock solution of 0.52 mg in 1.3 mL Cell lysis buffer (CLB) and using this 10 different DOX concentrations were made in a 96-well plate maintaining the total volume to be 50 µL in order to generate a calibration plot. In each well of the 96-well plate, 5 µL of the plasma sample was taken followed by 45 µL of the cell lysis buffer (1:10 dilution) for n = 6 mice of group 1 (free DOX), group 2 (SB-60+DOX) and group 3 (LB-60+DOX), and these were subjected to absorbance measurements at λ_{exc} = 487 nm using a microplate reader. Using the standard DOX curve, quantified the amount of DOX (µg) per mL of plasma and determined the pharmacokinetics parameters.

Brain, Heart, Liver, Kidneys and Spleen were obtained at 24-hour time point after the injection for the DOX containing 3 groups. Mouse received Thiopentone injections intra-peritoneally (Thiosol sodium, Neon laboratories, 50mg/kg) to achieve deep anesthesia state. Mice then were decapitated and organs were dissected. The organs were blot dried using gauze, weighed, separately put in the vials, flash frozen in liquid nitrogen and then stored in cryo-boxes at -80°C until the biochemical assay was carried out. The organs were crushed using a mortar pestle in the presence of liquid nitrogen into a fine powder, followed by the addition of cell lysis buffer. These samples were brought to room temperature and dissolved in the buffer by

pipetting. Aliquoted 50 µL of these tissue samples in CLB for further biochemical analysis. The aforementioned DOX standards were used for the assay and the calibration curve was generated by subjecting these samples to fluorescence measurements (λ_{exc} = 487 nm, λ_{em} = 580 nm, excitation bandwidth = 12 nm) using a microplate reader. The aliquoted tissue samples were taken in a 96-well plate (5 µL) and diluted 10 times with 45 µL of CLB, then measured their fluorescence as per the previously mentioned settings. The amount of DOX (µg) per mg of the tissue was determined using the calibration curve and the weight of the organs measured post dissection.

4.2.5 Histological analyses of organs

Histological analyses involved collection of organs of the 5 groups of mice. At 24 h time-point, mice received Thiopentone injections intra-peritoneally (Thiosol sodium, Neon laboratories, 50mg/kg) to achieve deep anesthesia state in order to carry out perfusion. Transcardial perfusion was done using 1X Phosphate buffered saline (PBS). Organs were dissected out and were put in separate 15 mL falcons filled with 4 % Paraformaldehyde (PFA). Organs were kept immersed in 4 % PFA at 4 °C for 24 h. They were then transferred to falcons filled with 0.01 % Sodium Azide in PBS (1X) and kept at 4 °C until required for the assays. To carry out H&E staining, 10 µm organ sections were taken on gelatin coated slides in a cryotome. Before cryotomy, organs were further transferred to falcons filled with 30 % sucrose for 24-48 hours for cryo-preservation. Upon obtaining the sections, the slides were air-dried at 37 °C for 30 minutes before further processing was done. The solutions required for H&E staining were stored in Couplin jars kept at room temperature. Slides were moved through a sequential series of couplin jars containing Hematoxylin, Scott's tap water, Eosin, grades of alcohol (95%, 100%, 50% Xylene-50% alcohol) and 100% Xylene. Sections on slides were then mounted using DPX mountant (Fisher scientific) and stored at 4 °C before carrying out microscopy. The sections were imaged using bright field microscope (Carl Zeiss) to carry out qualitative analysis of any alterations in the tissue sections obtained from the organs of different groups of mice.

4.2.6 Quantification of biodistribution of Doxorubicin in organs using confocal microscopy

Organs were separately embedded in optimal cutting temperature (OCT) medium (Leica,14020108926) and sectioned at 50 µm thickness in a cryotome. Freely floating sections were collected in 24 well/6-well plates filled with 1X PBS. DAPI (Sigma, 1:500 in 1X PBS)

staining was carried out for a total of 6/8 sections per organ (approx. 300-400 µm apart). Sections were mounted on glass slides using Mowiol based aqueous mounting medium and stored at 4 °C until imaged. Confocal microscopy to image the amount of DOX in several field of views (FOVs) was carried out for 5 sections. Biodistribution quantification was done by calculating the mean gray value of the DOX intensity in the three groups of mice using Fiji Image J. The FOVs that were chosen for calculation were devoid of blood clots (checked using the DIC mode).

4.2.7 MAP 2 Antibody staining

The 50 µm thick brain tissue sections of groups free DOX, SB-60+DOX and LB-60+DOX obtained via cryotome were subjected to MAP 2 antibody staining. For permeabilization and blocking, 2/3 large sections of the brain were added to a single well of a 24-well plate followed by addition of 250 µL of blocking solution (5 % Normal goat serum (NGS) and 1 % triton-X in 1X PBS) in each well and incubation at room temperature for 2 h. After the 2 h incubation, removed the blocking solution from each well. Added 1:1000 dilution of MAP 2 antibody (1 µL in 1 mL) in the blocking solution (1 % NGS and 0.2 % triton-X in 1X PBS), mixed well and then added 250 µL of this solution to each well. Incubated the plate on the shaker at 25 rpm for 20 h at 4 °C, followed by three 1X PBS washes, wherein for each wash the plate was kept on the shaker at 25 rpm, room temperature for 15 min. After the third wash, the 1X PBS was inoculated from each well. The secondary antibody was added to the blocking solution (1 % NGS in 1X PBS) in a 1:500 dilution (2 µL in 1 mL) and was thoroughly mixed before adding 250 µL in each well followed by incubation at room temperature for 2 h on the shaker at 25 rpm in the dark. After the incubation, each of the wells were washed with 1X PBS thrice as mentioned before. This was followed by DAPI staining at1:500 dilution (2 µL in 1 mL) in the blocking solution (1 % NGS in 1X PBS), 250 µL of this solution was added to each well, covered the plate with foil and kept on the shaker at 25 rpm for 10-12 mins at room temperature. The sections were mounted using the Vectashield mounting medium and stored at 4 °C until imaged.

4.2.8 Immunogenicity Analysis

The BD Cytometric Bead Array (CBA) Mouse Th1/Th2/Th17 Cytokine kit was employed to quantify the expression of cytokines in the plasma samples corresponding to the 24 h time point for all the mice (n = 6) across the 5 groups and the one control mice injected with PBS. The

plasma samples were thawed at 4 °C for 2-3 h prior to the experiment. The lyophilized Mouse Th1/Th2/Th17 standard spheres were reconstituted with 2 mL of Assay diluent, referred to as the "Top standard", equilibrated for ~ 15 min at room temperature followed by gentle mixing of the spheres (reconstituted protein) by pipetting. Serial dilutions were performed of the Top standard with the Assay Diluent in the ratios 1:2, 1:4, 1:8, 1:16, 1:32, 1:64, 1:128, 1:256 and one negative control was prepared containing only the Assay diluent. The next step was mixing of the five capture beads IL-2, IL-4, IL-17A, IFN-ɣ and TNF-α, wherein 10 µL of each capture bead for each assay tube was taken together and vortexed thoroughly. The plasma samples were diluted by the desired dilution factor (1:2, 1:10, 1:50 or 1:100) using the Assay diluent and then mixed thoroughly for the assay. The mixed capture beads were vortexed before adding 50 µL of the stock to each of the assay tubes (10 cytokine standards and plasma samples). To the control tubes, 50 µL of the cytokine standard dilutions were added such that the cytokine concentrations varied from 20 pg/mL (1:256 dilution) to 5000 pg/mL (Top standard). Further 50 µL of the plasma samples (diluted as mentioned above) were added to assay tubes containing the mixed capture beads. To all the assay tubes, 50 µL of the PE detection reagent was added followed by 2 h incubation at room temperature. Then 1 mL of wash buffer was added to all the assay tubes and centrifuged at 200 g for 5 min. The supernatant from each assay tube was decanted followed by addition of 300 µL wash buffer to each of the assay tube in order to resuspend the pellet. The samples were acquired on the BD Celesta (3 laser, 12 color) flow cytometer and analyzed using the FCAP Array software, wherein using the cytokine standard values the amount of each of the 5 cytokines was determined in all the plasma samples.

4.2.9 Hemolysis Assay

For the assay, blood sample (0.4 ml) was collected from C57B1/6 male mice (~ 9 weeks old) via the retro-orbital plexus puncture in heparin coated eppendorfs. The sample was centrifuged at 8000 rpm, room temperature for 10 min to separate the plasma from the red blood cells (RBCs). The supernatant plasma was discarded carefully leaving behind the RBCs and these were then washed with freshly prepared 1X PBS buffer thrice. Discarded the supernatant and diluted the RBCs using 1X PBS (5 % v/v). 100 µL of this diluted RBCs stock was taken in a 96-well plate followed by addition of 100 µL of various polymer concentrations ranging from 10 µg/mL to 1000 µg/mL. PBS was chosen to be the negative control and Triton-X was the positive control required for the determination of % hemolysis. All the samples were recorded

in triplicates. The 96-well plate was incubated at 37 °C for an hour followed by centrifugation at 1400 rpm for 10 min. Carefully 100 µL of the supernatant was transferred to another 96-well plate and the erythrocyte rupture was determined as a function of the amount of hemoglobin released by taking the absorbance read-out at 576 nm. Hemolysis (%) was determined using the formula:

Hemolysis (%) = [($O.D._{576nm}$ in polymer sample - $O.D._{576nm}$ in PBS)/($O.D._{576nm}$ in Triton-X - $O.D._{576nm}$ in PBS)] X 100

4.2.10 Statistics

All the analyses were done using Graphpad Prism 8.0 (Graphpad Software Inc, USA). Ordinary One-way ANOVA Turkey test was performed, and the values are represented as mean ± SEM

4.3 Results and Discussion

4.3.1 Biodistribution and Pharmacokinetics

A total of 31 mice of 8-12 weeks old balb/c strain (~ 25g in weight) were utilized to carry out the biodistribution and biochemical analysis of the anticancer drug doxorubicin to investigate the effect of the polymer nanoparticle topology on the drug uptake by various tissues. Three groups of mice with n = 6, group 1 for 'free DOX', DOX loaded star-block copolymer 'SB-60+DOX' (group 2) and DOX loaded linear block copolymer 'LB-60+DOX' (group 3) were utilized. Each group comprised of 6 mice; half of the mice (n = 3) were used for confocal imaging analysis of drug uptake by organs and histological analysis while the other half (n = 3) were utilized for biochemical analysis to quantify the amount of DOX in each organ. In order to understand the biocompatibility of the polymers alone, two additional groups (n = 6) were constituted as the control groups, namely SB-60 (group 4) and LB-60 (group 5) wherein the effect of nascent polymers on the mice was studied (for the complete experimental design, see figure 4.5).

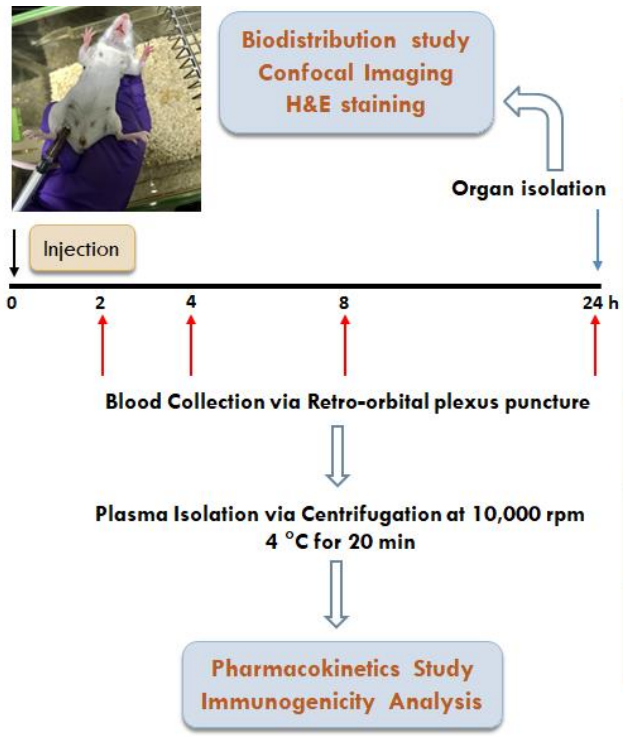

Treatment conditions	Number of mice
Free Drug (DOX) 2mg/kg body weight	6
Unimolecular SB-60+DOX 2mg/kg body weight	6
Linear Block LB-60+DOX 2mg/kg body weight	6
Unimolecular Nascent Nanoparticle SB-60	6
Linear Diblock Nascent Nanoparticle LB-60	6

Figure 4.5. *Schematic representing the experimental set-up along with the five different treatment conditions.*

As can be seen from figure 4.6a, for each mice the organs collected 24 h-post injection were the brain, heart, kidneys, liver and spleen. For the biodistribution quantification assay, the organs from n = 3 mice of the 3 groups (free DOX, SB-60+DOX, LB-60+DOX) were procured in eppendorfs that were flash frozen using liquid nitrogen and stored at -80 °C. These organs were crushed using a mortar pestle in the presence of liquid nitrogen, and then subjected to lysis using the Cell Lysis buffer in order to facilitate the membrane lysis of all the cellular organelles such that the DOX would come out into the solution. This was extremely important so that the absolute values of the amount of DOX in the various tissue samples for all the three groups could be measured using the microplate reader (Varioskan flash). To determine the accurate concentration of DOX in each tissue sample, a standard calibration curve was generated using known concentrations of DOX in the cell lysis buffer such that this curve could then be used to determine the unknown DOX concentrations from the respective absorbance/fluorescence values. Using the aforementioned calibration plot, all the exact DOX concentrations were determined and have been summarized in the bar diagram plot, as shown in figure 4.6b. The % injected dose (% ID) was determined by comparing the amount of DOX

in each organ with the amount of DOX injected into the mice and these values were plotted separately for all the organs. The % ID in heart was the highest in the case of free DOX whereas the values for the other two samples SB-60+DOX and LB-60+DOX were substantially lower. This was one of the highlight points of the study considering the fact that the major side effect of chemotherapy with DOX is cardiotoxicity and hence, reducing uptake of DOX by the heart tissue by means of the nano-formulations would greatly overcome the toxic effects of the drug. The uptake by the liver and spleen tissue was almost similar across the three groups with no significant difference. In case of the kidneys, the % ID for the SB-60+DOX group was higher compared to the other two groups that implied effective renal filtration of the unimolecular micelles. Another highlight point was the uptake difference in the brain tissue, wherein only the unimolecular micelles SB-60+DOX were taken up by the brain tissue and there was no significant uptake of free DOX and LB-60+DOX. This result was extremely substantial in proving our initial hypothesis that polymer topology had major influence on not only the size and encapsulation capability but also on the ability to cross biological barriers such as cellular barriers and the blood brain barrier (BBB). The DOX concentration was also determined in the plasma samples, that were collected via retro-orbital plexus puncture at various time points (see figure 4.5), and these values are shown in the Pharmacokinetics plot (figure 4.6c). As can be seen from the plot, the DOX concentration in plasma for the free DOX group and the linear block group were already less than half of the injected dose at the initial time points, thus their half-life could not be determined. The $t_{1/2}$ for the SB-60+DOX group was determined to be 4.0 h using the non-compartmental analysis in the PK Solver software employing the log-linear trapezoidal method.

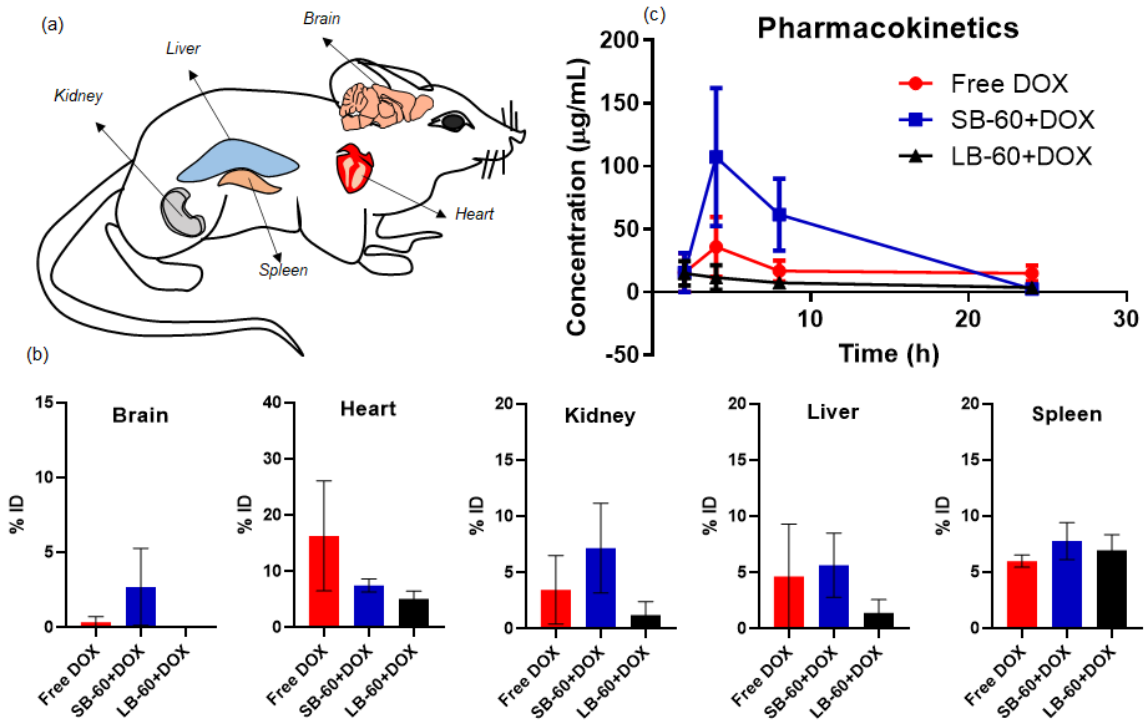

Figure 4.6. *(a) Illustration of the mice with organs that were procured for biodistribution analysis. (b) Quantification of DOX in kidneys, liver, spleen, heart and brain for free DOX, SB-60+DOX and LB-60+DOX represented as the % Injected dose (% ID). (c) Concentration of DOX in plasma for free DOX, SB-60+DOX and LB-60+DOX.*

4.3.2 Immunogenicity, Histology and Hemolysis

Another crucial pre-requisite for a nano-formulation is non immunogenicity, i.e. the ability to not provoke an immune response upon entering the system and this can be easily monitored by determining the cytokine expression. When the body recognizes a foreign substance as harmful, it triggers an immune response in the body to fight the threat and in this process several anti and pro-inflammatory cytokines are released in the body. Monitoring the concentration of a few of the important cytokines upon injecting the different formulations to mice would give us a direct read out of any immune response in the mice. In order to quantify the cytokine expressions, the BD Cytometric Bead Array (CBA) Mouse TH1/Th2/Th17 Cytokine kit was employed, and the sample acquisition was done on BD Celesta flow cytometer followed by data analysis using the FCAP Array software. For the purpose, the plasma samples collected from all the 31 mice (5 groups plus 1 mouse injected with 1X PBS as control) at 24 h time point were subjected to the aforementioned analysis and the

concentration of five different cytokines, i.e. IL-2, IL-4, IL-17A, IFN-ɣ and TNF-α were determined using the Cytokine standard values. As can be seen from figure 4.7a, the amount of cytokine expression was similar across all groups and similar to the values obtained from the plasma sample of the mice injected with PBS. The mice injected with PBS acts as the negative control wherein no immune response is expected in the mice since PBS is non immunogenic. Across all five groups, the cytokine expressions were very similar to that observed in the case of PBS and the values were < 5 pg/mL, which clearly pointed out that there was no immune response in the mice and that the nano-formulations were not immunogenic; hence suitable to be used as drug delivery vehicles.

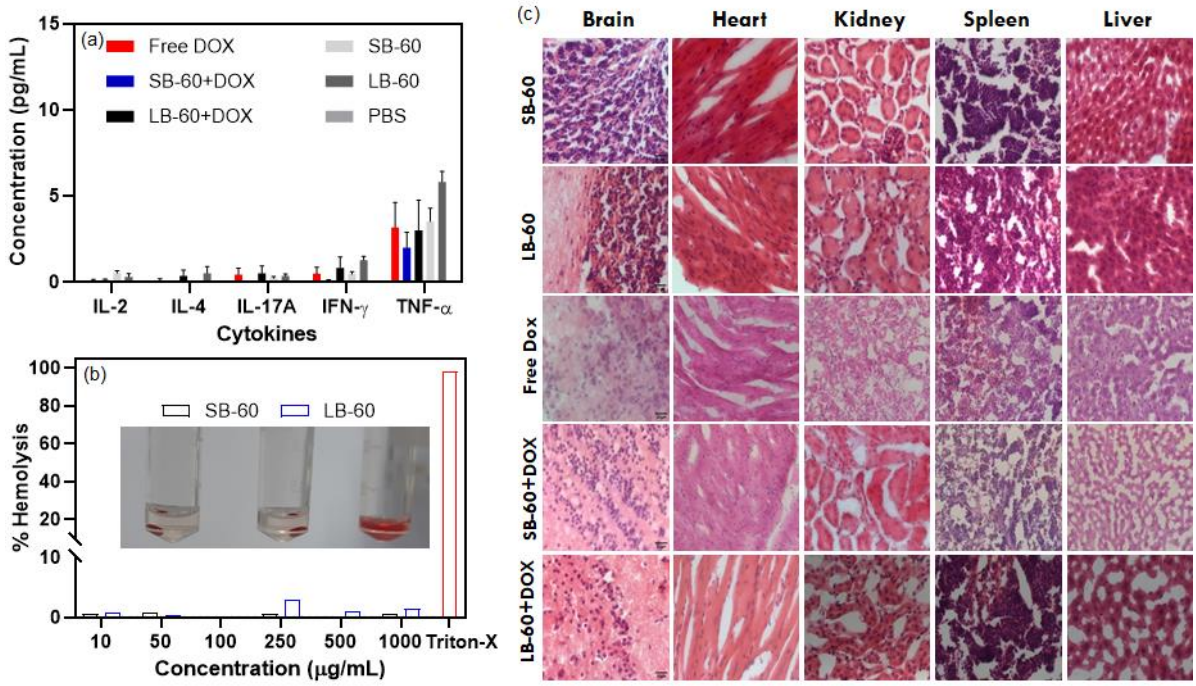

Figure 4.7. *(a) Concentration of the cytokines IL-2, IL-4, IL-17A, IFN-ɣ and TNF-α in the plasma samples of all the 31 mice. (b) Plot of % Hemolysis vs. polymer concentration for the star and linear block copolymers SB-60 and LB-60. Triton-X served as the positive control (c) H&E (Hematoxylin & Eosin) stained tissue samples for SB-60 (first panel), LB-60 (second panel), free DOX (third panel), SB-60+DOX (fourth panel) and LB-60+DOX (fifth panel) imaged using Carl Zeiss microscope at 40 X.*

Having determined that the star and linear block copolymers were non-immunogenic, the next obvious step was to investigate the biocompatibility of these polymers with respect to red blood cells (RBCs). For this, the hemolysis assay was employed that gives information on whether the polymer interaction with the erythrocytes results in their rupture by monitoring the

hemoglobin release using an absorbance read-out. Herein, PBS buffer was used as the negative control and triton-X served as the positive control. Triton-X causes RBCs lysis due to osmosis resulting in 100 % hemoglobin release, as can be seen from the red color in the last eppendorf (figure 4.7b). In the presence of PBS, star and linear block copolymers, the erythrocytes remained stable displaying no significant hemoglobin release (no visible red color was observed in the first 2 eppendorfs corresponding to the star and linear block copolymer, respectively). The plot of hemolysis (%) vs polymer concentrations clearly exhibited that the polymers were highly biocompatible with almost negligible hemolysis values at concentrations as high as 1000 µg/mL (figure 4.7b).

Half of the mice from each group (3) were used for histological analysis and confocal imaging analysis of DOX uptake by organs. These organs were sectioned using cryotome into 10 µm thin sections and were directly taken onto gelatin-formaldehyde coated glass slides, which were then subjected to histological analysis. Histological analysis involved Hematoxylin-Eosin (H&E) staining to confirm that the DOX delivered using different polymer topologies and the polymers itself did not cause any morphological alterations in the tissue. The images (40X) obtained using bright field microscope (Carl Zeiss) showed no signs of necrosis, blood clotting or morphological alterations in any of the tissue samples for the SB-60+DOX and LB-60+DOX group, as can be seen in the fourth and fifth panel in figure 4.7c. However, in the first panel some blood clotting was observed in the heart tissue and according to the literature, that is a sign of cardiotoxicity augmented by free DOX. Hence, the star and linear block copolymer DOX loaded assemblies did not result in any damage to the tissues whereas, on the other hand, free DOX group showed signs of cardiotoxicity, inherent to it's nature. The polymer alone samples SB-60 and LB-60 did not result in any morphological changes in the tissue samples either (see panels 1 and 2 in figure 4.7c). Images were also captured at a lower resolution (10 X) for all the 5 groups (see figure 4.8).

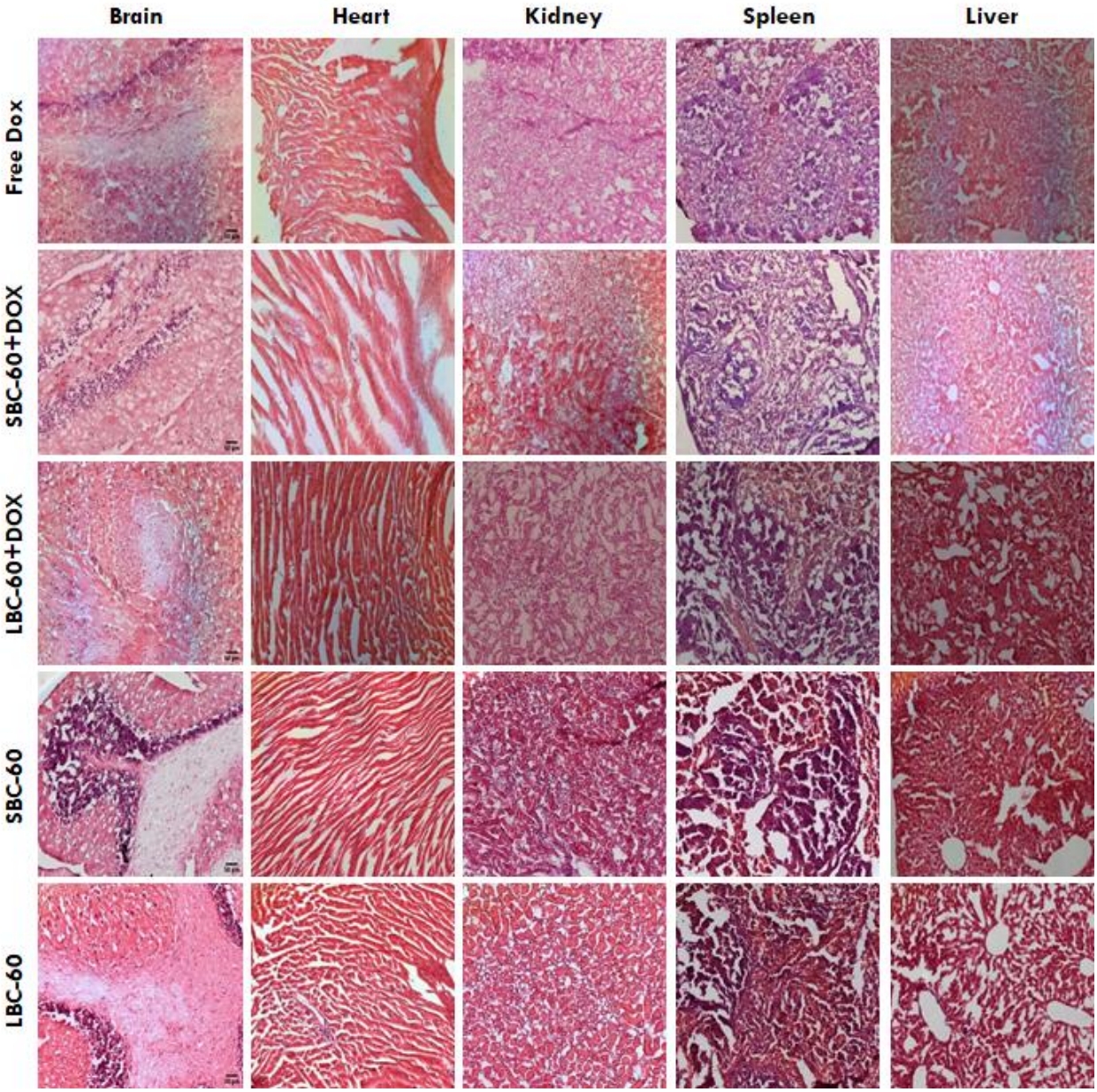

Figure 4.8. *Representative images (10X) of H&E stained tissue samples. Scale bar = 50 µm*

4.3.3 DOX uptake visualization using Confocal imaging

All the retrieved organs were subjected to cryotome sectioning resulting in 50 µm sections. These sections were collected in 1X PBS in 24-well/6-well plates, as per the requirement and stored at 4 °C. For each organ, 5-6 sections were selected to be stained with DAPI and these were then imaged using Leica SP8 to visualize the uptake of DOX by various

organs. These sections were imaged at 10 X, the brain and heart tissues are shown in figures 4.9 and 4.10. For images from kidney, liver and spleen are shown in figures 4.11 to 4.13. In figure 4.9 representing the brain images, only SB-60+DOX nano-formulation exhibited a strong red fluorescence signal whereas, no signal was observed in the other two groups. As is known from the literature, small molecule chemotherapeutic drugs are unable to cross the blood brain barrier (BBB) which has translated to the failure in treating various types of brain tumor and other neurodegenerative diseases. The BBB heterogeneity is such that only certain molecules are allowed to pass through the barrier and size of the nano-formulation seems to play a crucial role in crossing the BBB. These novel SB-60+DOX micelles are in the size range of 18-30 nm (as can be seen in figure 3.12), which are in the ideal range of nano-formulations suitable to cross the BBB. These SB-60+DOX micelles were able to passive selectively cross the BBB, accumulate in the brain tissue and these being stable at infinite dilution would not result in a premature drug release.

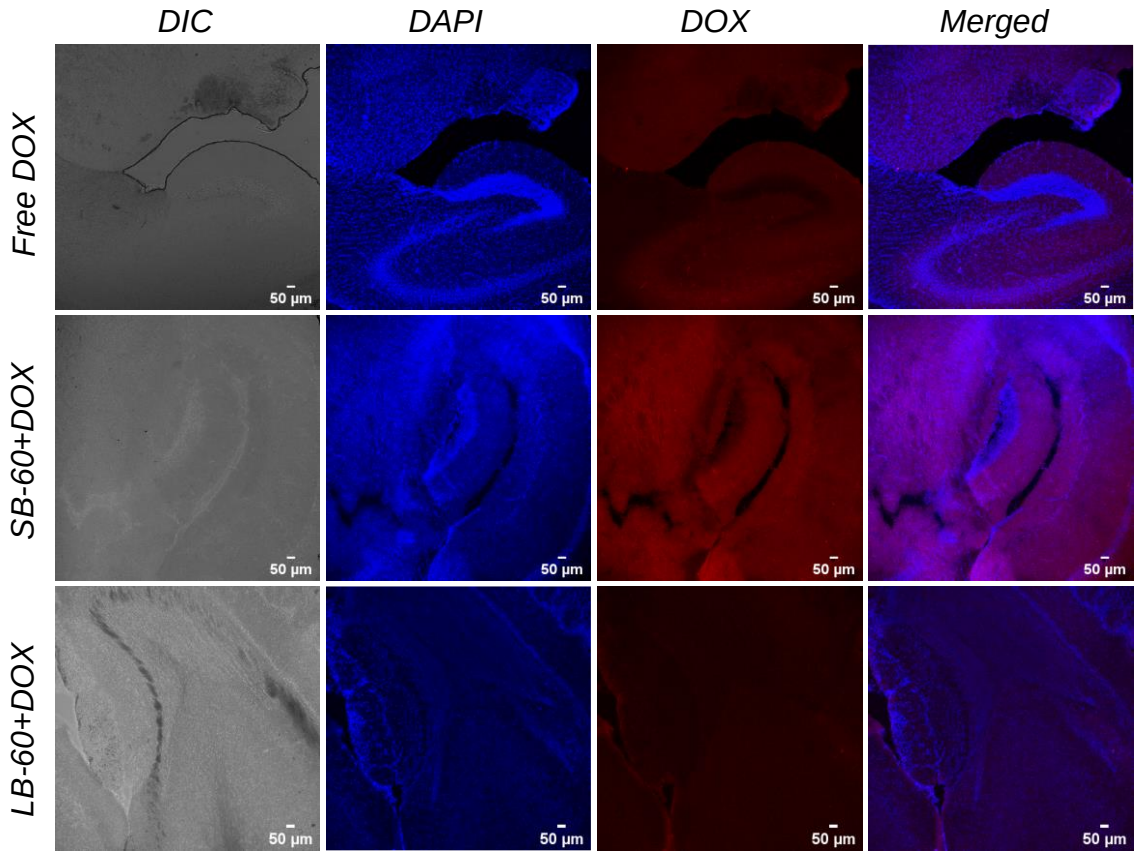

Figure 4.9. *Representative CLSM images (10X) depicting the uptake of free DOX, SB-60+DOX and LB-60+DOX for the Brain tissue.*

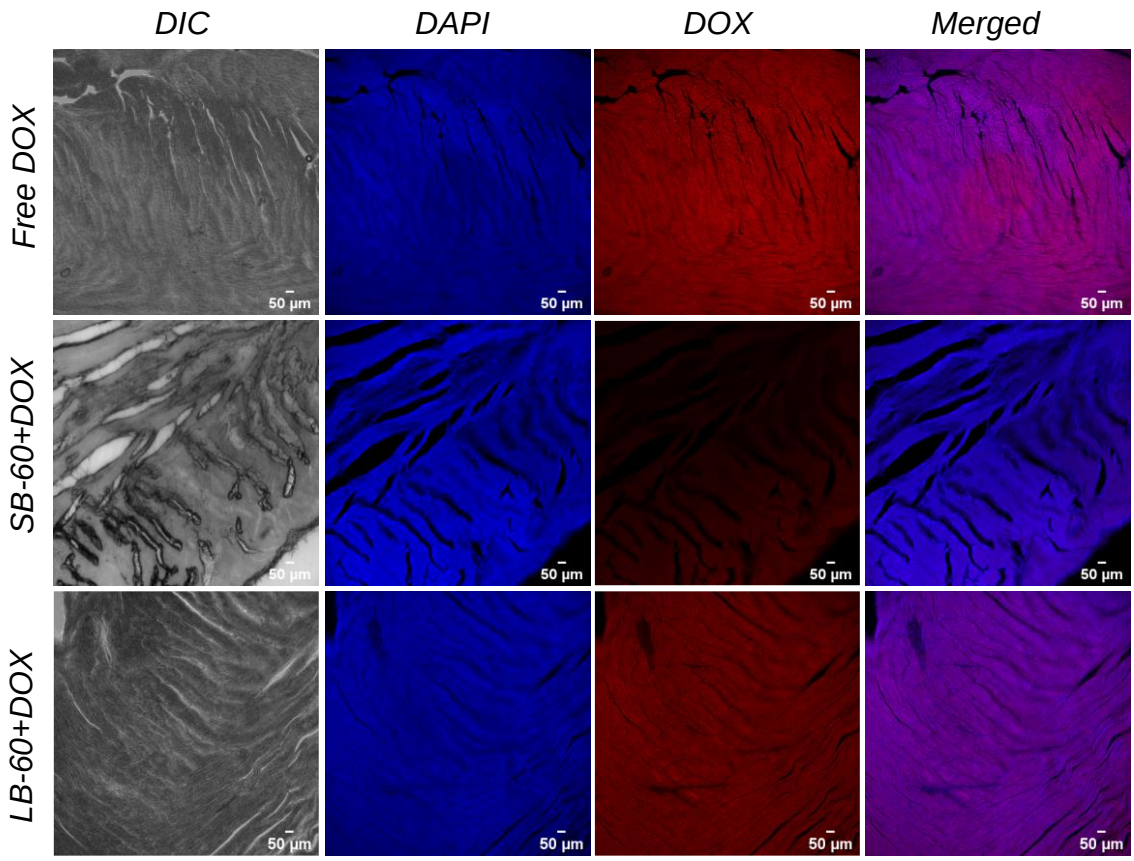

Figure 4.10. *Representative CLSM images (10X) depicting the uptake of free DOX, SB-60+DOX and LB-60+DOX for the Heart tissue.*

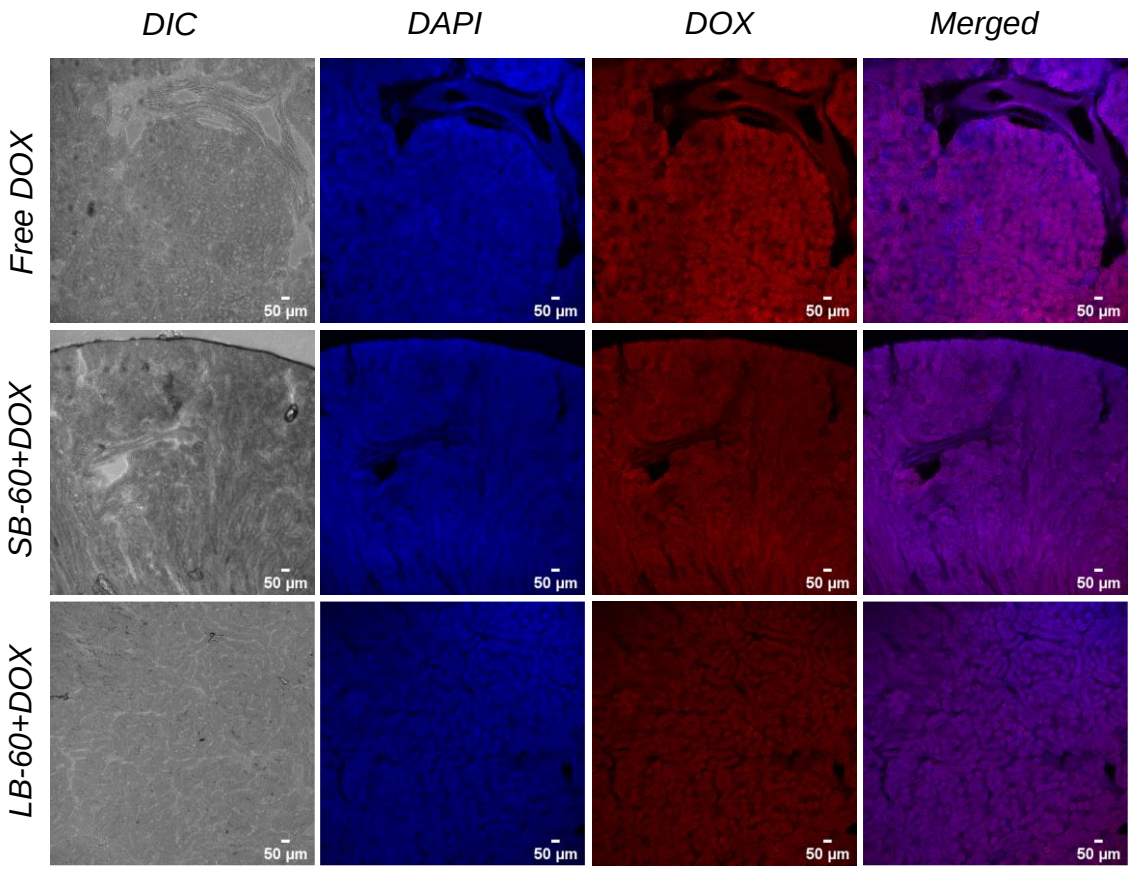

Figure 4.11. *Representative CLSM images (10X) depicting the uptake of free DOX, SB-60+DOX and LB-60+DOX for the Kidney tissue.*

Another brownie point for these SB-60+DOX micelles was their ability to reduce uptake in the heart tissue, as can be seen from the second panel of the heart tissue images. The signal of the SB-60-DOX micelles was extremely weak compared to the strong red signal corresponding to free DOX and the faintly higher signal from the linear block LB-60+DOX group. Thus, the current design of SB-60 UMM can overcome the aforementioned limitation and facilitate the use of even higher doses of DOX for chemotherapy in long term. The unprecedented stability of unimolecular micelles against external factors such as dilution or the pressure of blood pumping makes them highly resilient and avoids rupturing of these nano-carriers in the heart tissue. Also, the size of these SB-60+DOX micelles allows for easy filtration or escape from the heart muscles and all these factors combined result in reduced cardiotoxicity.

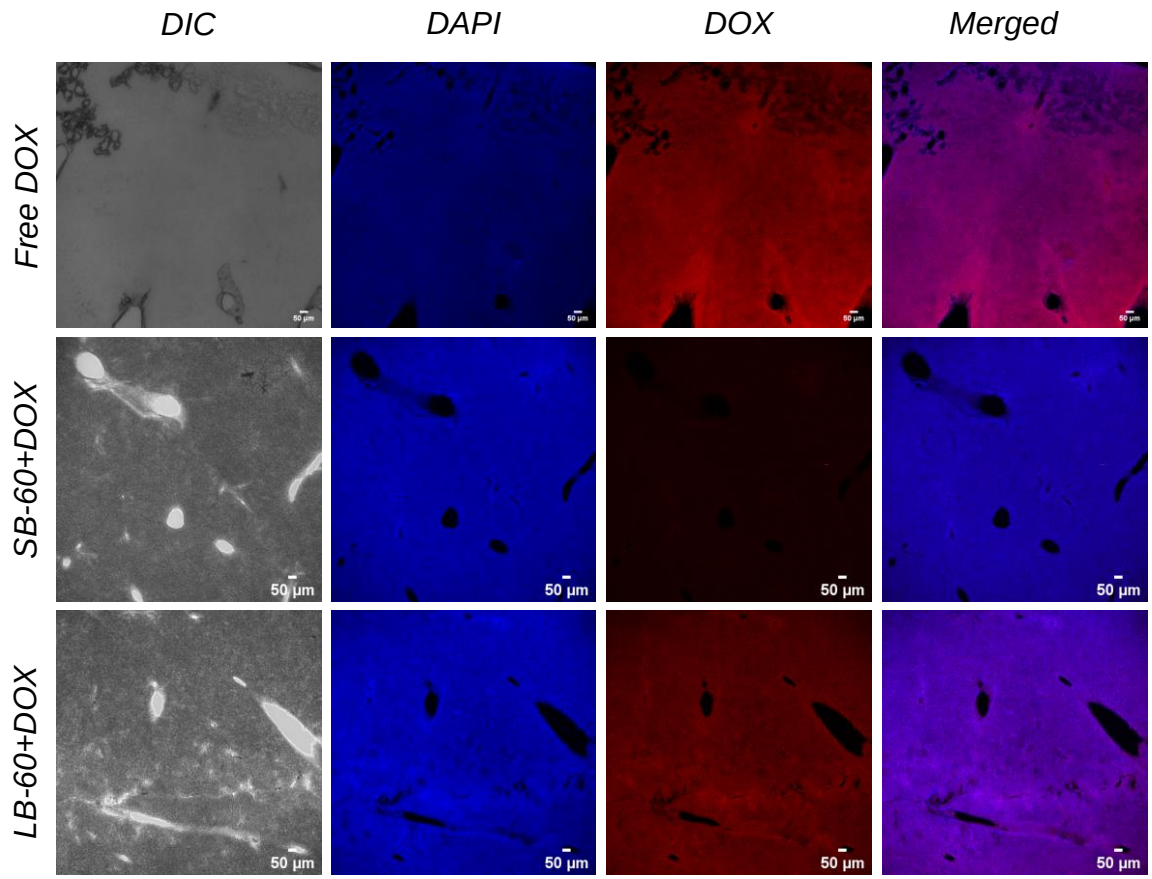

Figure 4.12. *Representative CLSM images (10X) depicting the uptake of free DOX, SB-60+DOX and LB-60+DOX for the Liver tissue.*

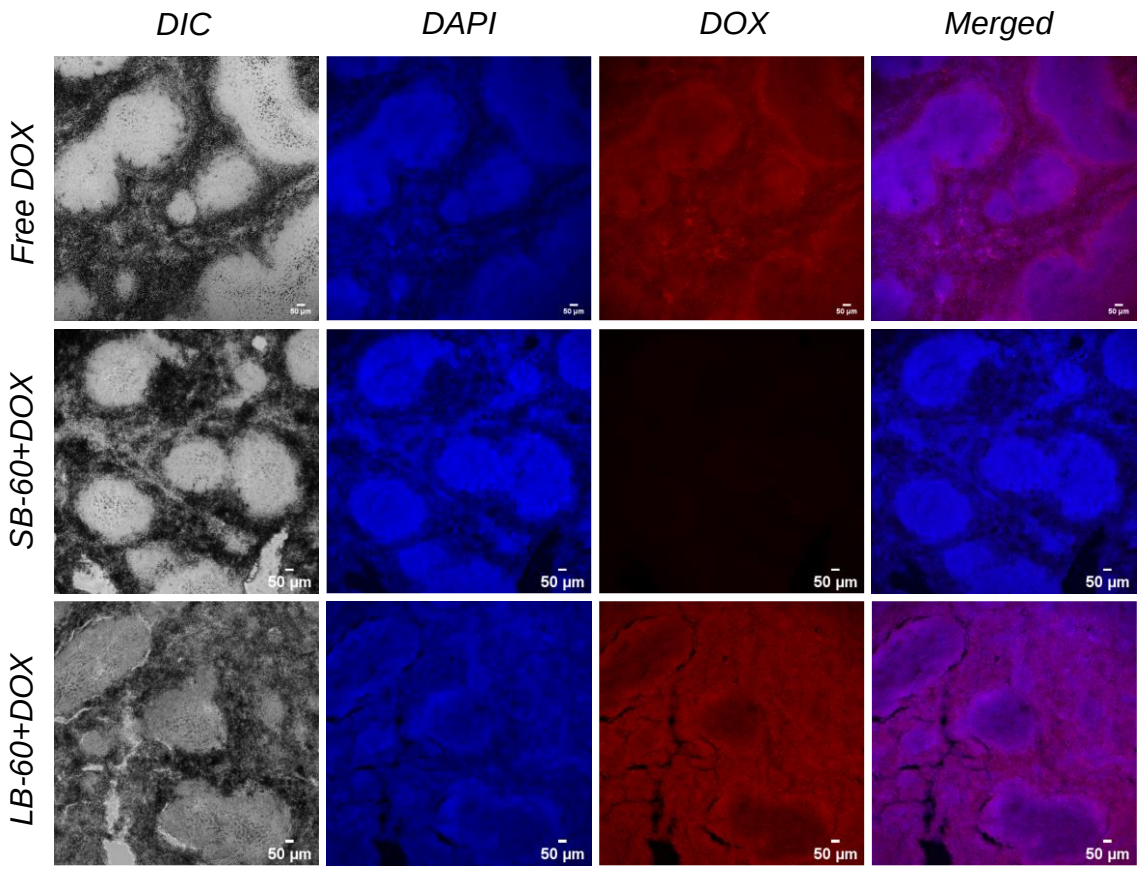

Figure 4.13. *Representative CLSM images (10X) depicting the uptake of free DOX, SB-60+DOX and LB-60+DOX for the Spleen tissue.*

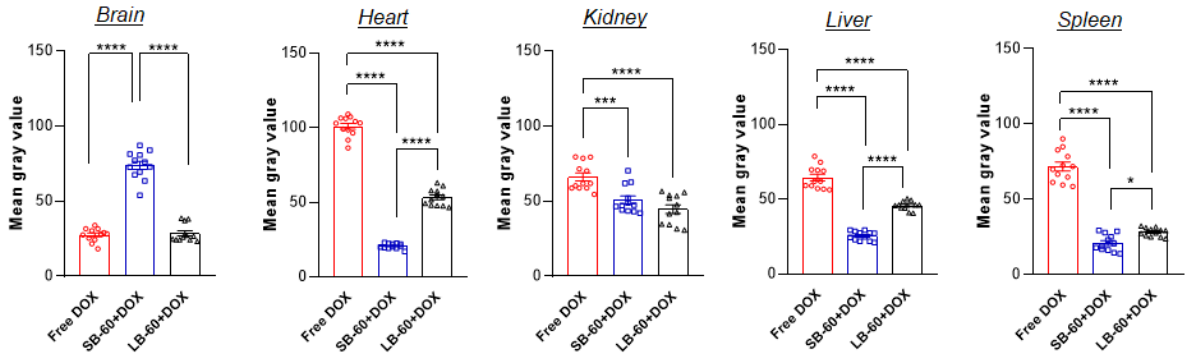

Figure 4.14. *Plot of Mean gray values representing the quantification of uptake of Free DOX, SB-60+DOX and LB-60+DOX by the Brain, Heart, Kidney, Liver and Spleen tissue samples. Each point represents mean ± SEM (n = 12) (**** P < 0.0001, *** P = 0.001).*

The uptake of all the three groups by various tissue samples from the confocal images was analyzed by determining the mean gray values in order to be able to quantify the DOX uptake. As can be seen from Figure 4.14, the mean gray values of the DOX uptake of all the three groups by various tissue samples has been summarized. The SB-60+DOX micelle exhibited enhanced uptake in the brain tissue and drastically reduced uptake by the heart tissue compared to an opposite trend in the other two groups. The renal clearance was the highest in case of free DOX compared to the other two groups. The SB-60+DOX group exhibited reduced RES uptake as can be seen from the low mean gray value in the liver and spleen tissue, significantly lower than the other 2 groups. The mean gray value quantification done from the confocal imaging analysis observed here was quite similar to the trend observed via the biodistribution trend. Tissues images at 63 X are provided in figures 4.15 to 4.19.

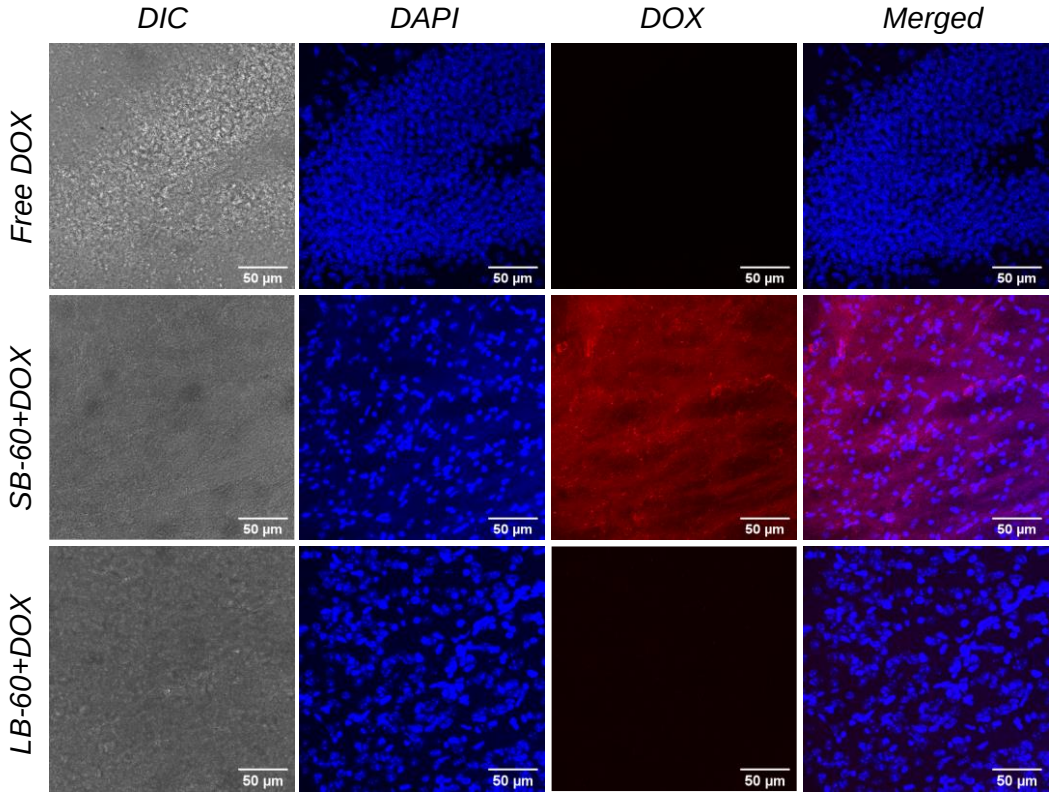

Figure 4.15. *Representative CLSM images (63X) depicting the uptake of free DOX, SB-60+DOX and LB-60+DOX for the Brain tissue.*

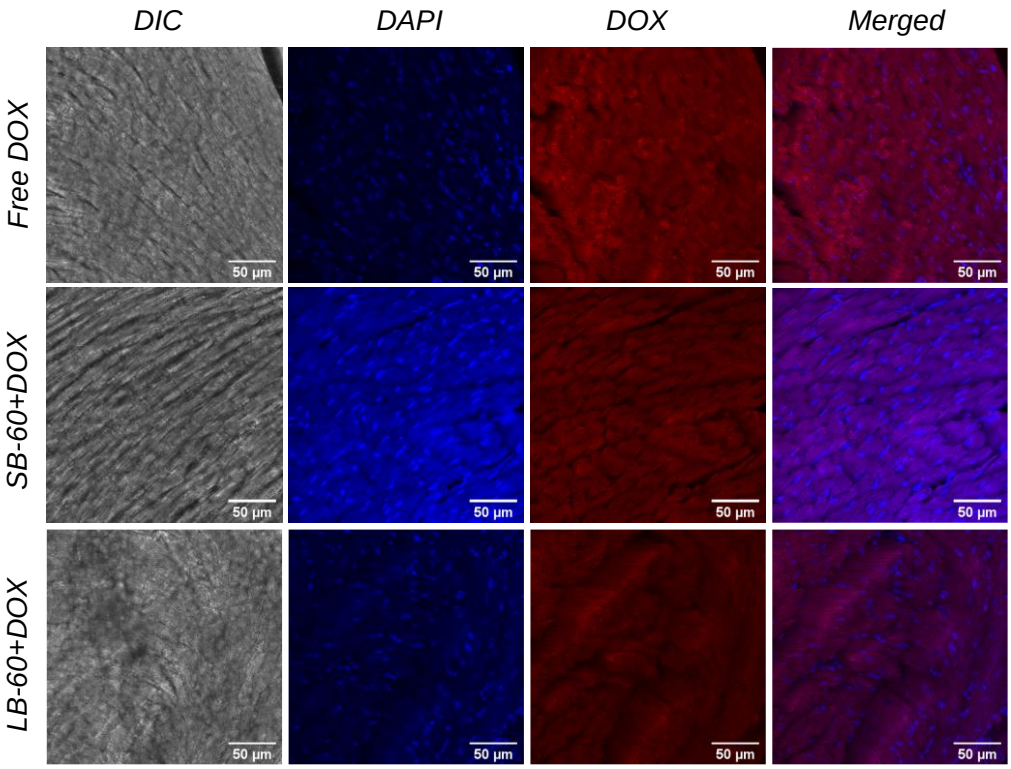

Figure 4.16. *Representative CLSM images (63X) depicting the uptake of free DOX, SB-60+DOX and LB-60+DOX for the Heart tissue.*

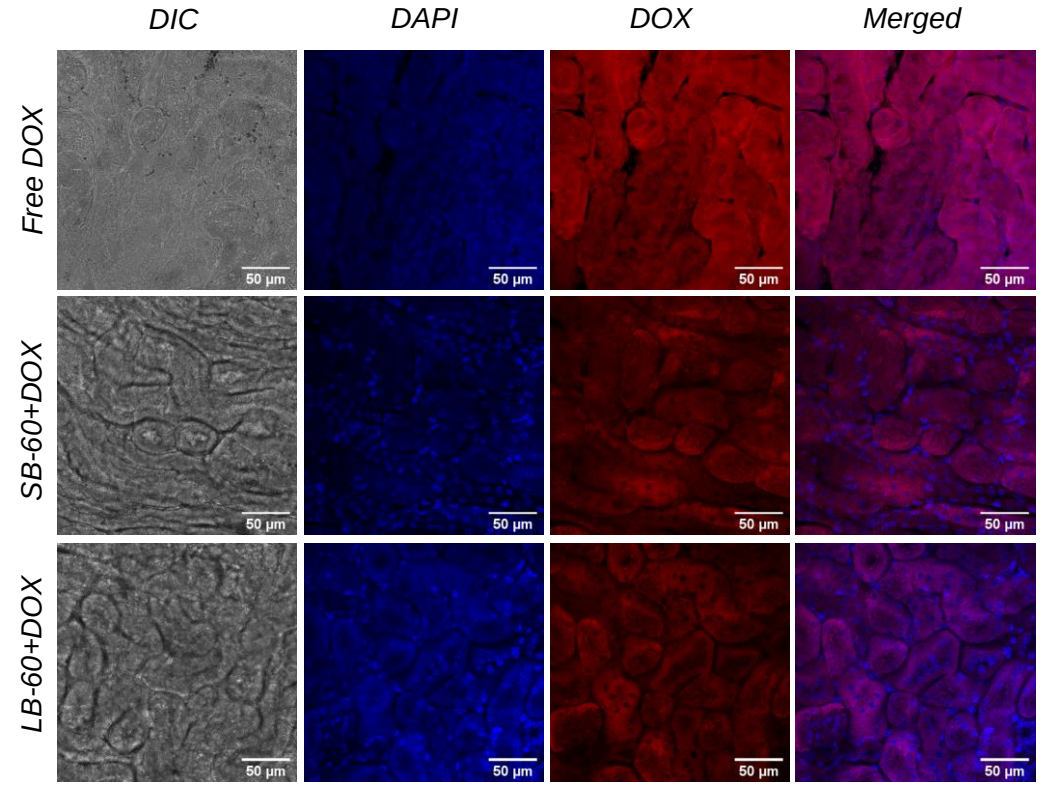

Figure 4.17. *Representative CLSM images (63X) depicting the uptake of free DOX, SB-60+DOX and LB-60+DOX for the Kidney tissue.*

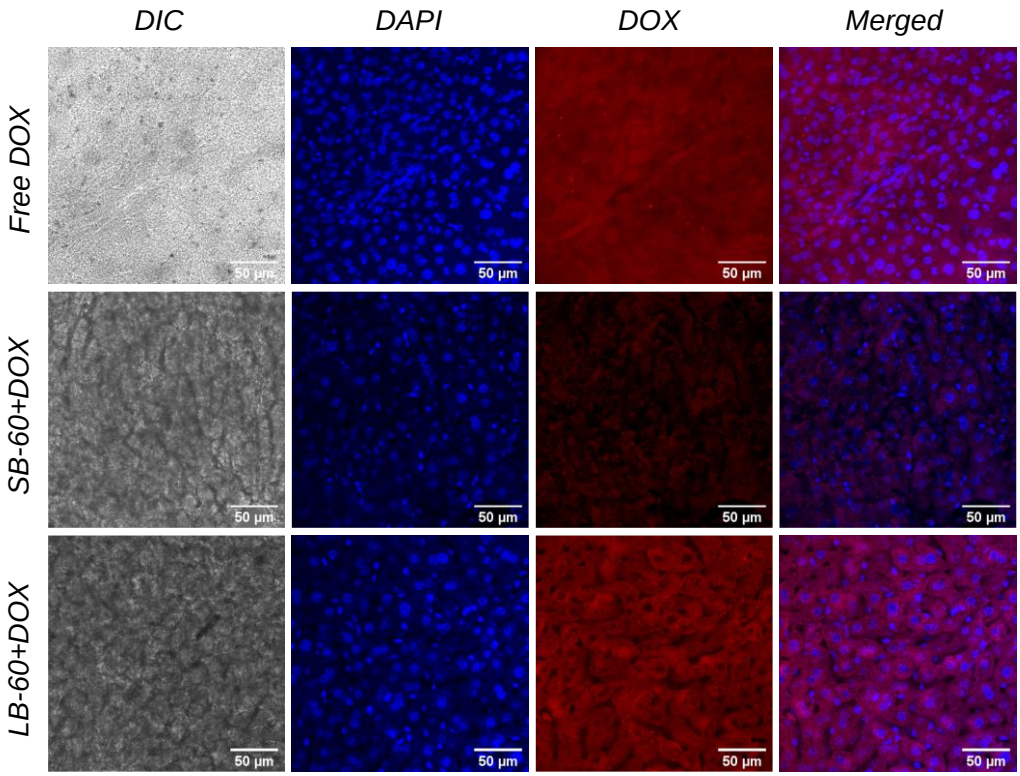

Figure 4.18. *Representative CLSM images (63X) depicting the uptake of free DOX, SB-60+DOX and LB-60+DOX for the Liver tissue.*

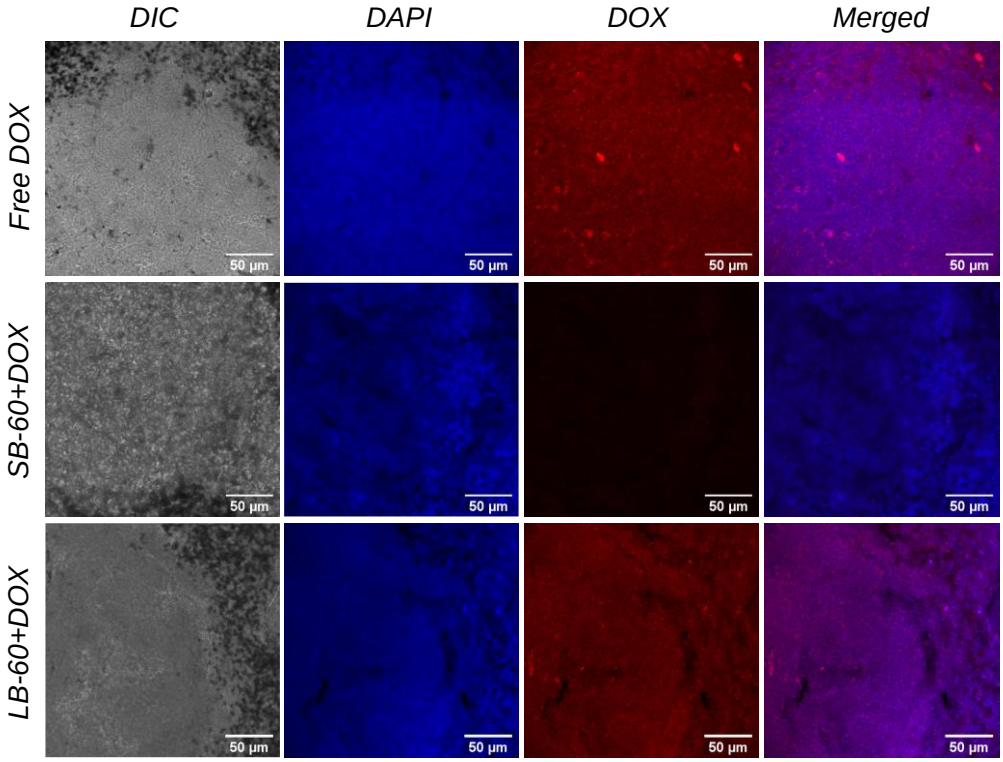

Figure 4.19. *Representative CLSM images (63X) depicting the uptake of free DOX, SB-60+DOX and LB-60+DOX for the Spleen tissue.*

4.3.4 Blood Brain Barrier Crossing

It is well articulated in the literature that the blood brain barrier strictly regulates the passage of molecules into the brain parenchyma across the tight junctions and this depends on various factors such as the molecular weight, lipophilicity, size etc. However, Allen et al. were the first to report that another major player contributing in the ability to breach the BBB is the surface charge of the nano-carriers. The work laid out that slightly anionic charged and neutral nanoparticles were able to cross the BBB more significantly than the cationic counterparts and they also did not disintegrate the barrier. Hence, the presence of negatively charged carboxylic groups along with the small size of the unimolecular micellar shape in SB-60 contributed the much-needed attributes to be able to cross the BBB. We hypothesize that the nanoparticle uptake into the brain tissue was mediated via transcytosis with the aid of the anionic surface charge and compact size. The biochemical and confocal imaging analysis established that the novel design SB-60+DOX unimolecular micelles were able to cross the blood brain barrier. This led to the interrogation of whether the nano-formulations were taken up equally by different parts of the brain tissue and this was executed by quantifying the DOX intensities from the confocal images.

To substantiate this above claim, confocal imaging analysis was carried out for five parts of the brain tissue, namely cerebellum, amygdala, hippocampus, cortex and olfactory bulb (posterior to anterior, see brain tissue section in figure 4.20a), wherein 10 different regions of interest were selected across n = 3 mice belonging to the SB-60+DOX group. The representative confocal images are shown in figure 4.20b and the DOX intensities visibly decreased upon going from the posterior part of the brain (cerebellum) to the anterior part (olfactory bulb). This was corroborated by the quantification of DOX intensities as mean gray values plotted against the corresponding part of the brain tissue, see figure 4.20c. The plot exhibited highest mean gray values for the cerebellum, amygdala and hippocampus; whereas the SB-60+DOX uptake was significantly less by the cortex and olfactory bulb. This can be attributed to the variation in the blood brain barrier heterogeneity and permeability across different parts of the brain, which depends on factors such as the astrocyte and pericyte concentration, structural differences, differences in tight-junction proteins like ZO-1 and ZO-2, so on and so forth.

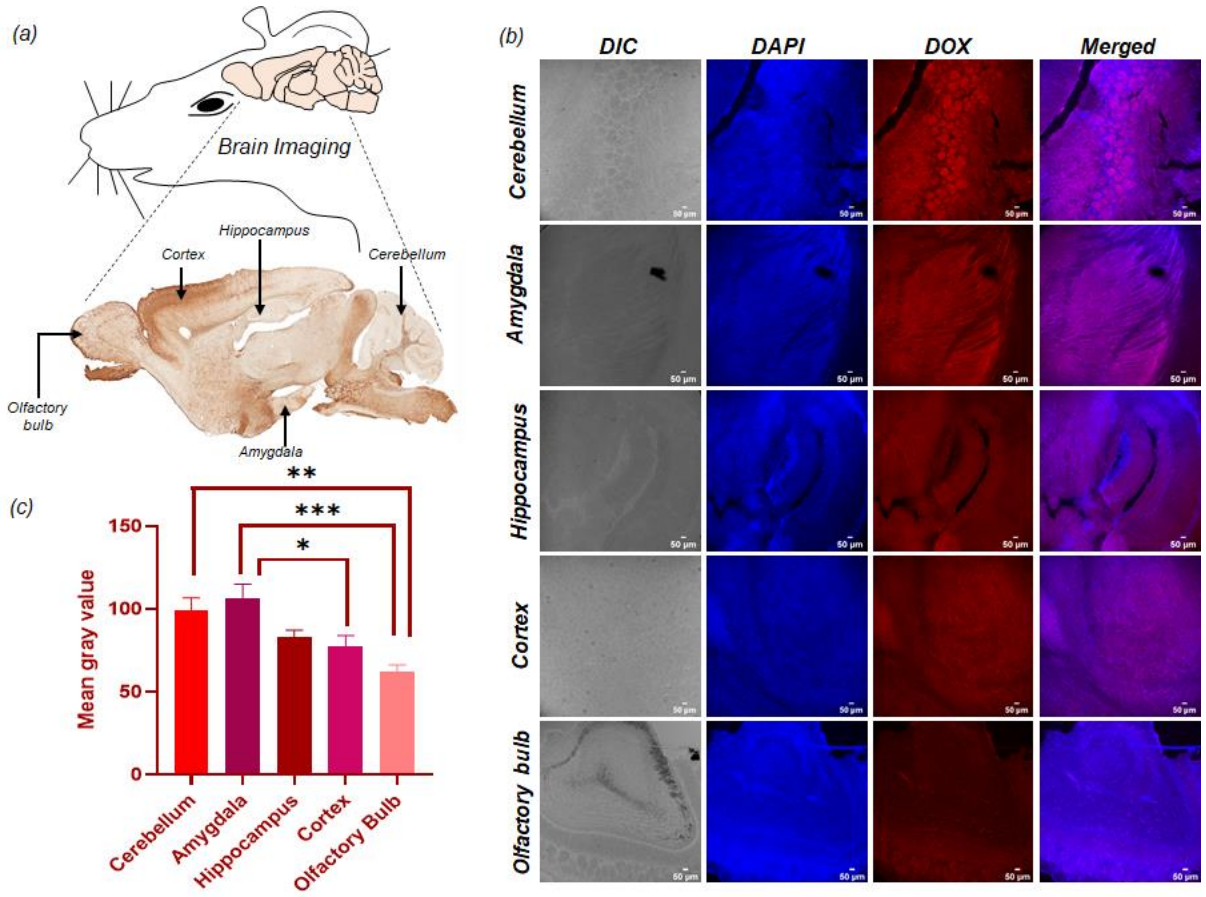

Figure 4.20. *(a) Representative Brain tissue section labelled with different parts, taken from the Mouse Brain Atlas. (b) CLSM images (10X) depicting the uptake of unimolecular micelle SB-60+DOX across different parts of the brain. (c) Plot of Mean gray value vs. different parts of the brain tissue for the SB-60+DOX nanoparticle. Each point represents mean ± SEM (n = 10) (*** P = 0.0001, ** P = 0.002, * P = 0.02).*

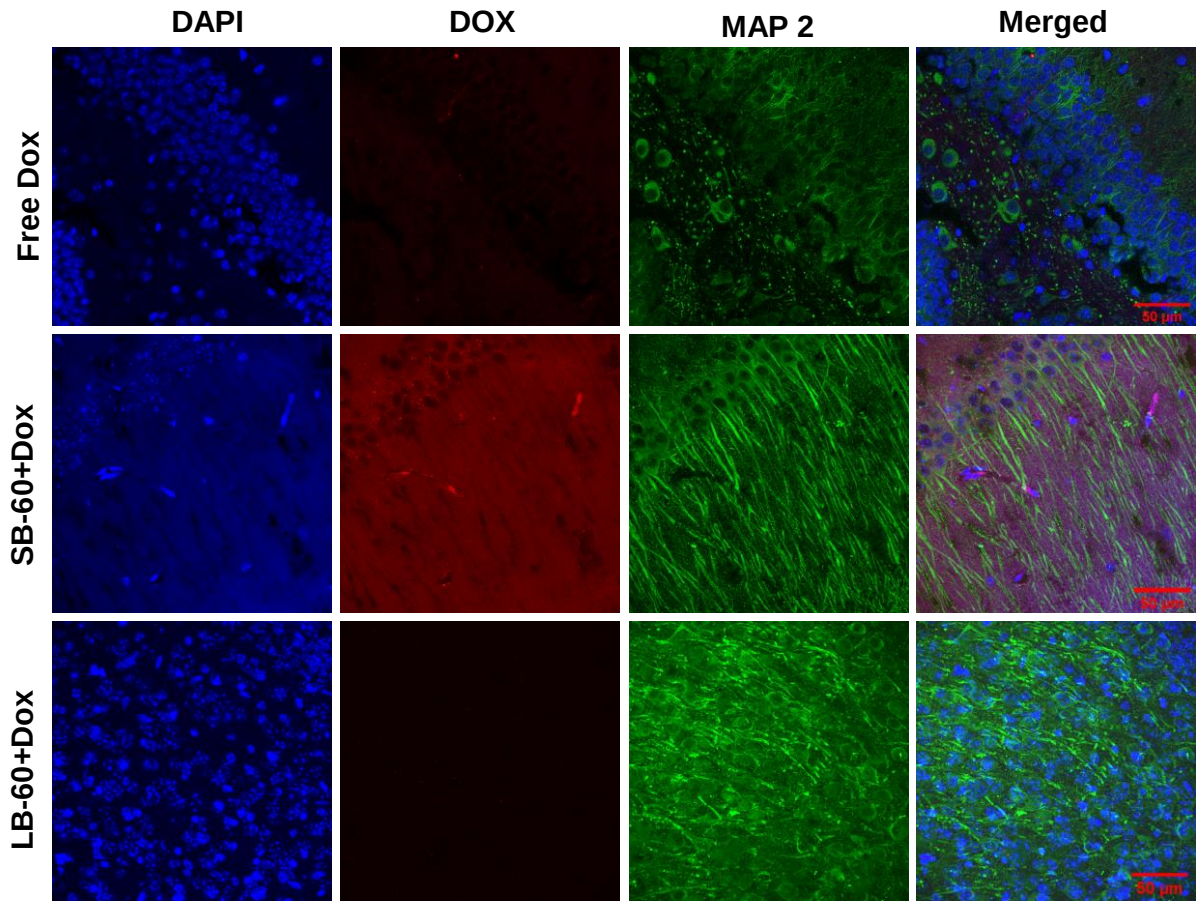

Figure 4.21. *CLSM images (63X) of the MAP 2 antibody staining carried out for the brain sections of free DOX, SB-60+DOX and LB-60+DOX.*

The unimolecular micelles SB-60+DOX were successful in crossing the blood brain barrier, as is evident from the aforementioned analysis; however, there was still a question of whether the DOX was only present in the extracellular tissue or was taken up by the cells. In order to examine the intracellular uptake of these micelles, the MAP 2 antibody staining was carried out. Microtubule associated protein 2 (MAP 2) is a cytoskeleton protein responsible for maintaining structural integrity of microtubule network, neuronal plasticity and is a marker for the differentiated mature neurons. MAP 2 stains the mature neurons in the brain tissue and the emission of DOX coming from within the mature neurons was an affirmation of the intracellular uptake of the cargo. The 50 µm brain tissue sections of the free DOX, SB-60+DOX and LB-60+DOX groups were subjected to the antibody staining and these stained sections were then imaged using Leica SP8. The 63 X representative images of DAPI and MAP 2 stained brain sections are shown in figure 4.21 (for the 10X images, see figure 4.22). As can

be seen from the first and third panel, there was no DOX emission in the tissue as has been already shown in figure 4.9. The second panel in figure 4.21 corresponding to the SB-60+DOX nano-scaffolds displayed significant DOX emission (red) coming from within the matured neurons stained with MAP 2 (green) and was highly evident from the merged image. This experiment reiterated the fact that only SB-60+DOX unimolecular micelles were able to cross the blood brain barrier compared to free DOX and LB-60+DOX; also apart from crossing the blood brain barrier the star-shaped DOX loaded micelles were also taken up by the cells.

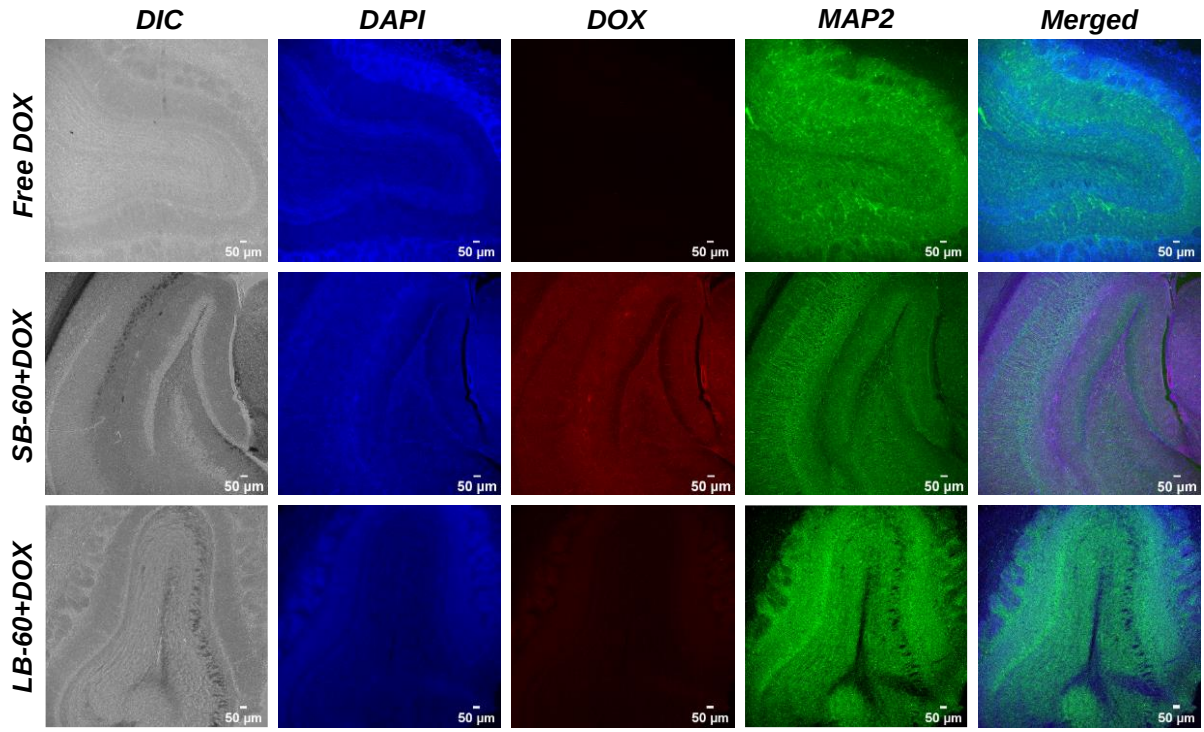

Figure 4.22. *Representative CLSM images (10X) of MAP 2 antibody stained brain tissue samples.*

Taking cognizance of the *in vivo* analysis, it can be stated that single polymer chain nanocarriers (UMs) demonstrated exceeding capability to be able to breach one of the most difficult biological barriers, i.e. the blood brain barrier. These UMs successfully overcame the cardiotoxicity side effect of DOX by reduced uptake in the heart tissue. Herein, polymer topology dictated the self-assembly property, DOX loading content, biodistribution and pharmacokinetics of the nanocarriers. This work provides a novel fully biodegradable unimolecular micelle with high DLC, compact size, resilience against dilution, reduced cardiotoxicity and the ability to cross the BBB making it a sought-after drug delivery vehicle.

4.4 Conclusion

Herein, tailor-made star-shaped and linear block copolymer topologies were chosen as model systems to investigate the role of macromolecular architectures on their biodistribution, pharmacokinetics and specifically their ability to penetrate the impermeable blood brain barrier. The star-block copolymer unimolecular micelle exhibited it's ability to cross the blood brain barrier and accumulate in the brain tissue as opposed to the free DOX and linear block copolymer. These UMMs were also able to reduce the cardiotoxicity of DOX by depleting the amount in the heart tissue thus, overcoming the major limitation in the use of DOX for chemotherapy. The pharmacokinetics evaluation revealed a $t_{1/2}$ of 4.0 h for the star polymer and the half-life could not be determined for the linear polymer as well as free DOX due to their faster removal from the circulation. The polymer nano-formulations were non-immunogenic which was established from the low cytokine expressions in the plasma samples. The H&E histological analysis revealed no morphological alteration in the tissue sections reiterating the biocompatibility of the polymer drug nano-carriers. Confocal imaging analysis re-instated the superior ability of the star-block DOX loaded UMM to selectively cross the BBB with negligible uptake in the heart tissue. Opposing trend was observed in the case of the linear block DOX-loaded micelle and free DOX. The UMMs also exhibited reduced RES uptake (uptake by liver and spleen tissue) and preferred renal clearance, adding yet another merit to its credit. The *in vivo* biodistribution and pharmacokinetics data established our hypothesis that polymer topology indeed played a crucial role in the aforementioned factors. The unimolecular micelle successfully delivered DOX into the brain tissue by crossing the BBB; however, the uptake was influenced by the BBB heterogeneity such that the uptake was higher in the posterior parts of the brain compared to the anterior section. In order to confirm the intra-cellular localization of DOX in the brain tissue, MAP 2 antibody staining was employed to mark the mature neurons. Hence, the current polymer design opens up new opportunities for fully enzymatic-biodegradable PCL-based amphiphilic star-block copolymer unimolecular micelles and successfully demonstrates their ability to deliver the drugs at the *in vivo* level with the ability to penetrate the BBB overcoming the limitations in treatment of brain-related malignancies.

5

Role of Surface Charge on the Star-Block Nanoparticle Cellular Internalization

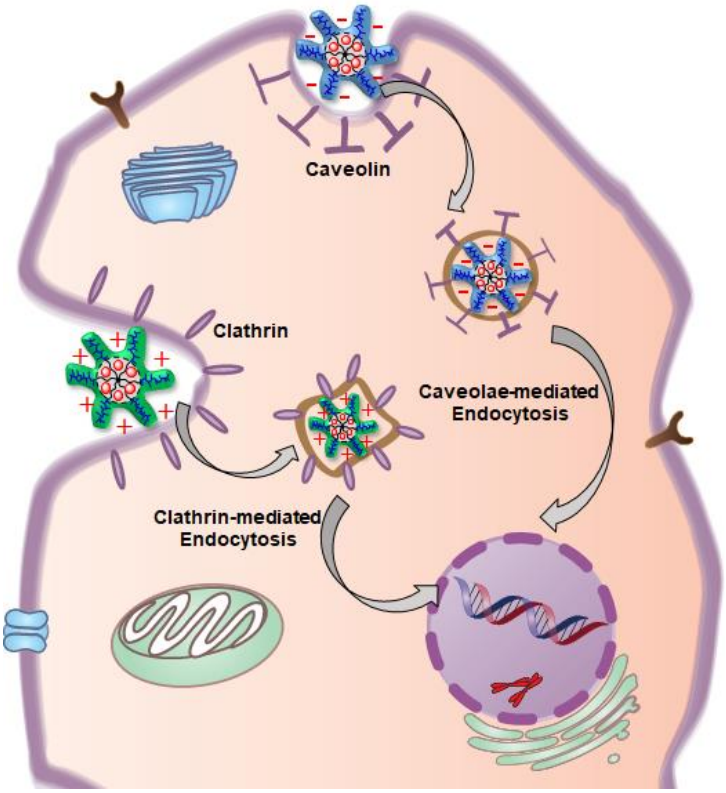

Abstract

Nanotechnology mediated drug delivery is the most sought-after approach in the field of cancer treatment today. The major hurdles faced by nanocarriers *in vivo* include opsonization leading to clearance via phagocytosis, non-specific interactions, systemic toxicity and renal clearance resulting in shorter half-life. Engineering the nanoparticle size, shape and surface properties can help overcome the aforementioned barriers. In this regard, surface charge plays a vital role in the nanoparticle colloidal stability, cellular internalization, biodistribution and pharmacokinetics. To this effect, star-shaped polycaprolactone based anionic, neutral and cationic block copolymers were designed maintaining the same topology, chemical composition and molecular weight with the only variation in their net surface charge. These star-block copolymers self-assembled into 40-100 nm size spherical nanoparticles with zeta values ranging from -40.7 mV to +33.2 mV. The anionic, neutral and cationic nanoparticles successfully encapsulated dye molecules such as Nile red (neutral dye) and 8-Hydroxypyrene-1,3,6-trisulfonic acid trisodium salt (HPTS, anionic dye) whilst maintaining their morphology. The nanoparticles exhibited biocompatibility in WT-MEF cells up to a concentration of 50 µg/mL. Cellular uptake investigation executed in WT-MEF and HEK293T cells revealed the effect of surface charge on the ability to permeate cellular barriers as a function of the endocytosis pathway. Herein, anionic and neutral nanoparticles demonstrated much better uptake in WT-MEF cells via the caveolae-mediated endocytosis. On the other hand, the uptake of cationic nanoparticles was the most promising in HEK293T cells and they preferred internalization via the clathrin-mediated endocytosis. The neuronal cells also exhibited higher uptake of cationic nanoparticles owing to the presence of the clathrin pathway. Thus, these star-shaped anionic, neutral and cationic block copolymers proved to be excellent delivery candidates *in vitro* and should be exploited for *in vivo* applications, specifically their ability to cross the blood brain barrier dependent on their surface charge.

5.1 Introduction

The field of nanomedicine has opened avenues and provided solutions to the problem of cancer treatment for the past few decades. Nanomedicine is the junction where nanotechnology meets medicine to overcome the existing limitations of conventional chemotherapy[325–327]. Engineering nanoparticles to efficiently deliver the cargo to the tumor site selectively in order to avoid systemic toxicity is a major challenge. This is due to the substantial number of roadblocks faced by nanoparticles while making their way from the site of administration to the target site under circulation. These include overcoming fast renal clearance, avoiding opsonization and reticuloendothelial system (RES) uptake in order to achieve longer circulation time, biodistribution, immune response etc.[4,6,76,328] The factors that influence all the aforementioned points are the nanoparticle size, shape, architecture as well as the surface properties, especially the surface charge[7,10,329,330].

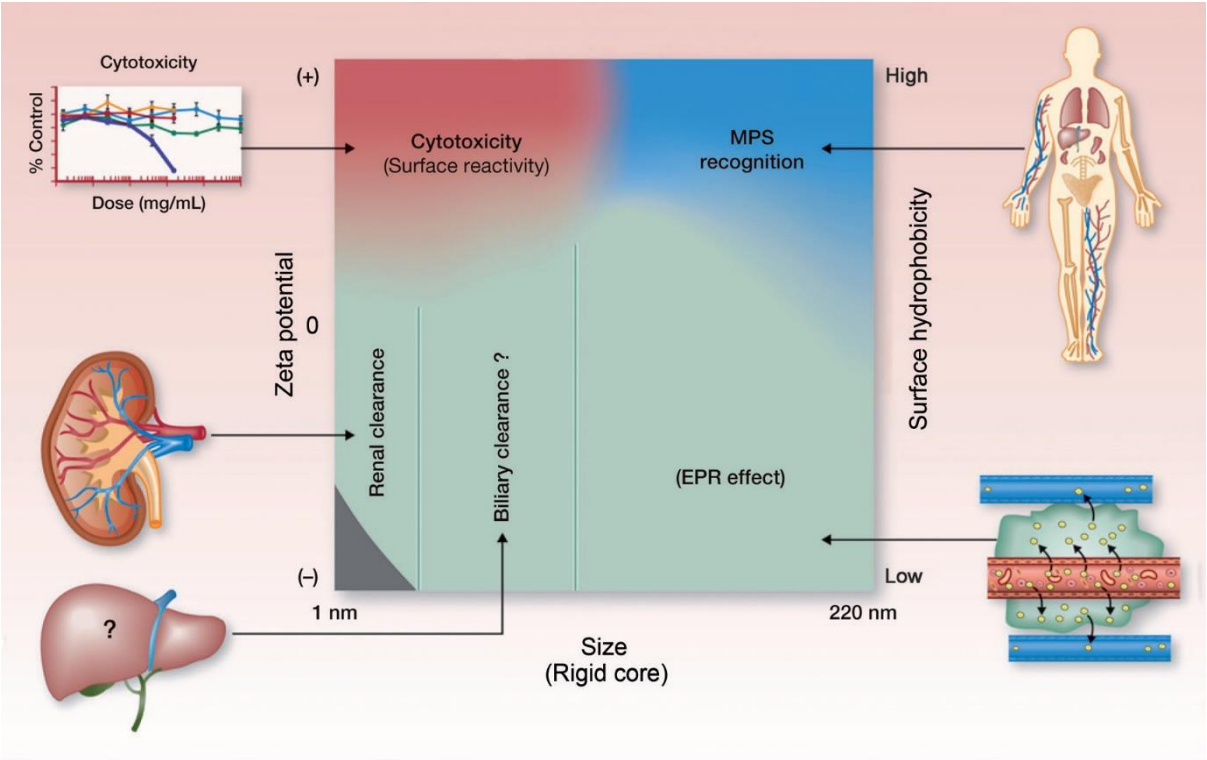

Figure 5.1. *Schematic representing the impact of size, surface charge and hydrophobicity on cytotoxicity, MPS recognition, renal or liver clearance and the EPR effect. (adapted from Zamboni et al. Clin. Cancer Res.* **2012**, *18,* 3229 - 3241).

Few of these parameters, i.e. the macromolecular architecture and size of the nanoparticles have been tweaked and their role in the *in vitro* as well as *in vivo* drug delivery has been studied at length in the previous chapters (see chapter 3 and 4). Another crucial

parameter that is the surface charge of the nanoparticles is also a major stakeholder in deciding the nanoparticle fate. Nanoparticles that exhibit zeta potential values of around 30 mV, either positive or negative, seem to demonstrate better colloidal stability due to reduced aggregation owing to the repulsive forces.[4,10] Surface charge values much higher than that can result in enhanced macrophages uptake and as a result, clearance from the body by mononuclear phagocyte system (MPS).[328,331] Nanoparticles with positive surface charge have, in certain cases, resulted in systemic toxicity due to platelet aggregation or hemolysis and are also more prone to clearance by MPS resulting in a shorter half-life.[67] Whereas, the negatively charged and neutral nanoparticles demonstrate longer half-life in blood due to decreased clearance.[332] Thus, engineering nanoparticles by tuning the surface charge could, in principle, limit the non-specific interactions of nanoparticles rendering them stability, longer $t_{1/2}$, reduced clearance and toxicity.

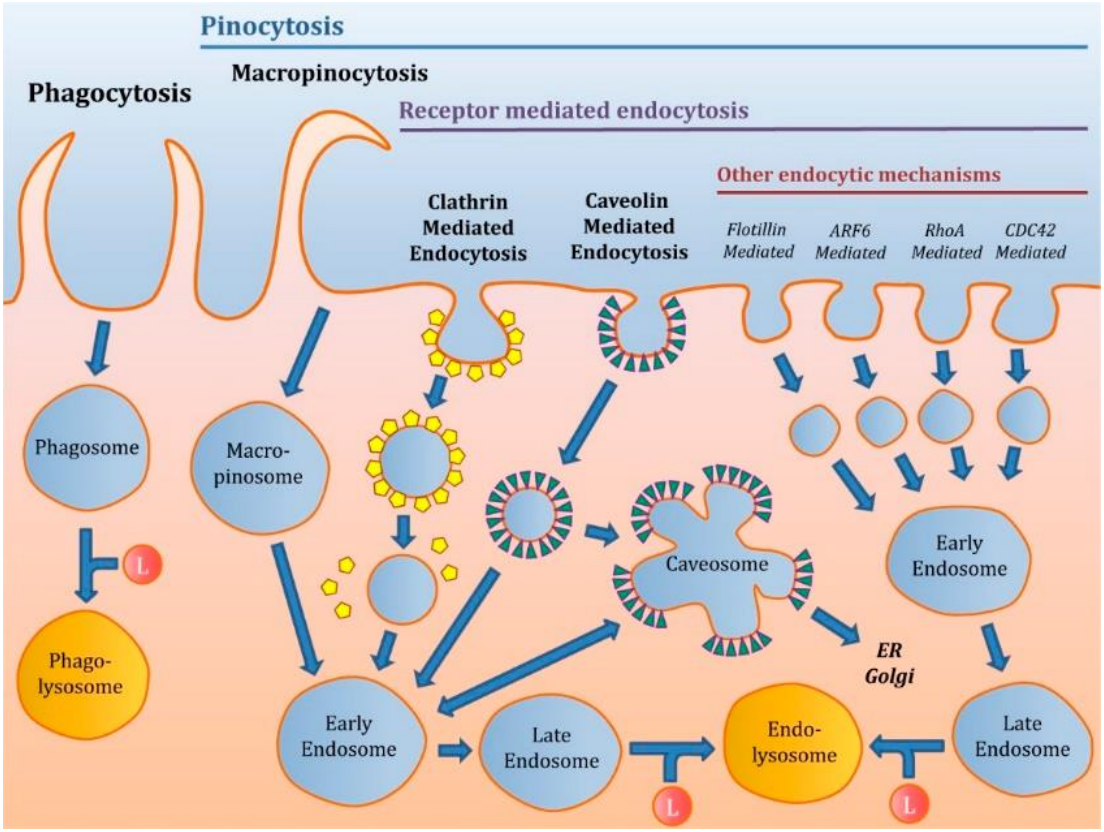

Figure 5.2. *Schematic depicting the various mechanisms of endocytosis for cellular uptake. (adapted from Manzanares et al. Pharmaceutics* **2020***, 12,* 371*)*

In order to be able to design nanoparticles to overcome the limitations listed above, it is important to first investigate the effect of surface charge at the *in vitro* level by understanding the nanoparticle and cell interactions before employing the system for *in vivo* applications. The nanoparticles are generally taken up by the cells via endocytosis, an energy-dependent process wherein the particle is engulfed by the membrane vesicle from the extracellular matrix into the cells.[333,334] The major pathways responsible for cellular internalization of nanoparticles based on their size and surface properties are as follows: (i) phagocytosis, (ii) pinocytosis, (iii) clathrin-mediated endocytosis and (iv) caveolae-mediated endocytosis.[335–339] Phagocytosis and pinocytosis are responsible for the internalization of large particles (in the micrometer range) whereas smaller particles are taken up by either clathrin or caveolae-mediated endocytosis.[330] Surface charge also dictates the pathway chosen by nanoparticles for entering the cell based on their interactions with membrane proteins. Clathrin-mediated endocytosis seems to be the preferred choice for positively charged particles, whereas anionic nanoparticles are internalized via the caveolae-mediated endocytic pathway. Omathanu et al. designed PAMAM dendrimers having variable surface functional groups, i.e. amine (cationic), carboxyl (anionic) and hydroxyl terminated (neutral) dendrimers and established that anionic dendrimers chose the caveolae mediated pathway for internalization in A549 cells.[303] Oshrat and co-workers synthesized positively charged mPEG-PLA nanoparticles and discovered that these were internalized by HeLa cells via the clathrin-mediated endocytosis pathway.[340] Xiue et al. compared the uptake of cationic polystyrene (PS) nanoparticles with their neutral counterpart in mesenchymal stem cells (see figure 5.3).[341] They found that the cationic PS nanoparticles were rapidly internalized by the cells as compared to the neutral particles and the endocytosis mechanism chosen by the cationic nanoparticles was the clathrin pathway.

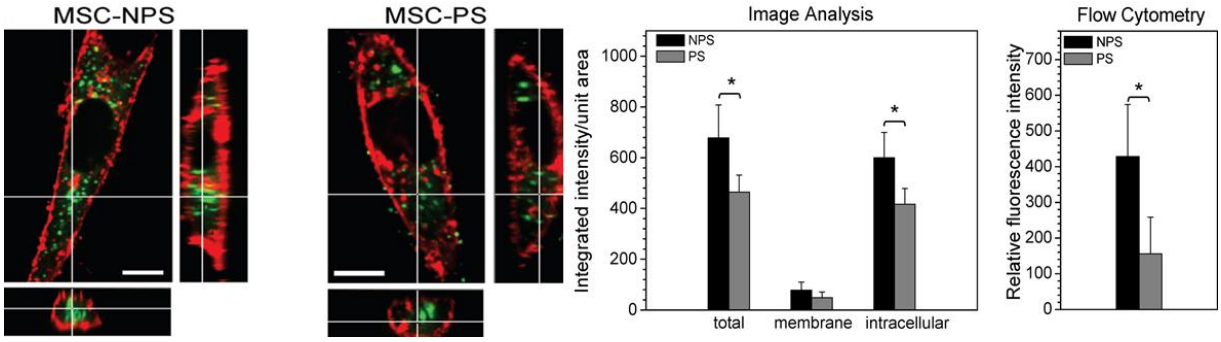

Figure 5.3. *Figure demonstrating the cellular uptake of amine functionalized (NPS) and nascent polystyrene nanoparticles (PS) by mesenchymal stem cells determined by confocal and flow cytometry. (adapted from Xiue et al. Biomacromolecules* **2010**, *11,* 748-753*).*

All the literature reports known so far on the understanding of surface charge potential on the cellular internalization involved the use of biocompatible polymers. However, an essential pre-requisite for any drug delivery vehicle is biodegradability upon entering the cell to release the cargo and be excreted out of the system with ease. In the previous chapters, we established the supremacy of polycaprolactone based fully biodegradable amphiphilic star-shaped block copolymers in terms of their enhanced cellular uptake, ability to breach the BBB and overcome cardiotoxicity. To the best of our knowledge, star-shaped polycaprolactone systems have not been explored in the literature for studying the effect of surface charge potential on cellular uptake ability and the pathway selection for endocytosis.

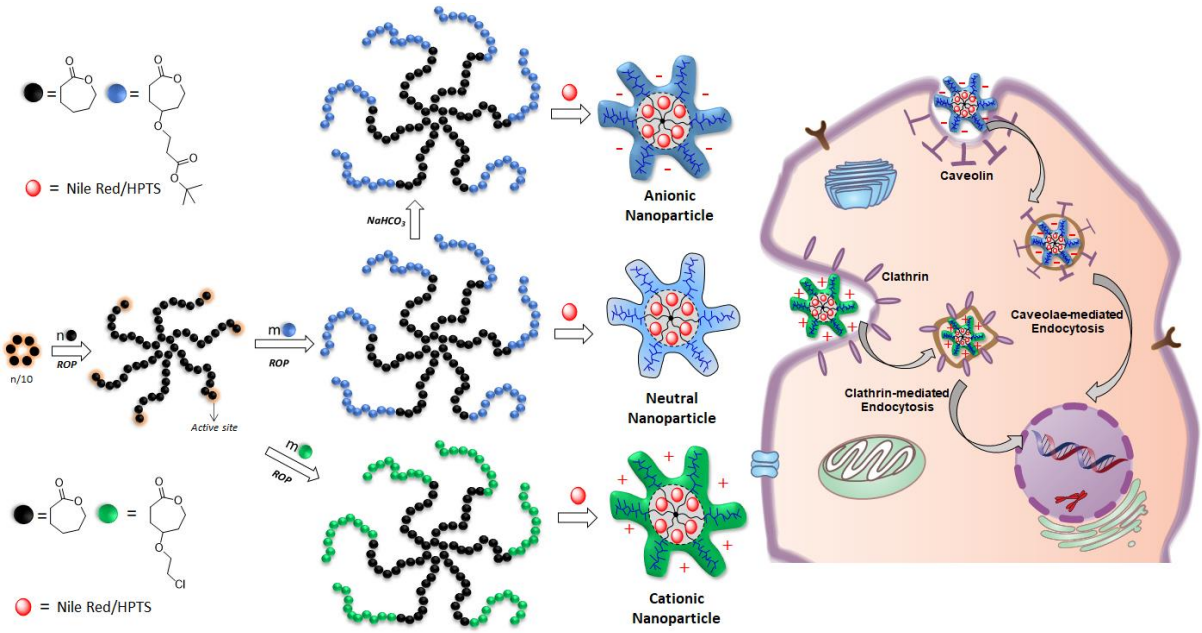

Figure 5.4. *Design and development of anionic, neutral and cationic star block copolymers to investigate the role of surface charge on the in vitro cellular internalization pathway.*

In the present chapter, we utilized the star-shaped topology composed entirely of a fully biodegradable polycaprolactone backbone for investigating the role played by the nanoparticle surface charge on the dye encapsulation capability and the cellular internalization. Herein, three different star-shaped polymers were synthesized having the exact same topology, repeating units, chemical composition and molecular weight with the only difference being in their surface charge (see figure 5.4). A 6-arm dipentaerythritol was chosen as the initiator for the

ring opening polymerization of ε-caprolactone and this served as the macroinitiator for the ɣ-tertiary butyl ester substituted and chlorine-substituted caprolactone monomers. The deprotection of the tertiary butyl group into carboxylic acid yielded the neutral star-block copolymer; and the deprotonation of this polymer resulted in the carboxylate substituted anionic star polymer. The quaternization of the chlorine substituted polymer using triethylamine gave us the cationic star-block copolymer. These anionic, neutral and cationic nanoparticles self-assembled into spherical nanoparticles with surface potential values of -40.7 mV, -3.7 mV and +33.2 mV with sizes around 60 nm, 50 nm and 120 nm respectively. The nanoparticles were able to encapsulate dyes such as, Nile red (neutral dye) and 8-Hydroxypyrene-1,3,6-trisulfonic acid trisodium salt (anionic dye) without any morphological alterations. The nanoparticles demonstrated their biocompatibility in wild-type mouse embryonic fibroblast (WT-MEF) cell lines up to a concentration of 50 µg/mL. The *in vitro* cellular uptake of the NR and HPTS-loaded nanoparticles in WT-MEF and HEK293T (Human embryonic kidney) shed light on the dependence of cellular uptake ability on the surface charge of nanoparticles as a result of the variation in internalization mechanism. The data established that negatively charged nanoparticles underwent internalization via the caveolae-mediated endocytosis and hence, demonstrated enhanced uptake in WT-MEF cells. Whereas, the uptake of the positively charged nanoparticles was the highest in HEK293T cells via the clathrin-mediated endocytosis. The nanoparticles were able to successfully internalize in the neuronal cells (procured from chick embryo) as well, wherein the cationic particles again depicted better uptake due to the presence of the clathrin mechanism. Thus, the anionic, neutral and cationic star-shaped polycaprolactone block copolymers gave insight into the importance of surface charge on cellular permeability and can be employed for investigating the blood brain barrier penetration capability.

5.2 Experimental Methods

5.2.1 Materials

Nile red (NR), methylene blue and 8-Hydroxypyrene-1,3,6-trisulfonic acid trisodium salt (HPTS) were acquired from Sigma Aldrich. Doxorubicin hydrochloride was purchased from Alfa Aesar. All the salts were purchased locally (Rankem). Wild-type mouse embryonic fibroblast cells (WT-MEF) and human embryonic kidney (HEK293T) cells were maintained in DMEM (phenol red free medium: Gibco) containing 10 % (v/v) fetal bovine serum (FBS)

and 1 % (v/v) penicillin–streptomycin at 37 °C under a 5 % CO_2 humidified atmosphere. Cells were trypsinised using 0.05 % trypsin (Gibco) and seeded in 96 well or 6-well (as per experiment) flat bottomed plastic plates (Eppendorf) for all assays. Tetrazolium salt, 3-(4,5-dimethylthiazolyl)-2,5 diphenyltetrazolium bromide (MTT), DAPI and paraformaldehyde were obtained from Sigma Aldrich chemicals. Acridine orange and Alexa fluor-488 and 568 phalloidin was procured from Dr. Aurnab Ghose lab. Primary chick spinal neuronal culture DIV-2 (days *in vitro*) was obtained from Dr. Aurnab Ghose lab. Acetonitrile (ACN), methanol, hexane, dimethyl sulfoxide, diethyl ether and trifluoroacetic acid (TFA) solvents were are all HPLC grade. The star-block copolymer SB-60 synthesized and well-characterized in chapter 3 was employed here as the "neutral" polymer and was also used for the synthesis of the anionic polymer.

5.2.2 Methods

Jeol 400 MHz spectrophotometer was used for recording NMR samples in $CDCl_3$ and $(CD_3)_2SO$ solvent using TMS as the standard. Perkin-Elmer Lambda 45 UV-Visible Spectrophotometer was used for the absorption studies. Emission spectra for determining the nile red and HPTS encapsulation were recorded using a SPEX Fluorolog HORIBA JOBIN VYON fluorescence spectrophotometer. A 450 W Xe lamp serves as the source of excitation at room temperature. Nile red and 8-Hydroxypyrene-1,3,6-trisulfonic acid trisodium salt (HPTS) were employed as the fluorophore. Nile red molecules were excited at 540 nm and the emission was collected from 555-750 nm. The HPTS molecules were excited at 403 nm and recorded the emission spectra from 418-618 nm. Dynamic light scattering (DLS) was performed using Nano ZS-90 setup (Malvern instruments). DLS utilizes a 633 nm laser as the light source, and the detector collects the scattered light at 90° angle. This gives information about the correlation function [$g^2(t)$], from which the diffusion coefficient (D) is calculated using cumulant method and further the diameter of the particle is determined using the Stokes-Einstein equation. The experiment was performed thrice with independent amphiphilic solutions to yield reproducible data. FE-SEM analysis requires the sample to be drop casted on silicon wafer and the experiment was done on a Zeiss Ultra Plus scanning electron microscope. HR-TEM samples were prepared by drop-casting the dialyzed polymer solutions on copper TEM grids and the images were recorded using Jeol JEM2200FS 200 KeV systems. Again the reproducibility of the data was confirmed using three independent polymer solutions. Confocal

microscopic analysis was done using Leica SP8 microscope. The cell viability determination was done by measuring the absorbance of the formazan crystals on a microplate reader (Varioskan Flash).

5.2.3 Synthesis of the carboxylate substituted star-block copolymers SB-X (Anionic)

The carboxylic acid substituted star-block copolymer SB-60 was treated with saturated solution of sodium bicarbonate. This was followed by dialysis against water (pH = 7.8) for 24 h with periodic change of outside water. The dialyzed solution was lyophilized and stored at 4 °C until further use. ^{1}H NMR (400 MHz, $(CD_3)_2SO$) δ ppm: 4.04 (m, 2.03 H), 3.98 (t, 2.00 H), 3.53 (m, 2.22 H), 2.32 (t, 2.72 H), 2.26 (t, 2.72 H), 1.69 (m, 3.46 H), 1.54 (m, 3.81 H), 1.29 (m, 1.96 H). ^{13}C NMR (100 MHz, $(CD_3)_2SO$) δ ppm: 173.5, 173.3, 75.1, 65.9, 64.0, 61.7, 59.5, 33.9, 33.0, 29.9, 29.2, 28.3, 25.4, 24.6.

5.2.4 Synthesis of the chlorine substituted star-block copolymers SB-X (Cationic)

The S-60 macroinitiator, synthesized in chapter 3, was used for the ring opening polymerization of the chlorine substituted monomer (synthesized by Ms. Ruma Ghosh)[237] in dry toluene at 110 °C. The chlorin substituted star block copolymer was quaternized using triethylamine in DMF for 4 days yielding the “Cationic” star block copolymer (Cationic SB-60). The entire cationic polymer synthesis was carried out by Ms. Ruma Ghosh and donated to me for further studies.

5.2.5 Self-assembly of copolymers

The anionic, neutral and cationic polymers **SB-60** (5 mg) were dissolved in 0.8 mL DMSO and this solution was then added dropwise to 4.2 mL milli-Q water with constant stirring for 4 h at 25 °C. The solution was then transferred to a semi-permeable membrane of MWCO = 3.5 kD and dialyzed against milli-Q water for 24 h. In the case of the anionic polymer, the water was maintained at pH = 7.8 throughout the dialysis. The water was replenished at regular intervals in order to substantiate the removal of DMSO.

5.2.6 Dye Encapsulation in the Copolymer Scaffolds

The anionic, neutral and cationic star-block polymer **SB-60** (5 mg) and nile red/HPTS/Methylene blue (0.5 mg) were dissolved in 0.8 mL DMSO followed by dropwise addition of the cocktail to 4.2 mL water with continuous stirring for 4 h. The dialysis was carried out in a dialysis tube of MWCO = 3.5 kD against large amount of milli-Q water for 48 h. Here also the pH was maintained at 7.8 for the dialysis of the anionic polymer. At regular

intervals the water was changed in order to facilitate the removal of un-encapsulated DOX and DMSO.

The dye loading efficiency (DLE) and dye loading content (DLC) were determined by UV-Visible spectroscopy using the following equations:

DLE (%) = {weight of dye in micelles/weight of dye in feed} X 100%

DLC (%) = {weight of dye in micelles/weight of dye-loaded nanoparticles} X 100%

5.2.7 Cell Viability Assay (MTT Assay)

The biocompatibility of the anionic, neutral and cationic star block copolymers was investigated via the cell viability assay in wild type mouse embryonic fibroblast cell lines (WT-MEF) employing the tetrazolium salt, 3-(4,5 dimethylthiazolyl)-2,5-diphenyl tetrazolium bromide (MTT). In a typical experiment, 0.5 X 10^3 cells were seeded in each well of a 96-well plate (Eppendorf) in 100 µL of complete DMEM containing 1 % penicillin streptomycin and 10 % FBS (fetal bovine serum). The cells were incubated at 37 °C in a 5 % CO_2 humidified atmosphere for 16 h allowing the cells to adhere following which media aspiration was carried out from each well. The desired concentrations of the nascent polymers were then added to each of the wells for the cell treatment and all of these were done in triplicates. For each of these experiments, there was a control without any compound containing only the complete DMEM and the cells were then incubated at conditions mentioned before for 72 h. At the end of the incubation, the compound containing media was replaced with a freshly prepared MTT solution (0.5 mg/mL) in complete DMEM followed by 4 h incubation at 37 °C, 5% CO_2. The mitochondrial dehydrogenase enzyme present in the viable cells reduces the tetrazolium salt into formazan crystals, whose purple colour gives the read out for number of viable cells. At the end of 4 h, the MTT containing media was aspirated and the purple formazan crystals were dissolved in 100 µL DMSO; the plate was then subjected to absorbance measurements at 570 nm using the Varioskan flash microplate reader. The absorbance values from the sample treated wells were compared with the control wells considering the control value to be 100 % and thus, the cell viability % was determined for all the samples as mean ± SEM.

5.2.8 Monitoring Cellular Uptake of NR and HPTS-loaded Star block polymer Nanocarriers

In order to investigate the cellular uptake mechanism of nanoparticles based on their net surface charge, two different cell lines were selected namely, wild-type mouse embryonic fibroblast (WT-MEF) and human embryonic kidney (HEK) cell lines. The cells were seeded at a density of a 1 X 10^5 cells per well in a 6-well plate in 2 mL of DMEM containing 10 % FBS and 1 % penicillin streptomycin. The cells were incubated in a 5 % CO_2 humidified atmosphere at 37 °C for 24 h followed by compound addition. The NR and HPTS-loaded anionic, neutral and cationic nanoparticles along with free NR and HPTS were added to individual wells such that the concentration of NR was 2 µg/mL and that of HPTS was 5 µg/mL. The cells were incubated with the compounds for 4 h at 37 °C followed by fixing using 4 % paraformaldehyde (PFA). The NR incubated cells were stained with DAPI, whereas the cells containing HPTS were stained with acridine orange for nucleus staining under dark conditions. The cells were mounted using 70 % glycerol followed by imaging on a Leica SP8 system with a sequential scan setting using the lasers $\lambda = 405$ nm for DAPI and HPTS excitation, $\lambda = 488$ nm for acridine orange and $\lambda = 561$ nm for excitation of the NR dye followed by the imaging analysis done using Fiji software.

5.2.9 In vitro cellular uptake in Primary Neuronal cells

The primary neuronal cells procured from chick embryo were cultured in petridishes at 37 °C and after 2 days, the NR and HPTS-loaded nanoparticles were added followed by a 4 h incubation. The cells were then fixed using 4 % PFA and stained using alexa fluor 488 conjugated phalloidin to visualize the neurons. The mounting medium used was 70 % glycerol followed by confocal imaging on a Leica SP8 system wherein the laser with $\lambda = 405$ nm was used for HPTS excitation, $\lambda = 488$ nm for phalloidin and $\lambda = 561$ nm for excitation of the NR dye.

5.3 Results and Discussion

5.3.1 Synthesis of PCL based Star architecture block copolymers

The synthesis of the star-shaped neutral, anionic and cationic polymers has been outlined in scheme 5.1 and 5.2. The star-shaped polymer **SB-60**, design principle explained in chapter 3, exhibited exceptional qualities namely (i) sub-30 nm size unimolecular micelles with high drug loading content, (ii) fully biodegradable backbone, (iii) enhanced *in vitro* cellular uptake via endocytosis and (iv) the unique ability to cross the blood brain barrier along with reduced cardiotoxicity (as can be seen in chapters 3 and 4). Hence, it was a no-brainer to choose the same star-shaped topology for investigating the role of surface charge on the ability to cross biological barriers. The **SB-60** star-block copolymer served the purpose of the **"Neutral"** polymer constituting of polycaprolactone as the hydrophobic core and carboxylic acid-substituted polycaprolactone as the hydrophilic shell (see synthesis in scheme 5.1). This polymer was then subjected to sodium bicarbonate ($NaHCO_3$) treatment in order to completely convert the carboxylic groups on the periphery to carboxylate anions (as can be seen in scheme 5.1). Following the treatment, the polymer was dialyzed against water (pH = 8.0) for 24 h to ensure the complete removal of $NaHCO_3$ whilst maintain the surface charge of the polymer. Further, the polymer was lyophilized and stored at 4 °C for further use. This resulted in the formation of the carboxylate substituted star-block copolymer, hereby referred to as the **"Anionic"** polymer.

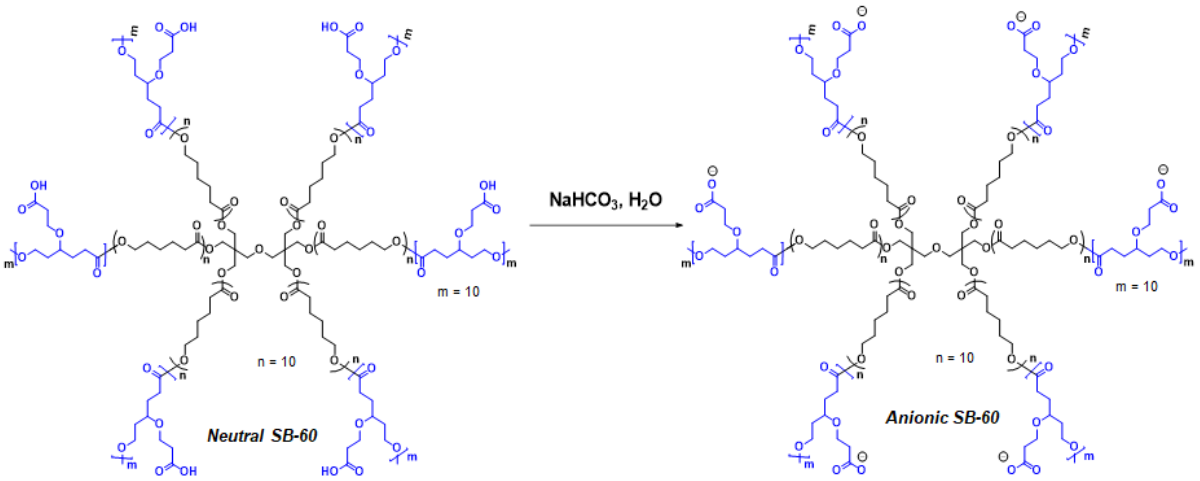

Scheme 5.1. *Synthetic scheme of ε-caprolactone and γ-substituted tert-butyl caprolactone based anionic star block copolymer.*

The cationic polymer was generously provided by my labmate Ms. Ruma Ghosh and its synthetic outline is shown in scheme 5.2. Solution-route ring opening polymerization (ROP) methodology was employed for the synthesis of the cationic star-block copolymer in a sequential process. Herein, the 6-arm dipentaerythritol and tin (II) 2-ethylhexanoate ($Sn(Oct)_2$) were chosen as the initiator and catalyst, respectively and the polymerization was carried out in dry toluene. The initiator and catalyst were taken in a ratio of 1:3 that generate the active initiator *in situ* used to ring open ε-caprolactone (feed, [M]/[I] = 60) yielding the 6-arm macroinitiator (MI). This MI was then used for the ring opening polymerization of the chlorine-substituted monomer (synthesized by Ms. Ruma Ghosh)[237] employing $Sn(Oct)_2$ as the catalyst, wherein the feed [M]/[MI] was taken to be 60, aiming for statistically 10 repeating units per arm. The chlorine-substituted star block copolymer was then subjected to quaternization via reaction with triethylamine in dimethylformamide resulting in the **"Cationic"** polymer (see the complete synthetic protocol in scheme 5.2).

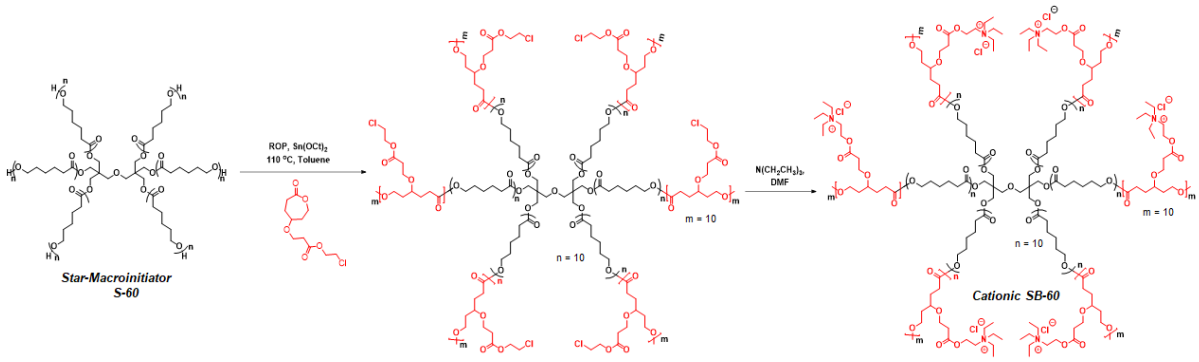

Scheme 5.2. *Synthetic scheme of ring opening polymerization of ɣ-substituted chlorine caprolactone monomer followed by quaternization to yield cationic star block copolymer.*

The degree of polymerization (X_n) for the cationic polymer was also determined from the ^1H NMR analysis comparing the integration of one of the peaks from the initiator with that of the polymer backbone. In case of the macroinitiator S-60, integration of the initiator peak at 3.64 ppm was compared to the new ester peak at 4.04 ppm corresponding to the polycaprolactone backbone. The peak at 3.64 ppm was given the reference integration of 12 and accordingly the integration value of the ester peak gave us the degree of polymerization,

X_n = 60 (see the appendix). Similarly, the X_n was determined for the chlorine-substituted star-block copolymer wherein the reference integration was given to the polycaprolactone ester peak at 4.03 ppm. Corresponding to that the integration of the newly formed ester peak at 4.13 ppm yielded the X_n for the chlorine-substituted polycaprolactone (X_n = 60). This chlorine-substituted polymer was subjected to triethylamine treatment that resulted in the formation of the quaternized cationic star-block copolymer. The quaternization process was confirmed from ^{1}H NMR by the appearance of a new peaks at 3.09 ppm corresponding to the triethylamine unit (as can be seen in the figure in appendix). The integration of the other peaks was intact, thus implying that the structural integrity of the polymer was not disturbed due to quaternization.

5.3.2 Self-assembly and Dye Encapsulation

All the three star-block copolymers, i.e. anionic, neutral and cationic, are composed of a hydrophobic polycaprolactone core and a hydrophilic substituted polycaprolactone shell rendering them the appropriate amphiphilicity. This amphiphilic balance allows the polymers to self-assemble in aqueous medium into nanoparticles. Their self-assembly was carried out utilizing the dialysis method wherein the polymers are dissolved in an organic solvent (DMSO) and this solution is then added dropwise to water followed by dialysis in a semi-permeable membrane of MWCO = 3.5 kD. The dialysis was carried out against water for 24 h and over the entire duration, the water in the container was replaced at regular intervals to facilitate the removal of DMSO. The dialyzed solutions were filtered followed by lyophilization and were stored at 4 °C until further use. The primary investigation carried out was the determination of surface charge of these self-assembled nanoparticles using zeta potential measurements. The aim here was to be able to design nanoparticles having the exact same topology and polymer backbone with the only difference being in their surface charge, resulting in anionic, neutral and cationic star-shaped nanoparticles. As can be seen from figure 5.5a, the self-assembled nanoparticles exhibited zeta potential values of -40.7 mV, -3.69 mV and +33.2 mV for the respective anionic, neutral and cationic star block copolymer nanoparticles. The zeta potential values give information about the surface charge of nanoparticles and the aforementioned values gave affirmation of the formation of nanoparticles with negative, neutral and positive surface charge. Having achieved the three types of nanoparticles, these were further subjected

to dynamic light scattering (DLS) measurements to determine their hydrodynamic diameter (D_h). The DLS histograms exhibited the D_h for the anionic, neutral and cationic polymers to be 60 ± 5 nm, 50 ± 10 nm and 120 ± 10 nm, respectively (see the histograms in figure 5.5b to 5.5d). The size, shape and morphology of the self-assembled anionic, neutral and cationic nanoparticles was visualized by employing field emission scanning electron microscope (FESEM). The FESEM images exhibited the presence of spherical shaped nanoparticles with average sizes of 40 nm, 50 nm and 100 nm corresponding to the anionic, neutral, and cationic nanoparticles, respectively (see figures 5.5e to 5.5g). The sizes obtained from FESEM were in good correlation with those provided by DLS.

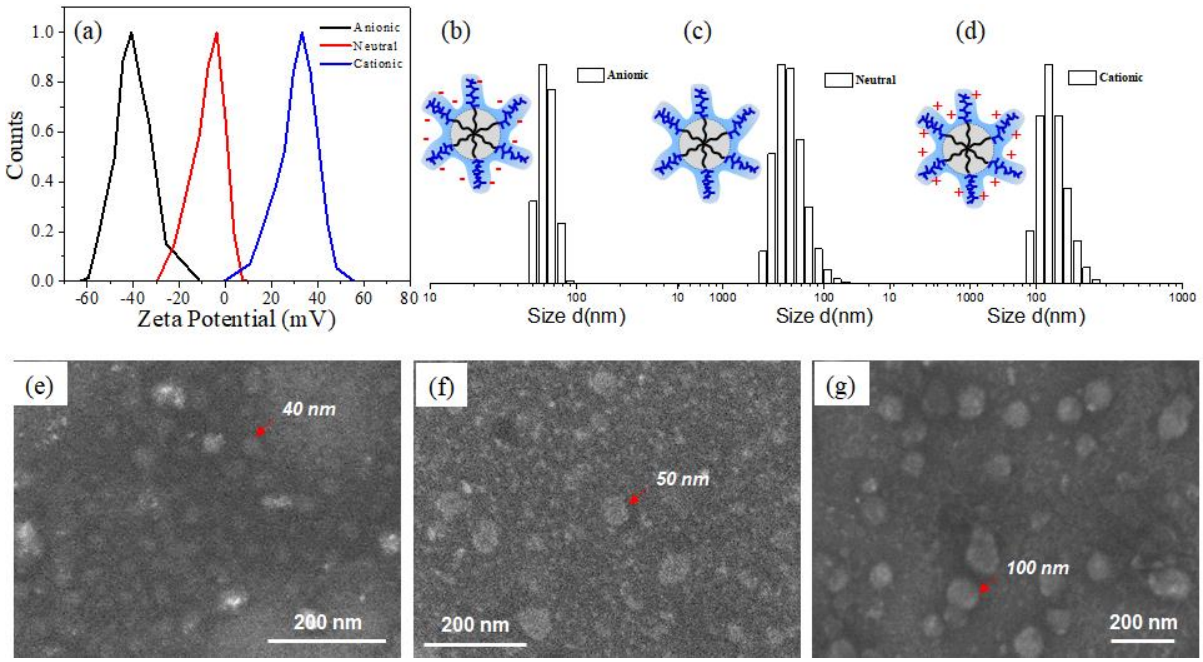

Figure 5.5. *Zeta potential (a) and Hydrodynamic diameter of self-assembled anionic (b), neutral (c) and cationic (d) star block copolymers at 0.1 mg/mL concentration in water. FESEM images for anionic (e), neutral (f) and cationic (g) SB-60 recorded at 0.1 mg/mL concentration in water.*

The variation in surface charge of the star-block copolymer nanoparticles was bound to impact their encapsulation capability based on the charge of the cargo (dye/drug). To elucidate this hypothesis, three dye molecules were chosen namely, Nile red (neutral dye), 8-Hydroxypyrene-1,3,6-trisulfonic acid trisodium salt (anionic dye), IR780 (cationic dye), cardiogreen (zwitterionic dye) and anticancer drug Doxorubicin. The idea was to investigate the role of surface charge on the dye loading content of all the three nanoparticles, wherein

multiple factors are at play such as electrostatic or van der waals interactions. The dye encapsulation was carried out by employing the dialysis method, wherein the polymer and dye are both dissolved in DMSO followed by dropwise addition to water. The dialysis protocol followed was same as explained in the previous section. The dialyzed solutions were filtered using a whatmann filter paper (0.45 µm) followed by lyophilization and storage at 4 °C. The dye encapsulated dialyzed solutions were subjected to absorbance spectroscopy in order to determine the dye loading content (DLC) (all the DLC values have been tabulated in figure 5.6a). As can be seen from the table, the DLC for the neutral dye, i.e. Nile red (NR) was similar in the case of the cationic (0.3 %) and neutral nanoparticles (0.2 %) albeit it was higher for the anionic nanoparticles (0.6 %). The cationic dye, i.e. IR780 did not load significantly in the cationic polymeric nanoparticle, probably due to repulsion of the positive surface charges. The DLC for IR780 was the highest in the neutral nanoparticle (4.7 %); and was similar in the case of the anionic nanoparticle (3.4 %) owing to the presence of electrostatic attractions. The outlier in this experiment was the HPTS encapsulation results, as can be seen from the DLC values in figure 5.6a. The DLC values for HPTS were similar in the neutral (0.9 %) and cationic nanoparticles (0.8 %), whereas the HPTS loading turned out to be the highest for the anionic nanoparticle (1.8 %). This result can be explained by considering that apart from the electrostatic attraction, other factors such as the van der waals interaction could also be playing a role in the dye encapsulation capability. Cardiogreen and DOX loading only happened in the neutral and anionic polymers and there was complete precipitation observed in the case of the cationic polymer. From this point forth only the NR and HPTS-loaded nanoparticles were employed for all the investigations. The absorbance spectra for the NR and HPTS-loaded nanoparticles (0.1 mg/mL concentration) can be seen in figures 5.6b and 5.6c. The λ_{max} for the NR-loaded star block copolymer nanoparticles was found to be at 540 nm (see figure 5.6b) and that for the HPTS-loaded nanoparticles, the peak max was observed at 403 nm (see figure 5.6c). The photographs of the dye loaded nanoparticles can be seen in figures 5.6b and 5.6c, arranged in the following order: anionic, neutral and cationic. These dye-loaded nanoparticles were then subjected to fluorescence spectroscopy. The NR-loaded star block copolymer nanoparticles were excited at 540 nm and their emission was collected from 555-750 nm. As can be seen from the spectra in figure 5.6d, all the nanoparticles exhibited the same fluorescence signature with the λ_{max} at 620 nm. The excitation wavelength for the HPTS-loaded nanoparticles was 403 nm and the emission were recorded from 418 to 718 nm (see figure 5.6e), wherein the λ_{max} was

observed to be at 520 nm. The photographs of the dye loaded nanoparticles taken under UV lamp can be seen along with the fluorescence spectra in figures 5.6d and 5.6e in the same order as mentioned above.

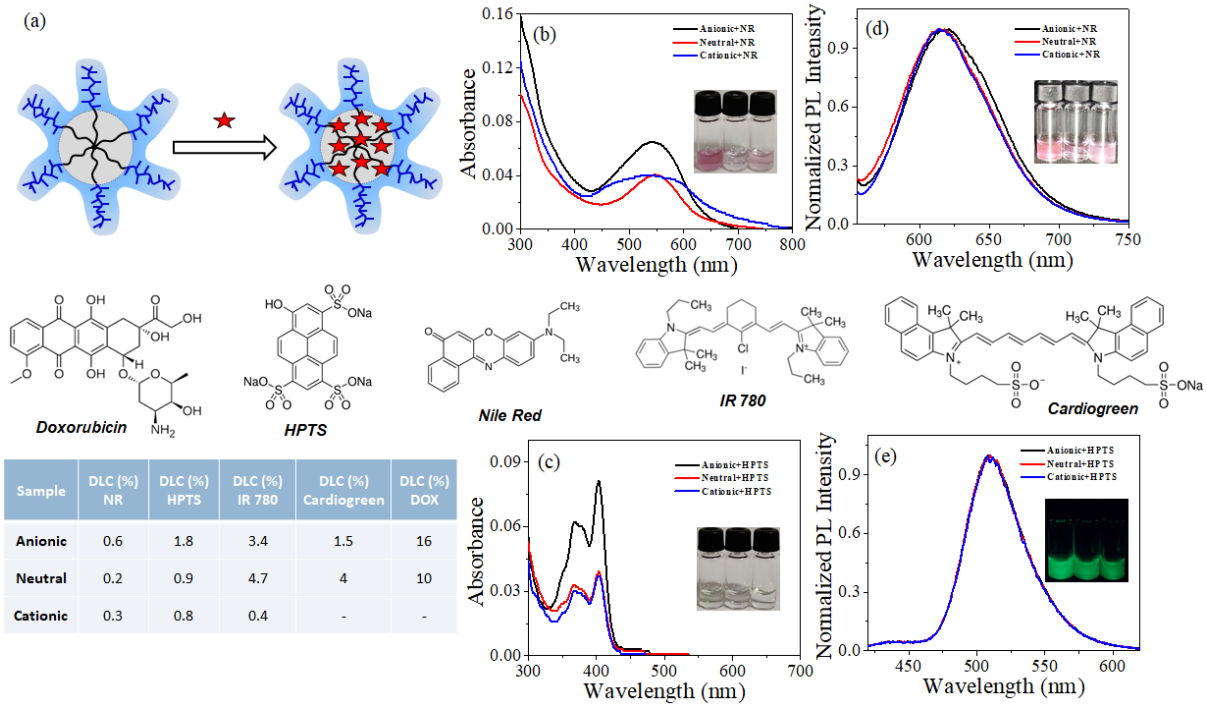

Sample	DLC (%) NR	DLC (%) HPTS	DLC (%) IR 780	DLC (%) Cardiogreen	DLC (%) DOX
Anionic	0.6	1.8	3.4	1.5	16
Neutral	0.2	0.9	4.7	4	10
Cationic	0.3	0.8	0.4	-	-

Figure 5.6. *Nile red, HPTS, IR 780, Cardiogreen and DOX encapsulation in star-block copolymers. Tabulated the dye loading content (%) for all the nanoparticles (a). Absorbance spectra and fluorescence spectra of NR-loaded (b, d) and HPTS-loaded (c, e) anionic, neutral and cationic star-block copolymers at 0.1 mg/mL concentration in water.*

These dye-loaded nanoparticles were then subjected to DLS measurements in order to deduce their hydrodynamic diameter. As can be seen from figures 5.7a to 5.7c, the DLS histograms exhibited the D_h to be 70 ± 5 nm, 18 ± 3 nm, and 100 ± 10 nm for the NR-loaded anionic, neutral and cationic nanoparticles, respectively. The DLS histograms exhibited a monomodal distribution with narrow PDI for all the nanoparticles. In order to visualize the morphology and size of these NR-loaded nanoparticles, they were subjected to FESEM and HR-TEM analysis. As can be seen from figure 5.7d, the images from FESEM and HR-TEM revealed the formation of spherical nanoparticles with sizes around 80 nm and 75 nm, respectively for the NR-loaded anionic star polymer. The FESEM images for the NR-loaded neutral nanoparticles also exhibited spherical morphology of the nanoparticles with sizes in the range of 28 nm and this was corroborated by the HR-TEM data, that also showed 17 nm size

spherical nanoparticles (see figure 5.7e). The sizes obtained from the FESEM (86 nm) and HR-TEM (105 nm) images for the spherical shaped NR-loaded cationic nanoparticles were in complete correlation with the DLS data (see figure 5.7f).

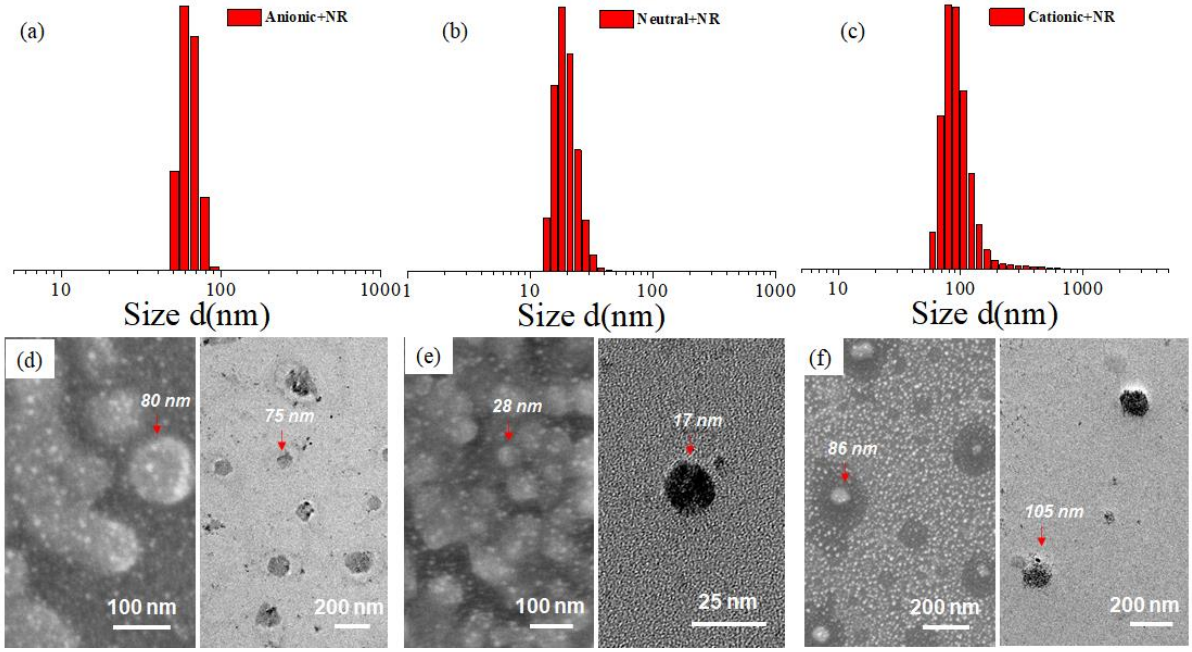

Figure 5.7. *Hydrodynamic diameter of NR-loaded anionic (a), neutral (b) and cationic (c) star block copolymers at 0.1 mg/mL concentration in water. FESEM and HR-TEM images for NR-loaded anionic (d), neutral (e) and cationic (f) star block copolymer nanoparticles recorded at 0.1 mg/mL concentration in water.*

The HPTS-loaded nanoparticles were also characterized using the DLS, FESEM and HR-TEM techniques (see figure 5.8). As can be seen from the DLS histograms in figures 5.8a and 5.8b, the hydrodynamic diameter for the HPTS-loaded anionic and neutral nanoparticles was observed to be 65 ± 5 nm and 20 ± 5 nm, respectively with a monomodal size distribution. However, the HPTS-loaded cationic nanoparticles exhibited a bimodal size distribution with the majority of nanoparticles having D_h to be 190 ± 10 nm (see figure 5.8c). The size and shape of these HPTS-loaded nanoparticles were investigated by employing FESEM and HR-TEM (see figures 5.8d to 5.8f). FESEM and HR-TEM images of the HPTS-loaded anionic star polymer revealed the formation of nanoparticles having spherical morphology with sizes around 60 nm and 64 nm, respectively (see figure 5.8d). As can be seen from figure 5.8e, the sizes obtained from FESEM and HR-TEM images for HPTS-loaded spherical shaped neutral nanoparticles were observed to be 28 nm and 20 nm, respectively. The spherical morphology

was retained in the case of the HPTS-loaded cationic nanoparticles with sizes around 100 nm and 60 nm exhibited from FESEM and HR-TEM, respectively (see figure 5.8f).

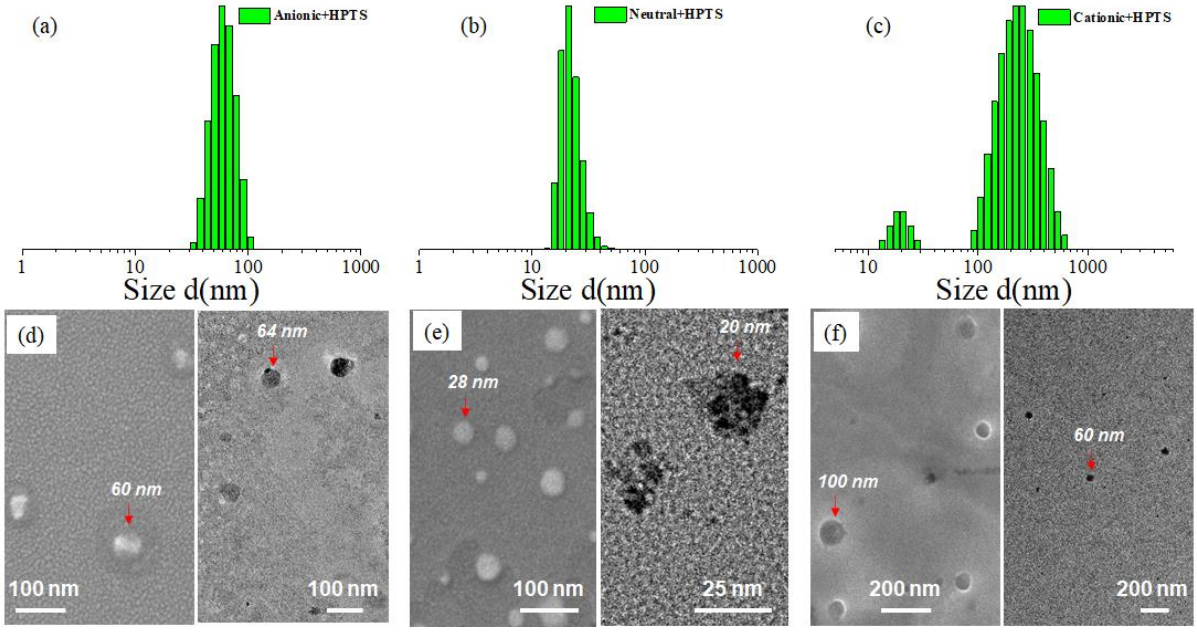

Figure 5.8. *Hydrodynamic diameter of HPTS-loaded anionic (a), neutral (b) and cationic (c) star block copolymers at 0.1 mg/mL concentration in water. FESEM and HR-TEM images for HPTS-loaded anionic (d), neutral (e) and cationic (f) star block copolymer nanoparticles recorded at 0.1 mg/mL concentration in water.*

An important investigation was the determination of the surface charge of nanoparticles after the encapsulation of dye molecules and this was carried out by measuring the zeta potential of all the dye-loaded nanoparticles. As can be seen in figure 5.9, the zeta potential values for the NR-loaded nanoparticles turned out to be -27 mV, -12 mV and +20 mV for the anionic, neutral and cationic counterparts, respectively. These values were reflective of the negative, neutral and positive surface charge for the respective nanoparticles implying that the encapsulation of a neutral dye did not impact the overall surface charge drastically. On the other hand, the encapsulation of HPTS (anionic dye) resulted in a transformation of the positive surface charge on the cationic nanoparticles to a negative surface potential as indicated by the zeta potential value of -15 mV. The zeta potential value for the neutral HPTS-loaded nanoparticle also dropped to -18 mV; however, there was not much change in the value of the HPTS-loaded anionic nanoparticle that was observed to be -28 mV (see figure 5.9). This was a crucial experiment to deduce the surface potential of the nanoparticles upon dye loading in

order to be able to better comprehend their *in vitro* cellular uptake or interaction with other biological barriers such as the blood brain barrier.

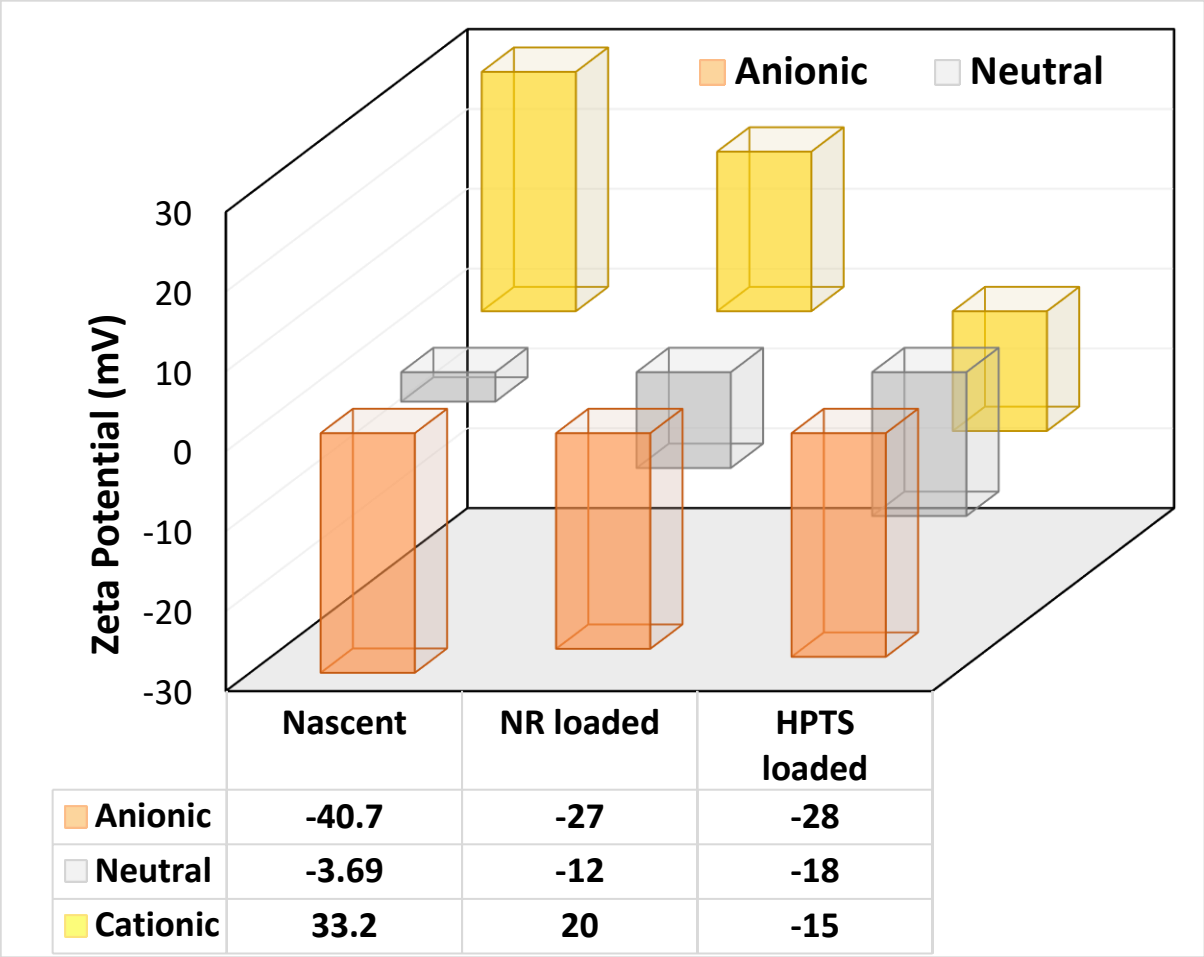

	Nascent	NR loaded	HPTS loaded
Anionic	-40.7	-27	-28
Neutral	-3.69	-12	-18
Cationic	33.2	20	-15

Figure 5.9. *Zeta potential values for the nascent, NR and HPTS-loaded anionic, neutral, and cationic star block nanoparticles at 0.1 mg/mL concentration in water.*

5.3.3 Cytotoxicity and Cellular Uptake

A preliminary investigation prior to undertaking the cellular uptake studies was determination of the biocompatibility of the anionic, neutral and cationic nanoparticles in wild-type mouse embryonic fibroblast (WT-MEF) cell lines. Various concentrations of the nascent star block copolymer nanoparticles were incubated with WT-MEF cells up to 72 h followed by the cell viability analysis using the widely employed MTT assay. As can be seen from the histogram in figure 5.10, the cationic nanoparticles were highly biocompatible with 100 % cell viability up to a concentration of 50 µg/mL. The neutral nanoparticles also did not exhibit any

toxicity towards the cells with more than 70 % viable cells after 72 h. The anionic nanoparticles exhibited 50 % cell viability after 72 h at a concentration of 50 µg/mL (see histogram in figure 5.10). Thus, these star-shaped block copolymer nanoparticles were biocompatible and safe to be used for further *in vitro* cellular uptake investigations.

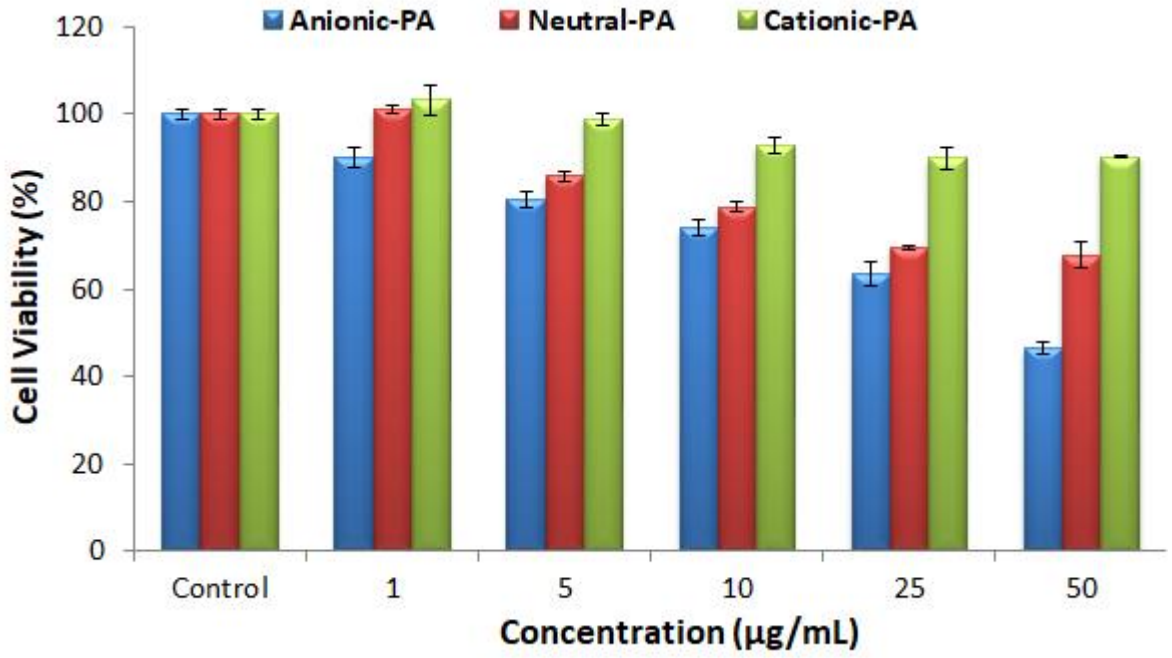

Figure 5.10. *MTT plot depicting the cytocompatibility of the anionic, neutral and cationic star block copolymers upto a concentration of 50 µg/mL.*

In order to investigate our hypothesis about the role played by surface potential on the ability of nanoparticles to cross biological barriers, the obvious choice was employing the *in vitro* cellular uptake model. Herein, the expectation was that the uptake of nanoparticles would be impacted by their surface charge owing to the selectivity in endocytosis pathways with respect to the charge on the nanoparticles. As per reports in the literature, negatively charged nanoparticles are taken up into the cells via caveolae-mediated endocytosis whereas, the clathrin pathway is responsible for the cellular uptake of positively charged nanoparticles.[303,341–345] The idea here was to substantiate the aforementioned finding in the current star-block copolymer design wherein the polymer topology was maintained the same with only change in the surface potential. For this purpose, two different cell lines were selected namely the wild-type mouse embryonic fibroblast (WT-MEF) and human embryonic kidney

(HEK293T) cell lines that are known to exhibit caveolae-mediated and clathrin-mediated endocytosis pathways, respectively.[77,270,346]

The NR-loaded anionic, neutral and cationic nanoparticles along with free NR were incubated with WT-MEF cells for 4 h followed by fixing, staining with DAPI and then imaging on a Leica SP8 system (see figure 5.11). The confocal laser scanning microscopy (CLSM) images for DAPI stained nuclei and free NR along with NR-loaded nanoparticles were visualized at blue (λ = 405 nm) and red (λ = 561 nm) channels, respectively. The emission range for the DAPI channel was λ_{em} = 410-489 nm and that for the NR channel was kept as λ_{em} = 572-757 nm. As can be seen from figure 5.11, uptake of the NR-loaded anionic and neutral nanoparticles was much higher as compared to the NR-loaded cationic nanoparticles as well as free NR. The uptake of the Cationic-NR nanoparticles was almost negligible, much less compared to free NR as well (see panel 4 of figure 5.11). The NR accumulation was restricted to the cytoplasm, as can be seen from the clearly defined blue coloured nucleus surrounded by the red emission corresponding to NR. As mentioned before, the WT-MEF cells prefer nanoparticle uptake via caveolae-mediated endocytosis, thus, the uptake of the anionic and neutral NR-loaded nanoparticles was substantially enhanced due to their negatively charged surface potential (see figure 5.9). This also explains the cytotoxicity data such that there was no significant uptake of the cationic particles and hence, no cytotoxicity was observed as a result.

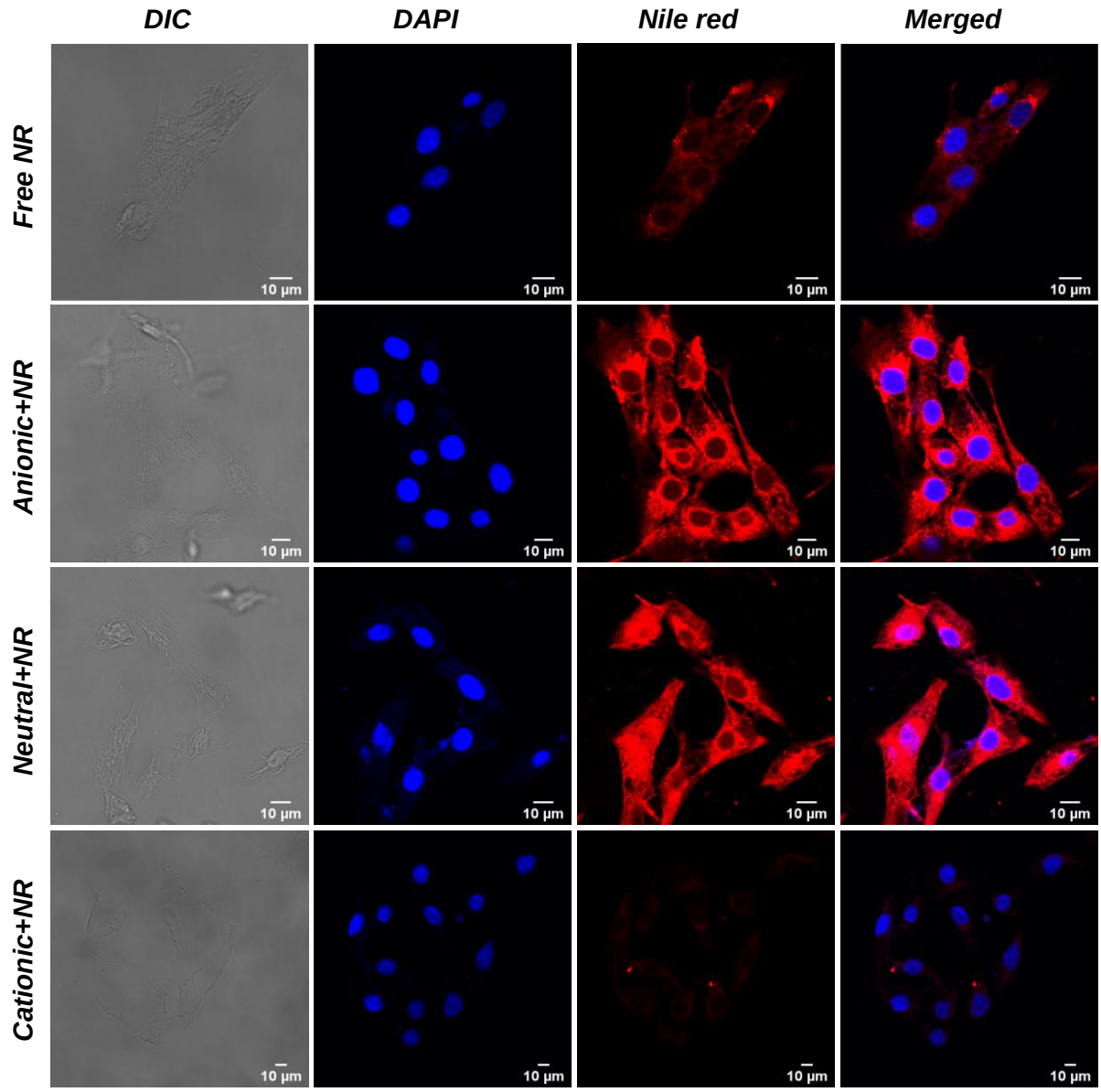

Figure 5.11. *Representative CLSM images depicting cellular uptake of free NR and NR-loaded anionic, neutral and cationic nanoparticles (NR concentration = 2 µg/mL) in WT-MEF cells stained with DAPI. NR was excited using the 561 nm laser and the DAPI excitation was done using the 405 nm laser.*

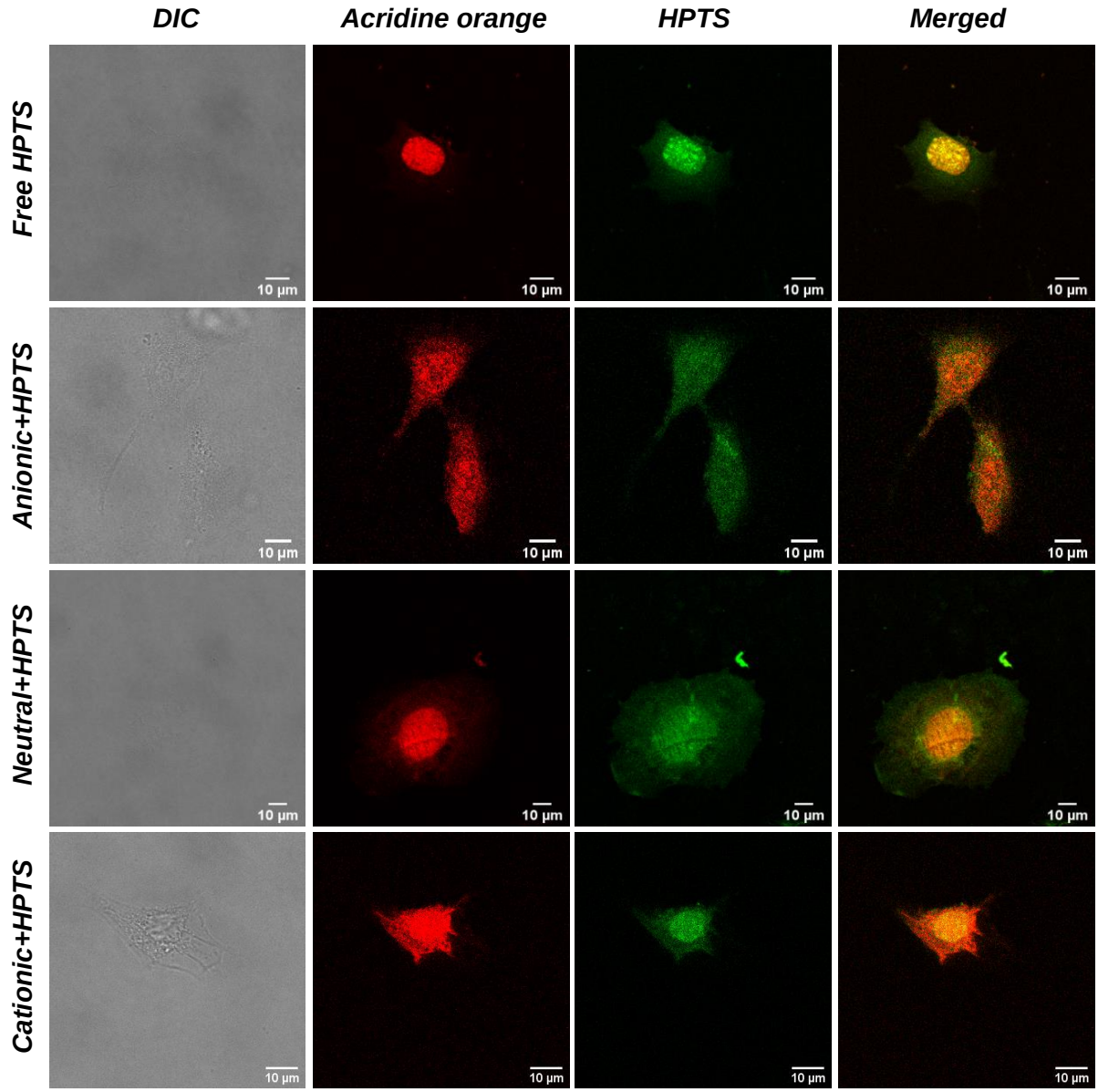

Figure 5.12. *Representative CLSM images depicting cellular uptake of free HPTS and HPTS-loaded anionic, neutral and cationic nanoparticles (HPTS concentration = 5 µg/mL) in WT-MEF cells stained with Acridine orange. HPTS was excited using the 405 nm laser and the acridine orange excitation was done using the 488 nm laser.*

In a similar manner, the HPTS-loaded anionic, neutral and cationic nanoparticles were also fed to the WT-MEF cells and after 4 h the cells were fixed and stained with acridine orange. In this particular experiment, acridine orange was used to stain the nucleus instead of DAPI since the dye of interest, i.e. HPTS also excites at 405 nm and hence, to avoid any spectral overlap we chose acridine orange, that is excited using the 488 nm laser. As can be seen from the CLSM images in figure 5.12, the HPTS loaded nanoparticles along with free HPTS and acridine orange stained nuclei were excited at $\lambda = 405$ nm (green channel) and $\lambda = 488$ nm (red channel), respectively. The λ_{em} for HPTS channel was set at 410-500 nm and that for the acridine orange channel was in the range of 500-650 nm. The CLSM images clearly depicted that the uptake of the HPTS-loaded anionic, neutral and cationic nanoparticles was comparable to each other as well as free HPTS. This observation was in complete coherence with our hypothesis, i.e. the fact that all the HPTS-loaded nanoparticles (anionic, neutral and cationic) exhibited an overall negative surface charge, translated to their ability to penetrate the WT-MEF cellular barrier to the same extent (caveolae-mediated uptake). Even free HPTS being an anionic dye demonstrated similar cellular uptake capabilities as the star polymer nanoparticles. Thus, the aforementioned findings were able to corroborate that anionic surfaces are indeed taken up by the cells via caveolae-mediated endocytosis.

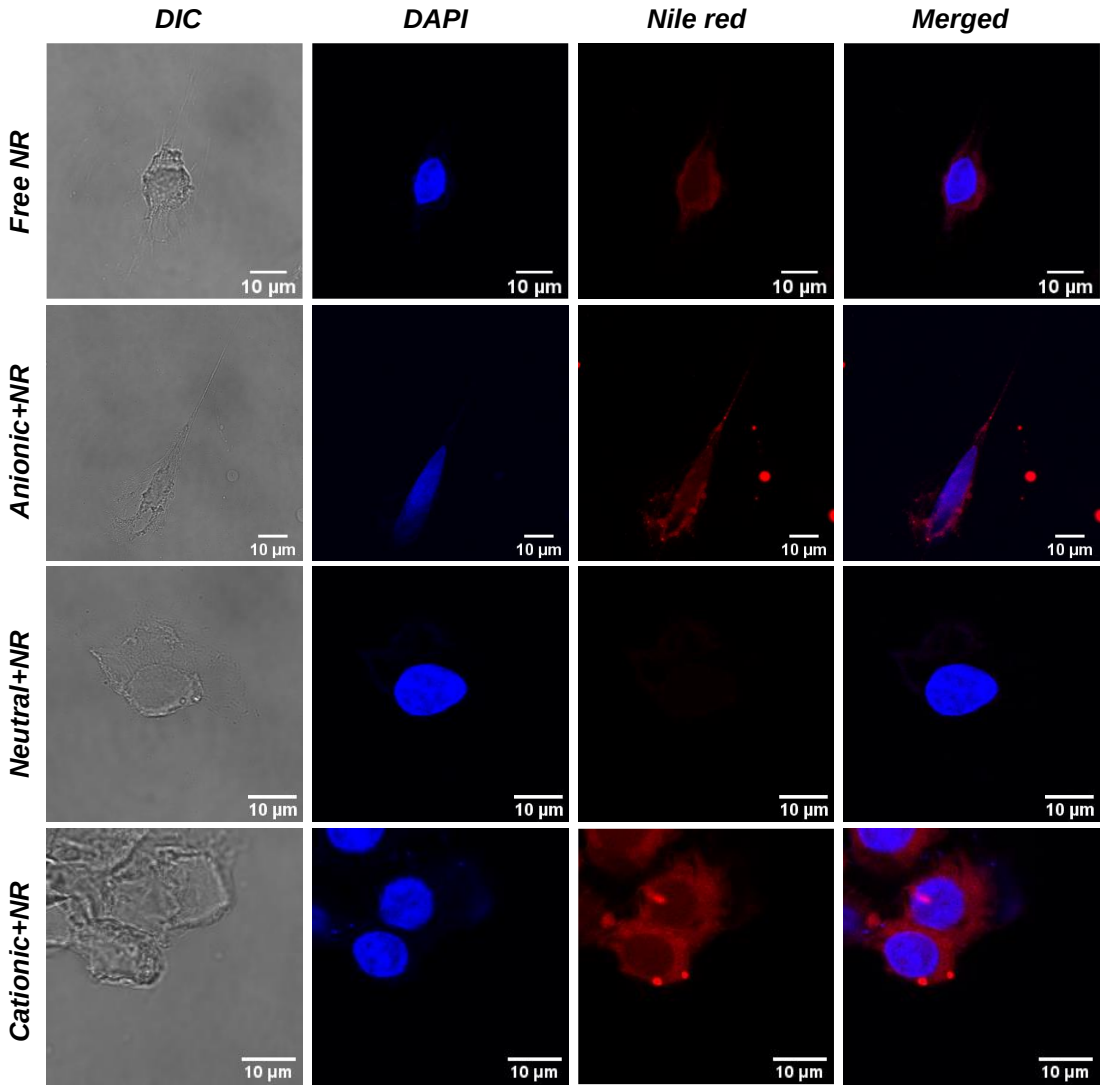

Figure 5.13. *Representative CLSM images depicting cellular uptake of free NR and NR-loaded anionic, neutral and cationic nanoparticles (NR concentration = 2 µg/mL) in HEK293T cells stained with DAPI. NR was excited using the 561 nm laser and the DAPI excitation was done using the 405 nm laser.*

In order to establish that surface charge dictates the cellular uptake ability depending on the different endocytosis pathways followed by different cell types, we chose another cell line namely HEK293T cells that are known to exhibit clathrin-mediated endocytosis. In addition, cationic nanoparticles are known to undergo cellular internalization via the clathrin pathway. These points were addressed by incubating NR-loaded anionic, neutral and cationic nanoparticles with HEK293T cells for 4 h followed by imaging using confocal laser scanning microscopy. As can be seen in figure 5.13, the uptake of the NR-loaded cationic nanoparticles

surpassed that of the anionic and neutral nanoparticles as well as free NR. Here also, the NR internalization was prominent in the cytoplasmic and peri-nuclear region. The enhanced uptake of the cationic-NR nanoparticles by the HEK293T cells re-iterated that their cellular internalization was mediated via the clathrin pathway. The results so far supported our hypothesis that surface charge played a crucial in governing the cellular uptake based on the interactions of the nanoparticle surface with the membrane proteins.

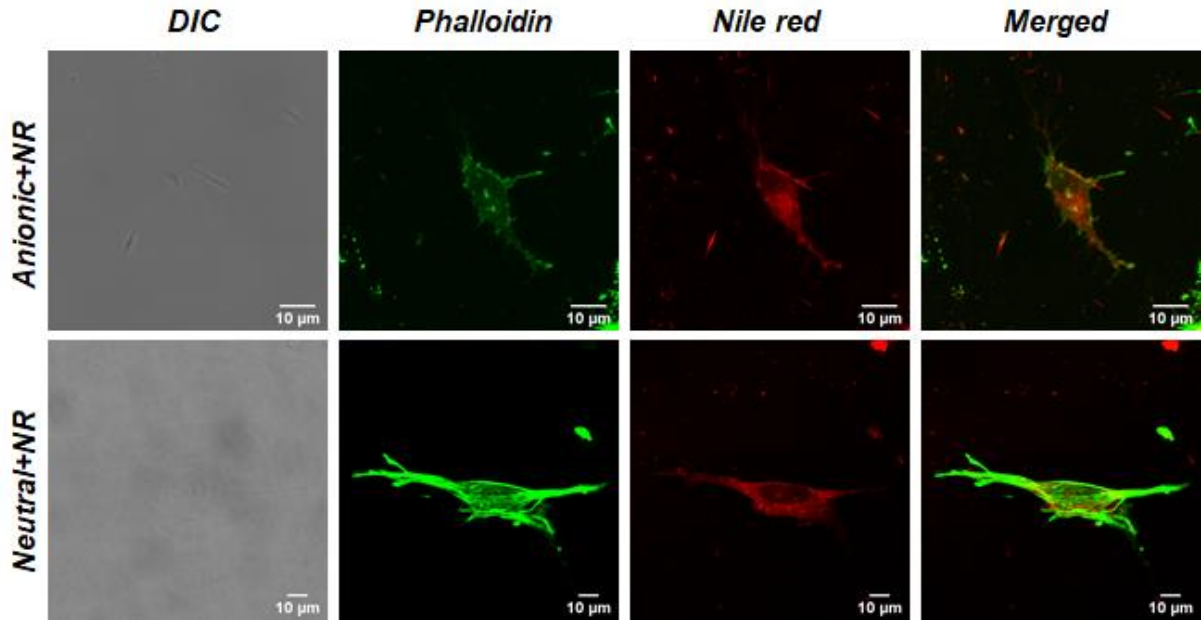

Figure 5.14. *Representative CLSM images depicting cellular uptake of NR-loaded anionic and neutral nanoparticles (NR concentration = 2 µg/mL) in primary chick spinal neuronal cells stained with phalloidin. NR was excited using the 561 nm laser and the phalloidin excitation was done using the 488 nm laser.*

Having established the importance of the surface properties of nano-carriers on the *in vitro* cellular uptake, the next important investigation was the cellular internalization analysis in primary neuronal culture before taking these systems *in vivo*. From our findings in chapter 4, the ability of star-shaped polymer topology to penetrate the blood brain barrier (BBB) had been well-established. Here, the idea was to understand if surface charge potential would also influence the BBB penetration ability and before investigating this hypothesis *in vivo* we decided to experiment with the primary neuronal culture (*in vitro*). The NR-loaded anionic and neutral nanoparticles were incubated with primary chick spinal neuronal cells (days *in vitro*-2)

for 4 h followed by phalloidin staining and confocal imaging. As can be seen in figure 5.14, the anionic-NR and neutral-NR nanoparticles exhibited significant uptake by the neurons. Hence, the anionic and neutral nanoparticles can be employed for investigations in breaching the blood brain barrier *in vivo*. Due to the pandemic, the cellular imaging for IR780 and DOX-loaded nanoparticles could not be completed, however, the work is going on in that direction and will soon be completed.

All the aforementioned findings gave some crucial insight into the effect of surface properties on the *in vitro* cellular uptake capabilities. However, the ultimate goal is to investigate the same *in vivo* on the BBB penetration ability of the different charged nanoparticles. But an important point to consider here is that various factors would affect the ability of the nanoparticles to cross the BBB such as size, shape, surface potential etc. Hence, it will be interesting to employ the anionic, neutral and cationic star block copolymer nanoparticles having different size and surface charge to better understand the BBB crossing ability of particles.

5.4 Conclusion

The star-shaped block copolymer topology was employed to design fully biodegradable anionic, neutral and cationic polycaprolactone based nanoparticles. These served as tools to better understand the role played by surface charge on the nanoparticle and cell interactions impacting the endocytosis pathway and uptake ability. Herein, 6-arm star-shaped block copolymers were developed where polycaprolactone constituted the hydrophobic part and substituted polycaprolactone represented the hydrophilic shell imparting the appropriate amphiphilicity. Their aqueous self-assemblies exhibited spherical nanoparticles with negative (-40.7 mV), neutral (-3.7 mV) and positive (33.2 mV) net surface charge and sizes in the range of 40-100 nm. The anionic, neutral and cationic nanoparticles were able to successfully load Nile red (neutral dye) and HPTS (anionic dye) dyes without any morphological alterations. These dye-loaded nanoparticles maintained their spherical shape with sizes in the range of 18-120 nm. The NR-loaded nanoparticles yielded anionic, neutral and cationic nanoparticles having surface potential of -27 mV, -12 mV and 20 mV, respectively. Upon loading HPTS, an anionic dye, all the nanoparticles exhibited negative zeta potential values in the range of -28 mV to -15 mV. The *in vitro* cellular uptake investigation gave the much-needed insight on the effect of surface charge on the ability of nanoparticle internalization into the cell. The NR-loaded anionic and neutral nanoparticles were much superior in their cellular uptake by WT-MEF cells compared to their cationic counterpart. Cellular internalization of the HPTS-loaded anionic, neutral and cationic nanoparticles was similar to each other and free HPTS owing to the fact that they all exhibited negative surface potential. These findings established that anionic nanoparticles, i.e. nanoparticles having a net negative surface charge, preferred to undergo internalization into the cell via caveolae-mediated endocytosis, the predominant pathway in WT-MEF cells. Cellular uptake of the NR-loaded nanoparticles in HEK293T cells, that are known for the presence of clathrin proteins, established the supremacy of the cationic nanoparticles over the anionic and neutral counterparts. This pointed out that the cationic nanoparticles chose the clathrin-mediated endocytosis pathway for cellular uptake. The anionic and neutral nanoparticles also exhibited internalization by the neurons in the primary chick spinal culture. Thus, these anionic, neutral and cationic star-block copolymers are ideal candidates for investigating the role of surface charge on the ability to breach the blood brain barrier *in vivo*.

6

Summary and Future Directions

In a nutshell, new classes of fully biodegradable and amphiphilic carboxylic functionalized polycaprolactone-co-polycaprolactone random and block copolymers were custom designed via ring opening polymerization methodology. The variation in composition of the carboxylic acid substituted PCL in the polymer backbone resulted in transformation from semi-crystalline to completely amorphous polymers. *In vitro* enzymatic-biodegradation and drug release kinetics analysis of the DOX loaded polymer nanoparticles demonstrated a transition from "slow" to "controlled" to "burst" release depending on the carboxylic acid content. *In vitro* cytotoxicity studies in cervical and breast cancer cells revealed that the nascent polymer scaffolds were non-toxic to cells. The DOX loaded nanoparticles exhibited excellent cell killing ability in cervical and breast cancer cells and accomplished more than > 90 % cell death for 1.0 μg/mL. Confocal microscopic analysis elucidated that the polymer loaded drugs are predominantly internalized at the nucleus of the cells and support their enzymatic-biodegradation pathway of drug delivery and their excellent cell killing ability. Flow cytometry analysis revealed that the random and block copolymer nanoparticles were more efficiently taken up by the cells as compared to free DOX.

Novel star-shaped fully biodegradable and amphiphilic carboxylic functionalized polycaprolactone-based block copolymers were designed via sequential ring opening polymerization methodology in a custom-made melt reactor set up with an overhead stirrer. The melt reactor set up afforded the formation of high molecular weight up to 50 kDa star architectures with narrow polydispersity (< 1.4). The pyrene CMC experiment confirmed the formation of unimolecular micelles that were stable under infinite dilution, i.e. their self-assembly process was concentration independent for the star block copolymers SB-60 and SB-100. Whereas, the linear block copolymer exhibited the formation of aggregated micelles with a CMC of 1 μg/mL. The amphiphilic star polymers exhibited excellent loading tendency (DLC = 14%) for anticancer drug DOX that was ~ 7-fold high compared to the DLC of the linear block copolymer (DLC = 2 %). Cytotoxicity assay in WT-MEF cells showed the cyto-compatibility of the star block copolymer up to 500 μg/mL concentration. Their DOX-loaded counterparts were less toxic to the WT-MEF cells compared to free DOX up to a concentration of 1 μg/mL after 72 h. Confocal microscopic analysis demonstrated that the polymer loaded drugs internalized at the lysosomal compartment of the cells. Herein, the unimolecular star block SB-60+DOX micelle surpassed it's linear block copolymer analogue LB-60+DOX in

terms of the cellular uptake via endocytosis as was visualized from the live cell experiment in WT-MEF cells.

Tailor-made star-shaped and linear block copolymer topologies were chosen as model systems to investigate the role of macromolecular architectures on their biodistribution, pharmacokinetics and specifically their ability to penetrate the impermeable blood brain barrier. The star-block copolymer unimolecular micelle exhibited it's ability to cross the blood brain barrier and accumulate in the brain tissue as opposed to the free DOX and linear block copolymer. These UMMs were also able to reduce the cardiotoxicity of DOX by depleting the amount in the heart tissue thus, overcoming the major limitation in the use of DOX for chemotherapy. The pharmacokinetics evaluation revealed a $t_{1/2}$ of 4.0 h for the star polymer and the half-life could not be determined for the linear polymer as well as free DOX due to their faster removal from the circulation. The polymer nano-formulations were non-immunogenic which was established from the low cytokine expressions in the plasma samples. The H&E histological analysis revealed no morphological alteration in the tissue sections reiterating the biocompatibility of the polymer drug nano-carriers. The unimolecular micelle successfully delivered DOX into the brain tissue by crossing the BBB; however, the uptake was influenced by the BBB heterogeneity such that the uptake was higher in the posterior parts of the brain compared to the anterior section. In order to confirm the intra-cellular localization of DOX in the brain tissue, MAP 2 antibody staining was employed to mark the mature neurons.

The star-shaped block copolymer topology was employed to design fully biodegradable anionic, neutral and cationic polycaprolactone based nanoparticles. These served as tools to better understand the role played by surface charge on the nanoparticle and cell interactions impacting the endocytosis pathway and uptake ability. Their aqueous self-assemblies exhibited spherical nanoparticles with negative (-40.7 mV), neutral (-3.7 mV) and positive (33.2 mV) net surface charge and sizes in the range of 40-100 nm. The NR-loaded nanoparticles yielded anionic, neutral and cationic nanoparticles having surface potential of -27 mV, -12 mV and 20 mV, respectively. Upon loading HPTS, an anionic dye, all the nanoparticles exhibited negative zeta potential values in the range of -28 mV to -15 mV. The NR-loaded anionic and neutral nanoparticles were much superior in their cellular uptake by WT-MEF cells compared to their cationic counterpart. Cellular internalization of the HPTS-loaded anionic, neutral and cationic

nanoparticles was similar to each other and free HPTS owing to the fact that they all exhibited negative surface potential. These findings established that anionic nanoparticles, i.e. nanoparticles having a net negative surface charge, preferred to undergo internalization into the cell via caveolae-mediated endocytosis, the predominant pathway in WT-MEF cells. Cellular uptake of the NR-loaded nanoparticles in HEK293T cells, that are known for the presence of clathrin proteins, established the supremacy of the cationic nanoparticles over the anionic and neutral counterparts. This pointed out that the cationic nanoparticles chose the clathrin-mediated endocytosis pathway for cellular uptake. The anionic and neutral nanoparticles also exhibited internalization by the neurons in the primary chick spinal culture.

Future Directions

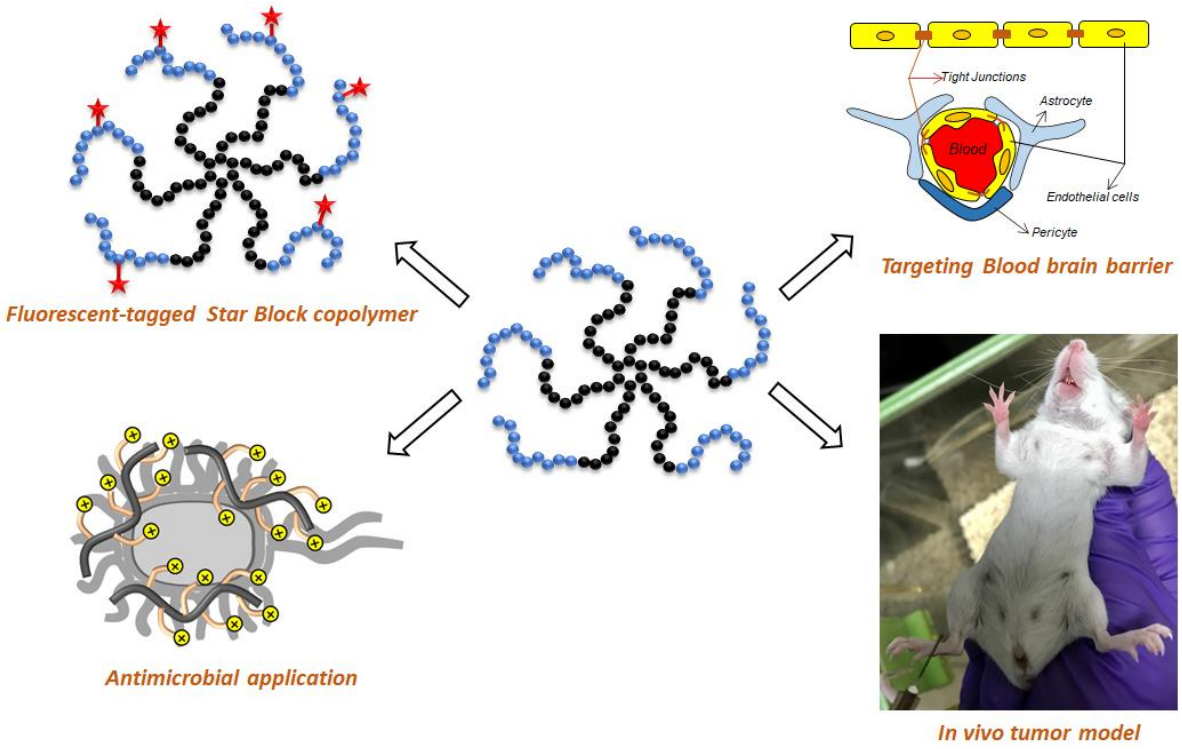

Figure 6.1. *Schematic representation of the different avenues possible for enhancing the research in the star-block copolymer field.*

The work presented here highlights the importance of fundamental understanding of the role played by polymer topology on all the drug delivery aspects. The star-shaped unimolecular micelles provide a unique platform for exploitation in a plethora of biomedical applications. The figure 6.1 demonstrates few such approaches for the next obvious steps in the field of star-block copolymers. In order to be able to track the formulations in vivo in real-time, it is crucial to fluorescently tag the polymer backbone. These fluorescently tagged star-block copolymers can further be employed for targeting the blood brain barrier as well as investigating their anticancer efficacy in an animal model. These star block copolymers can also be exploited for antimicrobial applications by making the polymer backbone cationic that would selectively bind to the bacterial membrane.

7

References

(1) Cerqueira, B. B. S.; Lasham, A.; Shelling, A. N.; Al-Kassas, R. Nanoparticle Therapeutics: Technologies and Methods for Overcoming Cancer. *Eur. J. Pharm. Biopharm.* **2015**, *97*, 140–151. https://doi.org/10.1016/j.ejpb.2015.10.007.

(2) Falzone, L.; Salomone, S.; Libra, M. Evolution of Cancer Pharmacological Treatments at the Turn of the Third Millennium. *Front. Pharmacol.* **2018**, *9* (NOV). https://doi.org/10.3389/fphar.2018.01300.

(3) Arruebo, M.; Vilaboa, N.; Sáez-Gutierrez, B.; Lambea, J.; Tres, A.; Valladares, M.; González-Fernández, Á. Assessment of the Evolution of Cancer Treatment Therapies. *Cancers (Basel).* **2011**, *3* (3), 3279–3330. https://doi.org/10.3390/cancers3033279.

(4) Sun, T.; Zhang, Y. S.; Pang, B.; Hyun, D. C.; Yang, M.; Xia, Y. Engineered Nanoparticles for Drug Delivery in Cancer Therapy. *Angew. Chemie - Int. Ed.* **2014**, *53* (46), 12320–12364. https://doi.org/10.1002/anie.201403036.

(5) Shi, J.; Votruba, A. R.; Farokhzad, O. C.; Langer, R. Nanotechnology in Drug Delivery and Tissue Engineering: From Discovery to Applications. *Nano Lett.* **2010**, *10* (9), 3223–3230. https://doi.org/10.1021/nl102184c.

(6) Alexis, F.; Pridgen, E.; Molnar, L. K.; Farokhzad, O. C. Factors Affecting the Clearance and Biodistribution of Polymeric Nanoparticles. *Mol. Pharm.* **2008**, *5* (4), 505–515. https://doi.org/10.1021/mp800051m.

(7) Farokhzad, O. C.; Langer, R. Impact of Nanotechnology on Drug Delivery. *ACS Nano* **2009**, *3* (1), 16–20. https://doi.org/10.1021/nn900002m.

(8) Cho, K.; Wang, X.; Nie, S.; Chen, Z.; Shin, D. M. Therapeutic Nanoparticles for Drug Delivery in Cancer. *Clin. Cancer Res.* **2008**, *14* (5), 1310–1316. https://doi.org/10.1158/1078-0432.CCR-07-1441.

(9) Mitchell, M. J.; Billingsley, M. M.; Haley, R. M.; Wechsler, M. E.; Peppas, N. A.; Langer, R. Engineering Precision Nanoparticles for Drug Delivery. *Nat. Rev. Drug Discov.* **2021**, *20* (2), 101–124. https://doi.org/10.1038/s41573-020-0090-8.

(10) Davis, M. E.; Chen, Z.; Shin, D. M. Nanoparticle Therapeutics: An Emerging Treatment Modality for Cancer. *Nat. Rev. Drug Discov.* **2008**, *7* (9), 771–782. https://doi.org/10.1038/nrd2614.

(11) Wang, J.; Potocny, A. M.; Rosenthal, J.; Day, E. S. Gold Nanoshell-Linear Tetrapyrrole Conjugates for Near Infrared-Activated Dual Photodynamic and Photothermal Therapies. *ACS Omega* **2019**, *5* (1), 926–940. https://doi.org/10.1021/ACSOMEGA.9B04150.

(12) LS, A.; JP, P.; APM, V.; TMT, L.; ACB, D.; DR, M. Iron Oxide Nanoparticles for Biomedical Applications: A Perspective on Synthesis, Drugs, Antimicrobial Activity, and Toxicity. *Antibiot. (Basel, Switzerland)* **2018**, *7* (2). https://doi.org/10.3390/ANTIBIOTICS7020046.

(13) BB, M.; J, J.; U, H.; SJ, S. Personalized Medicine and Follow-up of Therapeutic Delivery through Exploitation of Quantum Dot Toxicity. *Biomaterials* **2017**, *127*, 1–12.

https://doi.org/10.1016/J.BIOMATERIALS.2017.02.039.

(14) Vines, J. B.; Yoon, J.-H.; Ryu, N.-E.; Lim, D.-J.; Park, H. Gold Nanoparticles for Photothermal Cancer Therapy. *Front. Chem.* **2019**, *7* (APR), 167. https://doi.org/10.3389/FCHEM.2019.00167.

(15) Kresge, C. T.; Leonowicz, M. E.; Roth, W. J.; Vartuli, J. C.; Beck, J. S. Ordered Mesoporous Molecular Sieves Synthesized by a Liquid-Crystal Template Mechanism. *Nat. 1992 3596397* **1992**, *359* (6397), 710–712. https://doi.org/10.1038/359710a0.

(16) S, G.; BG, T.; VS, L. Mesoporous Silica Nanomaterial-Based Biotechnological and Biomedical Delivery Systems. *Nanomedicine (Lond).* **2007**, *2* (1), 99–111. https://doi.org/10.2217/17435889.2.1.99.

(17) Slowing, I. I.; Trewyn, B. G.; Giri, S.; Lin, V. S.-Y. Mesoporous Silica Nanoparticles for Drug Delivery and Biosensing Applications. *Adv. Funct. Mater.* **2007**, *17* (8), 1225–1236. https://doi.org/10.1002/ADFM.200601191.

(18) JL, V.-E.; II, S.; BG, T.; VS, L. Mesoporous Silica Nanoparticles for Intracellular Controlled Drug Delivery. *Small* **2010**, *6* (18), 1952–1967. https://doi.org/10.1002/SMLL.200901789.

(19) Xu, C.; Nam, J.; Hong, H.; Xu, Y.; Moon, J. J. Positron Emission Tomography-Guided Photodynamic Therapy with Biodegradable Mesoporous Silica Nanoparticles for Personalized Cancer Immunotherapy. *ACS Nano* **2019**, *13* (10), 12148. https://doi.org/10.1021/ACSNANO.9B06691.

(20) Zheng, J.; Zhang, C.; Dickson, R. M. Highly Fluorescent, Water-Soluble, Size-Tunable Gold Quantum Dots. *Phys. Rev. Lett.* **2004**, *93* (7), 077402. https://doi.org/10.1103/PhysRevLett.93.077402.

(21) CA, L.; TY, Y.; CH, L.; SH, H.; RA, S.; M, Z.; JK, L.; JL, S.; HH, W.; HI, Y.; WJ, P.; WH, C. Synthesis, Characterization, and Bioconjugation of Fluorescent Gold Nanoclusters toward Biological Labeling Applications. *ACS Nano* **2009**, *3* (2), 395–401. https://doi.org/10.1021/NN800632J.

(22) Wang, H.; Huff, T. B.; Zweifel, D. A.; He, W.; Low, P. S.; Wei, A.; Cheng, J.-X. In Vitro and in Vivo Two-Photon Luminescence Imaging of Single Gold Nanorods. *Proc. Natl. Acad. Sci. U. S. A.* **2005**, *102* (44), 15752. https://doi.org/10.1073/PNAS.0504892102.

(23) Tong, L.; Cobley, C. M.; Chen, D. J.; Xia, P. Y.; Cheng, P. J.-X. Bright Three-Photon Luminescence from Au-Ag Alloyed Nanostructures for Bioimaging with Negligible Photothermal Toxicity. *Angew. Chem. Int. Ed. Engl.* **2010**, *49* (20), 3485. https://doi.org/10.1002/ANIE.201000440.

(24) J, C.; C, G.; R, L.; Q, Z.; M, Y.; M, G.; MJ, W.; Y, X. Gold Nanocages as Photothermal Transducers for Cancer Treatment. *Small* **2010**, *6* (7), 811–817. https://doi.org/10.1002/SMLL.200902216.

(25) D, B.; KJ, R.; J, I.; KJ, T.; SR, C. Nanoparticle-Based Medicines: A Review of FDA-

Approved Materials and Clinical Trials to Date. *Pharm. Res.* **2016**, *33* (10), 2373–2387. https://doi.org/10.1007/S11095-016-1958-5.

(26) M, W.; K, A.; S, S.; CL, A.; Q, X. Combinatorially Designed Lipid-like Nanoparticles for Intracellular Delivery of Cytotoxic Protein for Cancer Therapy. *Angew. Chem. Int. Ed. Engl.* **2014**, *53* (11), 2893–2898. https://doi.org/10.1002/ANIE.201311245.

(27) KS, S.; TM, A.; AR, K.; WE, R. Biodegradable Polymeric Nanoparticles as Drug Delivery Devices. *J. Control. Release* **2001**, *70* (1–2), 1–20. https://doi.org/10.1016/S0168-3659(00)00339-4.

(28) L, Z.; A, B.; L, L.; A, A.; TM, M.; G, W.; Q, W. Microfluidic-Assisted Polymer-Protein Assembly to Fabricate Homogeneous Functionalnanoparticles. *Mater. Sci. Eng. C. Mater. Biol. Appl.* **2020**, *111*. https://doi.org/10.1016/J.MSEC.2020.110768.

(29) M, C.-M.; JE, V. R.; NA, P. Transport and Delivery of Interferon-α through Epithelial Tight Junctions via PH-Responsive Poly(Methacrylic Acid-Grafted-Ethylene Glycol) Nanoparticles. *J. Drug Target.* **2019**, *27* (5–6), 582–589. https://doi.org/10.1080/1061186X.2018.1547732.

(30) FC, K.; P, G.; A, K.; KW, B.; S, S.; ME, J.; N, S.; L, W.-B.; KL, B.; JE, C.; S, J.; JT, W. Mucosal Immunization with a PH-Responsive Nanoparticle Vaccine Induces Protective CD8 + Lung-Resident Memory T Cells. *ACS Nano* **2019**, *13* (10), 10939–10960. https://doi.org/10.1021/ACSNANO.9B00326.

(31) MS, S.; BA, K.; H, P.; X, Z.; Y, B.; C, B.; C, W.; N, S.; T, F.; SP, G.; DG, D.; WE, G.; WG, H.; SA, W.; RC, F. Precision Delivery of RAS-Inhibiting SiRNA to KRAS Driven Cancer via Peptide-Based Nanoparticles. *Oncotarget* **2019**, *10* (46), 4761–4775. https://doi.org/10.18632/ONCOTARGET.27109.

(32) Liu, X.; Li, C.; Lv, J.; Huang, F.; An, Y.; Shi, L.; Ma, R. Glucose and H2O2 Dual-Responsive Polymeric Micelles for the Self-Regulated Release of Insulin. *ACS Appl. Bio Mater.* **2020**, *3* (3), 1598–1606. https://doi.org/10.1021/ACSABM.9B01185.

(33) M, A.; M, H.; A, M.; K, A.; M, R. Recent Advances in Co-Delivery Systems Based on Polymeric Nanoparticle for Cancer Treatment. *Artif. cells, nanomedicine, Biotechnol.* **2018**, *46* (6), 1095–1110. https://doi.org/10.1080/21691401.2017.1376675.

(34) Patra, J. K.; Das, G.; Fraceto, L. F.; Campos, E. V. R.; Rodriguez-Torres, M. del P.; Acosta-Torres, L. S.; Diaz-Torres, L. A.; Grillo, R.; Swamy, M. K.; Sharma, S.; Habtemariam, S.; Shin, H.-S. Nano Based Drug Delivery Systems: Recent Developments and Future Prospects. *J. Nanobiotechnology 2018 161* **2018**, *16* (1), 1–33. https://doi.org/10.1186/S12951-018-0392-8.

(35) LR, V.; MA, M.; AB, C.; D, D.; KB, D.; R, L.; DG, A. Glucose-Responsive Nanoparticles for Rapid and Extended Self-Regulated Insulin Delivery. *ACS Nano* **2020**, *14* (1), 488–497. https://doi.org/10.1021/ACSNANO.9B06395.

(36) Rideau, E.; Dimova, R.; Schwille, P.; Wurm, F. R.; Landfester, K. Liposomes and Polymersomes: A Comparative Review towards Cell Mimicking. *Chem. Soc. Rev.* **2018**,

47 (23), 8572–8610. https://doi.org/10.1039/C8CS00162F.

(37) D, S.; KW, B.; P, C.; DS, Y.; AKR, L.-J.; S, S.; M, A.; M, K.; DB, J.; JM, B.; JT, W. Endosomolytic Polymersomes Increase the Activity of Cyclic Dinucleotide STING Agonists to Enhance Cancer Immunotherapy. *Nat. Nanotechnol.* **2019**, *14* (3), 269–278. https://doi.org/10.1038/S41565-018-0342-5.

(38) Zelmer, C.; Zweifel, L. P.; Kapinos, L. E.; Craciun, I.; Güven, Z. P.; Palivan, C. G.; Lim, R. Y. H. Organelle-Specific Targeting of Polymersomes into the Cell Nucleus. *Proc. Natl. Acad. Sci.* **2020**, *117* (6), 2770–2778. https://doi.org/10.1073/PNAS.1916395117.

(39) SW, L.; YM, K.; CH, C.; YT, K.; SM, K.; SY, H.; JH, K.; BG, K.; SC, K.; HS, R.; SB, K. An Open-Label, Randomized, Parallel, Phase II Trial to Evaluate the Efficacy and Safety of a Cremophor-Free Polymeric Micelle Formulation of Paclitaxel as First-Line Treatment for Ovarian Cancer: A Korean Gynecologic Oncology Group Study (KGOG-3021). *Cancer Res. Treat.* **2018**, *50* (1), 195–203. https://doi.org/10.4143/CRT.2016.376.

(40) DM, V.; MN, D.; MA, S.; ES, D. Nanoparticle-Mediated Co-Delivery of Notch-1 Antibodies and ABT-737 as a Potent Treatment Strategy for Triple-Negative Breast Cancer. *ACS Nano* **2020**, *14* (3), 3378–3388. https://doi.org/10.1021/ACSNANO.9B09263.

(41) L, X.; H, Z.; Y, W. Dendrimer Advances for the Central Nervous System Delivery of Therapeutics. *ACS Chem. Neurosci.* **2014**, *5* (1), 2–13. https://doi.org/10.1021/CN400182Z.

(42) L, P. M.; J, P.; VP, T. Dendrimers as Nanocarriers for Nucleic Acid and Drug Delivery in Cancer Therapy. *Molecules* **2017**, *22* (9). https://doi.org/10.3390/MOLECULES22091401.

(43) RM, K.; E, N.; S, K.; DA, T. Emerging Concepts in Dendrimer-Based Nanomedicine: From Design Principles to Clinical Applications. *J. Intern. Med.* **2014**, *276* (6), 579–617. https://doi.org/10.1111/JOIM.12280.

(44) AR, M.; RM, K.; DA, T. Dendrimer-Based Drug and Imaging Conjugates: Design Considerations for Nanomedical Applications. *Drug Discov. Today* **2010**, *15* (5–6), 171–185. https://doi.org/10.1016/J.DRUDIS.2010.01.009.

(45) Anselmo, A. C.; Mitragotri, S. Nanoparticles in the Clinic: An Update. *Bioeng. Transl. Med.* **2019**, *4* (3). https://doi.org/10.1002/BTM2.10143.

(46) Kolhar, P.; Anselmo, A. C.; Gupta, V.; Pant, K.; Prabhakarpandian, B.; Ruoslahti, E.; Mitragotri, S. Using Shape Effects to Target Antibody-Coated Nanoparticles to Lung and Brain Endothelium. *Proc. Natl. Acad. Sci. U. S. A.* **2013**, *110* (26), 10753–10758. https://doi.org/10.1073/pnas.1308345110.

(47) JA, C.; YK, K.; S, M. Particle Shape: A New Design Parameter for Micro- and Nanoscale Drug Delivery Carriers. *J. Control. Release* **2007**, *121* (1–2), 3–9. https://doi.org/10.1016/J.JCONREL.2007.03.022.

(48) Tao, L.; Hu, W.; Liu, Y.; Huang, G.; Sumer, B. D.; Gao, J. Shape-Specific Polymeric Nanomedicine: Emerging Opportunities and Challenges: *https://doi.org/10.1258/ebm.2010.010243* **2011**, *236* (1), 20–29. https://doi.org/10.1258/EBM.2010.010243.

(49) Lee, S.-Y.; Ferrari, M.; Decuzzi, P. Shaping Nano-/Micro-Particles for Enhanced Vascular Interaction in Laminar Flows. *Nanotechnology* **2009**, *20* (49), 495101. https://doi.org/10.1088/0957-4484/20/49/495101.

(50) Devarajan, P. V.; Jindal, A. B.; Patil, R. R.; Mulla, F.; Gaikwad, R. V.; Samad, A. Particle Shape: A New Design Parameter for Passive Targeting in Splenotropic Drug Delivery. *J. Pharm. Sci.* **2010**, *99* (6), 2576–2581. https://doi.org/10.1002/JPS.22052.

(51) N, D.; B, P.; A, R.-R.; K, P.; S, S.; S, M. Flow and Adhesion of Drug Carriers in Blood Vessels Depend on Their Shape: A Study Using Model Synthetic Microvascular Networks. *J. Control. Release* **2010**, *146* (2), 196–200. https://doi.org/10.1016/J.JCONREL.2010.04.007.

(52) Y, G.; P, D.; S, C.; R, T.; M, T.; T, M.; DE, D. Shape Effects of Filaments versus Spherical Particles in Flow and Drug Delivery. *Nat. Nanotechnol.* **2007**, *2* (4), 249–255. https://doi.org/10.1038/NNANO.2007.70.

(53) G, S.; DT, V.; Y, A.; S, H.; H, X.; S, M.; JW, S. Polymer Particle Shape Independently Influences Binding and Internalization by Macrophages. *J. Control. Release* **2010**, *147* (3), 408–412. https://doi.org/10.1016/J.JCONREL.2010.07.116.

(54) MK, P.; JB, L. Pinocytosis and Phagocytosis: The Effect of Size of a Particulate Substrate on Its Mode of Capture by Rat Peritoneal Macrophages Cultured in Vitro. *Biochim. Biophys. Acta* **1986**, *881* (3), 307–313. https://doi.org/10.1016/0304-4165(86)90020-6.

(55) Phagocytosis and the actin cytoskeleton - PubMed https://pubmed.ncbi.nlm.nih.gov/11228151/ (accessed Jul 16, 2021).

(56) M, S.; K, S.; Y, U.; T, O. Microelastic Mapping of Living Endothelial Cells Exposed to Shear Stress in Relation to Three-Dimensional Distribution of Actin Filaments. *Acta Biomater.* **2007**, *3* (3), 311–319. https://doi.org/10.1016/J.ACTBIO.2006.07.009.

(57) Roemeling, C. von; Jiang, W.; Chan, C. K.; Weissman, I. L.; Kim, B. Y. S. Breaking Down the Barriers to Precision Cancer Nanomedicine. *Trends Biotechnol.* **2017**, *35* (2), 159–171. https://doi.org/10.1016/J.TIBTECH.2016.07.006.

(58) Xie, X.; Liao, J.; Shao, X.; Li, Q.; Lin, Y. The Effect of Shape on Cellular Uptake of Gold Nanoparticles in the Forms of Stars, Rods, and Triangles. *Sci. Reports 2017 71* **2017**, *7* (1), 1–9. https://doi.org/10.1038/s41598-017-04229-z.

(59) Wang, W.; Gaus, K.; Tilley, R. D.; Gooding, J. J. The Impact of Nanoparticle Shape on Cellular Internalisation and Transport: What Do the Different Analysis Methods Tell Us? *Mater. Horizons* **2019**, *6* (8), 1538–1547. https://doi.org/10.1039/C9MH00664H.

(60) Garapaty, A.; Champion, J. A. Shape of Ligand Immobilized Particles Dominates and

Amplifies the Macrophage Cytokine Response to Ligands. *PLoS One* **2019**, *14* (5), e0217022. https://doi.org/10.1371/JOURNAL.PONE.0217022.

(61) Fox, M. E.; Szoka, F. C.; Fréchet, J. M. J. Soluble Polymer Carriers for the Treatment of Cancer: The Importance of Molecular Architecture. *Acc. Chem. Res.* **2009**, *42* (8), 1141–1151. https://doi.org/10.1021/ar900035f.

(62) N, K.; Z, X.; PM, V.; AF, R.-M.; OC, F. Targeted Polymeric Therapeutic Nanoparticles: Design, Development and Clinical Translation. *Chem. Soc. Rev.* **2012**, *41* (7), 2971–3010. https://doi.org/10.1039/C2CS15344K.

(63) X, X.; M, Y.; Y, W.; Y, Z.; Q, L.; J, C.; Y, X. Quantifying the Coverage Density of Poly(Ethylene Glycol) Chains on the Surface of Gold Nanostructures. *ACS Nano* **2012**, *6* (1), 512–522. https://doi.org/10.1021/NN2038516.

(64) N, H.; S, G.; H, H.; G, B. The Effect of Nanoparticle Size on in Vivo Pharmacokinetics and Cellular Interaction. *Nanomedicine (Lond).* **2016**, *11* (6), 673–692. https://doi.org/10.2217/NNM.16.5.

(65) Duncan, R.; Kopeček, J. Soluble Synthetic Polymers as Potential Drug Carriers. **1984**, 51–101. https://doi.org/10.1007/3-540-12796-8_10.

(66) E, W.; F, B.; D, L.; R, D. Z.; D, J.; E, C.; A, V. Structure and Function of Sinusoidal Lining Cells in the Liver. *Toxicol. Pathol.* **1996**, *24* (1), 100–111. https://doi.org/10.1177/019262339602400114.

(67) Albanese, A.; Tang, P. S.; Chan, W. C. W. The Effect of Nanoparticle Size, Shape, and Surface Chemistry on Biological Systems. *Annu. Rev. Biomed. Eng. 2012* **2012**, *14*, 1–16. https://doi.org/10.1146/annurev-bioeng-071811-150124.

(68) Jain, R. K.; Stylianopoulos, T. Delivering Nanomedicine to Solid Tumors. *Nat. Rev. Clin. Oncol. 2010 711* **2010**, *7* (11), 653–664. https://doi.org/10.1038/nrclinonc.2010.139.

(69) Nagayama, S.; Ogawara, K. ichi; Fukuoka, Y.; Higaki, K.; Kimura, T. Time-Dependent Changes in Opsonin Amount Associated on Nanoparticles Alter Their Hepatic Uptake Characteristics. *Int. J. Pharm.* **2007**, *342* (1–2), 215–221. https://doi.org/10.1016/j.ijpharm.2007.04.036.

(70) MP, D.; V, L.; GL, A.; RJ, L. Gastrointestinal Uptake of Biodegradable Microparticles: Effect of Particle Size. *Pharm. Res.* **1996**, *13* (12), 1838–1845. https://doi.org/10.1023/A:1016085108889.

(71) MP, D.; V, L.; E, W.; RJ, L.; GL, A. The Mechanism of Uptake of Biodegradable Microparticles in Caco-2 Cells Is Size Dependent. *Pharm. Res.* **1997**, *14* (11), 1568–1573. https://doi.org/10.1023/A:1012126301290.

(72) M. Rabanel, J.; Aoun, V.; Elkin, I.; Mokhtar, M.; Hildgen, P. Drug-Loaded Nanocarriers: Passive Targeting and Crossing of Biological Barriers. *Curr. Med. Chem.* **2012**, *19* (19), 3070–3102. https://doi.org/10.2174/092986712800784702.

(73) P, C.; G, B.; E, F.; P, L.; C, V. Nanocapsule Technology: A Review. *Crit. Rev. Ther. Drug Carrier Syst.* **2002**, *19* (2), 99–134. https://doi.org/10.1615/CRITREVTHERDRUGCARRIERSYST.V19.I2.10.

(74) M, R.; D, F.; T, K. Surface-Modified Biodegradable Albumin Nano- and Microspheres. II: Effect of Surface Charges on in Vitro Phagocytosis and Biodistribution in Rats. *Eur. J. Pharm. Biopharm.* **1998**, *46* (3), 255–263. https://doi.org/10.1016/S0939-6411(98)00038-1.

(75) A, G.; A, L.; B, P.; R, M. Influence of Surface Charge Density on Protein Adsorption on Polymeric Nanoparticles: Analysis by Two-Dimensional Electrophoresis. *Eur. J. Pharm. Biopharm.* **2002**, *54* (2), 165–170. https://doi.org/10.1016/S0939-6411(02)00081-4.

(76) Owens, D. E.; Peppas, N. A. Opsonization, Biodistribution, and Pharmacokinetics of Polymeric Nanoparticles. *Int. J. Pharm.* **2006**, *307* (1), 93–102. https://doi.org/10.1016/j.ijpharm.2005.10.010.

(77) Asati, A.; Santra, S.; Kaittanis, C.; Perez, J. M. Surface-Charge-Dependent Cell Localization and Cytotoxicity of Cerium Oxide Nanoparticles. *ACS Nano* **2010**, *4* (9), 5321–5331. https://doi.org/10.1021/nn100816s.

(78) Kamaly, N.; Yameen, B.; Wu, J.; Farokhzad, O. C. Degradable Controlled-Release Polymers and Polymeric Nanoparticles: Mechanisms of Controlling Drug Release. *Chem. Rev.* **2016**, *116* (4), 2602–2663. https://doi.org/10.1021/acs.chemrev.5b00346.

(79) Injectable and implantable contraceptives - PubMed https://pubmed.ncbi.nlm.nih.gov/1387011/ (accessed Jul 16, 2021).

(80) R, L. Implantable Controlled Release Systems. *Pharmacol. Ther.* **1983**, *21* (1), 35–51. https://doi.org/10.1016/0163-7258(83)90066-9.

(81) NA, P.; EW, M. Development of Semicrystalline Poly(Vinyl Alcohol) Hydrogels for Biomedical Applications. *J. Biomed. Mater. Res.* **1977**, *11* (3), 423–434. https://doi.org/10.1002/JBM.820110309.

(82) RS, L.; NA, P. Present and Future Applications of Biomaterials in Controlled Drug Delivery Systems. *Biomaterials* **1981**, *2* (4), 201–214. https://doi.org/10.1016/0142-9612(81)90059-4.

(83) J, H. Controlled Release of Biologically Active Compounds from Bioerodible Polymers. *Biomaterials* **1980**, *1* (1), 51–57. https://doi.org/10.1016/0142-9612(80)90060-5.

(84) J, H.; KJ, H. Poly(Ortho Ester) Biodegradable Polymer Systems. *Methods Enzymol.* **1985**, *112* (C), 422–436. https://doi.org/10.1016/S0076-6879(85)12033-1.

(85) Batz, H.-G.; Franzmann, G.; Ringsdorf, H. Model Reactions for Synthesis of Pharmacologically Active Polymers by Way of Monomeric and Polymeric Reactive Esters. *Angew. Chemie Int. Ed. English* **1972**, *11* (12), 1103–1104. https://doi.org/10.1002/ANIE.197211031.

(86) Ringsdorf, H. STRUCTURE AND PROPERTIES OF PHARMACOLOGICALLY ACTIVE POLYMERS. In *J Polym Sci Polym Symp*; 1975; pp 135–153. https://doi.org/10.1002/polc.5070510111.

(87) Khanna, S. C.; Jecklin, T.; Speiser, P. Bead Polymerization Technique for Sustained-Release Dosage Form. *J. Pharm. Sci.* **1970**, *59* (5), 614–618. https://doi.org/10.1002/JPS.2600590508.

(88) G, B.; PP, S. Polymerized Micelles and Their Use as Adjuvants in Immunology. *J. Pharm. Sci.* **1976**, *65* (12), 1763–1766. https://doi.org/10.1002/JPS.2600651217.

(89) Zaffaroni, A. Systems for Controlled Drug Delivery. *Med. Res. Rev.* **1981**, *1* (4), 373–386. https://doi.org/10.1002/MED.2610010404.

(90) AS, H. The Origins and Evolution of "Controlled" Drug Delivery Systems. *J. Control. Release* **2008**, *132* (3), 153–163. https://doi.org/10.1016/J.JCONREL.2008.08.012.

(91) R, L.; J, F. Polymers for the Sustained Release of Proteins and Other Macromolecules. *Nature* **1976**, *263* (5580), 797–800. https://doi.org/10.1038/263797A0.

(92) J, F.; DM, L. THE USE OF SILICONE RUBBER AS A CARRIER FOR PROLONGED DRUG THERAPY. *J. Surg. Res.* **1964**, *4* (3), 139–142. https://doi.org/10.1016/S0022-4804(64)80040-8.

(93) Higuchi, T.; Kuramoto, R. Study of Possible Complex Formation between Macromolecules and Certain Pharmaceuticals*: I. Polyvinylpyrrolidone with Sulfathiazole, Procaine Hydrochloride, Sodium Salicylate, Benzyl Penicillin, Chloramphenicol, Mandelic Acid, Caffeine, Theophylline, and Cortisone. *J. Am. Pharm. Assoc. (Scientific ed.)* **1954**, *43* (7), 393–397. https://doi.org/10.1002/JPS.3030430704.

(94) F, T.; A, H.; T, H. Quantitative Analytical Method for Determination of Drugs Dispersed in Polymers Using Differential Scanning Calorimetry. *J. Pharm. Sci.* **1974**, *63* (3), 427–429. https://doi.org/10.1002/JPS.2600630325.

(95) TJ, R.; WI, H. Release of Medroxyprogesterone Acetate from a Silicone Polymer. *J. Pharm. Sci.* **1970**, *59* (3), 353–357. https://doi.org/10.1002/JPS.2600590317.

(96) TJ, R. Release of Steroids from a Silicone Polymer. *J. Pharm. Sci.* **1972**, *61* (1), 46–50. https://doi.org/10.1002/JPS.2600610106.

(97) H, M. Tumor-Selective Delivery of Macromolecular Drugs via the EPR Effect: Background and Future Prospects. *Bioconjug. Chem.* **2010**, *21* (5), 797–802. https://doi.org/10.1021/BC100070G.

(98) H, C.; K, K. Progress of Drug-Loaded Polymeric Micelles into Clinical Studies. *J. Control. Release* **2014**, *190*, 465–476. https://doi.org/10.1016/J.JCONREL.2014.06.042.

(99) H, O.; Y, N.; K, K. PEGylated Nanoparticles for Biological and Pharmaceutical Applications. *Adv. Drug Deliv. Rev.* **2003**, *55* (3), 403–419.

https://doi.org/10.1016/S0169-409X(02)00226-0.

(100) Y, M.; T, H.; T, U.; K, M.; Y, Y.; Y, S.; K, S.; T, O.; H, U.; M, I.; N, W. Phase I Clinical Trial and Pharmacokinetic Evaluation of NK911, a Micelle-Encapsulated Doxorubicin. *Br. J. Cancer* **2004**, *91* (10), 1775–1781. https://doi.org/10.1038/SJ.BJC.6602204.

(101) JW, V.; A, A.; C, N.; V, A.; G, P.; J, B.; S, C.; P, C.; EK, R.; M, R. A Phase 2 Study of SP1049C, Doxorubicin in P-Glycoprotein-Targeting Pluronics, in Patients with Advanced Adenocarcinoma of the Esophagus and Gastroesophageal Junction. *Invest. New Drugs* **2011**, *29* (5), 1029–1037. https://doi.org/10.1007/S10637-010-9399-1.

(102) S, D.; D, F.; V, A.; J, M.; D, K.; D, J.; M, B.; G, H.; M, R. Phase I Dose Escalation and Pharmacokinetic Study of Pluronic Polymer-Bound Doxorubicin (SP1049C) in Patients with Advanced Cancer. *Br. J. Cancer* **2004**, *90* (11), 2085–2091. https://doi.org/10.1038/SJ.BJC.6601856.

(103) TY, K.; DW, K.; JY, C.; SG, S.; SC, K.; DS, H.; NK, K.; YJ, B. Phase I and Pharmacokinetic Study of Genexol-PM, a Cremophor-Free, Polymeric Micelle-Formulated Paclitaxel, in Patients with Advanced Malignancies. *Clin. Cancer Res.* **2004**, *10* (11), 3708–3716. https://doi.org/10.1158/1078-0432.CCR-03-0655.

(104) C, O.; W, B.; M, B.; G, S.; JF, N.; WE, H. Polymeric Micelles in Anticancer Therapy: Targeting, Imaging and Triggered Release. *Pharm. Res.* **2010**, *27* (12), 2569–2589. https://doi.org/10.1007/S11095-010-0233-4.

(105) Evaluate the Efficacy and Safety of Genexol®-PM Compared to Genexol® in Recurrent or Metastatic Breast Cancer - Full Text View - ClinicalTrials.gov https://clinicaltrials.gov/ct2/show/NCT00876486 (accessed Jul 16, 2021).

(106) OC, F.; S, J.; A, K.; TN, T.; DA, L.; R, L. Nanoparticle-Aptamer Bioconjugates: A New Approach for Targeting Prostate Cancer Cells. *Cancer Res.* **2004**, *64* (21), 7668–7672. https://doi.org/10.1158/0008-5472.CAN-04-2550.

(107) J, H.; D, V. H.; M, M. A.; E, A.; J, A.; T, C.; D, D. W.; M, F.; M, F.; A, H.; S, L.; K, M.; E, P.; B, R.; A, S.; E, S.; JJ, S.; YH, S.; J, S.; D, T.; G, T.; T, V. G. H.; J, W.; P, L.; PW, K.; NH, B.; C, S.; OC, F.; R, L.; S, Z. Preclinical Development and Clinical Translation of a PSMA-Targeted Docetaxel Nanoparticle with a Differentiated Pharmacological Profile. *Sci. Transl. Med.* **2012**, *4* (128). https://doi.org/10.1126/SCITRANSLMED.3003651.

(108) ME, D. The First Targeted Delivery of SiRNA in Humans via a Self-Assembling, Cyclodextrin Polymer-Based Nanoparticle: From Concept to Clinic. *Mol. Pharm.* **2009**, *6* (3), 659–668. https://doi.org/10.1021/MP900015Y.

(109) JD, H.; JY, L.; Y, Y.; B, Z.; BS, H.; JJ, R.; DW, B.; ME, D. Potent SiRNA Inhibitors of Ribonucleotide Reductase Subunit RRM2 Reduce Cell Proliferation in Vitro and in Vivo. *Clin. Cancer Res.* **2007**, *13* (7), 2207–2215. https://doi.org/10.1158/1078-0432.CCR-06-2218.

(110) Fan, X.; Li, Z.; Loh, X. J. Recent Development of Unimolecular Micelles as Functional

Materials and Applications. *Polym. Chem.* **2016**, *7* (38), 5898–5919. https://doi.org/10.1039/c6py01006g.

(111) Radoslav Savić; Tony Azzam; Adi Eisenberg, and; Maysinger*, D. Assessment of the Integrity of Poly(Caprolactone)-b-Poly(Ethylene Oxide) Micelles under Biological Conditions: A Fluorogenic-Based Approach. *Langmuir* **2006**, *22* (8), 3570–3578. https://doi.org/10.1021/LA0531998.

(112) J, G.; M, C.; Y, Z.; S, W.; Y, W. Polymeric Micelles Drug Delivery System in Oncology. *J. Control. Release* **2012**, *159* (3), 312–323. https://doi.org/10.1016/J.JCONREL.2011.12.012.

(113) KM, T.; Y, Y.; A, D.; S, I.; TA, T.; K, T.; K, O.; K, K. Effect of Shear Stress on Structure and Function of Polyplex Micelles from Poly(Ethylene Glycol)-Poly(l-Lysine) Block Copolymers as Systemic Gene Delivery Carrier. *Biomaterials* **2017**, *126*, 31–38. https://doi.org/10.1016/J.BIOMATERIALS.2017.02.012.

(114) Sun, X.; Wang, G.; Zhang, H.; Hu, S.; Liu, X.; Tang, J.; Shen, Y. The Blood Clearance Kinetics and Pathway of Polymeric Micelles in Cancer Drug Delivery. *ACS Nano* **2018**, *12* (6), 6179–6192. https://doi.org/10.1021/ACSNANO.8B02830.

(115) H, M.; M, K. Analyses of Repeated Failures in Cancer Therapy for Solid Tumors: Poor Tumor-Selective Drug Delivery, Low Therapeutic Efficacy and Unsustainable Costs. *Clin. Transl. Med.* **2018**, *7* (1). https://doi.org/10.1186/S40169-018-0185-6.

(116) Chen, G.; Wang, Y.; Xie, R.; Gong, S. A Review on Core–Shell Structured Unimolecular Nanoparticles for Biomedical Applications. *Adv. Drug Deliv. Rev.* **2018**, *130*, 58–72. https://doi.org/10.1016/j.addr.2018.07.008.

(117) Gao, H.; Jones, M.-C.; Chen, J.; Prud'homme, R. E.; Leroux, J.-C. Core Cross-Linked Reverse Micelles from Star-Shaped Polymers. *Chem. Mater.* **2008**, *20* (9), 3063–3067. https://doi.org/10.1021/CM703370R.

(118) X, Y.; JJ, G.; IJ, R.; A, J.; SA, H.; DA, S.; S, G. Multifunctional SPIO/DOX-Loaded Wormlike Polymer Vesicles for Cancer Therapy and MR Imaging. *Biomaterials* **2010**, *31* (34), 9065–9073. https://doi.org/10.1016/J.BIOMATERIALS.2010.08.039.

(119) Nostrum, C. F. van. Covalently Cross-Linked Amphiphilic Block Copolymer Micelles. *Soft Matter* **2011**, *7* (7), 3246–3259. https://doi.org/10.1039/C0SM00999G.

(120) U, K.; P, P.; S, S.; V, K. Advances in Polymeric Micelles for Drug Delivery and Tumor Targeting. *Nanomedicine* **2010**, *6* (6), 714–729. https://doi.org/10.1016/J.NANO.2010.05.005.

(121) Talelli, M.; Barz, M.; Rijcken, C. J.; Kiessling, F.; Hennink, W. E.; Lammers, T. Core-Crosslinked Polymeric Micelles: Principles, Preparation, Biomedical Applications and Clinical Translation. *Nano Today* **2015**, *10* (1), 93. https://doi.org/10.1016/J.NANTOD.2015.01.005.

(122) Sunder, A.; Krämer, M.; Hanselmann, R.; Mülhaupt, R.; Frey, H. Molecular Nanocapsules Based on Amphiphilic Hyperbranched Polyglycerols. *Angew. Chemie* -

Int. Ed. **1999**, *38* (23), 3552–3555. https://doi.org/10.1002/(SICI)1521-3773(19991203)38:23<3552::AID-ANIE3552>3.0.CO;2-G.

(123) Newkome, G. R.; Moorefield, C. N.; Baker, G. R.; Saunders, M. J.; Grossman, S. H. Unimolecular Micelles. *Angew. Chemie Int. Ed. English* **1991**, *30* (9), 1178–1180. https://doi.org/10.1002/ANIE.199111781.

(124) Liu, H.; Jiang, A.; Guo, J.; Uhrich, K. E. Unimolecular Micelles: Synthesis and Characterization of Amphiphilic Polymer Systems. *J. Polym. Sci. Part A Polym. Chem.* **1999**, *37* (6), 703–711. https://doi.org/10.1002/(SICI)1099-0518(19990315)37:6<703::AID-POLA5>3.0.CO;2-O.

(125) Xu, J.; Luo, S.; Shi, W.; Liu, S. Two-Stage Collapse of Unimolecular Micelles with Double Thermoresponsive Coronas. *Langmuir* **2006**, *22* (3), 989–997. https://doi.org/10.1021/la0522707.

(126) MC, L.; BN, T.; R, H. Dendritic Core-Shell Systems as Soft Drug Delivery Nanocarriers. *Biotechnol. Adv.* **2015**, *33* (6 Pt 3), 1327–1341. https://doi.org/10.1016/J.BIOTECHADV.2015.03.014.

(127) Abbasi, E.; Aval, S. F.; Akbarzadeh, A.; Milani, M.; Nasrabadi, H. T.; Joo, S. W.; Hanifehpour, Y.; Nejati-Koshki, K.; Pashaei-Asl, R. Dendrimers: Synthesis, Applications, and Properties. *Nanoscale Res. Lett. 2014 91* **2014**, *9* (1), 1–10. https://doi.org/10.1186/1556-276X-9-247.

(128) HT, C.; MF, N.; AR, P.; EE, S. Cytotoxicity, Hemolysis, and Acute in Vivo Toxicity of Dendrimers Based on Melamine, Candidate Vehicles for Drug Delivery. *J. Am. Chem. Soc.* **2004**, *126* (32), 10044–10048. https://doi.org/10.1021/JA048548J.

(129) Boas, U.; Heegaard, P. M. H. Dendrimers in Drug Research. *Chem. Soc. Rev.* **2004**, *33* (1), 43–63. https://doi.org/10.1039/B309043B.

(130) ER, G.; JM, F. Dendrimers and Dendritic Polymers in Drug Delivery. *Drug Discov. Today* **2005**, *10* (1), 35–43. https://doi.org/10.1016/S1359-6446(04)03276-3.

(131) C, D.; IF, U.; AG, S. Dendrimers in Gene Delivery. *Adv. Drug Deliv. Rev.* **2005**, *57* (15), 2177–2202. https://doi.org/10.1016/J.ADDR.2005.09.017.

(132) AU, B.; A, Y.; HL, W.; KM, Z.; R, S.; ND, W.; JR, B.; BJ, R. Application of Membrane-Based Dendrimer/DNA Complexes for Solid Phase Transfection in Vitro and in Vivo. *Biomaterials* **2000**, *21* (9), 877–887. https://doi.org/10.1016/S0142-9612(99)00229-X.

(133) and, M. E.; Aida*, T. Self-Assembly of a Copper-Ligating Dendrimer That Provides a New Non-Heme Metalloprotein Mimic: "Dendrimer Effects" on Stability of the Bis(μ-Oxo)Dicopper(III) Core. *J. Am. Chem. Soc.* **1999**, *121* (4), 874–875. https://doi.org/10.1021/JA982282X.

(134) Azagarsamy, M. A.; Sokkalingam, P.; Thayumanavan, S. Enzyme-Triggered Disassembly of Dendrimer-Based Amphiphilic Nanocontainers. *J. Am. Chem. Soc.* **2009**, *131* (40), 14184–14185. https://doi.org/10.1021/JA906162U.

(135) Chang, D. W.; Sohn, G.-J.; Dai, L.; Baek, J.-B. Reversible Adsorption of Conjugated Amphiphilic Dendrimers onto Reduced Graphene Oxide (RGO) for Fluorescence Sensing. https://doi.org/10.1039/c1sm05755c.

(136) SM, G.; JM, F. Convergent Dendrons and Dendrimers: From Synthesis to Applications. *Chem. Rev.* **2001**, *101* (12), 3819–3867. https://doi.org/10.1021/CR990116H.

(137) Hawker, C. J.; Wooley, K. L.; Fréchet, J. M. J. Unimolecular Micelles and Globular Amphiphiles: Dendritic Macromolecules as Novel Recyclable Solubilization Agents. *J. Chem. Soc. Perkin Trans. 1* **1993**, No. 12, 1287–1297. https://doi.org/10.1039/p19930001287.

(138) Fan, X.; Li, Z.; Loh, X. J. Recent Development of Unimolecular Micelles as Functional Materials and Applications. *Polym. Chem.* **2016**, *7*, 5898. https://doi.org/10.1039/c6py01006g.

(139) Brinkman, A. M.; Chen, G.; Wang, Y.; Hedman, C. J.; Sherer, N. M.; Havighurst, T. C.; Gong, S.; Xu, W. Aminoflavone-Loaded EGFR-Targeted Unimolecular Micelle Nanoparticles Exhibit Anti-Cancer Effects in Triple Negative Breast Cancer. *Biomaterials* **2016**, *101*, 20–31. https://doi.org/10.1016/j.biomaterials.2016.05.041.

(140) He, H.; Wang, Y.; Wen, H.; Jia, X. Dendrimer-Based Multilayer Nanocarrier for Potential Synergistic Paclitaxel–Doxorubicin Combination Drug Delivery. *RSC Adv.* **2013**, *4* (7), 3643–3652. https://doi.org/10.1039/C3RA43803A.

(141) Jaskula-Sztul, R.; Chen, G.; Dammalapati, A.; Harrison, A.; Tang, W.; Gong, S.; Chen, H. AB3-Loaded and Tumor-Targeted Unimolecular Micelles for Medullary Thyroid Cancer Treatment †. *J. Mater. Chem. B* **2017**, *5*, 151–159. https://doi.org/10.1039/c6tb02530g.

(142) Chen, G.; Jaskula-Sztul, R.; Harrison, A.; Dammalapati, A.; Xu, W.; Cheng, Y.; Chen, H.; Gong, S. KE108-Conjugated Unimolecular Micelles Loaded with a Novel HDAC Inhibitor Thailandepsin-A for Targeted Neuroendocrine Cancer Therapy. *Biomaterials* **2016**, *97*, 22–33. https://doi.org/10.1016/j.biomaterials.2016.04.029.

(143) Guo, J.; Hong, H.; Chen, G.; Shi, S.; Zheng, Q.; Zhang, Y.; Theuer, C. P.; Barnhart, T. E.; Cai, W.; Gong, S. Image-Guided and Tumor-Targeted Drug Delivery with Radiolabeled Unimolecular Micelles. *Biomaterials* **2013**, *34* (33), 8323–8332. https://doi.org/10.1016/j.biomaterials.2013.07.085.

(144) Chen, G.; Shi, X.; Wang, B.; Xie, R.; Guo, L. W.; Gong, S.; Kent, K. C. Unimolecular Micelle-Based Hybrid System for Perivascular Drug Delivery Produces Long-Term Efficacy for Neointima Attenuation in Rats. *Biomacromolecules* **2017**, *18* (7), 2205–2213. https://doi.org/10.1021/acs.biomac.7b00617.

(145) Suzuki, M.; Ii, A.; Saegusa, T. Multibranching Polymerization: Palladium-Catalyzed Ring-Opening Polymerization of Cyclic Carbamate to Produce Hyperbranched Dendritic Polyamine. *Macromolecules* **2002**, *25* (25), 7071–7072. https://doi.org/10.1021/MA00051A055.

(146) Feast, W. J.; Stainton, N. M. Synthesis, Structure and Properties of Some Hyperbranched Polyesters. *J. Mater. Chem.* **1995**, *5* (3), 405–411. https://doi.org/10.1039/JM9950500405.

(147) Bakhshi, H.; Agarwal, S. Hyperbranched Polyesters as Biodegradable and Antibacterial Additives. *J. Mater. Chem. B* **2017**, *5* (33), 6827–6834. https://doi.org/10.1039/C7TB01301A.

(148) P, B.; S, S.; M, C.; S, B.; DF, S. A Flexible Approach to the Preparation of Polymer Scaffolds for Tissue Engineering. *Macromol. Biosci.* **2007**, *7* (2), 201–207. https://doi.org/10.1002/MABI.200600212.

(149) and, E. Ž.; Žigon, M. Characterization of a Commercial Hyperbranched Aliphatic Polyester Based on 2,2-Bis(Methylol)Propionic Acid. *Macromolecules* **2002**, *35* (27), 9913–9925. https://doi.org/10.1021/MA021070O.

(150) Kontoyianni, C.; Sideratou, Z.; Theodossiou, T.; Tziveleka, L.-A.; Tsiourvas, D.; Paleos, C. M. A Novel Micellar PEGylated Hyperbranched Polyester as a Prospective Drug Delivery System for Paclitaxel. *Macromol. Biosci.* **2008**, *8* (9), 871–881. https://doi.org/10.1002/MABI.200800015.

(151) Zhang, S.; Xu, J.; Chen, H.; Song, Z.; Wu, Y.; Dai, X.; Kong, J. Acid-Cleavable Unimolecular Micelles from Amphiphilic Star Copolymers for Triggered Release of Anticancer Drugs. *Macromol. Biosci.* **2017**, *17* (3), 1–10. https://doi.org/10.1002/mabi.201600258.

(152) Nabid, M. R.; Bide, Y. H40-PCL-PEG Unimolecular Micelles Both as Anchoring Sites for Palladium Nanoparticles and Micellar Catalyst for Heck Reaction in Water. *Appl. Catal. A Gen.* **2014**, *469*, 183–190. https://doi.org/10.1016/j.apcata.2013.09.016.

(153) M, P.; JJ, G.; S, P.; DA, S.; S, G. Folate-Conjugated Amphiphilic Hyperbranched Block Copolymers Based on Boltorn H40, Poly(L-Lactide) and Poly(Ethylene Glycol) for Tumor-Targeted Drug Delivery. *Biomaterials* **2009**, *30* (16), 3009–3019. https://doi.org/10.1016/J.BIOMATERIALS.2009.02.011.

(154) M, P.; JJ, G.; S, P.; DA, S.; S, G. Amphiphilic Multi-Arm Block Copolymer Based on Hyperbranched Polyester, Poly(L-Lactide) and Poly(Ethylene Glycol) as a Drug Delivery Carrier. *Macromol. Biosci.* **2009**, *9* (5), 515–524. https://doi.org/10.1002/MABI.200800269.

(155) Xiao, Y.; Hong, H.; Javadi, A.; Engle, J. W.; Xu, W.; Yang, Y.; Zhang, Y.; Barnhart, T. E.; Cai, W.; Gong, S. Multifunctional Unimolecular Micelles for Cancer-Targeted Drug Delivery and Positron Emission Tomography Imaging. *Biomaterials* **2012**, *33* (11), 3071. https://doi.org/10.1016/J.BIOMATERIALS.2011.12.030.

(156) Abbina, S.; Vappala, S.; Kumar, P.; Siren, E. M. J.; La, C. C.; Abbasi, U.; Brooks, D. E.; Kizhakkedathu, J. N. Hyperbranched Polyglycerols: Recent Advances in Synthesis, Biocompatibility and Biomedical Applications. *J. Mater. Chem. B* **2017**, *5* (47), 9249–9277. https://doi.org/10.1039/C7TB02515G.

(157) F, D.; S, H.; F, N.; J, K.; W, C.; N, M.; S, H.; R, H. Development of Biodegradable Hyperbranched Core-Multishell Nanocarriers for Efficient Topical Drug Delivery. *J. Control. Release* **2016**, *242*, 42–49. https://doi.org/10.1016/J.JCONREL.2016.06.048.

(158) Weizhong Yuan, †; Jinying Yuan, *,†; Fengbo Zhang, ‡; Xuming Xie, ‡ and; Pan§, C. Synthesis, Characterization, Crystalline Morphologies, and Hydrophilicity of Brush Copolymers with Double Crystallizable Side Chains. *Macromolecules* **2007**, *40* (25), 9094–9102. https://doi.org/10.1021/MA071841U.

(159) and, H. G.; Matyjaszewski*, K. Synthesis of Molecular Brushes by "Grafting onto" Method: Combination of ATRP and Click Reactions. *J. Am. Chem. Soc.* **2007**, *129* (20), 6633–6639. https://doi.org/10.1021/JA0711617.

(160) Johnson, J. A.; Lu, Y. Y.; Burts, A. O.; Lim, Y.-H.; Finn, M. G.; Koberstein, J. T.; Turro, N. J.; Tirrell, D. A.; Grubbs, R. H. Core-Clickable PEG-Branch-Azide Bivalent-Bottle-Brush Polymers by ROMP: Grafting-Through and Clicking-To. *J. Am. Chem. Soc.* **2010**, *133* (3), 559–566. https://doi.org/10.1021/JA108441D.

(161) Johnson, J. A.; Lu, Y. Y.; Burts, A. O.; Xia, Y.; Durrell, A. C.; Tirrell, D. A.; Grubbs, R. H. Drug-Loaded, Bivalent-Bottle-Brush Polymers by Graft-through ROMP. *Macromolecules* **2010**, *43* (24), 10326–10335. https://doi.org/10.1021/MA1021506.

(162) P, Z.; L, L.; X, F.; C, W.; X, S.; Y, C. Molecular Nanoworm with PCL Core and PEO Shell as a Non-Spherical Carrier for Drug Delivery. *Macromol. Rapid Commun.* **2012**, *33* (16), 1351–1355. https://doi.org/10.1002/MARC.201200172.

(163) Guo, J.; Hong, H.; Chen, G.; Shi, S.; Nayak, T. R.; Theuer, C. P.; Barnhart, T. E.; Cai, W.; Gong, S. Theranostic Unimolecular Micelles Based on Brush-Shaped Amphiphilic Block Copolymers for Tumor-Targeted Drug Delivery and Positron Emission Tomography Imaging. *ACS Appl. Mater. Interfaces* **2014**, *6* (24), 21769–21779. https://doi.org/10.1021/am5002585.

(164) XY, T.; C, M.; YF, W.; LW, M.; BY, W.; JL, H.; PH, N.; XL, J.; MZ, L.; H, W. Fabrication of Thermosensitive Cyclic Brush Copolymer with Enhanced Therapeutic Efficacy for Anticancer Drug Delivery. *Macromol. Rapid Commun.* **2018**, *39* (5). https://doi.org/10.1002/MARC.201700744.

(165) Ren, J. M.; McKenzie, T. G.; Fu, Q.; Wong, E. H. H.; Xu, J.; An, Z.; Shanmugam, S.; Davis, T. P.; Boyer, C.; Qiao, G. G. Star Polymers. *Chem. Rev.* **2016**, *116* (12), 6743–6836. https://doi.org/10.1021/acs.chemrev.6b00008.

(166) Kaupp, M.; Hiltebrandt, K.; Trouillet, V.; Mueller, P.; Quick, A. S.; Wegener, M.; Barner-Kowollik, C. Wavelength Selective Polymer Network Formation of End-Functional Star Polymers. *Chem. Commun.* **2016**, *52* (9), 1975–1978. https://doi.org/10.1039/C5CC09444E.

(167) Hu, M.; Shen, Y.; Zhang, L.; Qiu, L. Polymersomes via Self-Assembly of Amphiphilic β-Cyclodextrin-Centered Triarm Star Polymers for Enhanced Oral Bioavailability of Water-Soluble Chemotherapeutics. *Biomacromolecules* **2016**, *17* (3), 1026–1039. https://doi.org/10.1021/ACS.BIOMAC.5B01676.

(168) Jianhui Xia; Xuan Zhang, and; Matyjaszewski*, K. Synthesis of Star-Shaped Polystyrene by Atom Transfer Radical Polymerization Using an "Arm First" Approach. *Macromolecules* **1999**, *32* (13), 4482–4484. https://doi.org/10.1021/MA9900378.

(169) and, H. G.; Matyjaszewski*, K. Synthesis of Star Polymers by a Combination of ATRP and the "Click" Coupling Method. *Macromolecules* **2006**, *39* (15), 4960–4965. https://doi.org/10.1021/MA060926C.

(170) Pang, X.; Zhao, L.; Akinc, M.; Kim, J. K.; Lin, Z. Novel Amphiphilic Multi-Arm, Star-like Block Copolymers as Unimolecular Micelles. *Macromolecules* **2011**, *44* (10), 3746–3752. https://doi.org/10.1021/ma200594j.

(171) Lin, W.; Zhang, X.; Qian, L.; Yao, N.; Pan, Y.; Zhang, L. Doxorubicin-Loaded Unimolecular Micelle-Stabilized Gold Nanoparticles as a Theranostic Nanoplatform for Tumor-Targeted Chemotherapy and Computed Tomography Imaging. *Biomacromolecules* **2017**, *18* (12), 3869–3880. https://doi.org/10.1021/acs.biomac.7b00810.

(172) Xu, Z.; Liu, S.; Liu, H.; Yang, C.; Kang, Y.; Wang, M. Unimolecular Micelles of Amphiphilic Cyclodextrin-Core Star-like Block Copolymers for Anticancer Drug Delivery. *Chem. Commun.* **2015**, *51* (87), 15768–15771. https://doi.org/10.1039/c5cc02743h.

(173) RK, K.; EG, M.; AF, H.; F, L. Biodegradable Poly(Lactic Acid) Polymers. *J. Biomed. Mater. Res.* **1971**, *5* (3), 169–181. https://doi.org/10.1002/JBM.820050305.

(174) S, F.; M, W.; M, R.; A, A. The Mechanisms of Drug Release in Poly(Lactic-Co-Glycolic Acid)-Based Drug Delivery Systems--a Review. *Int. J. Pharm.* **2011**, *415* (1–2), 34–52. https://doi.org/10.1016/J.IJPHARM.2011.05.049.

(175) Ulery, B. D.; Nair, L. S.; Laurencin, C. T. Biomedical Applications of Biodegradable Polymers. *J. Polym. Sci. Part B Polym. Phys.* **2011**, *49* (12), 832–864. https://doi.org/10.1002/POLB.22259.

(176) M, Q.; X, L.; Y, Y.; S, Z. Electrospun Fibers of Acid-Labile Biodegradable Polymers Containing Ortho Ester Groups for Controlled Release of Paracetamol. *Eur. J. Pharm. Biopharm.* **2008**, *70* (2), 445–452. https://doi.org/10.1016/J.EJPB.2008.05.003.

(177) Polymeric Biomaterials, Revised and Expanded - Google Books https://books.google.co.in/books?id=l4O1DwAAQBAJ&pg=PA118&lpg=PA118&dq=Seymour,+L.+W.;+Duncan,+R.;+Duffy,+J.;+Ng,+S.;+Heller,+J.+Poly+(ortho+ester)+matrices+for+controlled+release+of+the+antitumour+agent+5-+fluorouracil.+J.+Controlled+Release+1994,+31,+201.&source=bl&ots=LI7Io0LnDy&sig=ACfU3U19VB5-yrNG_44Z3BNxHk8rcEeTig&hl=en&sa=X&ved=2ahUKEwjHlKexlefxAhWEyDgGHfCPCmEQ6AEwAHoECAIQAw#v=onepage&q=Seymour%2C L. W.%3B Duncan%2C R.%3B Duffy%2C J.%3B Ng%2C S.%3B Heller%2C J. Poly (ortho ester) matrices for controlled release of the antitumour agent 5- fluorouracil. J. Controlled Release 1994%2C 31%2C 201.&f=false (accessed Jul 16, 2021).

(178) J, H.; J, B.; SY, N.; HR, S.; K, S.-A.; S, E.; A, R.-W.; R, G. Poly(Ortho Esters) - Their Development and Some Recent Applications. *Eur. J. Pharm. Biopharm.* **2000**, *50* (1), 121–128. https://doi.org/10.1016/S0939-6411(00)00085-0.

(179) ES, P.; M, M.; JC, S. Biodegradable Polyanhydride Devices of Cefazolin Sodium, Bupivacaine, and Taxol for Local Drug Delivery: Preparation, and Kinetics and Mechanism of in Vitro Release. *J. Control. Release* **1998**, *52* (1–2), 179–189. https://doi.org/10.1016/S0168-3659(97)00223-X.

(180) N, K.; RS, L.; AJ, D. Polyanhydrides: An Overview. *Adv. Drug Deliv. Rev.* **2002**, *54* (7), 889–910. https://doi.org/10.1016/S0169-409X(02)00050-9.

(181) Petersen, L. K.; Huntimer, L.; Walz, K.; Ramer-Tait, A.; Wannemuehler, M. J.; Narasimhan, B. Combinatorial Evaluation of in Vivo Distribution of Polyanhydride Particle-Based Platforms for Vaccine Delivery. *Int. J. Nanomedicine* **2013**, *8*, 2213. https://doi.org/10.2147/IJN.S45317.

(182) LK, P.; CK, S.; B, N. High-Throughput Analysis of Protein Stability in Polyanhydride Nanoparticles. *Acta Biomater.* **2010**, *6* (10), 3873–3881. https://doi.org/10.1016/J.ACTBIO.2010.04.004.

(183) BA, P.; JA, B.; R, L. Formulation and Surface Modification of Poly(Ester-Anhydride) Micro- and Nanospheres. *Biomaterials* **2005**, *26* (2), 117–124. https://doi.org/10.1016/J.BIOMATERIALS.2004.02.015.

(184) JM, A.; DF, G.; RL, M.; A, H.; R, W. The Potential for Poly-Alpha-Amino Acids as Biomaterials. *J. Biomed. Mater. Res.* **1974**, *8* (3), 197–207. https://doi.org/10.1002/JBM.820080320.

(185) KE, U.; SM, C.; RS, L.; KM, S. Polymeric Systems for Controlled Drug Release. *Chem. Rev.* **1999**, *99* (11), 3181–3198. https://doi.org/10.1021/CR940351U.

(186) Marck, K. W.; Wildevuur, C. R. H.; Sederel, W. L.; Bantjes, A.; Feijen, J. Biodegradability and Tissue Reaction of Random Copolymers of L-Leucine, L-Aspartic Acid, and L-Aspartic Acid Esters. *J. Biomed. Mater. Res.* **1977**, *11* (3), 405–422. https://doi.org/10.1002/JBM.820110308.

(187) Martin, E. C.; May, P. D.; McMahon, W. A. Amino Acid Polymers for Biomedical Applications. I. Permeability Properties of L-Leucine DL-Methionine Copolymers. *J. Biomed. Mater. Res.* **1971**, *5* (1), 53–62. https://doi.org/10.1002/JBM.820050105.

(188) IL, S.; YT, V.; MH, S. Biomedical Applications of Chemically and Microbiologically Synthesized Poly(Glutamic Acid) and Poly(Lysine). *Mini Rev. Med. Chem.* **2004**, *4* (2), 179–188. https://doi.org/10.2174/1389557043487420.

(189) A, L.; AG, S.; M, M.; TB, L.; IF, U. Amphiphilic Poly(L-Amino Acids) - New Materials for Drug Delivery. *J. Control. Release* **2012**, *161* (2), 523–536. https://doi.org/10.1016/J.JCONREL.2012.04.046.

(190) RK, D.; AR, R. Synthesis, Characterization, and Blood Compatibility of Polyamidoamines Copolymers. *Biomaterials* **2003**, *24* (18), 2985–2993.

https://doi.org/10.1016/S0142-9612(03)00122-4.

(191) B, M.; A, M. Production and Characterization of Gamma-Polyglutamic Acid Nanoparticles for Controlled Anticancer Drug Release. *Crit. Rev. Biotechnol.* **2008**, *28* (2), 83–99. https://doi.org/10.1080/07388550802107483.

(192) G, L.; GR, R.-R.; J, B.; T, M.; C, P.; JP, B.; M, G.-F.; MJ, A.; D, T. Polyglutamic Acid-PEG Nanocapsules as Long Circulating Carriers for the Delivery of Docetaxel. *Eur. J. Pharm. Biopharm.* **2014**, *87* (1), 47–54. https://doi.org/10.1016/J.EJPB.2014.02.004.

(193) MJ, T.; Q, S.; FM, W.; JC, F. Polycation-Based Gene Therapy: Current Knowledge and New Perspectives. *Curr. Gene Ther.* **2011**, *11* (4), 288–306. https://doi.org/10.2174/156652311796150408.

(194) D, L.; E, J.; A, Z. Drug Delivery of Oligonucleotides by Peptides. *Eur. J. Pharm. Biopharm.* **2004**, *58* (2), 237–251. https://doi.org/10.1016/J.EJPB.2004.03.031.

(195) Guo, K.; Chu, C. C.; Chkhaidze, E.; Katsarava, R. Synthesis and Characterization of Novel Biodegradable Unsaturated Poly(Ester Amide)S. *J. Polym. Sci. Part A Polym. Chem.* **2005**, *43* (7), 1463–1477. https://doi.org/10.1002/POLA.20463.

(196) M, D.; J, W.; CA, R.-K.; CC, C. Synthesis and Characterization of Biodegradable Poly(Ester Amide)s with Pendant Amine Functional Groups and in Vitro Cellular Response. *Biomacromolecules* **2009**, *10* (11), 3037–3047. https://doi.org/10.1021/BM9006437.

(197) YH, L.; GS, H.; YH, R.; S, P.; JE, R.; M, E.; KL, W. Development of a Vinyl Ether-Functionalized Polyphosphoester as a Template for Multiple Postpolymerization Conjugation Chemistries and Study of Core Degradable Polymeric Nanoparticles. *Macromolecules* **2014**, *47* (14), 4634–4644. https://doi.org/10.1021/MA402480A.

(198) Mao, H. Q.; Leong, K. W. Design of Polyphosphoester-DNA Nanoparticles for Non-Viral Gene Delivery. *Adv. Genet.* **2005**, *53*, 275–306. https://doi.org/10.1016/S0065-2660(05)53011-6.

(199) Z, Z.; J, W.; HQ, M.; KW, L. Polyphosphoesters in Drug and Gene Delivery. *Adv. Drug Deliv. Rev.* **2003**, *55* (4), 483–499. https://doi.org/10.1016/S0169-409X(03)00040-1.

(200) YC, W.; LY, T.; TM, S.; CH, L.; MH, X.; J, W. Self-Assembled Micelles of Biodegradable Triblock Copolymers Based on Poly(Ethyl Ethylene Phosphate) and Poly(-Caprolactone) as Drug Carriers. *Biomacromolecules* **2008**, *9* (1), 388–395. https://doi.org/10.1021/BM700732G.

(201) YH, L.; KM, T.; GS, H.; PO, W.; YH, R.; S, Z.; F, Z.; WJ, Y.; DA, H.; KL, W. Preparation and in Vitro Antimicrobial Activity of Silver-Bearing Degradable Polymeric Nanoparticles of Polyphosphoester-Block-Poly(L-Lactide). *ACS Nano* **2015**, *9* (2), 1995–2008. https://doi.org/10.1021/NN507046H.

(202) M, E.; S, Z.; F, Z.; ZJ, D.; YH, L.; H, W.; P, P.; PT, H.; KL, W. Surface Charges and Shell Crosslinks Each Play Significant Roles in Mediating Degradation, Biofouling, Cytotoxicity and Immunotoxicity for Polyphosphoester-Based Nanoparticles. *Sci. Rep.*

2013, *3*. https://doi.org/10.1038/SREP03313.

(203) T, K.; S, R.; M, T. Trimethylated Chitosans as Non-Viral Gene Delivery Vectors: Cytotoxicity and Transfection Efficiency. *J. Control. Release* **2005**, *103* (3), 643–653. https://doi.org/10.1016/J.JCONREL.2005.01.001.

(204) P, F.; F, A.; C, S.; C, P.; S, R.; HA, S.; B, S. Polymer-Based Nanoparticles for Oral Insulin Delivery: Revisited Approaches. *Biotechnol. Adv.* **2015**, *33* (6 Pt 3), 1342–1354. https://doi.org/10.1016/J.BIOTECHADV.2015.02.010.

(205) SK, S.; AK, M.; OA, A.; BB, M. Chitosan-Based Nanomaterials: A State-of-the-Art Review. *Int. J. Biol. Macromol.* **2013**, *59*, 46–58. https://doi.org/10.1016/J.IJBIOMAC.2013.04.043.

(206) MP, R.; A, E.; D, S.; P, B.; J, H.; C, F.; JC, S.; JP, B.; E, P.; P, C.; IJ, C. Development of a New Chitosan Hydrogel for Wound Dressing. *Wound Repair Regen.* **2009**, *17* (6), 817–824. https://doi.org/10.1111/J.1524-475X.2009.00538.X.

(207) IY, K.; MK, Y.; JH, S.; SS, P.; HS, N.; HC, L.; SK, K.; CS, C. Evaluation of Semi-Interpenetrating Polymer Networks Composed of Chitosan and Poloxamer for Wound Dressing Application. *Int. J. Pharm.* **2007**, *341* (1–2), 35–43. https://doi.org/10.1016/J.IJPHARM.2007.03.042.

(208) R, M.; J, W.; C, F.; F, C.; L, D. M.; CA, V.; M, C.; C, C.; M, F. Polyethylenimine and Chitosan Carriers for the Delivery of RNA Interference Effectors. *Expert Opin. Drug Deliv.* **2013**, *10* (12), 1653–1668. https://doi.org/10.1517/17425247.2013.840286.

(209) L, C.; L, I. Chitosan in Nasal Delivery Systems for Therapeutic Drugs. *J. Control. Release* **2014**, *190*, 189–200. https://doi.org/10.1016/J.JCONREL.2014.05.003.

(210) G, K.; L, S.; R, S.; P, G. Hyaluronic Acid: A Natural Biopolymer with a Broad Range of Biomedical and Industrial Applications. *Biotechnol. Lett.* **2007**, *29* (1), 17–25. https://doi.org/10.1007/S10529-006-9219-Z.

(211) SC, G.; S, N. A.; J, K. CD44: A Validated Target for Improved Delivery of Cancer Therapeutics. *Expert Opin. Ther. Targets* **2012**, *16* (7), 635–650. https://doi.org/10.1517/14728222.2012.687374.

(212) SS, S.; C, G.; AD, T.; NK, K. Advances and Advantages of Nanomedicine in the Pharmacological Targeting of Hyaluronan-CD44 Interactions and Signaling in Cancer. *Adv. Cancer Res.* **2014**, *123*, 277–317. https://doi.org/10.1016/B978-0-12-800092-2.00011-3.

(213) Trollsås, M.; Lee, V. Y.; Mecerreyes, D.; Löwenhielm, P.; Möller, M.; Miller, R. D.; Hedrick, J. L. Hydrophilic Aliphatic Polyesters: Design, Synthesis, and Ring-Opening Polymerization of Functional Cyclic Esters. *Macromolecules* **2000**, *33* (13), 4619–4627. https://doi.org/10.1021/ma992161x.

(214) Woodruff, M. A.; Hutmacher, D. W. The Return of a Forgotten Polymer - Polycaprolactone in the 21st Century. *Prog. Polym. Sci.* **2010**, *35* (10), 1217–1256. https://doi.org/10.1016/j.progpolymsci.2010.04.002.

(215) Tang, M.; Purcell, M.; Steele, J. A. M.; Lee, K. Y.; McCullen, S.; Shakesheff, K. M.; Bismarck, A.; Stevens, M. M.; Howdle, S. M.; Williams, C. K. Porous Copolymers of ε-Caprolactone as Scaffolds for Tissue Engineering. *Macromolecules* **2013**, *46* (20), 8136–8143. https://doi.org/10.1021/ma401439z.

(216) Ikada, Y.; Tsuji, H. Biodegradable Polyesters for Medical and Ecological Applications. *Macromol. Rapid Commun.* **2000**, *21* (3), 117–132. https://doi.org/10.1002/(sici)1521-3927(20000201)21:3<117::aid-marc117>3.0.co;2-x.

(217) Labet, M.; Thielemans, W. Synthesis of Polycaprolactone: A Review. *Chem. Soc. Rev.* **2009**, *38* (12), 3484–3504. https://doi.org/10.1039/b820162p.

(218) Middleton, J. C.; Tipton, A. J. Synthetic Biodegradable Polymers as Orthopedic Devices. *Biomaterials* **2000**, *21* (23), 2335–2346. https://doi.org/10.1016/S0142-9612(00)00101-0.

(219) Chang, L.; Deng, L.; Wang, W.; Lv, Z.; Hu, F.; Dong, A.; Zhang, J. Poly(Ethyleneglycol)-b-Poly(ε-Caprolactone-Co-γ-Hydroxyl-ε- Caprolactone) Bearing Pendant Hydroxyl Groups as Nanocarriers for Doxorubicin Delivery. *Biomacromolecules* **2012**, *13* (10), 3301–3310. https://doi.org/10.1021/BM301086C.

(220) Tian, D.; Halleux, O.; Dubois, P.; Jerome, R.; Sobry, R.; Van den Bossche, G. Poly(2-Oxepane-1,5-Dione): A Highly Crystalline Modified Poly(ε-Caprolactone) of a High Melting Temperature. *Macromolecules* **1998**, *31* (3), 924–927. https://doi.org/10.1021/ma970903l.

(221) Xiong, X. B.; Uludağ, H.; Lavasanifar, A. Biodegradable Amphiphilic Poly(Ethylene Oxide)-Block-Polyesters with Grafted Polyamines as Supramolecular Nanocarriers for Efficient SiRNA Delivery. *Biomaterials* **2009**, *30* (2), 242–253. https://doi.org/10.1016/j.biomaterials.2008.09.025.

(222) Yan, J.; Zhang, Y.; Xiao, Y.; Zhang, Y.; Lang, M. Novel Poly(ε-Caprolactone)s Bearing Amino Groups: Synthesis, Characterization and Biotinylation. *React. Funct. Polym.* **2010**, *70* (7), 400–407. https://doi.org/10.1016/j.reactfunctpolym.2010.03.008.

(223) Yao, K.; Wang, J.; Zhang, W.; Lee, J. S.; Wang, C.; Chu, F.; He, X.; Tang, C. Degradable Rosin-Ester À Caprolactone Graft Copolymers. **2011**, 2171–2177.

(224) Zhang, Y.; Li, J.; Du, Z.; Lang, M. Synthesis and PH-Responsive Assembly of Methoxy Poly(Ethylene Glycol)-b-Poly(ε-Caprolactone) with Pendant Carboxyl Groups. *J. Polym. Sci. Part A Polym. Chem.* **2014**, *52* (2), 188–199. https://doi.org/10.1002/POLA.26987.

(225) Cheng, Y.; Hao, J.; Lee, L. A.; Biewer, M. C.; Wang, Q.; Stefan, M. C. Thermally Controlled Release of Anticancer Drug from Self-Assembled γ-Substituted Amphiphilic Poly(ε-Caprolactone) Micellar Nanoparticles. *Biomacromolecules* **2012**, *13* (7), 2163–2173. https://doi.org/10.1021/bm300823y.

(226) Rainbolt, E. A.; Washington, K. E.; Biewer, M. C.; Stefan, M. C. Towards Smart Polymeric Drug Carriers: Self-Assembling γ-Substituted Polycaprolactones with Highly

Tunable Thermoresponsive Behavior. *J. Mater. Chem. B* **2013**, *1* (47), 6532–6537. https://doi.org/10.1039/c3tb21488e.

(227) Rainbolt, E. A.; Washington, K. E.; Biewer, M. C.; Stefan, M. C. Recent Developments in Micellar Drug Carriers Featuring Substituted Poly(ε-Caprolactone)S. *Polym. Chem.* **2015**, *6* (13), 2369–2381. https://doi.org/10.1039/c4py01628a.

(228) Mahmud, A.; Patel, S.; Molavi, O.; Choi, P.; Samuel, J.; Lavasanifar, A. Self-Associating Poly(Ethylene Oxide)-b-Poly(α-Cholesteryl Carboxylate-ε-Caprolactone) Block Copolymer for the Solubilization of Stat-3 Inhibitor Cucurbitacin I. *Biomacromolecules* **2009**, *10* (3), 471–478. https://doi.org/10.1021/bm800846a.

(229) Rainbolt, E. A.; Miller, J. B.; Washington, K. E.; Senevirathne, S. A.; Biewer, M. C.; Siegwart, D. J.; Stefan, M. C. Fine-Tuning Thermoresponsive Functional Poly(ε-Caprolactone)s to Enhance Micelle Stability and Drug Loading. *J. Mater. Chem. B* **2015**, *3* (9), 1779–1787. https://doi.org/10.1039/C4TB02016B.

(230) Fan, J.; Zeng, F.; Wu, S.; Wang, X. Polymer Micelle with PH-Triggered Hydrophobic–Hydrophilic Transition and De-Cross-Linking Process in the Core and Its Application for Targeted Anticancer Drug Delivery. *Biomacromolecules* **2012**, *13* (12), 4126–4137. https://doi.org/10.1021/BM301424R.

(231) Surnar, B.; Jayakannan, M. Delivery under the Gastrointestinal Tract. *Biomacromolecules* **2013**, *14*, 4377–4387.

(232) Surnar, B.; Sharma, K.; Jayakannan, M. Core-Shell Polymer Nanoparticles for Prevention of GSH Drug Detoxification and Cisplatin Delivery to Breast Cancer Cells. *Nanoscale* **2015**, *7* (42), 17964–17979. https://doi.org/10.1039/c5nr04963f.

(233) Surnar, B.; Jayakannan, M. Triple Block Nanocarrier Platform for Synergistic Cancer Therapy of Antagonistic Drugs. *Biomacromolecules* **2016**, *17* (12), 4075–4085. https://doi.org/10.1021/acs.biomac.6b01608.

(234) Kulkarni, B.; Surnar, B.; Jayakannan, M. Dual Functional Nanocarrier for Cellular Imaging and Drug Delivery in Cancer Cells Based on π-Conjugated Core and Biodegradable Polymer Arms. *Biomacromolecules* **2016**, *17* (3), 1004–1016. https://doi.org/10.1021/acs.biomac.5b01654.

(235) Kulkarni, B.; Malhotra, M.; Jayakannan, M. Perylene-Tagged Polycaprolactone Block Copolymers and Their Enzyme-Biodegradable Fluorescent Nanoassemblies for Intracellular Bio-Imaging in Cancer Cells. *ACS Appl. Polym. Mater.* **2019**, *1* (12), 3375–3388. https://doi.org/10.1021/acsapm.9b00800.

(236) Kulkarni, B.; Jayakannan, M. Fluorescent-Tagged Biodegradable Polycaprolactone Block Copolymer FRET Probe for Intracellular Bioimaging in Cancer Cells. *ACS Biomater. Sci. Eng.* **2017**, *3* (9), 2185–2197. https://doi.org/10.1021/acsbiomaterials.7b00426.

(237) Ghosh, R.; Malhotra, M.; Madhuri Sathe, R. R.; Jayakannan, M. Biodegradable Polymer Theranostic Fluorescent Nanoprobe for Direct Visualization and Quantitative

Determination of Antimicrobial Activity. *Biomacromolecules* **2020**, *21* (7), 2896–2912. https://doi.org/10.1021/acs.biomac.0c00653.

(238) Grossen, P.; Witzigmann, D.; Sieber, S.; Huwyler, J. PEG-PCL-Based Nanomedicines: A Biodegradable Drug Delivery System and Its Application. *J. Control. Release* **2017**, *260*, 46–60. https://doi.org/10.1016/J.JCONREL.2017.05.028.

(239) Tyrrell, Z. L.; Shen, Y.; Radosz, M. Fabrication of Micellar Nanoparticles for Drug Delivery through the Self-Assembly of Block Copolymers. *Prog. Polym. Sci.* **2010**, *35* (9), 1128–1143. https://doi.org/10.1016/J.PROGPOLYMSCI.2010.06.003.

(240) Wei, X. W.; Gong, C. Y.; Gou, M. L.; Fu, S. Z.; Guo, Q. F.; Shi, S.; Luo, F.; Guo, G.; Qiu, L. Y.; Qian, Z. Y. Biodegradable Poly(ε-Caprolactone)–Poly(Ethylene Glycol) Copolymers as Drug Delivery System. *Int. J. Pharm.* **2009**, *381* (1), 1–18. https://doi.org/10.1016/J.IJPHARM.2009.07.033.

(241) Parrott, M. C.; DeSimone, J. M. Relieving PEGylation. *Nat. Chem.* **2012**, *4* (1), 13. https://doi.org/10.1038/NCHEM.1230.

(242) Barz, M.; Luxenhofer, R.; Zentel, R.; Vicent, M. J. Overcoming the PEG-Addiction: Well-Defined Alternatives to PEG, from Structure-Property Relationships to Better Defined Therapeutics. *Polym. Chem.* **2011**, *2* (9), 1900–1918. https://doi.org/10.1039/c0py00406e.

(243) Y, D.; S, L.; M, N.; CK, C.; S, R. Degradation Behaviors of Electrospun Resorbable Polyester Nanofibers. *Tissue Eng. Part B. Rev.* **2009**, *15* (3), 333–351. https://doi.org/10.1089/TEN.TEB.2008.0619.

(244) Shi, S.; Shi, K.; Tan, L. W.; Qu, Y.; Shen, G. B.; Chu, B. Y.; Zhang, S.; Su, X. L.; Li, X. Y.; Wei, Y. Q.; Qian, Z. Y. The Use of Cationic MPEG-PCL-g-PEI Micelles for Co-Delivery OfMsurvivin T34A Gene and Doxorubicin. *Biomaterials* **2014**, *35* (15), 4536–4547. https://doi.org/10.1016/j.biomaterials.2014.02.010.

(245) Kutikov, A. B.; Song, J. Biodegradable PEG-Based Amphiphilic Block Copolymers for Tissue Engineering Applications. *ACS Biomater. Sci. Eng.* **2015**, *1* (7), 463–480. https://doi.org/10.1021/ACSBIOMATERIALS.5B00122.

(246) Al-Itry, R.; Lamnawar, K.; Maazouz, A. Improvement of Thermal Stability, Rheological and Mechanical Properties of PLA, PBAT and Their Blends by Reactive Extrusion with Functionalized Epoxy. *Polym. Degrad. Stab.* **2012**, *97* (10), 1898–1914. https://doi.org/10.1016/J.POLYMDEGRADSTAB.2012.06.028.

(247) P, G.; V, C.; I, C.; PV, H. An Overview of Poly(Lactic-Co-Glycolic) Acid (PLGA)-Based Biomaterials for Bone Tissue Engineering. *Int. J. Mol. Sci.* **2014**, *15* (3), 3640–3659. https://doi.org/10.3390/IJMS15033640.

(248) F, von B.; L, S.; A, G. Why Degradable Polymers Undergo Surface Erosion or Bulk Erosion. *Biomaterials* **2002**, *23* (21), 4221–4231. https://doi.org/10.1016/S0142-9612(02)00170-9.

(249) D, C.; H, Y. Compositional and Structural Analysis of PELA Biodegradable Block

Copolymers Degrading under in Vitro Conditions. *Biomaterials* **1989**, *10* (7), 466–474. https://doi.org/10.1016/0142-9612(89)90088-4.

(250) Q, Y.; L, Y.; H, W.; J, C. Synthesis and Biomedical Applications of Functional Poly(α-Hydroxy Acids) via Ring-Opening Polymerization of O-Carboxyanhydrides. *Acc. Chem. Res.* **2015**, *48* (7), 1777–1787. https://doi.org/10.1021/AR500455Z.

(251) Z, G.; S, L. Functional Block Copolymer Assemblies Responsive to Tumor and Intracellular Microenvironments for Site-Specific Drug Delivery and Enhanced Imaging Performance. *Chem. Soc. Rev.* **2013**, *42* (17), 7289–7325. https://doi.org/10.1039/C3CS60048C.

(252) H, S.; F, M.; AA, D.; M, H.; J, F.; Z, Z. α-Amino Acid Containing Degradable Polymers as Functional Biomaterials: Rational Design, Synthetic Pathway, and Biomedical Applications. *Biomacromolecules* **2011**, *12* (6), 1937–1955. https://doi.org/10.1021/BM200043U.

(253) SC, W.; PS, B.; F, M.; A, S.; CG, P. The Intracellular Degradation of Poly(Epsilon-Caprolactone). *J. Biomed. Mater. Res.* **1985**, *19* (4), 437–444. https://doi.org/10.1002/JBM.820190408.

(254) Rieger, J.; Bernaerts, K. V.; Du Prez, F. E.; Jérôme, R.; Jérôme, C. Lactone End-Capped Poly(Ethylene Oxide) as a New Building Block for Biomaterials. *Macromolecules* **2004**, *37* (26), 9738–9745. https://doi.org/10.1021/ma048768h.

(255) Darcos, V.; El Habnouni, S.; Nottelet, B.; El Ghzaoui, A.; Coudane, J. Well-Defined PCL-Graft-PDMAEMA Prepared by Ring-Opening Polymerisation and Click Chemistry. *Polym. Chem.* **2010**, *1* (3), 280–282. https://doi.org/10.1039/c0py00004c.

(256) Silvers, A. L.; Chang, C. C.; Emrick, T. Functional Aliphatic Polyesters and Nanoparticles Prepared by Organocatalysis and Orthogonal Grafting Chemistry. *J. Polym. Sci. Part A Polym. Chem.* **2012**, *50* (17), 3517–3529. https://doi.org/10.1002/pola.26114.

(257) Ganivada, M. N.; N, V. R.; Dinda, H.; Kumar, P.; Sarma, J. Das; Shunmugam, R. Biodegradable Magnetic Nanocarrier for Stimuli Responsive Drug Release. *Macromolecules* **2014**, *47* (8), 2703–2711. https://doi.org/10.1021/MA500384M.

(258) Wilson, J. A.; Hopkins, S. A.; Wright, P. M.; Dove, A. P. Dependence of Copolymer Sequencing Based on Lactone Ring Size and ε-Substitution. *ACS Macro Lett.* **2016**, *5* (3), 346–350. https://doi.org/10.1021/ACSMACROLETT.5B00940.

(259) Newman, D.; Laredo, E.; Bello, A.; Dubois, P. Combined Effect of Humidity and Composition on the Molecular Mobilities of Poly(ε-Caprolactone- Ran -ε-Caprolactam) Copolymers. *Macromolecules* **2014**, *47* (7), 2471–2478. https://doi.org/10.1021/ma500260e.

(260) Surnar, B.; Subash, P. P.; Jayakannan, M. Biodegradable Block Copolymer Scaffolds for Loading and Delivering Cisplatin Anticancer Drug. *Zeitschrift für Anorg. und Allg. Chemie* **2014**, *640* (6), 1119–1126. https://doi.org/10.1002/ZAAC.201400030.

(261) Surnar, B.; Jayakannan, M. Structural Engineering of Biodegradable PCL Block Copolymer Nanoassemblies for Enzyme-Controlled Drug Delivery in Cancer Cells. *ACS Biomater. Sci. Eng.* **2016**, *2* (11), 1926–1941. https://doi.org/10.1021/acsbiomaterials.6b00310.

(262) Rajagopal, K.; Mahmud, A.; Christian, D. A.; Pajerowski, J. D.; Brown, A. E. X.; Loverde, S. M.; Discher, D. E. Curvature-Coupled Hydration of Semicrystalline Polymer Amphiphiles Yields Flexible Worm Micelles but Favors Rigid Vesicles: Polycaprolactone-Based Block Copolymers. *Macromolecules* **2010**, *43* (23), 9736–9746. https://doi.org/10.1021/ma101316w.

(263) Isono, T.; Miyachi, K.; Satoh, Y.; Nakamura, R.; Zhang, Y.; Otsuka, I.; Tajima, K.; Kakuchi, T.; Borsali, R.; Satoh, T. Self-Assembly of Maltoheptaose-Block-Polycaprolactone Copolymers: Carbohydrate-Decorated Nanoparticles with Tunable Morphology and Size in Aqueous Media. *Macromolecules* **2016**, *49* (11), 4178–4194. https://doi.org/10.1021/acs.macromol.6b00781.

(264) Isono, T.; Otsuka, I.; Suemasa, D.; Rochas, C.; Satoh, T.; Borsali, R.; Kakuchi, T. Synthesis, Self-Assembly, and Thermal Caramelization of Maltoheptaose-Conjugated Polycaprolactones Leading to Spherical, Cylindrical, and Lamellar Morphologies. *Macromolecules* **2013**, *46* (22), 8932–8940. https://doi.org/10.1021/ma4019526.

(265) Couffin, A.; Delcroix, D.; Martín-Vaca, B.; Bourissou, D.; Navarro, C. Mild and Efficient Preparation of Block and Gradient Copolymers by Methanesulfonic Acid Catalyzed Ring-Opening Polymerization of Caprolactone and Trimethylene Carbonate. *Macromolecules* **2013**, *46* (11), 4354–4360. https://doi.org/10.1021/ma400916k.

(266) Castillo, R. V.; Müller, A. J.; Raquez, J. M.; Dubois, P. Crystallization Kinetics and Morphology of Biodegradable Double Crystalline PLLA- b -PCL Diblock Copolymers. *Macromolecules* **2010**, *43* (9), 4149–4160. https://doi.org/10.1021/ma100201g.

(267) Seyednejad, H.; Vermonden, T.; Fedorovich, N. E.; Van Eijk, R.; Van Steenbergen, M. J.; Dhert, W. J. A.; Van Nostrum, C. F.; Hennink, W. E. Synthesis and Characterization of Hydroxyl-Functionalized Caprolactone Copolymers and Their Effect on Adhesion, Proliferation, and Differentiation of Human Mesenchymal Stem Cells. *Biomacromolecules* **2009**, *10* (11), 3048–3054. https://doi.org/10.1021/bm900693p.

(268) Keyes, C.; Duhamel, J.; Fung, S.-Y.; Bezaire, J.; Chen, P. Self-Assembling Peptide as a Potential Carrier of Hydrophobic Compounds. *J. Am. Chem. Soc.* **2004**, *126* (24), 7522–7532. https://doi.org/10.1021/JA0381297.

(269) Hao, J.; Servello, J.; Sista, P.; Biewer, M. C.; Stefan, M. C. Temperature-Sensitive Aliphatic Polyesters: Synthesis and Characterization of γ-Substituted Caprolactone Monomers and Polymers. *J. Mater. Chem.* **2011**, *21* (29), 10623–10628. https://doi.org/10.1039/C1JM11288K.

(270) Pramod, P. S.; Shah, R.; Chaphekar, S.; Balasubramanian, N.; Jayakannan, M. Polysaccharide Nano-Vesicular Multidrug Carriers for Synergistic Killing of Cancer Cells. *Nanoscale* **2014**, *6* (20), 11841–11855. https://doi.org/10.1039/c4nr03514c.

(271) Pramod, P. S.; Takamura, K.; Chaphekar, S.; Balasubramanian, N.; Jayakannan, M. Dextran Vesicular Carriers for Dual Encapsulation of Hydrophilic and Hydrophobic Molecules and Delivery into Cells. **2012**, *13*, 2021. https://doi.org/10.1021/bm301583s.

(272) S. Pramod, P.; Ruchira Shah; Manickam Jayakannan. Dual Stimuli Polysaccharide Nanovesicles for Conjugated and Physically Loaded Doxorubicin Delivery in Breast Cancer Cells. *Nanoscale* **2015**, *7* (15), 6636–6652. https://doi.org/10.1039/C5NR00799B.

(273) Duncan, R. The Dawning Era of Polymer Therapeutics. *Nat. Rev. Drug Discov.* **2003**, *2* (5), 347–360. https://doi.org/10.1038/nrd1088.

(274) Duncan, R.; Vicent, M. J. Polymer Therapeutics-Prospects for 21st Century: The End of the Beginning. *Advanced Drug Delivery Reviews*. Elsevier January 1, 2013, pp 60–70. https://doi.org/10.1016/j.addr.2012.08.012.

(275) Venkatachalam, M. A.; Rennke, H. G. The Structural and Molecular Basis of Glomerular Filtration. *Circ. Res.* **1978**, *43* (3), 337–347. https://doi.org/10.1161/01.RES.43.3.337.

(276) Lee, C. C.; Gillies, E. R.; Fox, M. E.; Guillaudeu, S. J.; Fréchet, J. M. J.; Dy, E. E.; Szoka, F. C. A Single Dose of Doxorubicin-Functionalized Bow-Tie Dendrimer Cures Mice Bearing C-26 Colon Carcinomas. *Proc. Natl. Acad. Sci. U. S. A.* **2006**, *103* (45), 16649–16654. https://doi.org/10.1073/pnas.0607705103.

(277) Sun, P.; Chen, D.; Deng, H.; Wang, N.; Huang, P.; Jin, X.; Zhu, X. "bottom-up" Construction of Multi-Polyprodrug-Arm Hyperbranched Amphiphiles for Cancer Therapy. *Bioconjug. Chem.* **2017**, *28* (5), 1470–1480. https://doi.org/10.1021/acs.bioconjchem.7b00146.

(278) Qiu, L.; Liu, Q.; Hong, C. Y.; Pan, C. Y. Unimolecular Micelles of Camptothecin-Bonded Hyperbranched Star Copolymers via β-Thiopropionate Linkage: Synthesis and Drug Delivery. *J. Mater. Chem. B* **2016**, *4* (1), 141–151. https://doi.org/10.1039/c5tb01905b.

(279) Knop, K.; Pretzel, D.; Urbanek, A.; Rudolph, T.; Scharf, D. H.; Schallon, A.; Wagner, M.; Schubert, S.; Kiehntopf, M.; Brakhage, A. A.; Schacher, F. H.; Schubert, U. S. Star-Shaped Drug Carriers for Doxorubicin with POEGMA and POEtOxMA Brush-like Shells: A Structural, Physical, and Biological Comparison. *Biomacromolecules* **2013**, *14* (8), 2536–2548. https://doi.org/10.1021/bm400091n.

(280) Tang, H.; Zhang, J.; Tang, J.; Shen, Y.; Guo, W.; Zhou, M.; Wang, R.; Jiang, N.; Gan, Z.; Yu, Q. Tumor Specific and Renal Excretable Star-like Triblock Polymer-Doxorubicin Conjugates for Safe and Efficient Anticancer Therapy. *Biomacromolecules* **2018**, *19* (7), 2849–2862. https://doi.org/10.1021/acs.biomac.8b00425.

(281) Huang, W.; Liang, Y.; Sang, C.; Mei, C.; Li, X.; Chen, T. Therapeutic Nanosystems Co-Deliver Anticancer Drugs and Oncogene SiRNA to Achieve Synergetic Precise Cancer Chemo-Gene Therapy. *J. Mater. Chem. B* **2018**, *6* (19), 3013–3022. https://doi.org/10.1039/c8tb00004b.

(282) Huang, H.; Cao, D.; Qin, L.; Tian, S.; Liang, Y.; Pan, S.; Feng, M. Dilution-Stable PAMAM G1-Grafted Polyrotaxane Supermolecules Deliver Gene into Cells through a Caveolae-Dependent Pathway. *Mol. Pharm.* **2014**, *11* (7), 2323–2333. https://doi.org/10.1021/mp5002608.

(283) Luo, S.; Han, M.; Cao, Y.; Ling, C.; Zhang, Y. Temperature- and PH-Responsive Unimolecular Micelles with a Hydrophobic Hyperbranched Core. *Colloid Polym. Sci.* **2011**, *289* (11), 1243–1251. https://doi.org/10.1007/s00396-011-2448-2.

(284) Chen, G.; Wang, L.; Cordie, T.; Vokoun, C.; Eliceiri, K. W.; Gong, S. Multi-Functional Self-Fluorescent Unimolecular Micelles for Tumor-Targeted Drug Delivery and Bioimaging. *Biomaterials* **2015**, *47*, 41–50. https://doi.org/10.1016/j.biomaterials.2015.01.006.

(285) Pu, K. Y.; Li, K.; Liu, B. Cationic Oligofluorene-Substituted Polyhedral Oligomeric Silsesquioxane as Light-Harvesting Unimolecular Nanoparticle for Fluorescence Amplification in Cellular Imaging. *Adv. Mater.* **2010**, *22* (5), 643–646. https://doi.org/10.1002/adma.200902409.

(286) Sun, C.; Lee, J. S. H.; Zhang, M. Magnetic Nanoparticles in MR Imaging and Drug Delivery. *Advanced Drug Delivery Reviews*. Elsevier August 17, 2008, pp 1252–1265. https://doi.org/10.1016/j.addr.2008.03.018.

(287) Xu, H.; Xu, J.; Zhu, Z.; Liu, H.; Liu, S. In-Situ Formation of Silver Nanoparticles with Tunable Spatial Distribution at the Poly(N-Isopropylacrylamide) Corona of Unimolecular Micelles. *Macromolecules* **2006**, *39* (24), 8451–8455. https://doi.org/10.1021/ma061584d.

(288) Gopidas, K. R.; Whitesell, J. K.; Fox, M. A. Metal-Core-Organic Shell Dendrimers as Unimolecular Micelles. *J. Am. Chem. Soc.* **2003**, *125* (46), 14168–14180. https://doi.org/10.1021/ja036626h.

(289) Huang, Y.; Qiu, F.; Chen, D.; Shen, L.; Xu, S.; Guo, D.; Su, Y.; Yan, D.; Zhu, X. Color-Convertible, Unimolecular, Micelle-Based, Activatable Fluorescent Probe for Tumor-Specific Detection and Imaging In Vitro and In Vivo. *Small* **2017**, *13* (20), 1–11. https://doi.org/10.1002/smll.201604062.

(290) Gu, D.; Ladewig, K.; Klimak, M.; Haylock, D.; Mclean, K. M.; O'connor, A. J.; Qiao, G. G. Amphiphilic Core Cross-Linked Star Polymers as Water-Soluble, Biocompatible and Biodegradable Unimolecular Carriers for Hydrophobic Drugs. *Polym. Chem.* **2015**, *6*, 6475. https://doi.org/10.1039/c5py00655d.

(291) Khor, S. Y.; Hu, J.; McLeod, V. M.; Quinn, J. F.; Porter, C. J. H.; Whittaker, M. R.; Kaminskas, L. M.; Davis, T. P. The Pharmacokinetics and Biodistribution of a 64 KDa PolyPEG Star Polymer after Subcutaneous and Pulmonary Administration to Rats. *J. Pharm. Sci.* **2016**, *105* (1), 293–300. https://doi.org/10.1016/j.xphs.2015.11.038.

(292) Xin, H.; Sha, X.; Jiang, X.; Chen, L.; Law, K.; Gu, J.; Chen, Y.; Wang, X.; Fang, X. The Brain Targeting Mechanism of Angiopep-Conjugated Poly(Ethylene Glycol)-Co-Poly(E{open}-Caprolactone) Nanoparticles. *Biomaterials* **2012**, *33* (5), 1673–1681.

https://doi.org/10.1016/j.biomaterials.2011.11.018.

(293) Knop, K.; Hoogenboom, R.; Fischer, D.; Schubert, U. S. Poly(Ethylene Glycol) in Drug Delivery: Pros and Cons as Well as Potential Alternatives. *Angew. Chemie - Int. Ed.* **2010**, *49* (36), 6288–6308. https://doi.org/10.1002/anie.200902672.

(294) Malhotra, M.; Surnar, B.; Jayakannan, M. Polymer Topology Driven Enzymatic Biodegradation in Polycaprolactone Block and Random Copolymer Architectures for Drug Delivery to Cancer Cells. *Macromolecules* **2016**, *49* (21), 8098–8112. https://doi.org/10.1021/acs.macromol.6b01793.

(295) Tang, W.; Fan, W.; Lau, J.; Deng, L.; Shen, Z.; Chen, X. Emerging Blood-Brain-Barrier-Crossing Nanotechnology for Brain Cancer Theranostics. *Chem. Soc. Rev.* **2019**, *48* (11), 2967–3014. https://doi.org/10.1039/c8cs00805a.

(296) Chen, Y.; Liu, L. Modern Methods for Delivery of Drugs across the Blood-Brain Barrier. *Adv. Drug Deliv. Rev.* **2012**, *64* (7), 640–665. https://doi.org/10.1016/j.addr.2011.11.010.

(297) Wohlfart, S.; Gelperina, S.; Kreuter, J. Transport of Drugs across the Blood-Brain Barrier by Nanoparticles. *J. Control. Release* **2012**, *161* (2), 264–273. https://doi.org/10.1016/j.jconrel.2011.08.017.

(298) Zhou, Y.; Peng, Z.; Seven, E. S.; Leblanc, R. M. Crossing the Blood-Brain Barrier with Nanoparticles. *Journal of Controlled Release*. Elsevier B.V. January 28, 2018, pp 290–303. https://doi.org/10.1016/j.jconrel.2017.12.015.

(299) Kreuter, J. Drug Delivery to the Central Nervous System by Polymeric Nanoparticles: What Do We Know? *Adv. Drug Deliv. Rev.* **2014**, *71*, 2–14. https://doi.org/10.1016/j.addr.2013.08.008.

(300) Lockman, P. R.; Koziara, J. M.; Mumper, R. J.; Allen, D. Nanoparticle Surface Charges Alter Blood-Brain Barrier Integrity and Permeability. *J. Drug Target.* **2004**, *12* (9–10), 635–641. https://doi.org/10.1080/10611860400015936.

(301) Sharma, A.; Porterfield, J. E.; Smith, E.; Sharma, R.; Kannan, S.; Kannan, R. M. Effect of Mannose Targeting of Hydroxyl PAMAM Dendrimers on Cellular and Organ Biodistribution in a Neonatal Brain Injury Model. *J. Control. Release* **2018**, *283*, 175–189. https://doi.org/10.1016/j.jconrel.2018.06.003.

(302) Zhang, F.; Nance, E.; Zhang, Z.; Jasty, V.; Kambhampati, S. P.; Mishra, M. K.; Burd, I.; Romero, R.; Kannan, S.; Kannan, R. M. Surface Functionality Affects the Biodistribution and Microglia-Targeting of Intra-Amniotically Delivered Dendrimers. *J. Control. Release* **2016**, *237*, 61–70. https://doi.org/10.1016/j.jconrel.2016.06.046.

(303) Perumal, O. P.; Inapagolla, R.; Kannan, S.; Kannan, R. M. The Effect of Surface Functionality on Cellular Trafficking of Dendrimers. *Biomaterials* **2008**, *29* (24–25), 3469–3476. https://doi.org/10.1016/j.biomaterials.2008.04.038.

(304) Srinageshwar, B.; Dils, A.; Sturgis, J.; Wedster, A.; Kathirvelu, B.; Baiyasi, S.; Swanson, D.; Sharma, A.; Dunbar, G. L.; Rossignol, J. Surface-Modified G4 PAMAM

Dendrimers Cross the Blood-Brain Barrier Following Multiple Tail-Vein Injections in C57BL/6J Mice. *ACS Chem. Neurosci.* **2019**, *10* (9), 4145–4150. https://doi.org/10.1021/acschemneuro.9b00347.

(305) Clark, A. J.; Davis, M. E. Increased Brain Uptake of Targeted Nanoparticles by Adding an Acid-Cleavable Linkage between Transferrin and the Nanoparticle Core. *Proc. Natl. Acad. Sci. U. S. A.* **2015**, *112* (40), 12486–12491. https://doi.org/10.1073/pnas.1517048112.

(306) Liu, Y.; Zou, Y.; Feng, C.; Lee, A.; Yin, J.; Chung, R.; Park, J. B.; Rizos, H.; Tao, W.; Zheng, M.; Farokhzad, O. C.; Shi, B. Charge Conversional Biomimetic Nanocomplexes as a Multifunctional Platform for Boosting Orthotopic Glioblastoma RNAi Therapy. *Nano Lett.* **2020**, *20* (3), 1637–1646. https://doi.org/10.1021/acs.nanolett.9b04683.

(307) Morad, G.; Carman, C. V.; Hagedorn, E. J.; Perlin, J. R.; Zon, L. I.; Mustafaoglu, N.; Park, T. E.; Ingber, D. E.; Daisy, C. C.; Moses, M. A. Tumor-Derived Extracellular Vesicles Breach the Intact Blood-Brain Barrier via Transcytosis. *ACS Nano* **2019**, *13* (12), 13853–13865. https://doi.org/10.1021/acsnano.9b04397.

(308) Lundy, D. J.; Lee, K. J.; Peng, I. C.; Hsu, C. H.; Lin, J. H.; Chen, K. H.; Tien, Y. W.; Hsieh, P. C. H. Inducing a Transient Increase in Blood-Brain Barrier Permeability for Improved Liposomal Drug Therapy of Glioblastoma Multiforme. *ACS Nano* **2019**, *13* (1), 97–113. https://doi.org/10.1021/acsnano.8b03785.

(309) Joseph, A.; Contini, C.; Cecchin, D.; Nyberg, S.; Ruiz-Perez, L.; Gaitzsch, J.; Fullstone, G.; Tian, X.; Azizi, J.; Preston, J.; Volpe, G.; Battaglia, G. Chemotactic Synthetic Vesicles: Design and Applications in Blood-Brain Barrier Crossing. *Sci. Adv.* **2017**, *3* (8). https://doi.org/10.1126/sciadv.1700362.

(310) Surnar, B.; Basu, U.; Banik, B.; Ahmad, A.; Marples, B.; Kolishetti, N.; Dhar, S. Nanotechnology-Mediated Crossing of Two Impermeable Membranes to Modulate the Stars of the Neurovascular Unit for Neuroprotection. *Proc. Natl. Acad. Sci. U. S. A.* **2018**, *115* (52), E12333–E12342. https://doi.org/10.1073/pnas.1816429115.

(311) Liu, J.; Yu, M.; Zhou, C.; Zheng, J. Renal Clearable Inorganic Nanoparticles: A New Frontier of Bionanotechnology. *Materials Today*. Elsevier December 1, 2013, pp 477–486. https://doi.org/10.1016/j.mattod.2013.11.003.

(312) Soo Choi, H.; Liu, W.; Misra, P.; Tanaka, E.; Zimmer, J. P.; Itty Ipe, B.; Bawendi, M. G.; Frangioni, J. V. Renal Clearance of Quantum Dots. *Nat. Biotechnol.* **2007**, *25* (10), 1165–1170. https://doi.org/10.1038/nbt1340.

(313) Frères, P.; Bouznad, N.; Servais, L.; Josse, C.; Wenric, S.; Poncin, A.; Thiry, J.; Moonen, M.; Oury, C.; Lancellotti, P.; Bours, V.; Jerusalem, G. Variations of Circulating Cardiac Biomarkers during and after Anthracycline-Containing Chemotherapy in Breast Cancer Patients. *BMC Cancer* **2018**, *18* (1), 1–9. https://doi.org/10.1186/s12885-018-4015-4.

(314) Yamamoto, Y.; Nagasaki, Y.; Kato, Y.; Sugiyama, Y.; Kataoka, K. Long-Circulating Poly(Ethylene Glycol)-Poly(D,L-Lactide) Block Copolymer Micelles with Modulated Surface Charge. *J. Control. Release* **2001**, *77* (1–2), 27–38.

https://doi.org/10.1016/S0168-3659(01)00451-5.

(315) Imran Ul-Haq, M.; Lai, B. F. L.; Chapanian, R.; Kizhakkedathu, J. N. Influence of Architecture of High Molecular Weight Linear and Branched Polyglycerols on Their Biocompatibility and Biodistribution. *Biomaterials* **2012**, *33* (35), 9135–9147. https://doi.org/10.1016/j.biomaterials.2012.09.007.

(316) Nasongkia, N.; Chen, B.; Macaraeg, N.; Fox, M. E.; Fréchet, J. M. J.; Szoka, F. C. Dependence of Pharmacokinetics and Biodistribution on Polymer Architecture: Effect of Cyclic versus Linear Polymers. *J. Am. Chem. Soc.* **2009**, *131* (11), 3842–3843. https://doi.org/10.1021/ja900062u.

(317) Müllner, M.; Dodds, S. J.; Nguyen, T. H.; Senyschyn, D.; Porter, C. J. H.; Boyd, B. J.; Caruso, F. Size and Rigidity of Cylindrical Polymer Brushes Dictate Long Circulating Properties in Vivo. *ACS Nano* **2015**, *9* (2), 1294–1304. https://doi.org/10.1021/nn505125f.

(318) Wu, W.; Wang, W.; Li, J. Star Polymers: Advances in Biomedical Applications. *Progress in Polymer Science*. Elsevier Ltd July 1, 2015, pp 55–85. https://doi.org/10.1016/j.progpolymsci.2015.02.002.

(319) Panja, S.; Dey, G.; Bharti, R.; Mandal, P.; Mandal, M.; Chattopadhyay, S. Metal Ion Ornamented Ultrafast Light-Sensitive Nanogel for Potential in Vivo Cancer Therapy. *Chem. Mater.* **2016**, *28* (23), 8598–8610. https://doi.org/10.1021/acs.chemmater.6b03440.

(320) Ostermann, J.; Merkl, J. P.; Flessau, S.; Wolter, C.; Kornowksi, A.; Schmidtke, C.; Pietsch, A.; Kloust, H.; Feld, A.; Weller, H. Controlling the Physical and Biological Properties of Highly Fluorescent Aqueous Quantum Dots Using Block Copolymers of Different Size and Shape. *ACS Nano* **2013**, *7* (10), 9156–9167. https://doi.org/10.1021/nn4037859.

(321) Washington, K. E.; Kularatne, R. N.; Du, J.; Ren, Y.; Gillings, M. J.; Geng, C. X.; Biewer, M. C.; Stefan, M. C. Thermoresponsive Star-like γ-Substituted Poly(Caprolactone)s for Micellar Drug Delivery. *J. Mater. Chem. B* **2017**, *5* (28), 5632–5640. https://doi.org/10.1039/c7tb01291h.

(322) Sun, M.; Yin, W.; Dong, X.; Yang, W.; Zhao, Y.; Yin, M. Fluorescent Supramolecular Micelles for Imaging-Guided Cancer Therapy. *Nanoscale* **2016**, *8* (9), 5302–5312. https://doi.org/10.1039/c6nr00450d.

(323) Alhoranta, A. M.; Lehtinen, J. K.; Urtti, A. O.; Butcher, S. J.; Aseyev, V. O.; Tenhu, H. J. Cationic Amphiphilic Star and Linear Block Copolymers: Synthesis, Self-Assembly, and in Vitro Gene Transfection. *Biomacromolecules* **2011**, *12* (9), 3213–3222. https://doi.org/10.1021/bm2006906.

(324) Fukukawa, K. I.; Rossin, R.; Hagooly, A.; Pressly, E. D.; Hunt, J. N.; Messmore, B. W.; Wooley, K. L.; Welch, M. J.; Hawker, C. J. Synthesis and Characterization of Core-Shell Star Copolymers for in Vivo PET Imaging Applications. *Biomacromolecules* **2008**, *9* (4), 1329–1339. https://doi.org/10.1021/bm7014152.

(325) Ferrari, M. Cancer Nanotechnology: Opportunities and Challenges. *Nat. Rev. Cancer* **2005**, *5* (3), 161–171. https://doi.org/10.1038/nrc1566.

(326) Zhang, L.; Gu, F. X.; Chan, J. M.; Wang, A. Z.; Langer, R. S.; Farokhzad, O. C. Nanoparticles in Medicine: Therapeutic Applications and Developments. *Clin. Pharmacol. Ther.* **2008**, *83* (5), 761–769. https://doi.org/10.1038/sj.clpt.6100400.

(327) Gao, J.; Xu, B. Applications of Nanomaterials inside Cells. *Nano Today* **2009**, *4* (1), 37–51. https://doi.org/10.1016/J.NANTOD.2008.10.009.

(328) Nie, S. Editorial: Understanding and Overcoming Major Barriers in Cancer Nanomedicine. *Nanomedicine* **2010**, *5* (4), 523–528. https://doi.org/10.2217/nnm.10.23.

(329) Liu, Y.; Wang, J.; Xiong, Q.; Hornburg, D.; Tao, W.; Farokhzad, O. C. Nano-Bio Interactions in Cancer: From Therapeutics Delivery to Early Detection. *Acc. Chem. Res.* **2021**, *54* (2), 291–301. https://doi.org/10.1021/acs.accounts.0c00413.

(330) Petros, R. A.; Desimone, J. M. Strategies in the Design of Nanoparticles for Therapeutic Applications. *Nat. Rev. Drug Discov.* **2010**, *9* (8), 615–627. https://doi.org/10.1038/nrd2591.

(331) Zamboni, W. C.; Torchilin, V.; Patri, A. K.; Hrkach, J.; Stern, S.; Lee, R.; Nel, A.; Panaro, N. J.; Grodzinski, P. Best Practices in Cancer Nanotechnology: Perspective from NCI Nanotechnology Alliance Defining Oncology Applications for Nanotechnology Constructs. *Clin Cancer Res* **2012**, *18* (12). https://doi.org/10.1158/1078-0432.CCR-11-2938.

(332) Yoo, J.-W.; Chambers, E.; Mitragotri, S. Factors That Control the Circulation Time of Nanoparticles in Blood: Challenges, Solutions and Future Prospects. *Curr. Pharm. Des.* **2010**, *16* (21), 2298–2307. https://doi.org/10.2174/138161210791920496.

(333) Kettiger, H.; Schipanski, A.; Wick, P.; Huwyler, J. Engineered Nanomaterial Uptake and Tissue Distribution: From Cell to Organism. *Int. J. Nanomedicine* **2013**, *8*, 3255–3269. https://doi.org/10.2147/IJN.S49770.

(334) Manzanares, D.; Ceña, V. Endocytosis: The Nanoparticle and Submicron Nanocompounds Gateway into the Cell. *Pharmaceutics* **2020**, *12* (4), 1–22. https://doi.org/10.3390/pharmaceutics12040371.

(335) Kunzmann, A.; Andersson, B.; Thurnherr, T.; Krug, H.; Scheynius, A.; Fadeel, B. Toxicology of Engineered Nanomaterials: Focus on Biocompatibility, Biodistribution and Biodegradation. *Biochim. Biophys. Acta - Gen. Subj.* **2011**, *1810* (3), 361–373. https://doi.org/10.1016/J.BBAGEN.2010.04.007.

(336) Dobrovolskaia, M. A.; McNeil, S. E. Immunological Properties of Engineered Nanomaterials. *Nanosci. Technol. A Collect. Rev. from Nat. Journals* **2009**, 278–287. https://doi.org/10.1142/9789814287005_0029.

(337) Iversen, T. G.; Skotland, T.; Sandvig, K. Endocytosis and Intracellular Transport of Nanoparticles: Present Knowledge and Need for Future Studies. *Nano Today* **2011**, *6* (2), 176–185. https://doi.org/10.1016/J.NANTOD.2011.02.003.

(338) Bareford, L. M.; Swaan, P. W. Endocytic Mechanisms for Targeted Drug Delivery. *Adv. Drug Deliv. Rev.* **2007**, *59* (8), 748–758. https://doi.org/10.1016/J.ADDR.2007.06.008.

(339) Conner, S. D.; Schmid, S. L. *Regulated Portals of Entry into the Cell*; 2003.

(340) Harush-Frenkel, O.; Debotton, N.; Benita, S.; Altschuler, Y. Targeting of Nanoparticles to the Clathrin-Mediated Endocytic Pathway. *Biochem. Biophys. Res. Commun.* **2007**, *353* (1), 26–32. https://doi.org/10.1016/j.bbrc.2006.11.135.

(341) Jiang, X.; Dausend, J.; Hafner, M.; Musyanovych, A.; Rö, C.; Landfester, K.; Nienhaus, G. U. Specific Effects of Surface Amines on Polystyrene Nanoparticles in Their Interactions with Mesenchymal Stem Cells. https://doi.org/10.1021/bm901348z.

(342) Chang, C. C.; Wu, M.; Yuan, F. Role of Specific Endocytic Pathways in Electrotransfection of Cells. *Mol. Ther. - Methods Clin. Dev.* **2014**, *1* (July), 14058. https://doi.org/10.1038/mtm.2014.58.

(343) Billiet, L.; Gomez, J. P.; Berchel, M.; Jaffrès, P. A.; Le Gall, T.; Montier, T.; Bertrand, E.; Cheradame, H.; Guégan, P.; Mével, M.; Pitard, B.; Benvegnu, T.; Lehn, P.; Pichon, C.; Midoux, P. Gene Transfer by Chemical Vectors, and Endocytosis Routes of Polyplexes, Lipoplexes and Lipopolyplexes in a Myoblast Cell Line. *Biomaterials* **2012**, *33* (10), 2980–2990. https://doi.org/10.1016/j.biomaterials.2011.12.027.

(344) Harush-Frenkel, O.; Debotton, N.; Benita, S.; Altschuler, Y. Targeting of Nanoparticles to the Clathrin-Mediated Endocytic Pathway. *Biochem. Biophys. Res. Commun.* **2007**, *353* (1), 26–32. https://doi.org/10.1016/J.BBRC.2006.11.135.

(345) Dombu, C. Y.; Kroubi, M.; Zibouche, R.; Matran, R.; Betbeder, D. Characterization of Endocytosis and Exocytosis of Cationic Nanoparticles in Airway Epithelium Cells. *Nanotechnology* **2010**, *21* (35). https://doi.org/10.1088/0957-4484/21/35/355102.

(346) Mahmoud, K. A.; Mena, J. A.; Male, K. B.; Hrapovic, S.; Kamen, A.; Luong, J. H. T. Effect of Surface Charge on the Cellular Uptake and Cytotoxicity of Fluorescent Labeled Cellulose Nanocrystals. https://doi.org/10.1021/am1006222.

8

List of Publications

1. **Polymer Topology Driven Enzymatic Biodegradation in Polycaprolactone Block and Random Copolymer Architectures for Drug Delivery to Cancer Cells**
   Malhotra, Mehak; Surnar, Bapurao; Jayakannan, Manickam
   Macromolecules (2016), 49(21), 8098-8112.
   DOI:10.1021/acs.macromol.6b01793

2. **Perylene-Tagged Polycaprolactone Block Copolymers and Their Enzyme-Biodegradable Fluorescent Nanoassemblies for Intracellular Bio-imaging in Cancer Cells**
   Kulkarni, Bhagyashree; Malhotra, Mehak; Jayakannan, Manickam
   ACS Applied Polymer Materials (2019), 1(12), 3375-3388.
   DOI:10.1021/acsapm.9b00800

3. **Biodegradable Polymer Theranostic Fluorescent Nanoprobe for Direct Visualization and Quantitative Determination of Antimicrobial Activity**
   Ghosh, Ruma; Malhotra, Mehak; Madhuri Sathe, Rupali Ravindra; Jayakannan, Manickam,
   Biomacromolecules (2020), 21(7), 2896-2912.
   DOI:10.1021/acs.biomac.0c00653

4. **Tweaking Polymer Topology to Breach Blood Brian Barrier Together with Reduced Cardiotoxicity**
   Mehak Malhotra, Meenakshi Pardasani, Nixon M. Abraham., Manickam Jayakannan
   Manuscript Submitted for Publication

5. **The Role of Surface Charges of the Star-block Macromolecular Nano-carrier on the Cellular Internalization.**
   Mehak Malhotra, Ruma Ghosh, Manickam Jayakannan
   Manuscript under Preparation.

9

Appendix

Chapter 2

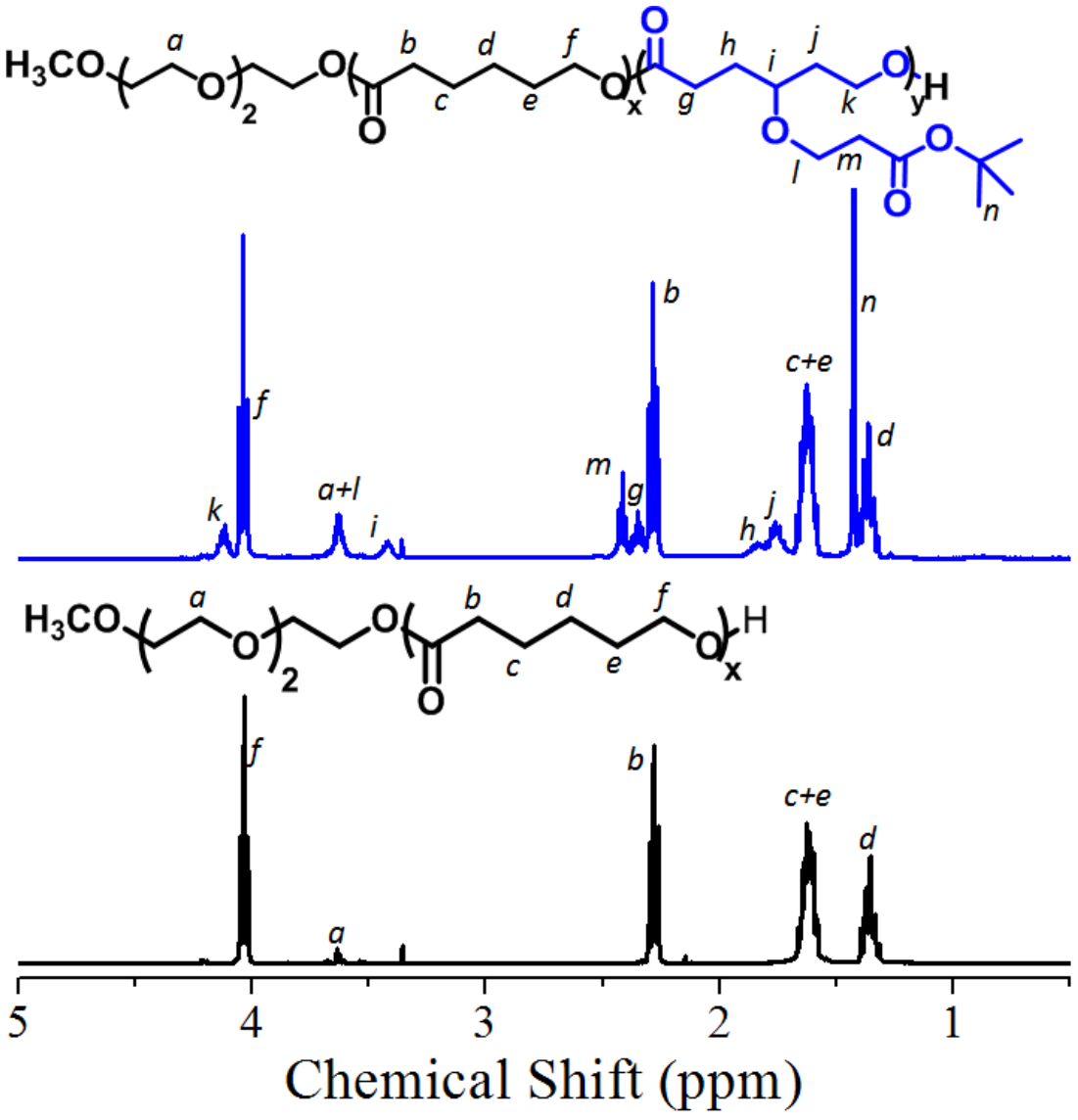

SF 2: Stack plot of ^{1}H NMR of block copolymer PCL_{75}-*b*-$BPCL_{25}$ and macro-initiator PCL-75.

Note: The stack plot of the ^{1}H NMR of PCL_{75}-*b*-$BPCL_{25}$ block copolymer and it's macro-initiator PCL-75 is provided here. The peaks corresponding to PCL as well as the additional BPCL peaks can be seen in the block copolymer NMR. The degree of polymerization DP_n was calculated in the similar manner as for the random copolymers.

ST 2.2: Transition temperature and respective enthalpies of transition (ΔH)

Polymer	DSC				
	T_c (°C)	T_m (°C)	ΔH_c (J/g)	ΔH_m (J/g)	T_g (°C)
PCL-100	35.70	55.49	68.91	68.40	-
BPCL-10	1.39	41.82	43.53	41.30	-
BPCL-20	-4.57	23.56	16.52	18.50	-
BPCL-30					-48.39
BPCL-50					-34.54
BPCL-70					-32.57
BPCL-80					-23.97
BPCL-100					-23.10
CPCL-10	8.95	47.43	42.71	54.79	-
CPCL-20	-3.64	30.21	10.26	11.18	-
CPCL-30					-46.43
CPCL-50					-30.60
CPCL-70					-21.09
CPCL-80					-18.60
CPCL-100					-4.77
PCL_{75}-b-$BPCL_{25}$	4.86	46.16	30.31	31.44	-
PCL_{50}-b-$BPCL_{50}$	5.10	43.28	24.39	29.31	-
PCL_{75}-b-$CPCL_{25}$	5.65	54.12	33.44	47.10	-
PCL_{50}-b-$CPCL_{50}$					-32.71

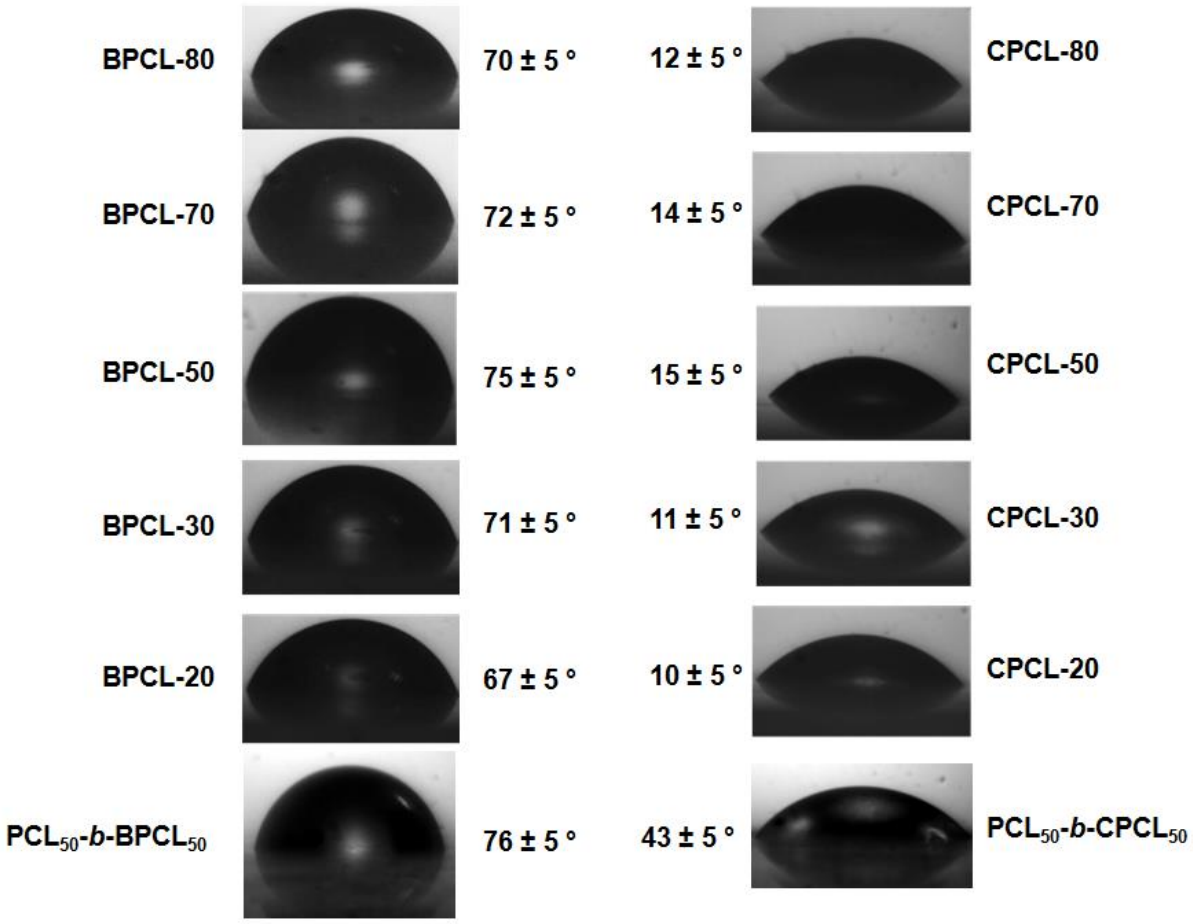

Figure 2.1. Water Contact Angle images of random and block copolymers

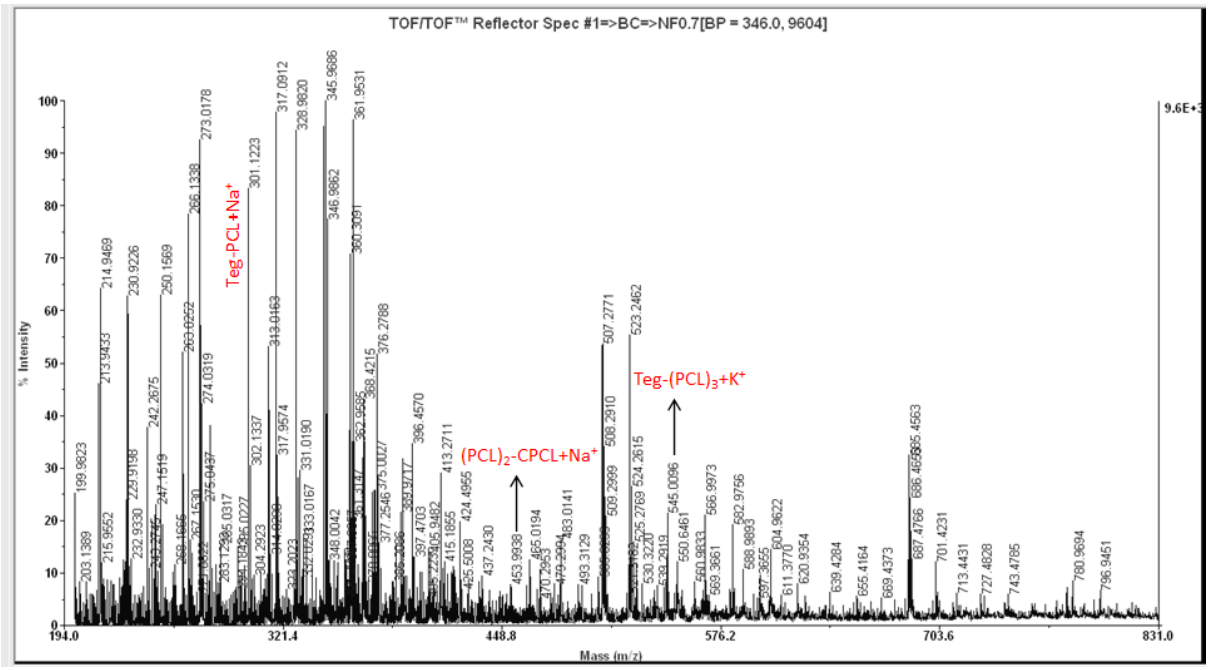

Figure 2.2. *MALDI-TOF spectrum of CPCL-50 nanoparticle after 48 h incubation in presence of esterase in PBS at 37 °C.*

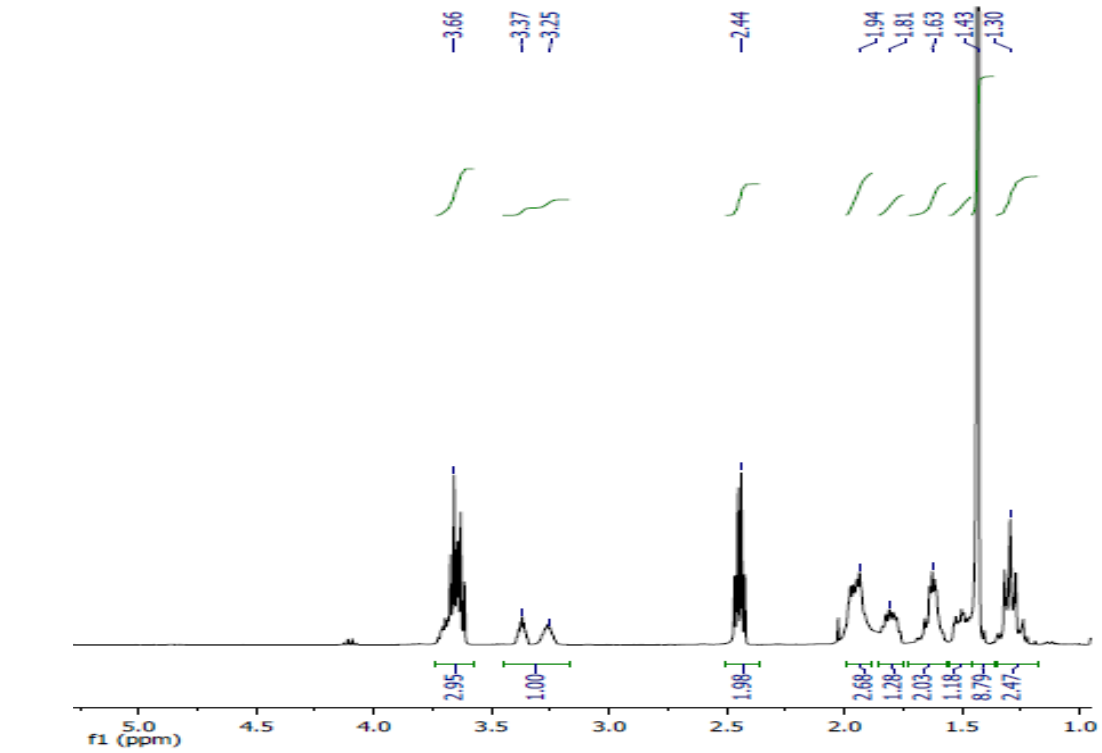

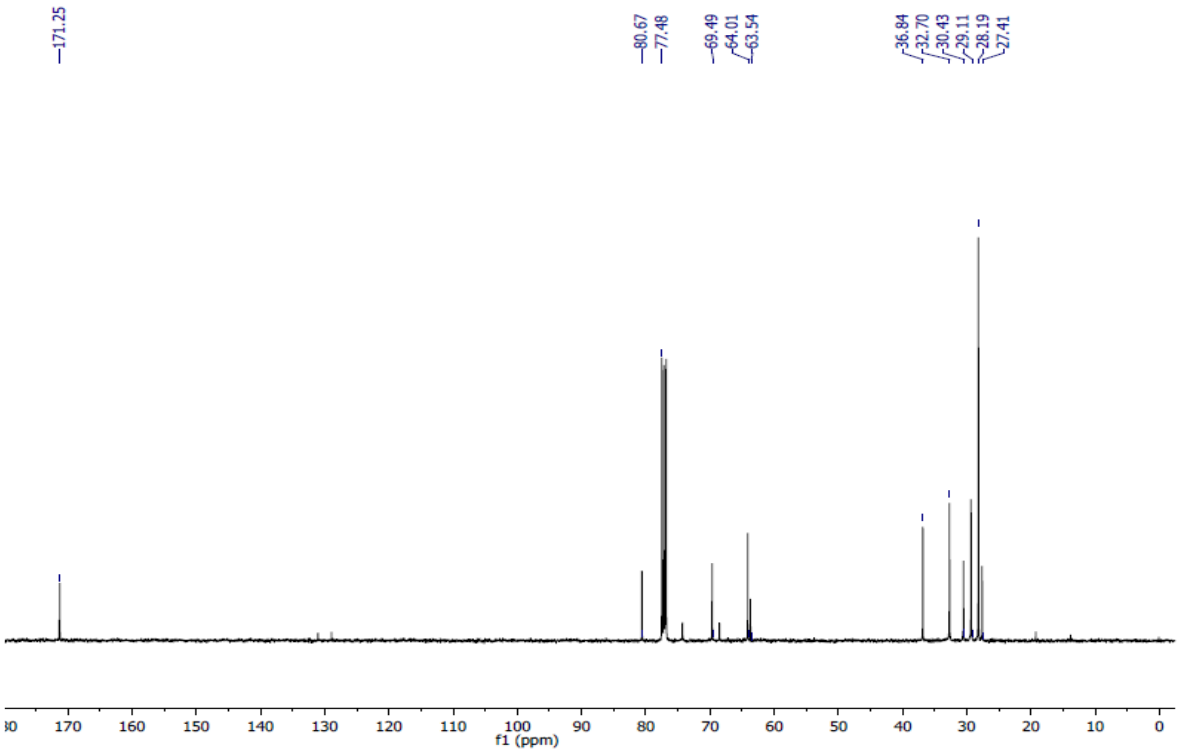

^{1}H-NMR and ^{13}C-NMR of compound (1)

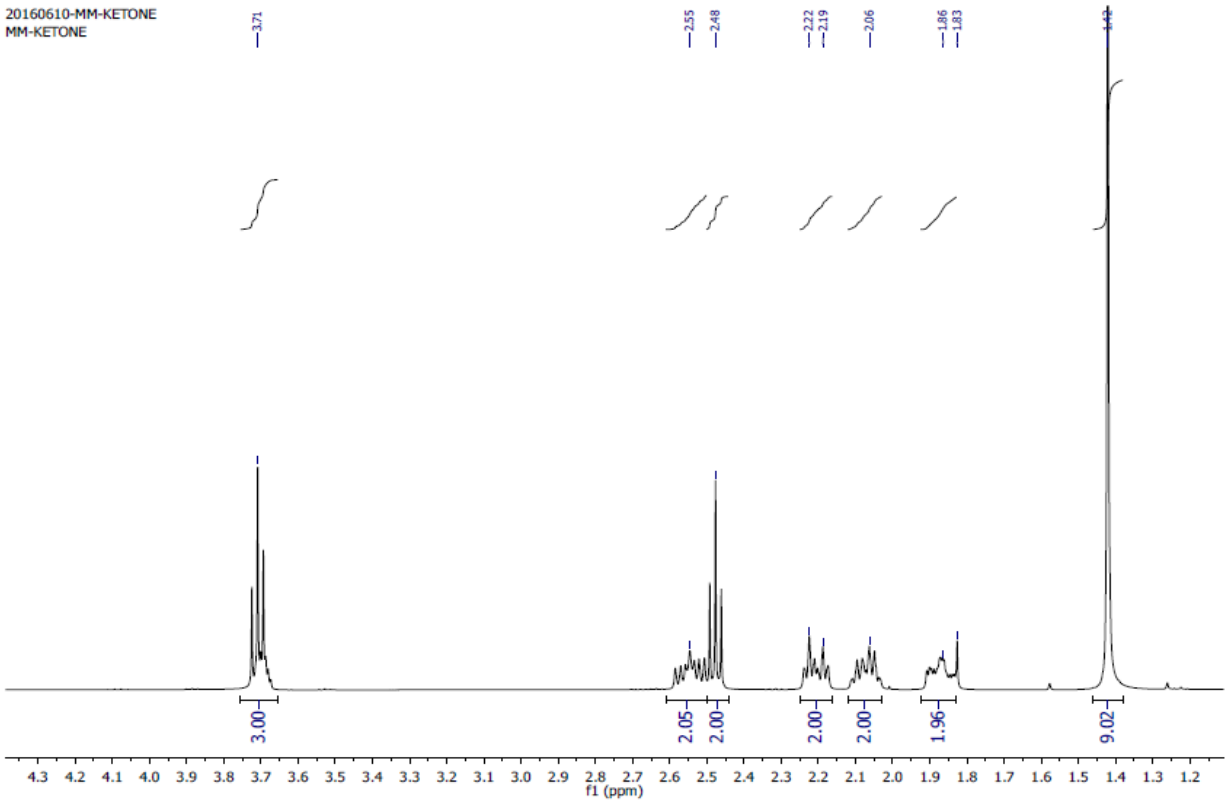

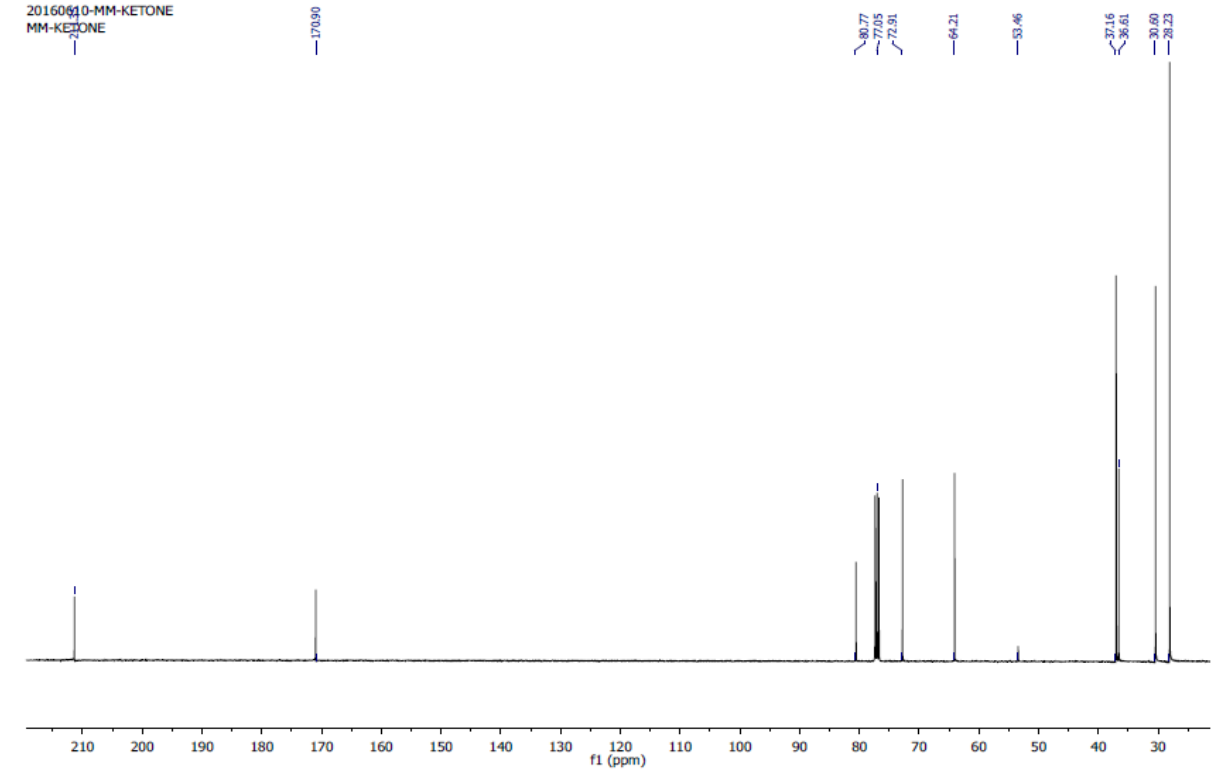

[1]H-NMR and [13]C-NMR of compound (2)

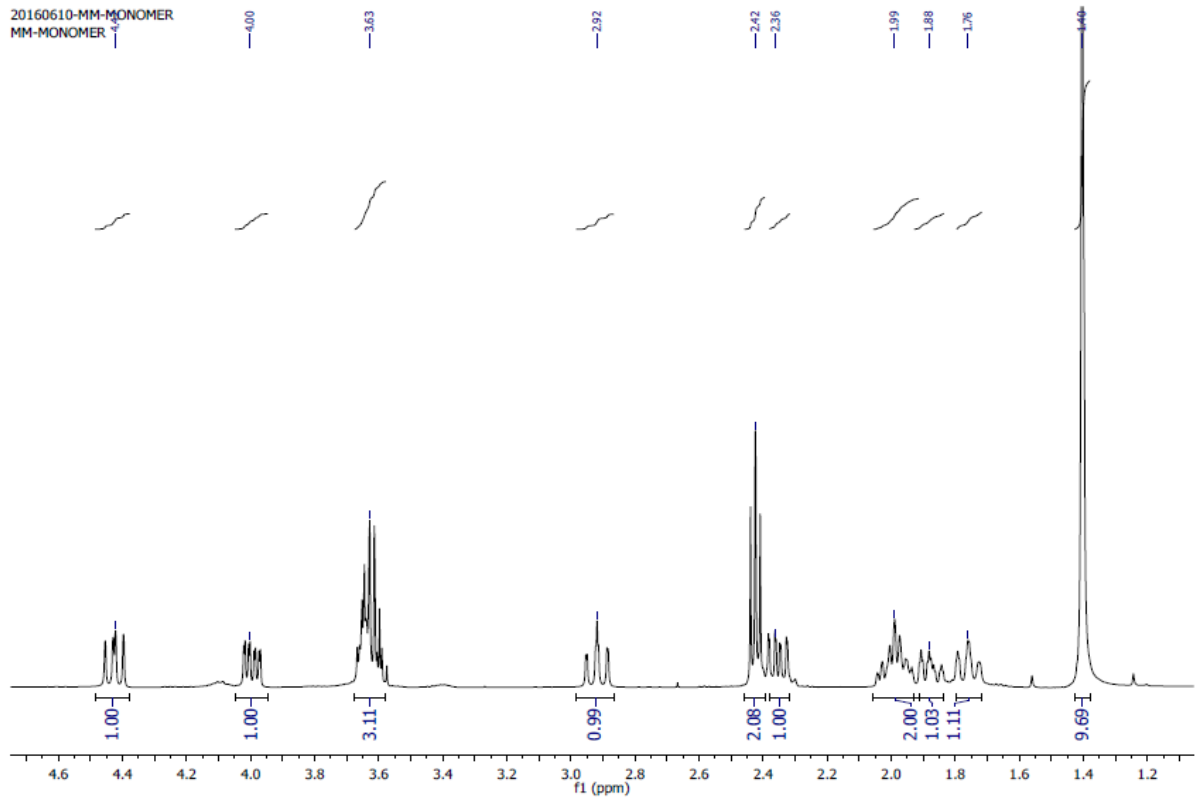

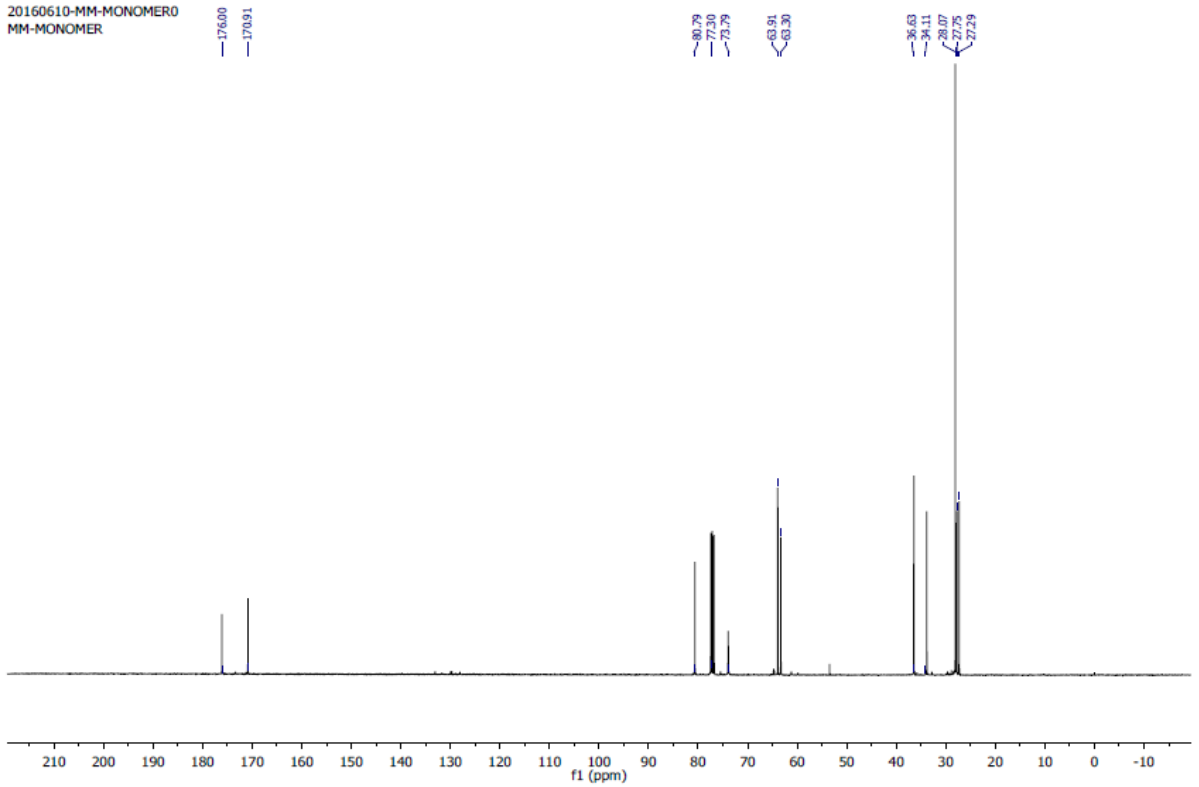

[1]H-NMR and [13]C-NMR of compound (3)

Chapter 5

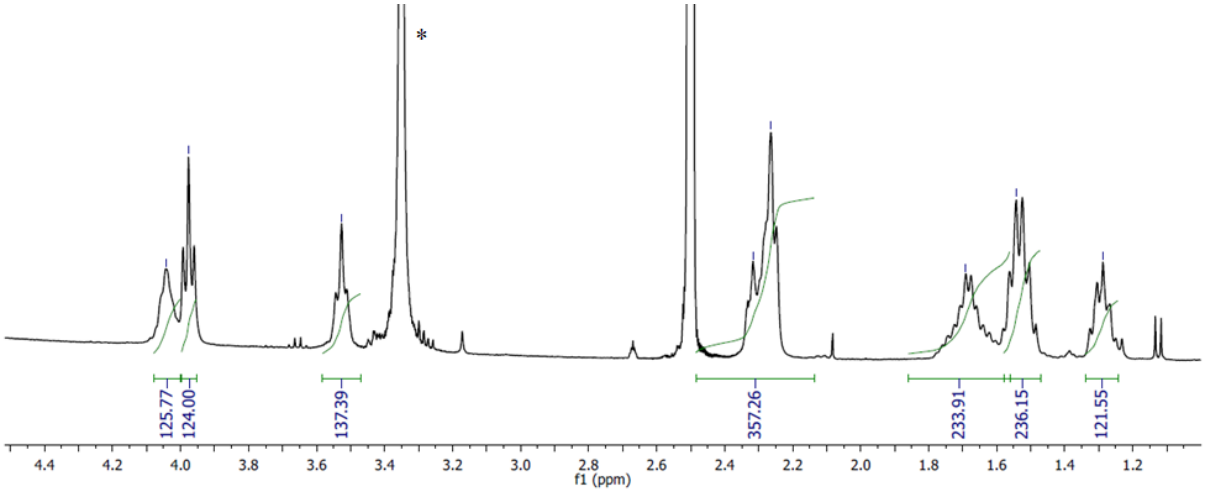

Figure 5.1. *^{1}H NMR spectra of carboxylate substituted SB-60 (anionic) in $(CD3)_2SO$. The spectra are plotted up to 4.50 ppm for simplicity.*

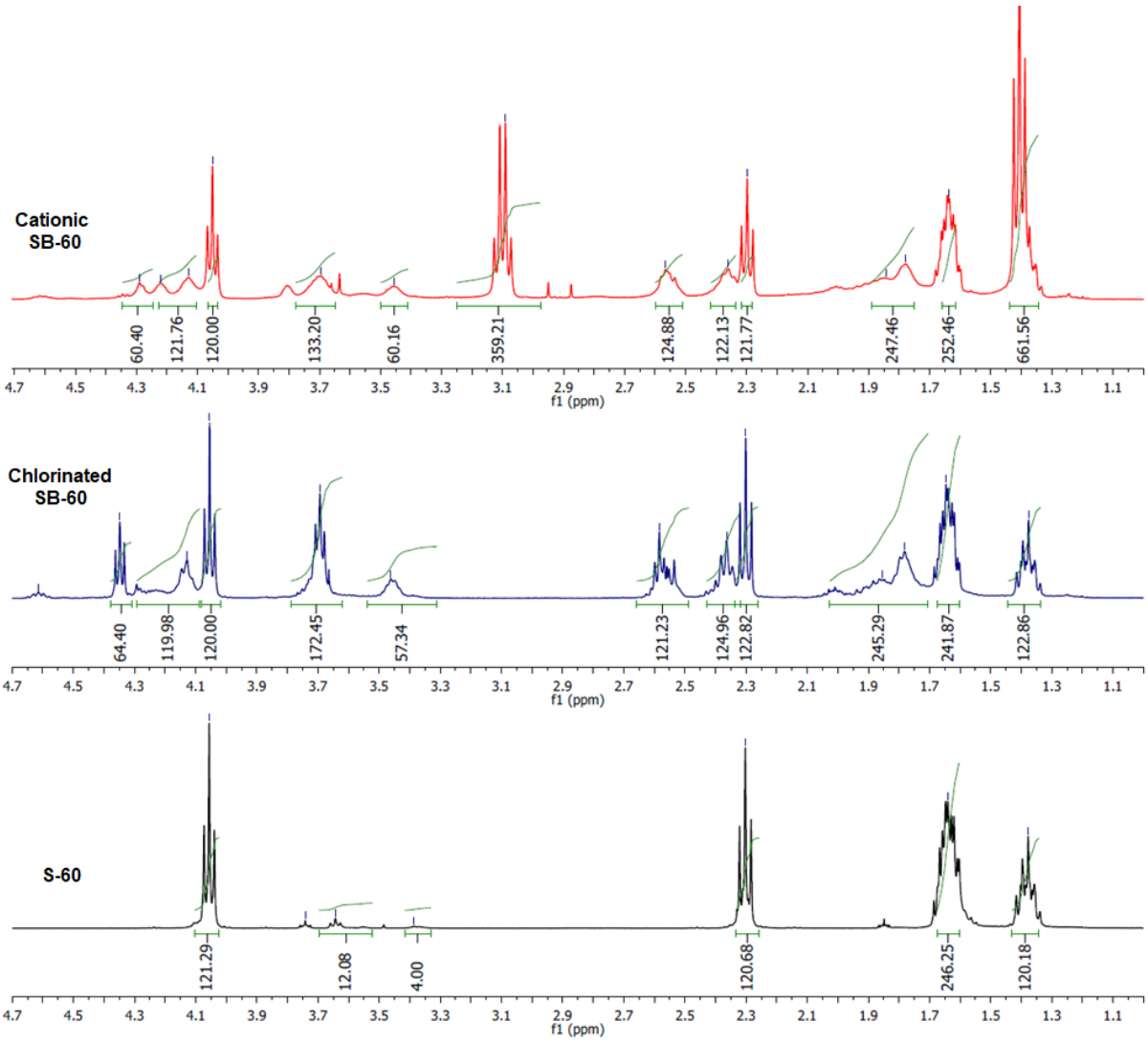

Figure 5.2. *^{1}H NMR stack plot of S-60, chlorinated SB-60 and cationic SB-60 in $CDCl_3$. The spectra are plotted up to 4.70 ppm for simplicity*

Macromolecules

Article

pubs.acs.org/Macromolecules

Polymer Topology Driven Enzymatic Biodegradation in Polycaprolactone Block and Random Copolymer Architectures for Drug Delivery to Cancer Cells

Mehak Malhotra, Bapurao Surnar, and Manickam Jayakannan*

Department of Chemistry, Indian Institute of Science Education and Research-Pune, Dr. Homi Bhabha Road, Pune 411008, Maharashtra, India

Supporting Information

ABSTRACT: The present investigation reports polymer topology design principle for programming the enzymatic biodegradation and delivery of anticancer drugs at the intracellular compartments of breast and cervical cancers. To accomplish this goal, new classes of biodegradable amphiphilic block and random copolymers based on hydrophilic carboxylic-functionalized polycaprolactone (CPCL) and hydrophobic polycaprolactone (PCL) units were designed via ring-opening polymerization methodology. The interchain interactions and their packing were directly controlled by the topology of the polymers, and the block copolymers were found to be as semicrystalline materials. These amphiphilic block and random polymers were readily dispersible in water, and they self-assembled into <200 nm nanoparticles. These nanoparticles exhibited excellent capability for loading anticancer drug doxorubicin (DOX) in the hydrophobic pocket. *In vitro* drug release kinetics revealed that the polymer nanoscaffolds were stable under physiological conditions, and they exclusively ruptured in the presence of lysosomal esterase enzyme at the intracellular compartments to deliver DOX. The "burst" and "controlled" release of drugs from the polymer nanocarriers was directly controlled by length and chemical composition of block and random copolymers. *In vitro* cytotoxicity studies in breast cancer (MCF 7) and cervical cancer (HeLa) cells revealed that the nascent polymer nanoparticle was highly biocompatible and nontoxic to cells whereas their DOX-loaded nanoparticles accomplished >95% cell killing. Confocal microscopy reinstated the cellular uptake of the DOX-loaded polymer scaffold wherein the nanoparticle was highly concentrated at the nucleus and revealed that the drugs were predominantly delivered at the nucleus of the cells for apoptosis. Flow cytometry investigation confirmed the enhanced DOX delivering capability of block and random copolymer nanoparticles compared to free DOX. The newly designed fully biodegradable PCL-based block and random nanocarriers are excellent scaffolds for enzyme-mediated intracellular delivery of DOX, and the proof of concept was established in breast and cervical cancers.

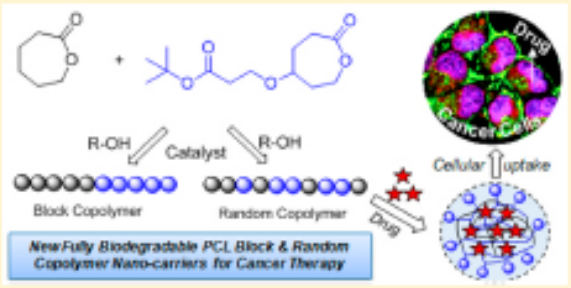

INTRODUCTION

Aliphatic polyesters are important classes of biomaterials, and they are extensively used in biodegradable implants,[1] tissue engineering,[2,3] drug and gene delivery,[4,5] etc. Poly(ethylene glycol) (PEG)-*block*-polyesters have very good hydrophilic−hydrophobic balance in the backbone, and they self-assembled into nanocarriers such as micelles.[6] PEG-*b*-poly(L-lactide)[7] and PEG-*b*-poly(L-gylycolide)[8] are excellent biodegradable materials; however, the poor hydrolytic and environmental stability[9,10] of their self-assembled nanocarriers in aqueous medium induced additional difficulties in handling them as drug carriers. PEG-*b*-poly(α-hydroxy esters) were made by the ring-opening polymerization of α-hydroxy-L-amino acid cyclic monomers,[11] and few attempts were made to explore these aliphatic polyesters for drug delivery.[12,13] PEG-*b*-polycaprolactone (PCL) is one of the most prominent polyesters due to its excellent mechanical strength, environmental stability, rheological and viscoelastic properties, and so on.[14] PCL is known to undergo degradation in a two-step process wherein random chain scission occurs first via hydrolytic cleavage at the tissues followed by the enzymatic biodegradation at the intracellular level.[15] PCL chains are highly hydrophobic and are most often found to experience slow degradation under physiological conditions for more than 24 months.[16] To introduce stimuli responsiveness and also make provision for anchoring drugs or targeting agents, substituted PCL with hydroxyl,[17,18] ketone,[19] imine,[20] amine,[21] azide,[22] carboxylic,[17,23] alkoxyloxy,[24−26] cholesteryl,[27] oligoethyleneoxy,[28] propargyl,[29−31] and menthide[32] functional groups were developed. Most of these substituted PCL copolymers were primarily designed to study the structure−property relationship.[33] Few of these substituted PCL copolymers were self-assembled in aqueous medium as

Received: August 17, 2016
Revised: October 2, 2016
Published: October 21, 2016

DOI: 10.1021/acs.macromol.6b01793
Macromolecules 2016, 49, 8098−8112

ACS APPLIED POLYMER MATERIALS

Article

Cite This: ACS Appl. Polym. Mater. 2019, 1, 3375−3388

pubs.acs.org/acsapm

Perylene-Tagged Polycaprolactone Block Copolymers and Their Enzyme-Biodegradable Fluorescent Nanoassemblies for Intracellular Bio-imaging in Cancer Cells

Bhagyashree Kulkarni, Mehak Malhotra, and Manickam Jayakannan*

Department of Chemistry, Indian Institute of Science Education and Research (IISER) Pune, Dr. Homi Bhabha Road, Pune 411008, Maharashtra, India

Supporting Information

ABSTRACT: The present investigation reports enzyme-biodegradable perylenebisimide (PBI)-tagged polycaprolactone (PCL) block copolymers, and their aqueous nanoassemblies were employed as probes for intracellular bio-imaging in cancer cells. Bishydroxyl functionalized PBI initiator was tailor-made, and it was employed as initiator for the ring opening polymerization (ROP) methodology to make PBI-tagged *tert*-butyl ester-substituted polycaprolactone (PBI-BPCL$_x$) block copolymers. The deprotection of these copolymers yielded carboxylic acid-substituted PBI-CPCL$_x$ amphiphilic block copolymers. The carboxylic blocks were self-assembled to produce stable red-fluorescent nanoparticles of <150 nm in size in aqueous medium with fluorescent quantum yield of ϕ = 0.25−0.30 suitable for bio-imaging application. In vitro studies confirmed that the aliphatic polyester backbone in the PBI-CPCL$_x$ polymer nanoparticles was readily biodegradable by lysosomal enzymes under physiological conditions. Dynamic light scattering, gel permeation chromatography, photophysical studies, and MALDI-TOF-MS analysis provided evidence of the enzymatic biodegradation. Cytotoxicity studies revealed that the PBI-CPCL$_x$ nanoparticles were highly biocompatible toward both cervical cancer and breast cancer cell lines up to a concentration of 100 μg/mL. Confocal microscopy analysis confirmed the uptake and accumulation of red-fluorescent PBI-CPCL$_x$ polymer nanoparticles in the perinuclear environment of the cells. The present approach puts forward a PBI-PCL block copolymer design as enzyme-responsive red-fluorescent nanoprobes for bio-imaging in cancer and normal cells.

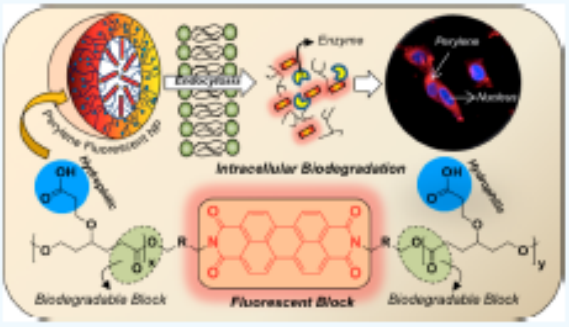

KEYWORDS: *polycaprolactone, block copolymers, perylenebisimide, bio-imaging, enzyme-responsiveness, cancer therapy*

INTRODUCTION

Fluorescent polymer nanoassemblies have gained significant importance in biomedical research as diagnostics and detection probes[1−4] for fundamental understanding of protein folding[5−7] and DNA interactions,[8] for photoacoustic imaging,[9] for photodynamic therapy,[10] and photothermal therapy,[11] etc. The excellent tunability of HOMO−LUMO optical band gaps in π-conjugated polymers created new avenues for imaging opportunities in biological systems.[12] Amphiphilic nanoarchitectures of polyfluorenes and their copolymers,[13−15] squaraines,[16,17] poly(phenylene-vinylenes),[18−20] and poly(phenylene-ethynylenes),[21] are some of the widely explored π-conjugated fluorescent probes. Molecular interactions in optical chromophores, such as aggregation induced emission (AIE),[22−24] aggregation caused quenching (ACQ),[25,26] and photophysical techniques such as two- or three-photon emission[27,28] and fluorescence resonance energy transfer (FRET),[29−31] etc., were also explored in biomedical imaging. Though the π-conjugated polymers provided excellent opportunity in the aforementioned diagnostic technologies, they have structural restrictions for exploration in the domain of intracellular therapeutics such as drug and gene delivery, tissue engineering, and so on. This limitation is partially associated with the non-biodegradability of the C−C and C−N chemical bonds in the backbone; thus, their biodegradation and clearance under physiological conditions is a challenging task. Alternatively, this problem could be overcome by incorporating only a minimal amount of π-conjugated chromophores (<2%) in a completely biodegradable polymer matrix (>98%), which could enable both intracellular degradation and bio-imaging simultaneously under physiological conditions. In the most recent decade, efforts have been taken by us[32−34] and others[35−37] to explore the above concept in a biodegradable aliphatic polyester platform. Tetraphenyl-

Received: August 25, 2019
Accepted: November 1, 2019
Published: November 1, 2019

DOI: 10.1021/acsapm.9b00000
ACS Appl. Polym. Mater. 2019, 1, 3375−3388

BioMACROMOLECULES

pubs.acs.org/Biomac

Article

Biodegradable Polymer Theranostic Fluorescent Nanoprobe for Direct Visualization and Quantitative Determination of Antimicrobial Activity

Runa Ghosh, Mehak Malhotra, Rupali Ravindra Madhuri Sathe, and Manickam Jayakannan*

Cite This: Biomacromolecules 2020, 21, 2896−2912

Read Online

ABSTRACT: We report a biodegradable fluorescent theranostic nanoprobe design strategy for simultaneous visualization and quantitative determination of antibacterial activity for the treatment of bacterial infections. Cationic-charged polycaprolactone (PCL) was tailor-made through ring-opening polymerization methodology, and it was self-assembled into well-defined tiny 5.0 ± 0.1 nm aqueous nanoparticles (NPs) having a zeta potential of +45 mV. Excellent bactericidal activity at 10.0 ng/mL concentration was accomplished in Gram-negative bacterium *Escherichia coli* (*E. coli*) while maintaining their nonhemolytic nature in mice red blood cells (RBC) and their nontoxic trend in wild-type mouse embryonic fibroblast cells with a selectivity index of $>10^4$. Electron microscopic studies are evident of the *E. coli* membrane disruption mechanism by the cationic NP with respect to their high selectivity for antibacterial activity. Anionic biomarker 8-hydroxy-pyrene-1,3,6-trisulfonic acid (HPTS) was loaded in the cationic PCL NP via electrostatic interaction to yield a new fluorescent theranostic nanoprobe to accomplish both therapeutics and diagnostics together in a single nanosystem. The theranostic NP was readily degradable by a bacteria-secreted lipase enzyme as well as by lysosomal esterase enzymes at the intracellular compartments in <12 h and support their suitability for biomedical application. In the absence of bactericidal activity, the theranostic nanoprobe functions exclusively as a biomarker to exhibit strong green-fluorescent signals in live *E. coli*. Once it became active, the theranostic probe induces membrane disruption on *E. coli*, which enabled the costaining of nuclei by red fluorescent propidium iodide. As a result, live and dead bacteria could be visualized via green and orange signals (merging of red+green), respectively, during the course of the antibacterial activity by the theranostic probe. This has enabled the development of a new image-based fluorescence assay to directly visualize and quantitatively estimate the real-time antibacterial activity. Time-dependent bactericidal activity was coupled with selective photoexcitation in a confocal microscope to demonstrate the proof-of-concept of the working principle of a theranostic probe in *E. coli*. This new theranostic nanoprobe creates a new platform for the simultaneous probing and treating of bacterial infections in a single nanodesign, which is very useful for a long-term impact in healthcare applications.

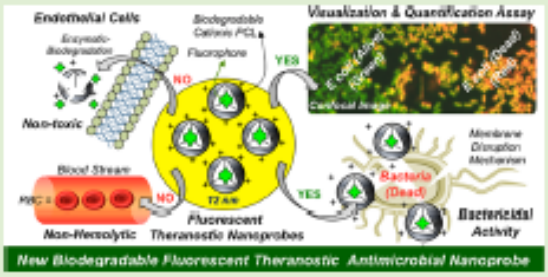

INTRODUCTION

Ever-increasing demand to treat the infectious diseases caused by bacteria, viruses, and other microorganisms in clinical contamination, wound healing, and respiratory chronic obstructive pulmonary diseases has become a major concern in healthcare and society.[1,2] Multidrug resistance and steadfast mutations of microorganisms[3] further obscure the treatment of the infectious diseases with existing drugs or antibiotics.[4] Development of new diagnostic tools and methods are also equally important to accomplish timely required therapeutic efficacies.[5] The next generation of antimicrobial candidates are essential to be smart multitasking probes having the capability to exhibit both therapeutics and diagnostics together (theranostics) in a single system so that maximum impact could be accomplished in a single dose of drug administration.[6,7] Among the diverse diagnostic tools used include fluorescent techniques that provide an excellent opportunity because they require very low probe concentrations and could also be employed under noninvasive protocols under physiological condition. Visible light to NIR-active fluorescent chromophores were encapsulated or tagged in antimicrobial polymers and antimicrobial peptides in the construction of fluorescent theranostic probes. Gold/silver nanoparticle-based photoacoustic[8] and fluorescent imaging,[9,10] NIR fluorophore-tagged silica−polyelectrolyte nanoparticles,[11] ROS-responsive

Received: April 27, 2020
Revised: June 12, 2020
Published: June 15, 2020

https://dx.doi.org/10.1021/acs.biomac.0c00653
Biomacromolecules 2020, 21, 2896−2912